Imidazolium based ionic liquids: Computational studies, synthesis and applications

Thesis submitted to

Cochin University of Science and Technology

in partial fulfilment of the requirements for

the award of degree of

Doctor of Philosophy

in

Chemistry

Under the Faculty of Science

by

Eapen Thomas
Reg. No. 4666

Analytical, Spectroscopy and Ceramics Group
Propellants, Polymers, Chemicals and Materials Entity
Vikram Sarabhai Space Centre
Thiruvananthapuram-695022
Kerala, India

November 2017

भारत सरकार

अंतरिक्ष विभाग

विक्रम साराभाई अंतरिक्ष केन्द्र

तिरुवनन्तपुरम-695 022

केरल, भारत

फोन : (0471) 2564624, 2564751

फैक्स : (0471) 2564096

Government of India
Department of Space
Vikram Sarabhai Space Centre
Thiruvananthapuram-695 022
Kerala, INDIA

Telephone : (0471) 2564624; 2564751

Fax   : (0471) 2564096

Email : benny_george@vssc.gov.in;

kp_vijayalakshmi@vssc.gov.in

दिनांक/Date: 7th November, 2017

CERTIFICATE

This is to certify that the work embodied in the thesis entitled "**Imidazolium based ionic liquids: Computational studies, synthesis and applications**" has been carried out by **Mr. Eapen Thomas** under our supervision and guidance at Analytical and Spectroscopy Division (ASD), Analytical, Spectroscopy and Ceramics Group (ASCG), Propellants, Polymers, Chemicals and Materials Entity (PCM), Vikram Sarabhai Space Centre, Thiruvananthapuram and the same has not been submitted elsewhere for any degree. To the best of our knowledge, the thesis is a bonafide record of research carried out by **Mr. Eapen Thomas** under our supervision. All the relevant corrections and modifications suggested by the audience during the pre-synopsis seminar and recommended by the Doctoral Committee of **Mr. Eapen Thomas** have been incorporated in the thesis.

(Guide)

Dr. K. P. Vijayalakshmi
Scientist/Engineer-SE
ASD/ASCG/PCM
Vikram Sarabhai Space Centre
Thiruvananthapuram

(Co-guide)

Dr. Benny K. George
Scientist/Engineer-G
Group Director, ASCG/PCM
Vikram Sarabhai Space Centre
Thiruvananthapuram

भारतीय अंतरिक्ष अनुसन्धान संगठन   **Indian Space Research Organisation**

DECLARATION

I hereby declare that the Ph.D. thesis entitled "**Imidazolium based ionic liquids: Computational studies, synthesis and applications**" is the outcome of the original work done by me at Analytical and Spectroscopy Division, Analytical, Spectroscopy and Ceramics Group, Propellants, Polymers, Chemicals and Materials Entity, Vikram Sarabhai Space Centre, Thiruvananthapuram, under the joint supervision of Dr. K. P. Vijayalakshmi and Dr. Benny K. George and the same has not form part of any degree, diploma, associateship, or any other title or recognition from any University/Institution.

Thiruvananthapuram-22

6th November, 2017   **(Eapen Thomas)**

Dedicated to my beloved teachers and dearest wife

Acknowledgements

CONTENTS

List of Tables

List of Figures

List of Schemes

xx

List of Abbreviations

$[NH_2tz]^-$	Aminotetrazolate
Br^-	Bromide
$[Tf_2N]^-$	Bis(trifluoromethylsulfonyl) imide
Cl^-	Chloride
$[CNtz]^-$	Cyanotetrazolate
$[dc]^-$	Dicyanamide
$[dn]^-$	Dinitramide
$[dtrz]^-$	Dinitrotriazine
$[PF_6]^-$	Hexafluorophosphate
$[mtz]^-$	Methyl tetrazolate
$[NO_2tz]^-$	Nitrotetrazolate
$[NO_2Otz]^-$	Nitrotetrazolate-2N-oxide
$[BF_4]^-$	Tetrafluoroborate
$[tz]^-$	Tetrazolate
$[trz]^-$	Triazolate anion
$[RMIm]^+$	1-alkyl-3-methylimidazolium
$[RMMIm]^+$	1-alkyl-2,3-dimethylimidazolium
$[C_nMIm]^+$	1-alkyl-3-methylimidazolium cation
$[C_2MIm]^+$	1-ethyl-3-methylimidazolium cation
$[C_4MIm]^+$	1-butyl-3-methylimidazolium cation
$[C_6MIm]^+$	1-hexyl-3-methylimidazolium cation
$[C_{10}MIm]^+$	1-decyl-3-methylimidazolium cation
$[C_{16}MIm]^+$	1-hexadecyl-3-methylimidazolium cation
$[C_nMIm]^+[X]^-$	1-alkyl-3-methylimidazolium-anion ion pair
C_nMIm/MMT	1-alkyl-3-methylimidazolium montmorillonite clay
C_4MIm/MMT	1-butyl-3-methylimidazolium montmorillonite clay
C_6MIm/MMT	1-hexyl-3-methylimidazolium montmorillonite clay
$C_{10}MIm/MMT$	1-decyl-3-methylimidazolium montmorillonite clay
$C_{16}MIm/MMT$	1-hexadecyl-3-methylimidazolium montmorillonite clay
C_4Im	1-butylimidazole
$[C_4MIm]$-2-ylidene	1-butyl-3-methylimidazole-2-ylidene
C_1Im	1-methylimidazole
$[RRIm]^+$	Symmetrical 1,3-dialkylimidazolium ILs
q_e	Adsorbed amount at equilibrium
q_t	Adsorbed amount at time t
A_n	Aggregation number of micelles
ADN	Ammonium dinitramide

AAS	Atomic absorption spectroscopy
AFM	Atomic force microscopy
ATR	Attenuated total reflectance
AM	Austin method
BSSE	Basis set superposition error
B3LYP	Becke three-parameter Lee-Yang-Parr
E_b	Binding energy
BASIL	Biphasic acid scavenging utilizing ionic liquids
B.P.	Boiling point
CHN	Carbon, hydrogen, nitrogen analyzer
CEA	Chemical equilibrium with applications computer code
CNDO	Complete neglect of differential overlap
CC	Coupled cluster theory
cmc	Critical micelle concentration
T_c	Crystallization temperature
DFT	Density functional theory
DSC	Differential scanning calorimetry
EIL	Energetic ionic liquid
EDS	Energy-dispersive X-ray spectroscopy
ΔE^*	Energy gap between highest occupied molecular orbital and lowest unoccupied molecular orbital
ΔH_c	Enthalpy of crystallization
ΔH_c	Enthalpy of crystallization
FE-SEM	Field emission scanning electron microscope
FWO	Flynn-Wall-Ozawa method
FTIR	Fourier transform infrared spectroscopy
G	Gauche
GTOs	Gaussian type orbitals
GGA	generalized gradient approximation
HF	Hartree–Fock Theory
HOMO	Highest occupied molecular orbital
HAN	Hydroxyl ammonium nitrate
INDO	Intermediate neglect of differential overlap
IC	Ion chromatograph
IL	Ionic liquid
KS	Kohn–Sham approach
LDA	Local density approximation
LSDA	Local spin density approximation

LUMO	Lowest unoccupied molecular orbital
T_s	Maximum decomposition temperature
T_m	Melting point
MK charge	Merz-Singh-Kollman charge
MESP	Molecular electrostatic potential plot
MP_n	Møller–Plesset perturbation theory
MMT	Montmorillonite
MD	Molecular dynamics
MM	Molecular mechanics
NDDO	Neglect of diatomic differential overlap
DMAc	N,N'-Dimethylacetamide
NMR	Nuclear magnetic resonance spectroscopy
X_c (%)	Percentage crystallinity
PVDF	Poly(vinylidene fluoride)
PVDF-C4	PVDF-1-butyl-3-methylimidazolium montmorillonite clay composite
PVDF-C6	PVDF-1-hexyl-3-methylimidazolium montmorillonite clay composite
PVDF-C10	PVDF-1-decyl-3-methylimidazolium montmorillonite clay composite
PVDF-C16	PVDF-1-hexadecyl-3-methylimidazolium montmorillonite clay composite
PVDF-MMT	PVDF-montmorillonite clay composite
Py-GC-MS	Pyrolysis gas chromatograph-mass spectrometer
QM/MM	Quantum mechanics/molecular mechanics
RTIL	Room temperature ionic liquid
SCF	Self consistent field
STOs	Slater type orbitals
$MMT\text{-}Na^+$	Sodium montmorillonite clay
Isp	Specific impulse
TIL	Task specific IL
$T_{1\%}$	Temperature for 1 % weight loss
$T_{5\%}$	Temperature for 5 % weight loss
$T_{50\%}$	Temperature for 50 % weight loss
TGA	Thermogravimetric analysis
T	Trans
UTM	Universal testing machine
XRD	X-ray diffraction

List of Publications

A) Articles in Journals

1. **Eapen Thomas**, K. P. Vijayalakshmi, Benny K. George, Imidazolium based energetic ionic liquids for monopropellant applications: A theoretical study. *RSC Advances*, **2015**, 5, 71896-71902.

2. **Eapen Thomas**, Deepthi Thomas, K. P. Vijayalakshmi, Benny K. George, Mechanistic outlook on thermal degradation of 1,3-dialkylimidazolium ionic liquids and organoclays. *RSC Advances*, **2016**, 6, 9421-9428.

3. **Eapen Thomas**, Rekha Krishnan G., Bhuvaneswari S., K. P. Vijayalakshmi, Benny K. George, 1,3-Dialkylimidazolium modified clay sorbents for perchlorate removal from water. *RSC Advances*, **2016**, 6, 80029-80036.

4. **Eapen Thomas**, Parvathy C., Nisha Balachandran, Bhuvaneswari S., K. P. Vijayalakshmi, Benny K. George, PVDF-Ionic liquid modified clay nanocomposites: Phase changes and shish-kebab structure. *Polymer*, **2017**, 115, 70-76.

5. **Eapen Thomas**, Deepthi Thomas, Bhuvaneswari S., K. P. Vijayalakshmi, Benny K. George, 1-Hexadecyl-3-methylimidazolium chloride: Structure, thermal stability and decomposition mechanism. *Journal of Molecular Liquids*, **2017,** DOI: 10.1016/j.molliq.2017.11.029.

6. **Eapen Thomas**, K. P. Vijayalakshmi, Benny K. George, Effect of alkyl chain length on cationic and ion-pair stability of 1-alkyl-3-methylimidazolium chloride ionic liquids. (*under preparation*).

B) Papers presented in conferences

1. Eapen Thomas, K. P. Vijayalakshmi, Benny K. George, 'DFT studies on thermochemical properties of energetic ionic liquids', International High Energy Materials Conference and Exhibits (HEMCE-2014), VSSC, Thiruvananthapuram, February 13-15, 2014.

2. Eapen Thomas, Nisha Balachandran, K. P. Vijayalakshmi, Sadhana R., Benny K. George, 'Functionalization of nanoclay with ionic liquids', National Conference on Materials Science and Technology (NCMST-2014), IIST, Thiruvananthapuram, July 28-30, 2014.

3. Eapen Thomas, Deepthi Thomas, K. P. Vijayalakshmi, Benny K. George, 'Thermal decomposition of ionic liquids and functionalized clay : Py-GC-MS and DFT study', National Conference on Advanced Technologies for Material Processing and Diagnostics (ISAS-2014), Kochi, September 18-20, 2014,

4. Eapen Thomas, Deepthi Thomas, K. P. Vijayalakshmi, Benny K. George, 'Synthesis and thermal characterization of 1-hexadecyl-3-methylimidazolium chloride', National Conference on Analytical Science and Technology (ISAS-2015), Munnar, September 24-26, 2015.

5. Eapen Thomas, Rekha Krishnan G., K. P. Vijayalakshmi, Benny K. George, 'Ionic liquid modified clay for removal of perchlorate from water', National Conference on Ionic liquids for Clean Energy and Environment (ILCEE-2015), Pune, December 16-17, 2015.

6. Eapen Thomas, K. P. Vijayalakshmi, Benny K. George, 'Theoretical studies on imidazolium based energetic ionic liquids for monopropellant applications', International Conference on High Energy Materials and Exhibits (HEMCE-2016), Hyderabad, February 11-13, 2016.

7. Eapen Thomas, Bhuvaneswari S, K. P. Vijayalakshmi, Benny K. George, 'A peek into the intergalleries of 1-alkyl-3-methylimidazolium modified MMT clay by Raman Spectroscopy, International Conference on Perspectives in Vibrational Spectroscopy (ICOPVS-2016) Lucknow, November 5-8, 2016.

8. Eapen Thomas, Bhuvaneswari S, K. P. Vijayalakshmi and Benny K. George, 'Formation of shish-kebab structure in poly(vinylidene fluoride)-ionic liquid modified clay nanocomposite', International Conference on Polymer Science and Technology (MACRO-2017), Thiruvananthapuram, January 8-11, 2017.

Synopsis

The scope of this research work involves design and development of imidazolium based ionic liquids (IL) and IL modified clay for space related applications. The thesis is divided into following chapters.

Chapter 1: Introduction

Chapter 1 gives an introduction to 1-alkyl-3-methylimidazolium ILs, its properties and various explored applications. The objectives of the present investigations and the motivation behind the work also form an integral part of this chapter.

Chapter 2: Computational and experimental methodologies

Detailed description of various computational methods and experimental techniques adopted in the present study is given.

Chapter 3: Computational studies on ionic liquids

Part I: Energetic ionic liquids (EILs)

The energetic properties of 1-ethyl-3-methylimidazolium based ionic liquids were investigated by suitably selecting the pairing anions containing energetic groups. The key property, the molar heat of formation, to determine the specific impulse was computed using ab initio method as implemented in *Gaussian 09* software. The accuracy of ab initio method was proved with compounds of known heat of formation values. Based on the studies new ionic liquids were predicted with equivalent or better specific impulse than the currently used hydrazine monopropellant.

Part II: Screening of ILs for clay modification

The structure and stability of imidazolium based ionic liquids were investigated using *Gaussian 09* software. The effect of alkyl chain length and pairing anions in 1-alkyl-3-methylimidazolium, $[RMIm]^+$ based ionic liquids were explored using computed parameters like Mulliken charge on the ring, charge transfer features from molecular electrostatic potential mapping and HOMO-LUMO energy gap at B3LYP level of density functional theory (DFT). Based on the studies $[C_4MIm]^+$, $[C_6MIm]^+$, and $[C_{16}MIm]^+$ based ILs were selected for experimental studies.

Chapter 4: Synthesis of designed ionic liquids for clay modification and experimental validation

Chapter 4 describe the synthesis and characterization of designed ILs for clay modification. $[C_6MIm]^+[Cl]^-$ and $[C_{16}MIm]^+[Cl]^-$ were synthesized by refluxing 1-methylimidazole with 1-chloro hexane and 1-chloro hexadecane respectively with 95 % yield. Commercially available $[C_4MIm]^+[Cl]^-$ and $[C_4MIm]^+[BF_4]^-$ were also used for experimental validation of computational studies. Thermal stability of ILs were analyzed using TG, decomposition products were identified using pyrolysis GC-MS (Py-GC-MS), activation energy for thermal decomposition was calculated by Kissinger method and Flynn-Wall-Ozawa method (FWO method). The experimental activation energy was comparable with theoretically calculated values at B3LYP level of DFT. The experimental results were remarkably conforming to the theoretical studies described in chapter 3.

Chapter 5: Modification of clay using ILs

Sodium montmorillonite clay was modified using cation exchange reaction of Na^+ with $[RMIm]^+$. The modification was followed using FTIR analysis, improved d-spacing in XRD, CHN analysis and TG analysis. The cation exchange efficiency was 60 – 64 %. The modified clay showed decrease in thermal stability with respect to increase in alkyl chain length complimenting the theoretical prediction. The decomposition products of modified clays were identified using Py-GC-MS and activation energy was calculated using FWO method. The predicted carbene mechanism was established by identifying 1-butyl-3-methylimidazol-2-ylidine using ^{13}C NMR spectroscopy.

Chapter 6: Perchlorate removal from water using IL modified clay

Ionic liquid modified clay was used for perchlorate adsorption from water. $C_{16}MIm/MMT$ showed the highest adsorption of 15.6 mg/g from 1000 ppm perchlorate solution at pH =2 and contact time of 15 min. The d-spacing of $C_{16}MIm/MMT$ (18.55 Å) decreased to 13.7 Å on perchlorate adsorption and observed a conformational change in $[C_{16}MIm]^+$ inside the clay gallery from trans to gauche, suggesting the possible formation of $[C_{16}MIm]^+[ClO_4]^-$ inside the clay gallery.

Chapter 7: PVDF- IL modified clay nanocomposite

Poly(vinylidene fluoride) (PVDF) exists mainly in α-phase and β-phase. α-phase is stable while β-phase finds electrical application. The phase conversion was done in presence of 2 % loading of IL modified clay. The phase change increased with alkyl chain length of imidazolium cation and 99 % β-phase was obtained with PVDF-C16-Clay nanocomposite from pristine PVDF (43 % β-phase). The phase conversion was confirmed using FTIR, XRD, DSC analysis and improved electrical properties. PVDF-C4 showed equal proportion of α and β-phases and resulted in self reinforced shish-kebab structure while PVDF, PVDF-pristine clay, PVDF-C6, PVDF-C16 showed spherulite morphology. The shish-kebab formation in PVDF-C4 was confirmed from improved thermal and mechanical properties. The shish-kebab formation was analyzed using computational studies and observed extended chain α-phase forms the 'shish' and folded chain β-phase forms the kebab.

Chapter 8 summarises the important results detailed in this thesis and also provides the future scope for this study.

xxx

Introduction
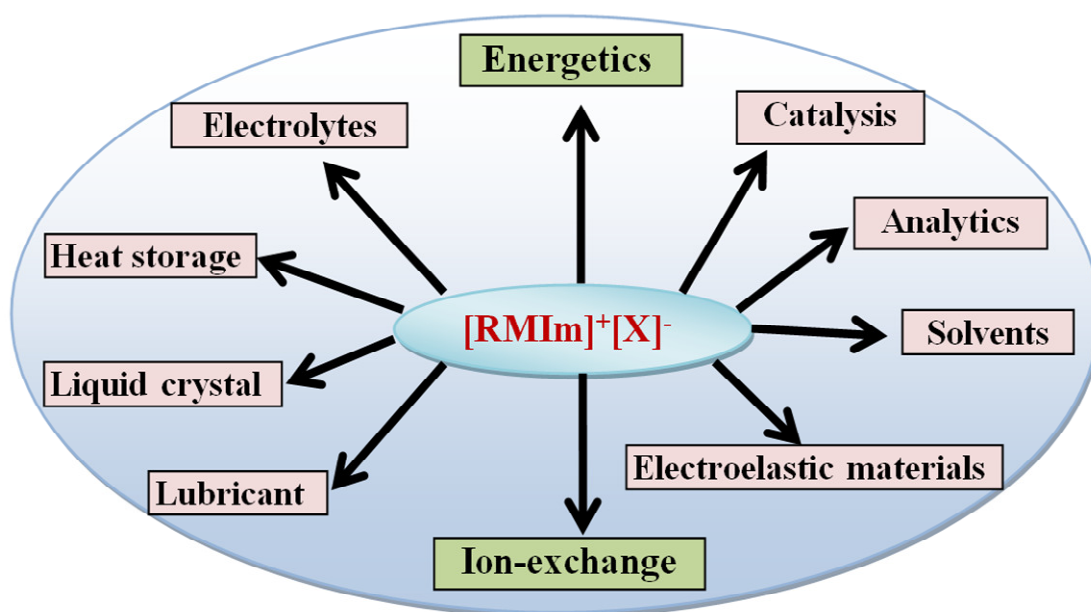
Abstract

　　Chapter 1 gives an overview on ionic liquids; detailed description of imidazolium based ionic liquids, their various properties and explored applications. The objectives of the present investigations and the motivation behind the work also form an integral part of the present chapter.

1.1 Introduction to ionic liquids

　　Ionic liquids (ILs) are a class of novel compounds typically composed of organic cations and inorganic or organic anions with melting point less than 100 ^{o}C. ILs as a "green" alternative for volatile, flammable and often toxic popular organic solvents evoked increased interest in the last two decades. ILs unique advantage of "designability" by selecting a proper cation and anion to obtain a compound with desired properties directly translates into potential applications of ILs in various technological processes [Sun *et al*. 2017; Nandwani *et al*. 2017; Troter *et al*. 2016; Chiappe and Pieraccini 2005]. ILs are rather unique in the sense that in addition to ionic and covalent interactions, there are relatively weaker interactions such as H-bondings and π-stacking, which are not commonly found in conventional solvents [Saha and Hamaguchi 2006]. The nature of the forces in different ILs may however differ from one another and mainly control their physical properties.

　　Major types of cations in ILs include ammonium, phosphonium, imidazolium, pyridinium and pyrrolidinium. Typical counter anions are chloride (Cl$^-$), bromide (Br$^-$), tetrafluoroborate (BF$_4^-$), hexafluorophosphate (PF$_6^-$), dicyanamide (dc) and bis(trifluoromethylsulfonyl) imide (Tf$_2$N) (Figure 1.1).
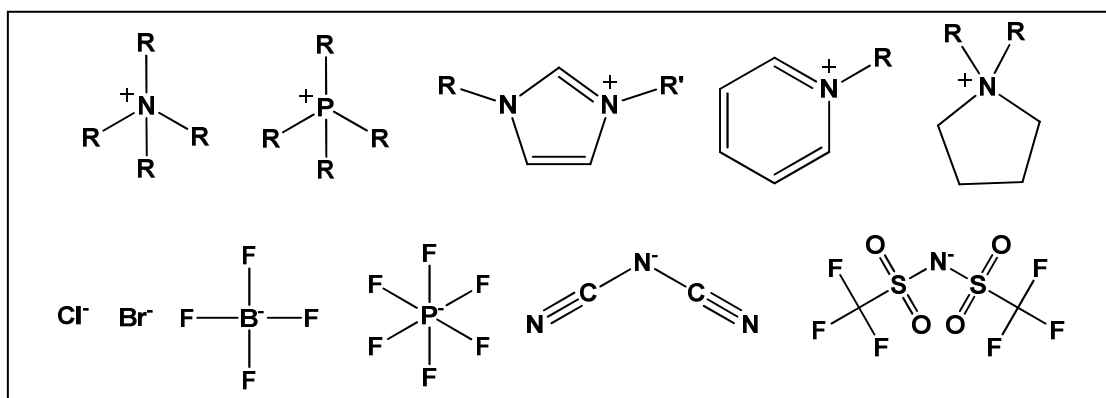
Figure 1.1 Ammonium, phosphonium, imidazolium, pyridinium and pyrrolidinium cations with typical counter anions in ILs.

The number of possible combinations of cations and anions were estimated to be at level of 10^{18} [Holbrey and Seddon 1999]. Such a great diversity makes it possible to design a structure that will provide optimum properties for very specific purposes. This makes computational methods a sole solution provider for selecting an IL for a specific property/application from this pool of ion-pairs. Theoretical calculations were used to predict molecular structure and interactions present in room temperature ILs. Katsyuba *et al*. [2007] have investigated possible variations of molecular structure of the ion pairs of several imidazolium based ILs by density functional theory method [DFT]. Molecular modeling simulation based on the force field is a powerful tool to predict solvent properties. Derecskei *et al*. [2008] investigated the density and two-component solubility parameter of a variety of ILs using atomistic level molecular modeling and the Materials Studio software package. The COSMO-RS (Conductor like Screening model for Real Solvents) [Klamt 1995] method based on quantum chemistry calculations was used to predict the specific density and molar liquid volume of imidazolium based ILs [Palomar *et al*. 2007]. Many quantitative correlations have been established to help in predicting physico-chemical properties and accelerate the exploration for new ILs [Katritzky *et al*. 2002]. A linear correlation of melting points (T_m, K) and binding energies (E_b, kJ/mol) were observed for dialkylimidazolium cation and different anion pairs *viz*. chloride, bromide, tetrafluoroborate and hexafluorophosphate [Dong *et al*. 2006]. Ye *et al*. [2007] proposed a group contribution model to estimate the density of ionic liquid. The model was checked by predicting 59 common imidazolium, pyridinium, pyrrolidinium, tetraalkylammonium, and phosphonium based room temperature ILs. Guan *et al*. [2010] presented a group contribution method to predict the molecular volume, the standard molar entropy, the surface tension and the molar enthalpy of vaporization of 1-alkyl-3-methylimidazolium glutamate ionic liquid.

The first report on low melting salt, ethanolammonium nitrate (T_m = 52 ^{o}C) was published in 1888 by Gabriel and Weiner. In 1914, first low-temperature ionic liquid, ethylammonium nitrate (T_m = 12 °C) was reported by Walden, later known as the father of ILs. The studies aimed to find an electrolyte for the thermal battery by U.S. Air Force Academy in 1960s marked the changing phase of ILs. King *et al*. in 1968, developed a cell containing an ionic liquid produced by the reaction of aluminium chloride with 1-ethylpyridinium bromide as an electrolyte.

The use of ionic liquids, although discovered a long time ago, was very limited until the late 1990s to few examples in electrochemistry and organic chemistry. This changed unexpectedly as a result of an article published by Freemantle in 1998, describing the potential applications of ionic liquids as novel solvents for green chemistry. Since then, ionic liquids have been the interest of many researchers, resulting in an expansion of the application field. So far, applications of ionic liquids have been reported in analytical chemistry [Berthod *et al.* 2008], biochemistry [Freemantle 2010], catalysis [Sheldon 2001; Zhao *et al.* 2002; Parvulescu and Hardacre 2007], electrochemistry [Buzzeo *et al.* 2004; MacFarlane *et al.* 2007], separation technology [Huddleston *et al.* 1998; Buzzeo *et al.* 2005; Han and Armstrong 2007], fluid engineering [Zhao 2006] and so on. ILs are nowadays used at industrial scale in the BASIL™ (Biphasic acid scavenging utilizing ionic liquids) process.
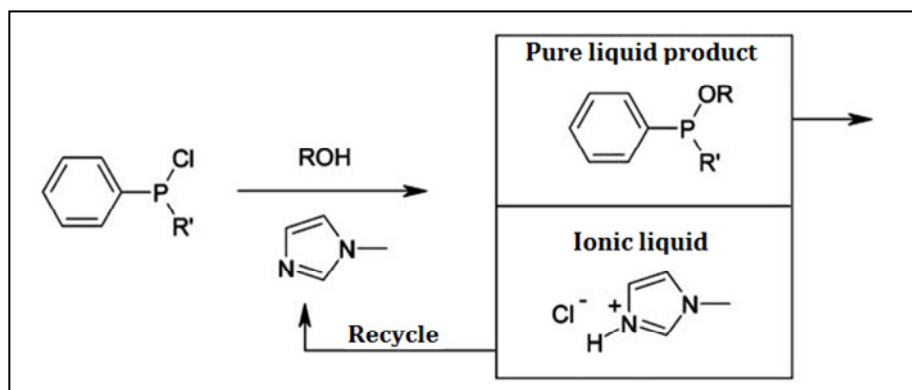
Scheme 1.1 The BASIL^TM process.

In 2002, BASF, as one of the first companies, has implemented a technology BASIL^TM for the production of the generic photoinitiator precursor alkoxyphenylphosphines (Scheme 1.1). In the original process, triethylamine was used to scavenge the acid that was formed in the course of the reaction, but this made the reaction mixture difficult to handle as the waste by-product, triethylammonium chloride formed a dense insoluble paste. Replacing triethylamine with 1-methylimidazole results in the formation of 1-methylimidazolium chloride, an ionic liquid, which separates out of the reaction mixture as a discrete phase. The yield increased from 50 to 98 % in this new process. 1-Methylimidazole is recycled, *via* base decomposition of 1-H-3-methylimidazolium chloride.

A breakthrough report on dissolving cellulose in ILs without any auxiliary substances [Swatloski *et al.* 2002] opened new possibilities in biomass processing and

contributed to an intensified research on biopolymer solubility in ILs. The dissolved cellulose can be recovered by addition of water to the ionic liquid. The water breaks up the cellulose–anion hydrogen bonds and precipitates the cellulose in a structurally disrupted form that is easier for enzymes to cleave into fermentable sugars to make ethanol [Dadi *et al*. 2007]. Ionic liquids have been used to solubilize other natural biopolymers in addition to cellulose, such as silk [Mantz *et al*. 2007] and wool keratin [Xie *et al*. 2005] and to make hybrid biopolymer materials with exotic items such as magnetic nanoparticles [Sun *et al*. 2008] and carbon nanotubes [Zhang *et al*. 2007]. ILs have enabled the exploitation of cheap, renewable biopolymers in many applications that used to be the province of fossil fuel-derived plastics.

ILs have been exploited as green solvents in many synthetic processes [Wasserscheid and Welton 2007]. At the industrial level, many chemical processes have been successfully implemented such as methanol carbonylation, oligomerization, hydrosilylation, acid catalysis and isobutane-butene alkylation [Durgal and Mishra 2016]. Besides organic syntheses, ionic liquids have also been exploited in syntheses of inorganic materials such as metal nanoparticles, metal oxides, metal chalcogenides, metal salts and zeolites [Durgal and Mishra 2016].

1.2 Imidazolium based ILs

Room temperature ILs (RTILs) based on 1-alkyl-3-methylimidazolium salts were first reported in 1982 by Wilkes *et al*. by combining 1-ethyl-3-methylimidazolium chloride with aluminium chloride and later it was used as a solvent in the Friedel-Crafts reaction proving its catalytic activity by Boon *et al*. in 1986. It was observed that imidazolium chloroaluminates (known as first generation imidazolium ILs) were sensitive to atmospheric moisture and their processing required anhydrous conditions. The first generation includes ILs in which the cation and anion structures were chosen to obtain a product of specific physical properties. Ions of the first generation ILs were selected to achieve specific values of melting point, density, viscosity, thermal stability, hydrophilicity/hydrophobicity and refractive index [Hough *et al*. 2007]. The effect of the cation or anion structures on conductivity translates into their specific applications as electrolytes [Lewandowski and Mocek 2009].

Replacement of moisture sensitive anion by the tetrafluoroborate ion and other anions led in 1992, to air and water stable (second generation) ILs [Wilkes *et al*. 1992]. The usefulness of the second generation ionic liquids is a result of both suitable

physical parameters and chemical properties. This includes reactivity, chirality [Roszak *et al.* 2011], solvating ability and ability to extract various chemical substances [Holbrey and Seddon 1999]. Davis in 2004, introduced task specific ILs (TILs, third generation), in which the anion, cation, or both covalently incorporate a functional group to provide them particular properties, either physical or chemical or in terms of reactivity. Energetic ionic liquids [Katritzky *et al.* 2005] and chemical reaction catalysts [Boon *et al.* 1986, Erfurt *et al.* 2014] belongs to the category of TILs.

Selection of the imidazolium ring as a cation is often due to its stability within oxidative and reductive conditions [Weingarth *et al.* 2012], thermal stability, low viscosity and ease of synthesis [Wang *et al.* 2010]. The major classes of imidazolium based ILs include 1-alkyl-3-methylimidazolium ([RMIm]$^+$), 1-alkyl-2,3-dimethylimidazolium ([RMMIm]$^+$) and symmetrical 1,3-dialkylimidazolium ILs ([RRIm]$^+$) (Figure 1.2).
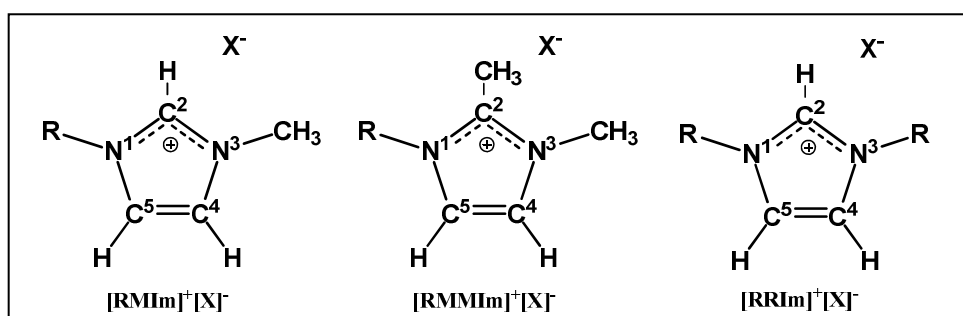
Figure 1.2 Major classes of imidazolium based ILs.

Symmetrical ILs (e.g.[RRIm]$^+$[X]$^-$) tend to pack more effectively in the solid state, and tend to form salts with higher melting points. However, for most applications a lower melting point is preferred for ionic liquids. This is one of the reasons that in many cases the cation with a reduced symmetry (e.g. 1-butyl-3-methylimidazolium, [C$_4$MIm]$^+$) is preferred. The work presented in this thesis mainly focuses on 1-alkyl-3-methylimidazolium based ILs.

1.3 Properties of 1-alkyl-3-methylimidazolium based ILs

1.3.1 Melting point

The key criterion for the evaluation of an ionic liquid is its melting point. In literature, the following features are discussed of low melting salts; (i) low symmetry [Seddon 1997; Seddon 1996], (ii) weak intermolecular interactions [Benhote *et al.* 1996; Elaiwi *et al.* 1995] and (iii) good distribution of charge in the cation [Stegemann

et al. 1992]. Alkali metal chlorides exhibit very high melting temperatures (803 ^{o}C for NaCl and 772 ^{o}C for KCl) whereas organic cation-inorganic/organic anion pairs showed drastic decrease in melting temperatures. Table 1.1 shows the melting points of [RMIm]Cl and [C$_2$MIm]$^+$[X]$^-$ ion-pairs. In the case of [RMIm]Cl, melting point decreases from [C$_1$MIm]Cl to [C$_8$MIm]Cl and then increases (Figure 1.3). [C$_6$MIm]Cl showed a glass transition (T$_g$) at -65 ^{o}C and no melting was observed. Besides the cation, the anion also influences the melting point. Comparison of melting points of different salts with 1-ethyl-3-methylimidazolium cation ([C$_2$MIm]$^+$) showed a decrease in the melting point with an increasing size of the anion of same charge.

Table 1.1 Melting point of [RMIm]Cl and [C$_2$MIm]$^+$[X]$^-$.

IL	M.P. (^{o}C)	Reference
[C$_1$MIm]$^+$[Cl]$^-$	125	Wasserscheid and Keim 2000
[C$_2$MIm]$^+$[Cl]$^-$	87	[Wilkes *et al.*1982]
[C$_2$MIm]$^+$[Br]$^-$	79	[Ngo *et al.*2000]
[C$_2$MIm]$^+$[PF$_6$]$^-$	60	[Fuller *et al.*1994]
[C$_2$MIm]$^+$[NO$_3$]$^-$	38	[Wilkes *et al.*1992]
[C$_2$MIm]$^+$[BF$_4$]$^-$	6	[Holbrey and Seddon 1999]
[C$_2$MIm]$^+$[Tf$_2$N]$^-$	4	[Huddleston *et al.* 2001]
[C$_3$MIm]$^+$[Cl]$^-$	60	[Fannin *et al.* 1984]
[C$_4$MIm]$^+$[Cl]$^-$	41	[Huddleston *et al.* 2001]
[C$_6$MIm]$^+$[Cl]$^-$	-65*	[This work] * indicates T$_g$ in ^{o}C.
[C$_8$MIm]$^+$[Cl]$^-$	12	[Domanska *et al.* 2003]
[C$_{10}$MIm]$^+$[Cl]$^-$	32	[This work]
[C$_{12}$MIm]$^+$[Cl]$^-$	44.5	[Bradley *et al.* 2002],
[C$_{14}$MIm]$^+$[Cl]$^-$	49.1	[Bradley *et al.* 2002]
[C$_{16}$MIm]$^+$[[Cl]$^-$	66.7	[Bradley *et al.* 2002]
[C$_{18}$MIm]$^+$[Cl]$^-$	71.7	[Bradley *et al.* 2002]

Figure 1.3 Variation of melting point with alkyl chain length in RMImCl.

1.3.2 Density of [RMIm]⁺[X]⁻

The reported density values of [RMIm]$^+$[X]$^-$ ILs are shown in Table 1.2. The density of ILs decreased with increase in alkyl chain length for similar anions. For the same cation, density increases with size of the anion; Cl$^-$ > BF$_4^-$ > PF$_6^-$ > Tf$_2$N. The density and its dependence on temperature and pressure are considered as important thermo-physical properties. These parameters are necessary for analyzing isothermal compressibility, thermal expansion, for the construction of equations of state, and so on. They are useful for designing industrial processes such as storage vessel sizing. The densities of ILs can be tuned by adjusting the structure of anions or cations.

Table 1.2 Density of [RMIm]$^+$[X]$^-$.

IL	Density	Reference
[C$_1$MIm]$^+$Cl$^-$	1.14	[Fannin *et al*. 1984]
[C$_2$MIm]$^+$Cl$^-$	1.14	[Fannin *et al*. 1984]
[C$_3$MIm]$^+$Cl$^-$	1.10	[Fannin *et al*. 1984]
[C$_4$MIm]$^+$Cl$^-$	1.08	[Huddleston *et al*. 2001; Visser *et al*. 2002]
[C$_6$MIm]$^+$Cl$^-$	1.03	[Huddleston *et al*. 2001; Visser *et al*. 2002]
[C$_8$MIm]$^+$Cl$^-$	1.01	[Letcher and Deenadayalu 2002]
[C$_2$MIm]$^+$[BF$_4$]$^-$	1.27	[Fan *et al*. 2016]
[C$_3$MIm]$^+$[BF$_4$]$^-$	1.24	[Nishida *et al*. 2003]
[C$_4$MIm]$^+$[BF$_4$]$^-$	1.19	[Wu *et al*. 2001]
[C$_6$MIm]$^+$[BF$_4$]$^-$	1.14	[Sanmamed *et al*. 2007]
[C$_8$MIm]$^+$[BF$_4$]$^-$	1.08	[Branco *et al*. 2002]
[C$_4$MIm]$^+$[PF$_6$]$^-$	1.35	[Huddleston *et al*. 2001; Visser *et al*. 2002]
[C$_5$MIm]$^+$[PF$_6$]$^-$	1.33	[Chun *et al*. 2001]
[C$_6$MIm]$^+$[PF$_6$]$^-$	1.29	[Huddleston *et al*. 2001]
[C$_7$MIm]$^+$[PF$_6$]$^-$	1.26	[Dzyuba and Bartsch 2002]
[C$_8$MIm]$^+$[PF$_6$]$^-$	1.22	[Huddleston *et al*. 2001]
[C$_1$MIm]$^+$[Tf$_2$N]$^-$	1.56	[Bonhôte *et al*. 1996]
[C$_2$MIm]$^+$[Tf$_2$N]$^-$	1.52	[Bonhôte *et al*. 1996; Matsumoto *et al*. 2002]
[C$_3$MIm]$^+$[Tf$_2$N]$^-$	1.47	[Dzyuba and Bartsch 2002]
[C$_4$MIm]$^+$[Tf$_2$N]$^-$	1.43	[Bockris *et al*. 1970]
[C$_5$MIm]$^+$[Tf$_2$N]$^-$	1.40	[Dzyuba and Bartsch 2002]
[C$_6$MIm]$^+$[Tf$_2$N]$^-$	1.37	[Dzyuba and Bartsch 2002]
[C$_7$MIm]$^+$[Tf$_2$N]$^-$	1.34	[Dzyuba and Bartsch 2002]
[C$_8$MIm]$^+$[Tf$_2$N]$^-$	1.32	[Dzyuba and Bartsch 2002]
[C$_9$MIm]$^+$[Tf$_2$N]$^-$	1.30	[Dzyuba and Bartsch 2002]

   Usually the densities of imidazolium based ILs are larger than 1 g/cm^3, while phosphonium based ILs have a density less than 1 g/cm^3, so in the imidazolium-based ionic liquid and water binary systems, the water rich phase is usually the top phase. The density of ammonium based ILs range from 1.08 to 1.37 g/cm^3 [Kilaru *et al*. 2007]. Gardas *et al*. provided experimental density data and correlation results over a wide range of temperature and pressure to understand the influence of cations on the physicochemical properties of the ILs [Gardas *et al*. 2008].

1.3.3 Viscosity of [RMIm]$^+$[X]$^-$

   Table 1.3 shows the reported viscosity values of [RMIm]$^+$[X]$^-$. Viscosity increased with alkyl chain length of cations with similar anions at constant temperature. [C$_n$MIm]$^+$[Tf$_2$N]$^-$ ion-pairs showed lower viscosity compared to [C$_n$MIm]$^+$[BF$_4$]$^-$ and [C$_n$MIm]$^+$[PF$_6$]$^-$ ion-pairs.

Table 1.3 Viscosity of [RMIm]$^+$[X]$^-$.

IL	Viscosity η (cP)	Temp. (^{o}C)	Reference
[C$_2$MIm]$^+$[BF$_4$]$^-$	37	25	[Nishida *et al*. 2003]
[C$_3$MIm]$^+$[BF$_4$]$^-$	103	25	[Nishida *et al*. 2003]
[C$_4$MIm]$^+$[BF$_4$]$^-$	219	25	[Wu *et al*. 2001]
[C$_6$MIm]$^+$[BF$_4$]$^-$	314	25	[Seddon *et al*. 2000]
[C$_8$MIm]$^+$[BF$_4$]$^-$	135	20	[Branco *et al*. 2002]
[C$_{10}$MIm]$^+$[BF$_4$]$^-$	416	20	[Branco *et al*. 2002]
[C$_4$MIm]$^+$[PF$_6$]$^-$	312	25	[Wu *et al*. 2001]
[C$_6$MIm]$^+$[PF$_6$]$^-$	560	25	[Liu *et al*. 2003]
[C$_8$MIm]$^+$[PF$_6$]$^-$	682	25	[Huddleston *et al*. 2001]
[C$_2$MIm]$^+$[Tf$_2$N]$^-$	34	25	[Matsumoto *et al*. 2002]
[C$_4$MIm]$^+$[Tf$_2$N]$^-$	54	25	[Wu *et al*. 2001]
[C$_6$MIm]$^+$[Tf$_2$N]$^-$	87	20	[Hardacre *et al*. 2002]
[C$_8$MIm]$^+$[Tf$_2$N]$^-$	119	20	[Evans *et al*. 2003]
[C$_{10}$MIm]$^+$[Tf$_2$N]$^-$	153	20	[Evans *et al*. 2003]

1.3.4 Conductivity of [RMIm]$^+$[X]$^-$

   The reported conductivity values of [RMIm]$^+$[X]$^-$ ion-pairs are shown in Table 1.4. [RMIm]$^+$[Cl]$^-$ ion-pairs showed higher conductivity values.

Table 1.4 Conductivity of $[RMIm]^+[X]^-$.

IL	Conductivity (S/m)	Temp. (^{o}C)	Reference
$[C_1MIm]^+Cl^-$	11.8	25	[Fannin et al. 1984]
$[C_2MIm]^+Cl^-$	0.34-3.71	25	[Fannin et al. 1984]
$[C_3MIm]^+Cl^-$	0.33-4.97	25	[Fannin et al. 1984]
$[C_2MIm]^+[BF_4]^-$	1.31	25	[Fuller et al. 1997]
$[C_3MIm]^+[BF_4]^-$	0.59	25	[Nishida et al. 2003]
$[C_2MIm]^+[PF_6]^-$	0.13	22	[Nanjundiah et al. 1997]
$[C_4MIm]^+[PF_6]^-$	0.15	25	[Suarez et al. 1998]
$[C_1MIm]^+[Tf_2N]^-$	0.84	20	[Bonhôte et al. 1996]
$[C_2MIm]^+[Tf_2N]^-$	0.92	25	[Matsumoto et al. 2000]
$[C_3MIm]^+[Tf_2N]^-$	0.25	25	[Koch et al. 1995]
$[C_4MIm]^+[Tf_2N]^-$	0.39	20	[Bonhôte et al. 1996]

1.3.5 Surface tension

The experimental values show that both the anion and cation have an influence on the surface tensions of ILs (Table 1.5). The increase in the cation alkyl chain length reduces the surface tension values. Similarly, an increase in the size of the anion leads to a decrease on the surface tensions [Freire et al. 2007]. The measured data presents surface tension values higher than conventional organic solvents, such as methanol (22.07 mN m^{-1}) and acetone (23.5 mN m^{-1}), but still lower than those of water (71.98 mN m^{-1}).

Table 1.5 Surface tension of ILs at 293.15 K.

IL	Surface tension (mN m^{-1})	Reference
$[C_4MIm]^+[BF_4]^-$	44.8	
$[C_4MIm]^+[PF_6]^-$	44.1	
$[C_4MIm]^+[Tf_2N]^-$	33.6	[Freire et al. 2007]
$[C_6MIm]^+[BF_4]^-$	39.0	
$[C_8MIm]^+[BF_4]^-$	34.1	
$[C_8MIm]^+[PF_6]^-$	35.2	

ILs find wide application as surfactants. Table 1.6 shows the aggregation number of micelles and critical micelle concentration of long chain $[RMIm]^+[X]^-$. The critical micelle concentration decreased with the length of hydrophobic chain.

Table 1.6 Aggregation number of micelles (A_n) and critical micelle concentration (cmc) of long chain $[RMIm]^+[X]^-$.

IL	A_n	cmc (mM)	Reference
$[C_6MIm]^+[Cl]^-$	-	900	[Blesic *et al*. 2007]
$[C_8MIm]^+[Cl]^-$	-	220	[Blesic *et al*. 2007]
$[C_{10}MIm]^+[Cl]^-$	13.4	58.2	[Sarac *et al*. 2017]
$[C_{12}MIm]^+[Cl]^-$	16.3	15.2	[Sarac *et al*. 2017]
$[C_{14}MIm]^+[Cl]^-$	20.6	3.70	[Sarac *et al*. 2017]
$[C_{16}MIm]^+[Cl]^-$	11.1	0.92	[Sarac *et al*. 2017]
$[C_{18}MIm]^+[Cl]^-$	-	0.43	[Luczak *et al*. 2010]
$[C_8MIm]^+[Br]^-$	-	74	[Vanyur *et al*. 2007]
$[C_{10}MIm]^+[Br]^-$	-	41	[Vanyur *et al*. 2007]
$[C_{12}MIm]^+[Br]^-$	16.8	10.5	[Sarac *et al*. 2017]
$[C_{14}MIm]^+[Br]^-$	-	2.80	[Vanyur *et al*. 2007]
$[C_{16}MIm]^+[Br]^-$	-	0.55	[Dong *et al*. 2008]
$[C_4MIm]^+[BF_4]^-$	-	850	[Comelles *et al*. 2014]

1.3.6 Electrochemical window

Electrochemical window of a substance is the voltage range between which the substance is neither oxidized nor reduced. The electrochemical window is one of the most important characteristics to be identified for solvents and electrolytes used in electrochemical applications. The electrochemical window of reported $[RMIm]^+[X]^-$ ion-pairs are shown in Table 1.7. ILs have attracting features to be used as electrolytes in electrochemical devices, due to their wide electrochemical window, low vapor pressure and high ionic conductivity.

Table 1.7 Electrochemical window of $[RMIm]^+[X]^-$.

IL	Electrochemical window (V)	Reference
$[C_2MIm]^+[Cl]^-$	5.00	[Fuller *et al*. 1997]
$[C_4MIm]^+[Cl]^-$	5.40	[Suarez *et al*. 1997]
$[C_2MIm]^+[Tf_2N]^-$	4.30	[Nanjundiah *et al*. 1997]
$[C_4MIm]^+[Tf_2N]^-$	4.76	[Evans *et al*. 2003]
$[C_8MIm]^+[Tf_2N]^-$	4.83	[Evans *et al*. 2003]
$[C_{10}MIm]^+[Tf_2N]^-$	4.89	[Evans *et al*. 2003]
$[C_2MIm]^+[BF_4]^-$	4.30	[Fuller *et al*. 1997]
$[C_4MIm]^+[PF_6]^-$	5.95	[Suarez *et al*. 1997]

1.3.7 Thermal stability

$[RMIm]^+[X]^-$ ion-pairs show a higher thermal stability depending on the counter anion. Thermal stability of these ILs lead to numerous high temperature applications

replacing conventional alkyl ammonium salts. Table 1.8 shows decomposition temperature of typical [RMIm]$^+$[X]$^-$ ion-pairs.

Table 1.8 Decomposition temperature (T$_d$) of [RMIm]$^+$[X]$^-$.

IL	T$_d$ (°C)	Reference
[C$_2$MIm]$^+$[Cl]$^-$	281	[Ngo *et al*. 2000]
[C$_3$MIm]$^+$[Cl]$^-$	281	[Ngo *et al*. 2000]
[C$_4$MIm]$^+$[Cl]$^-$	254	[Huddleston *et al*. 2001; Visser *et al*. 2002]
[C$_6$MIm]$^+$[Cl]$^-$	253	[Huddleston *et al*. 2001; Visser *et al*. 2002]
[C$_8$MIm]$^+$[Cl]$^-$	243	[Huddleston *et al*. 2001; Visser *et al*. 2002]
[C$_2$MIm]$^+$[Br]$^-$	311	[Ngo *et al*. 2000]
[C$_2$MIm]$^+$[BF$_4$]$^-$	447	[Nishida *et al*. 2003]
[C$_3$MIm]$^+$[BF$_4$]$^-$	435	[Nishida *et al*. 2003]
[C$_4$MIm]$^+$[BF$_4$]$^-$	435	[Nishida *et al*. 2003]
[C$_2$MIm]$^+$[PF$_6$]$^-$	481	[Ngo *et al*. 2000]
[C$_3$MIm]$^+$[PF$_6$]$^-$	440	[Ngo et al. 2000]
[C$_6$MIm]$^+$[PF$_6$]$^-$	417	[Huddleston *et al*. 2001]
[C$_2$MIm]$^+$[Tf$_2$N]$^-$	453	[Ngo *et al*. 2000]
[C$_3$MIm]$^+$[Tf$_2$N]$^-$	453	[Ngo *et al*. 2000]
[C$_4$MIm]$^+$[Tf$_2$N]$^-$	439	[Huddleston *et al*. 2001]

1.4 Applications of imidazolium based ILs

[RMIm]$^+$[X]$^-$ ion-pairs find wide applications in various fields due to their attractive properties such as tunability by either changing cationic chain length or counter anions, negligible vapor pressure, low melting point, higher density, viscosity, thermal stability, conductivity and wide electrochemical window (Table 1.9).

Major explored applications of 1-alkyl-3-methylimidazolium based ILs include its use as electrolytes [Noda *et al*. 2001; Olivier *et al*. 2010]. de Souza *et al*. used [C$_4$MIm]BF$_4$ as supporting electrolyte for commercially available alkaline fuel cells at room temperature and 67 % overall cell efficiency was achieved in comparison to proton exchange membrane fuel cells with nafion electrolyte which showed an efficiency of 45-50 % at 70-100 °C [de Souza *et al*. 2003]. There are also several reports regarding the application of imidazolium based ILs as catalysts for the improvement of reaction time, yield and selectivity of many organic reactions [Safaei-Ghomi and Emaeili 2010; Yu *et al*. 2010; Sarkar *et al*. 2011]. Dissolution of cellulose is an important application of ILs and Swatloski *et al*. studied the dissolution of cellulose with [C$_4$MIm]$^+$[Cl]$^-$, [C$_4$MIm]$^+$[Br]$^-$, [C$_4$MIm]$^+$[BF$_4$]$^-$, [C$_4$MIm]$^+$[PF$_6$]$^-$, [C$_6$MIm]$^+$[Cl]$^-$

and $[C_8MIm]^+[Cl]^-$ respectively and observed maximum solubility of 10 % with heating at 100 ^{o}C and 25 % with microwave heating in $[C_4MIm]^+[Cl]^-$ [Swatloski *et al*. 2002].

Table 1.9 Major applications of $[RMIm]^+[X]^-$.

[RMIm]⁺[X]⁻	**Electrolytes**	Fuel cells Sensor Batteries
	Solvents	Organic reactions Nano-particle synthesis Polymerization
	Catalysis	Organic reactions Bio-catalysis
	Separation	Extraction Membranes
	Analytics	Column material Mobile phase GC-head space solvent
	Electroelastic materials	Artificial muscles Robotics
	Lubricant	Fuel additive
	Heat storage	Thermal fluids
	Liquid crystal	Displays
Proposed work in this thesis	**Energetics**	Propellant
	Ion-exchange	Clay modifier Polymer nanocomposites

He *et al*. used $[C_4MIm]^+[BF_4]^-$ as an eluent for the chromatographic separation of ephedrines (norephedrine, ephedrine, pseudoephedrine and methylephedrine) on a C_{18} column and achieved decreased band tailing, reduced band broadening, and improved resolution [He *et al*. 2003]. Ma *et al*. achieved a well-controlled polymerization of methyl methacrylate in $[C_{12}MIm]^+[BF_4]^-$ ionic liquid [Ma *et al*. 2003]. Formentin *et al*. used $[C_4MIm]^+[PF_6]^-$ as a suitable reaction medium for base-catalysed Knoevenagel reaction [Formentin *et al*. 2004]. Jimenez *et al*. identified $[C_8MIm]^+[BF_4]^-$ as a suitable lubricant in steel-aluminium contacts [Jimenez *et al*. 2006]. Huddleston *et al*. [1998] showed that $[C_4MIm]^+[PF_6]^-$ could be used to extract aromatic compounds from water. Aki *et al*. [2004] investigated the solubility of CO_2 in $[C_4MIm]^+$ based ILs with different anions, namely; $[dc]^-$, $[BF_4]^-$, $[PF_6]^-$, $[Tf_2N]^-$ and showed that CO_2 has the highest solubility and strongest interactions with

$[C_4MIm]^+[PF_6]$-. The results also revealed that the solubility of CO_2 is strongly dependent on the choice of anion.

ILs have been anticipated, as the new generation green propellant fuels [Schneider *et al.* 2008; Zhang *et al.* 2011, 2013; Sebastiao *et al.* 2014; McCrary *et al.* 2014]. The energetic ILs (EILs) are formed by the combination of an energetic cation or anion in the ion-pair. The low melting point, higher density and high energy content are the decisive factors for a better performance. Considering the melting point and lower carbon content, 1-ethyl-3-methylimidazolium cations are preferred among 1-alkyl-3-methylimidazolium ILs. Higher carbon content results in soot formation and more oxidizers will be required for its application as propellant. In this work, 1-ethyl-3-methylimidazolium cations with energetic anions were analyzed for its application in replacing toxic and carcinogenic hydrazine monopropellant.

Recent reports show that ILs can also be used to overcome the lower thermal stability of conventional organic modifiers used for clay modification and can enhance the dispersion, wetting and compatibility of clay particle in organic media [Livi *et al.* 2014]. The poor dispersion of polar clay into a non polar polymer matrix restricts the use of clays in nanocomposite field. The attractiveness of polymer clay nanocomposite resides in the potential of adding small amount of modified clays to polymeric resin, to dramatically improve mechanical, thermal, barrier and flame retardant properties, which are necessary for a light weight composite material for aerospace applications. Commercial organophilic montmorillonite (MMT) used in polymer nanocomposites are often prepared from sodium montmorillonite (MMT-Na^+) by ion exchange of its interlayer sodium cations with long chain, C_{16}–C_{18} alkyl ammonium based ions, but lower thermal stability (<180 ^oC) limits its high temperature applications. Imidazolium based ILs are anticipated as a better candidate for thermally stable organoclays for high temperature applications.

Organoclays also find application in contaminant removal from water. Removal of contaminants from wastewater is frequently carried out by means of adsorption processes (Sun *et al.* 2017; Lawal *et al.* 2017; Gupta and Bhattacharyya 2012; Mirmohamadsadeghi *et al.* 2012; Nevskaia et al. 2004). Activated carbon is the most common adsorbent for this purpose due to its excellent adsorption ability. However, the high initial cost and the difficult and expensive regeneration process make it unattractive as an adsorbent (Ahmaruzzaman, 2008). Perchlorate ion is a major

contaminant originates mainly from different salts used in solid propellants for rockets and oxidizer components in various military and industrial processes [Chitrakar *et al*. 2012]. Perchlorates are highly soluble in water and enter into the human body through drinking water or the food chain and cause hypothyroidism by interfering with the ability of the thyroid gland to process iodine. In this thesis, use of 1-alkyl-3-methylimidazolium modified clays for perchlorate removal from water is also investigated.

1.5 Scope and objectives of the present work

The scope of this research work involves design and development of imidazolium based ionic liquids and ionic liquid modified clays for space related applications. Main objectives of the present work are:

- ➢ Design of imidazolium based energetic ionic liquids using computational chemistry tools.
- ➢ Structural studies of ionic liquids using computational methods for organic modification of clay.
- ➢ Synthesis of ionic liquids and experimental validation of predicted properties.
- ➢ Application of ionic liquid modified clay in the removal of perchlorate ion from water.
- ➢ Preparation and property evaluation of IL modified clay nanocomposite.

Computational and experimental methodology
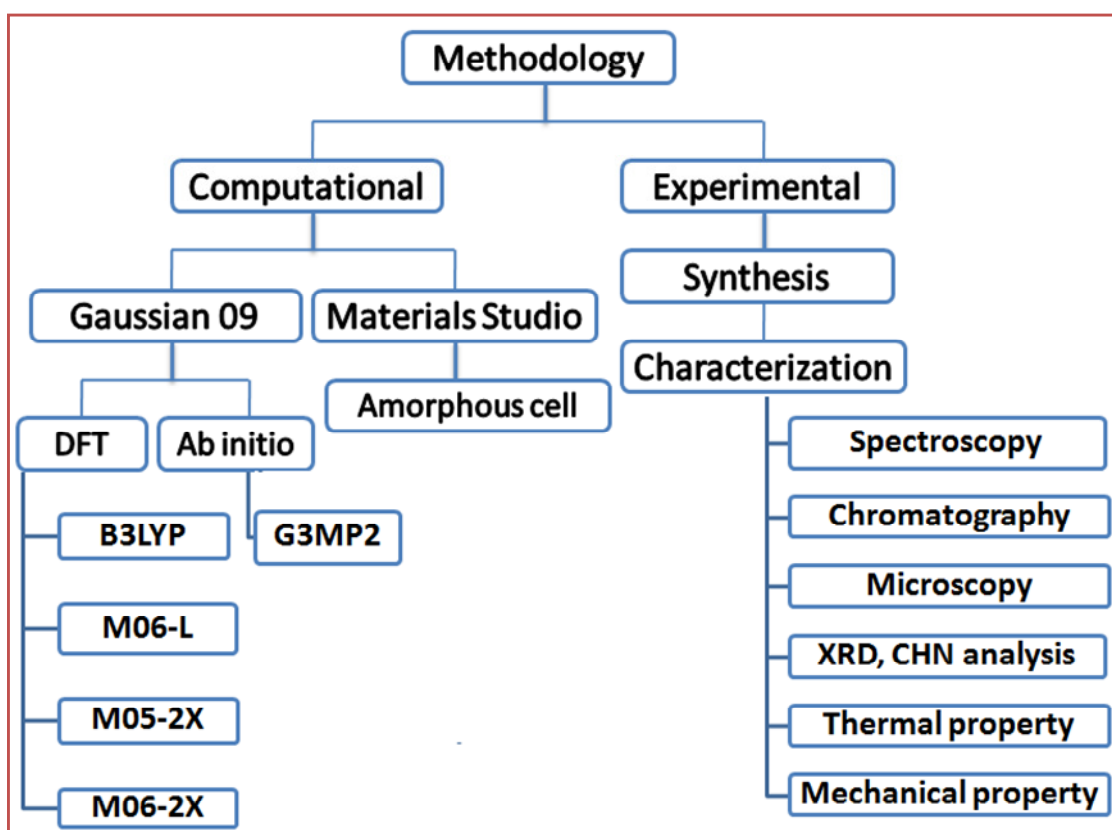
Abstract

Detailed description of various computational methods and experimental techniques adopted in the present study is given in this chapter. The *ab initio* and density functional theory calculations were carried out using *Gaussian 09* software. Amorphous cell minimization of polymer was performed using Materials Studio 4.0 software. Various analytical techniques *viz.* FTIR, Raman and NMR spectroscopy, AAS, XRD, IC, pyrolysis-GC-MS, AFM, FESEM-EDS, CHN analyzer, TGA, DSC and UTM were used for experimental validation. The chemicals and materials used are also detailed.

" I would like to emphasize my belief that the era of computing chemists, when hundreds if not thousands of chemists will go to the computing machine instead of the laboratory, for increasingly many facets of chemical information, is already at hand. There is only one obstacle, namely, that someone must pay for the computing time".

Robert S. Mulliken (Nobel Prize Chemistry-1966)

2.1 Computational chemistry

2.1.1 An overview of computational chemistry

Computational chemistry is used for finding solutions relevant to chemical problems by the application of chemical, mathematical and computing skills. This will also help to design new materials with desired properties especially in the areas involving hazardous and explosive chemicals and provide improvements in health, safety, and environment. Advances in computational chemistry are very helpful in chemical and material research. It also helps chemists make predictions before running the actual experiments so that one can be better prepared for making observations. The increased application of computational technologies are useful to investigate materials that are too difficult to handle or too expensive to purchase and will minimize production of waste.

Using mathematical methods in computational chemistry, two-particle systems can be solved exactly producing solutions in terms of analytical functions. For systems composed of more than two particles computational methods can, however, produce

approximate solutions, which in principle may be refined to any desired degree of accuracy. The numerically intensive tasks are typically related to simulating the behaviour of the real world, by a more or less sophisticated computational model. The dynamical equation describes the time evolution of a system. The mathematical form for the dynamical equation depends on the mass and velocity of the particles, and can be divided into four regimes (Figure 2.1). Newtonian mechanics, exemplified by Newton's second law (F = ma), applies for "heavy", "slow-moving" particles. Relativistic effects become important when the velocity is comparable to the speed of light, causing an increase in the particle mass 'm' relative to the rest mass m_o.

Velocity

Quantum   Classical

Dirac   Einstein   Relativistic
$H\Psi = id\Psi/dt$ $F = m\mathbf{a}$

~ 1/3 c
~ 10^8 m/s

Schrödinger   Newton   Non-relativistic
$H\Psi = id\Psi/dt$ $F = m\mathbf{a}$

Mass

~ 10^{-27} kg
~ 1 amu
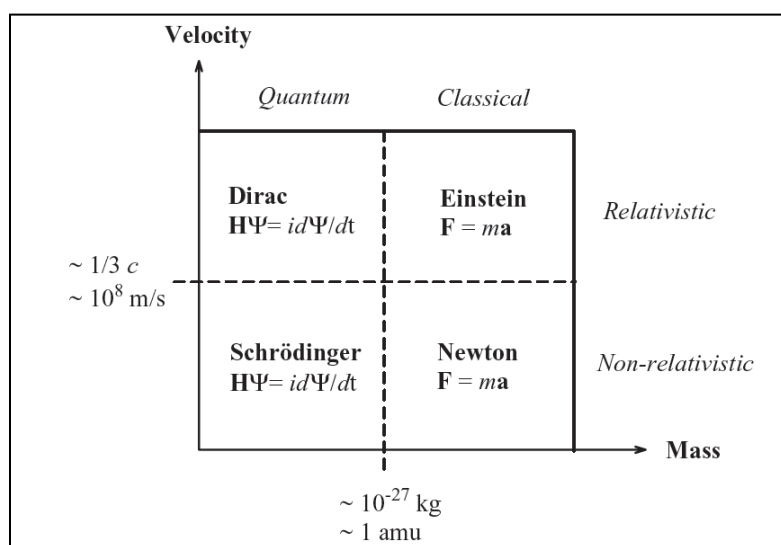
Figure 2.1 Domains of dynamical equations.

A realistic borderline between Newtonian and relativistic (Einstein) mechanics is ~ $\frac{1}{3}c$ (~10^8 m/s). Light particles display both wave and particle characteristics, and must be described by quantum mechanics, with the borderline being approximately the mass of a proton. Electrons are much lighter and can only be described by quantum mechanics. Quantum mechanics only allows calculation of the probability of a particle being at a certain position at a certain time. The probability function is given as the square of a wave function, P(r,t) = Ψ^2(r,t), where the wave function Ψ is obtained by solving either the Schrödinger (non-relativistic) or Dirac (relativistic) equation. Matter as described at a non-relativistic quantum mechanics represents a system of electrons and nuclei, treated as point-like particles with a definite mass and electric charge, moving in three-dimensional space and interacting by electrostatic forces. This model of matter is at the core of quantum chemistry.

The programs that are used in computational chemistry are either based on Schrödinger wave mechanics or Newtonian mechanics. Molecular modelling is a subset of computational chemistry that concentrates on predicting the behaviour of individual molecules within a chemical system. Molecular modelling techniques can be classified into (a) Molecular mechanics, (b) *ab initio* methods, (c) semi-empirical methods, (d) Density functional methods, (e) Molecular dynamics (MD) and Monte Carlo simulations and (f) hybrid quantum mechanics/molecular mechanics (QM/MM) methods.

2.1.2 Molecular mechanics

The molecular mechanics (MM) or forcefield methods use the laws of classical physics and calculate the energy of a system as a function of the nuclear coordinates [Weiner and Kollman 1981; Boyd and Lipkowitz 1982; Bowen and Allinger 1991; Dinur and Hagler 1991]. MM calculations are based on a model of a molecule as a collection of balls (atoms) held together by springs (bonds). Each atom is represented as one particle with a characteristic mass. The potential energy of a molecule can be written as the sum of terms involving bond stretching, angle bending, dihedral angles and nonbonded interactions. Giving these terms explicit mathematical forms constitutes devising a forcefield, and giving actual numbers to the constants in the forcefield constitutes parameterizing the field. MM method makes no reference to electrons, and so cannot throw light on electronic properties like charge distributions or nucleophilic and electrophilic behaviour. MM is the most widely used method for computing the geometries and energies of large biological molecules like proteins and nucleic acids. Because of its speed and the availability of parameters for almost all the elements MM even when it does not provide very accurate geometries can supply reasonably good input geometries for semiempirical, ab initio or density functional calculations.

2.1.3 Ab initio calculations

Ab initio calculations aim at solving the time-independent, non-relativistic Schrödinger equation, which in its simplest form is

$$\hat{H}\Psi = E\Psi \qquad \text{--- (2.1)}$$

Where $\hat{H}$ is the Hamiltönian operator which operates on Ψ, the wave function and returns E, the energy eigen value. The Hamiltönian operator for a system of N electrons and M nuclei comprises of the nuclear and electronic kinetic energy operators and the

potential energy operators corresponding to the nuclear-nuclear, nuclear-electron and electron-electron interactions.

Schrödinger equation cannot be solved exactly for any molecular systems and hence some approximations are introduced for its practical applications. A common approximation used is the Börn-Oppenheimer approximation [Born and Oppenheimer 1927] which takes into account the significant mass difference between an electron and nuclei. The mass of the lightest nucleus (i.e. mass of a proton, ^{1}H) is about 1800 times greater than that of an electron. Consequently, electrons move much faster than nuclei. In other words, the kinetic energy of the nuclei can be considered negligible compared to that of the electrons according to Börn-Oppenheimer approximation.

The simplest type of *ab initio* electronic structure calculation is the Hartree–Fock (HF) theory [Hartree 1928; Fock 1930; Slater 1930], in which the correlated electron–electron repulsion is not specifically taken into account. In the HF approach, the N electron wave function for a given state is written as a Slater determinant, an anti-symmetrized product of spin orbitals. The determinant wave function is used to approximate the exact wave function and energy is calculated as an expectation value of the Hamiltonian over the approximate wave function. The orbitals are found using the variational principle by minimization of the energy expectation value. The best approximate wave function can be obtained by varying all the wave function parameters, until the energy expectation value of the approximate wave function is minimized. Many types of calculations begin with a Hartree–Fock calculation and subsequently correct for electron-electron repulsion, referred to as post-Hartree–Fock methods. Møller–Plesset perturbation theory (MP_n) and coupled cluster theory (CC) are examples of these post-Hartree–Fock methods.

2.1.4 Semiempirical calculations

It is the mixing of theory and experiment that makes the method "semiempirical". It is based on the Schrödinger equation, However, more approximations are made in solving it, and the very complicated integrals that must be calculated in the *ab initio* method are not actually evaluated in semiempirical calculations: instead, the program draws on a kind of library of integrals that was compiled by finding the best fit of some calculated entity like geometry or energy (heat

of formation) to the experimental values. Semiempirical calculations are slower than molecular mechanics but much faster than *ab initio* calculations.

The self-consistent-field (SCF) semiempirical procedures developed are Pariser-Parr-Pople method (PPP) [Pariser and Parr 1953; Pople 1953], complete neglect of differential overlap (CNDO) [Pople *et al*. 1966], intermediate neglect of differential overlap (INDO) [Pople *et al*. 1967; Dixon 1967], and neglect of diatomic differential overlap (NDDO) [Pople *et al*. 1965, 1966]. NDDO methods are the gold standard in general purpose semiempirical methods. Today the most popular SCF semiempirical methods are Austin method 1 (AM1) [Dewar *et al*. 1985] and parametric method 3 (PM3), which are carefully parameterized to reproduce experimental quantities (primarily heats of formation). Recent extensions of AM1 (RM1) and PM3 (PM6 and PM7) represent the standard semiempirical methods.

2.1.5 Density functional calculations

Density functional calculations (DFT) are, like ab initio and semiempirical calculations, based on the Schrödinger equation. However, unlike the other two methods, DFT does not calculate a conventional wave function, rather derives the electron distribution (electron density function) directly. Thomas and Fermi [Fermi 1927; Fermi 1928; Thomas 1927] introduced the idea of expressing the energy of a system as a function of the total electron density. Hohenberg, Kohn and Sham [Hohenberg and Kohn 1964; Kohn and Sham 1965] made it to a reality in the 1960s. An important advantage of using electron density over the wave function is the reduced dimensionality. Regardless of how many electrons one has in the system, the density is always 3 dimensional whereas, the wave function for an N-electron system is a function of 3N spatial co-ordinates. This enables DFT to readily be applied to much larger systems with more number of atoms.

2.1.5.1 Hohenberg–Kohn theorems

The first Hohenberg-Kohn theorem [Hohenberg and Kohn 1964] says that all the properties of a molecule in a ground electronic state are determined by the ground state electron density function $\rho(r)$, e.g. for the energy (E_0)

$$E_0 = F[\rho(r)] = E[\rho(r)] \qquad --- (2.2)$$

The second Hohenberg–Kohn theorem [Hohenberg and Kohn 1964] says that any trial electron density function will give an energy higher than (or equal to, if it were exactly the true electron density function) the true ground state energy. i.e.,

$$E_v[\rho_t] \geq E_0[\rho(r)] \qquad \text{--- (2.3)}$$

where ρ_t is a trial electronic density, $E_v[\rho_t]$ is the E_v functional of the trial electronic density and $E_0[\rho(r)]$ is the true ground state energy corresponding to the true electronic density $\rho(r)$.

2.1.5.2 The Kohn–Sham energy and the Kohn–Sham equations

If we had an accurate molecular electron density function ρ and if we knew the correct energy functional, we could go straight from the electron density function to the molecular energy. Unfortunately we do not have an accurate ρ, and we certainly do not have the correct energy functional, being the key problem in DFT. The Kohn–Sham (KS) approach to DFT mitigates these two problems. The two basic ideas behind the KS approach are:

(1) To express the molecular energy as a sum of terms, only one of which, a relatively small term, involves the unknown functional. Thus, even moderately large errors in this term will not introduce large errors into the total energy.

(2) To use an initial guess of the electron density ρ in the KS equations to calculate an initial guess of the KS orbitals and energy levels. This initial guess is then used to iteratively refine these orbitals and energy levels. The final KS orbitals are used to calculate an electron density that in turn is used to calculate the energy.

The first KS theorem tells us that it is worth looking for a way to calculate molecular properties from the electron density. The second theorem suggests that a variational approach might yield a way to calculate the energy and electron density. Kohn and Sham showed that $F[\rho(r)]$ can be approximated as,

$$F[\rho(r)] = E_{KE}[\rho(r)] + E_H[\rho(r)] + E_{XC}[\rho(r)] \qquad \text{--- (2.4)}$$

where $E_{KE}[\rho(r)]$ is the kinetic energy, $E_H[\rho(r)]$ is the electron-electron Coulombic energy, and $E_{XC}[\rho(r)]$ contains contributions from exchange and correlation. The full expression for the energy of an N-electron system within the KS scheme is,

$$E[\rho(r)] = -\sum_{nuclei\ A} Z_A \int \frac{\rho(r_1)}{r_{1A}} dr_1 + \sum_{i=1}^{N} \int \Psi_i(r) \left[-\frac{\nabla^2}{2} \right] \Psi_i(r) dr + \frac{1}{2} \iint \frac{\rho(r_1)\rho(r_2)}{|r_1 - r_2|} dr_1 dr_2 + E_{XC}[\rho(r)] \quad \ldots (2.5)$$

where, the first term represent the integral of the density times the external potential, $\int \rho(r)v(r)dr$, the second term is the electronic kinetic energy of the noninteracting electrons reference system, i.e. is the expectation value of the sum of the one-electron kinetic energy operators over the ground state multielectron wave function of the reference system, the third term is the classical electrostatic repulsion energy term and the fourth term is the exchange correlation energy $E_{XC}[\rho(r)]$. The term most subject to error is the relatively small $E_{XC}[\rho(r)]$ term, which contains the unknown functional. Into this term the exact electron correlation and exchange energies have been swept, and for it we must find at least an approximate functional.

2.1.5.3 The exchange-correlation energy functional

Xu and Goddar quoted "DFT is the method of choice for first principles quantum chemical calculations of the electronic structure and properties of many molecular and solid systems. With the exact exchange-correlation functional, DFT would take into full account all complex many-body effects at a computation cost characteristic of mean field approximations. Unfortunately, the exact exchange-correlation functional is unknown, making it essential to pursue the quest of finding more accurate and reliable functionals" [Xu and Goddar 2004].
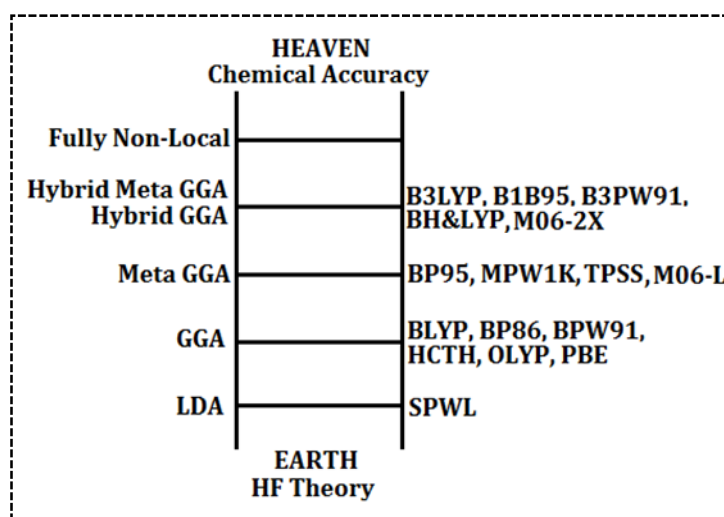
Figure 2.2 Jacob's ladder representing the five generations of density functional from the world of Hartree to the heaven of chemical accuracy, with examples from each class.

Several methods have been designed by modifying the exchange-correlation potential *viz.* (a) the local density approximation (LDA), (b) the local spin density approximation (LSDA), (c) the generalized gradient approximation (GGA), (d) meta-GGA (MGGA), (e) hybrid GGA (f) hybrid meta-GGA methods, and (g) "fully nonlocal" theory. This hierarchy of theory has been likened to the biblical ladder reaching up to heaven, and this DFT Jacob's ladder [Perdew and Schmidt 2001] will, culminate in what has been appropriately called the divine functional [Mattsson 2002].

The best results appear to come from so-called hybrid functionals, which include some contribution from Hartree–Fock type exchange. The most popular DFT method is the LSDA gradient-corrected hybrid method which uses the B3LYP (Becke three-parameter Lee-Yang-Parr) functional. Gradient-corrected hybrid functionals, give excellent geometries and reaction energies. Minnesota functional also represent a reliable class of functionals with one meta-GGA (M06-L) and seven global-hybrid meta GGAs (M05, M05-2X, M06-2X, M08-HX and M08-SO). The M06 family, the most popular among these is composed of four functionals that have similar functional forms for the DFT part, but each has parameters optimized with a different percentage of HF exchange. The four functionals are (i) M06-L, a local functional (no HF exchange), (ii) M06, a global-hybrid-meta GGA with 27 % HF exchange, leading to a well-balanced functional for overall good performance for chemistry, (iii) M06-2X, a global hybrid meta-GGA with 54 % HF exchange for top-level across all areas of chemistry including thermochemistry and reaction kinetics, but excluding multi-reference systems such as those containing transition metals, and (iv) M06-HF, a global-hybrid-meta-GGA with 100 % HF exchange, suitable for calculation of spectroscopic properties of charge-transfer transitions.

DFT gives reasonable IR frequencies and intensities, comparable to those from MP2 calculations. Dipole moments from DFT appear to be more accurate than those from MP2, Time-dependent DFT (TDDFT) is the best method for calculating UV spectra reasonably quickly. DFT is said to be better than Hartree–Fock for calculating NMR spectra. Electron affinities can be obtained from the negative LUMOs from LSDA functionals. For conjugated molecules, HOMO-LUMO gaps from hybrid functionals agree well with the $\pi \rightarrow \pi^*$ UV transitions. The mutually related concepts of electronic chemical potential, electronegativity, hardness, softness, and the Fukui

function are usually discussed within the context of DFT. They are readily calculated from ionization energy, electron affinity, and atom charges.

2.1.6 Molecular dynamics calculations

Molecular dynamics (MD) calculations apply the laws of motion to molecules. MD simulations are in many respects very similar to real experiments. Here first select the model system consisting of N particles and solve Newton's equation of motion for this system until the properties of the system no longer change with time (till system reach equilibrium). After equilibrium, actual measurements are performed. To measure an observable quantity in MD simulation, it must be expressed as a function of position and momenta of the particles in the system.

2.1.7 Basis sets

A basis set is a set of mathematical functions (basis functions), linear combinations of which yield molecular orbitals. There are two main types of basis functions *viz.* Slater type orbitals (STOs) [Allen and Karo 1960] and Gaussian type orbitals (GTOs) [Boys 1950; Feller and Davidson 1990]. The first basis sets used in molecular calculations were typically STOs, which correspond to a set of functions which decay exponentially with the distances from the nuclei. STOs have the exponential dependence, $e^{-\zeta r}$ and are given by the mathematical expression;

$$\phi_{abc}^{STO}(x, y, z) = Nx^a y^b z^c e^{-\zeta r} \qquad \text{--- (2.6)}$$

where N is the normalization constant, a, b, c control the angular momentum (L = a+b+c), ζ determines the width or spread of the orbital and x, y, z represent the cartesian coordinates. GTOs have the exponential dependence; $e^{-\zeta r^2}$ and mathematically expressed as;

$$\phi_{abc}^{GTO}(x, y, z) = Nx^a y^b z^c e^{-\zeta r^2} \qquad \text{--- (2.7)}$$

The computational advantage of GTOs over STOs is primarily due to the Gaussian product theorem, *viz.* the product of two GTOs is also a Gaussian function entered at the weighted midpoint of the two functions [Shavitt 1963]. In addition, the overlap and other integrals are easier to evaluate leading to huge computational savings. The Gaussian function shown in Eqn. 2.7 is generally known as primitive GTOs. When

primitive GTOs bunch together into one Gaussian function results in contracted Gaussian function (CGTO),

$$\phi_{abc}^{CGTO}(x, y, z) = \sum_{i=1}^{n} c_i x^a y^b z^c e^{-\zeta r^2} \qquad \text{--- (2.8)}$$

where n represent the number of Gaussians to mimic the STO and c_i represent coefficients. By contracting several primitive GTOs into one, the computational effort can be reduced through the optimization of several coefficients in one go. The degree of complexity, and thus precision of a basis set is defined by the number of contracted functions employed to represent each atomic orbital, the minimum being one contracted function to describe a basis function (minimal basis set). STO-3G function is the smallest basis function used in standard ab initio calculations by commercial programs. STO-3G basis set [Hehre et al. 1969] mean "Slater-type orbital (approximated by) three Gaussians".

The next higher, 3–21G basis set splits each valence orbital into two parts, an inner shell and an outer shell. The basis function of the inner shell is represented by two Gaussians, and that of the outer shell by one Gaussian (hence the "21"); the core orbitals are each represented by one basis function, each composed of three Gaussians (hence the "3"). For molecules with atoms beyond the first row (beyond neon), this "simple" 3–21G basis set tends to give poor geometries. This problem is largely overcome for second row elements (sodium to argon) by supplementing this basis with d functions, called polarization functions represented usually by *. The 3–21G basis set augmented (beyond neon) with six d functions is designated 3–21G(*), For H to Ne, the 3–21G and the 3–21G* basis sets are identical.

The next bigger widely-used basis, the 6–31G* is a split valence basis set with polarization functions. The valence shell of each atom is split into an inner part composed of three Gaussians and an outer part composed of one Gaussian, while the core orbitals are each represented by one basis function, each composed of six Gaussians. The polarization functions (*) are present beyond helium. The 6–31G* also often called 6–31G(d) is probably the most popular basis at present. Sometimes it is helpful to have polarization functions on the hydrogens as well; a 6–31G* basis with three 2p functions on each H and He atom is called the 6–31G** (or 6–31(d,p)) basis.

6–311G** (or 6–311(d,p)) set is a larger basis, a split valence set with each valence orbital split into three shells, composed of three, one and one Gaussian, while the core orbitals are represented by one basis function composed of six Gaussians; each heavy atom also has five 3d functions and each hydrogen and helium has three 2p functions. The number of basis functions on CH_2 using STO-3G, 3-21G, 6-31G(d), 6-31G(d,p) and 6-311G(d,p) are summarized (C + H + H) in Table 2.1. Similarly diffuse functions are sometimes included in the basis to improve the description at large distances from the nuclei and are denoted by + or ++ signs set (for example, 6–31+G(d,p)). This is important for anions as the additional electrons are loosely bound to nuclei.

Table 2.1 The number of basis functions on CH_2 using various basis sets.

Basis set	Functions			Total
	$_1$H	$_2$He	$_3$Li–$_{10}$Ne	
STO-3G	1s 1 function	1s 1 function	1s 2s 2p 2p 2p 5 functions	7 functions
3- 21G	1s' 1s'' 2 functions	1s' 1s'' 2 functions	1s 2s' 2p' 2p' 2p' 2s'' 2p'' 2p'' 2p'' 9 functions	13 functions
6-31G* or 6- 31G(d)	1s' 1s'' 2 functions	1s' 1s'' 2 functions	1s 2s' 2p' 2p' 2p' 2s'' 2p'' 2p'' 2p'' 3d 3d 3d 3d 3d 3d 15 functions	19 functions
6- 31G(d,p)	1s' 1s'' 2p 2p 2p 5 functions	1s' 1s'' 2p 2p 2p 5 functions	1s 2s' 2p' 2p' 2p' 2s'' 2p'' 2p'' 2p'' 3d 3d 3d 3d 3d 3d 15 functions	25 functions
6- 311G(d,p)	1s' 1s''1s''' 2p 2p 2p 6 functions	1s' 1s''1s''' 2p 2p 2p 6 functions	1s 2s' 2p' 2p' 2p' 2s'' 2p'' 2p'' 2p'' 2s''' 2p''' 2p''' 2p''' 3d 3d 3d 3d 3d 18 functions	30 functions

2.1.8 Basis set superposition error

When two fragments A and B approach each other to form a new species, their basis functions overlap. Basis functions ("atomic orbitals") of B are available to A so A in AB has a bigger basis set than does isolated A; likewise B has a bigger basis than isolated B. When in AB each of the two components can borrow basis functions from the other. The error arises from "imposing" B's basis set upon A and vice versa, hence the name basis set superposition error (BSSE). One widely used method to assess the BSSE is the counterpoise correction scheme of Boys and Bernardi [Boys and Bernardi 1970] in which the entire basis set is included in all calculations. Consider the binding energy of the dimer (AB) *viz.* A + B → AB. The binding energy (E_b) can be expressed as,

$$E_b = E(AB)_{ab} - [E(A)_a + E(B)_b] \quad \text{--- (2.9)}$$

where $E(AB)_{ab}$, $E(A)_a$ and $E(B)_b$ represent the energy of AB, monomer A and monomer B, respectively. Subscripts indicate the corresponding basis sets for AB, A and B. In counterpoise method, the calculation of the energy of the individual species A is performed in the presence of 'ghost' orbitals of B, without the nuclei or electrons of B. A similar calculation is performed for B using the 'ghost' orbitals on A. Using counterpoise method, BSSE can be evaluated with,

$$E_{BSSE} = E(\tilde{A})_{ab} + E(\widetilde{B})_{ab} - E(\tilde{A})_a - E(\widetilde{B})_b \quad \text{--- (2.10)}$$

where $E(\tilde{A})_{ab}$ and $E(\widetilde{B})_{ab}$ respectively represents the energy of monomer A and B in the structure it adopts in the dimer (AB) and with the full basis set of the dimer available. $E(\tilde{A})_a$ and $E(\widetilde{B})_b$ are the energies of A and B, respectively, with only their own basis functions but again in the structure they adopt in the dimer. The correction to the binding energy can be calculated as, $E_b - E_{BSSE}$.

2.1.9 Molecular electrostatic potential

Any distribution of electric charge, such as nuclei or electrons creates an electric potential $V(\mathbf{r})$ in the surrounding space. Molecular electrostatic potential or MESP can be regarded as the potential of a molecule to interact with an electric charge located at a point $\mathbf{r}$ [Scrocco and Tomasi 1978]. Thus a positive charge is attracted to those regions in which $V(\mathbf{r})$ is negative and is repelled from regions of positive potential. MESP

[Gadre and Shirsat 2000] can be calculated from the electron density function, $\rho(\mathbf{r})$ using the equation:

$$V(\mathbf{r})= \sum_{A}^{N} \frac{Z_A}{|\mathbf{r}-\mathbf{R}_A|} - \int \frac{\rho(\mathbf{r}')d^3\mathbf{r}'}{|\mathbf{r}-\mathbf{r}'|} \qquad \text{--- (2.11)}$$

where Z_A is the charge on nucleus A located at R_A and $\mathbf{r}'$ is a dummy integration variable. The two terms refer to the nuclear potential and the electronic contributions respectively. The value of MESP is positive in the region close to nuclei and negative in the electron-rich region. Topographical features of MESP as well as the pictorial representation of MESP in the form of contours and isosurfaces are extremely useful for exploring the structure and reactivity of molecules, intermolecular interactions, molecular recognition and a variety of chemical phenomena [Gadre *et al.* 1996; Luque *et al.* 1994; Politzer and Truhlar 1981]. In MESP topography analysis the electronic distribution of molecules is understood in terms of critical points *i.e.*, the points at which the partial derivatives of MESP vanish. The most negative value of the MESP (V_{min}) corresponds to a point at which electrostatic potential due to the electron density term dominates maximally over the bare nuclear term, the location of it indicates the electron-dense region of a molecule [Gadre and Pathak 1990; Gadre and Shirsat 2000; Pathak and Gadre 1990; Shirsat *et al.* 1992].

2.1.10 Computational methodology

The DFT calculations performed in this thesis were carried out with B3LYP, M06-L, M05-2X and M06-2X functionals using *Gaussian 09* software. The basis set used was 6-311+G(d,p) and the G3MP2 level thermodynamic data was used to calculate the heat of formation of ion-pairs. The BSSE corrected binding energy was reported. Amorphous cell minimization of polymer was performed using Materials Studio 4.0 (Accelrys Inc.) software.

2.2 Experimental methods

2.2.1 Materials

The chemicals and materials used in this study are listed in Table 2.2. Very specific materials and methods adopted have been described at places where they are referred to.

Table 2.2 Chemicals and materials used in the study.

Sl. No.	Materials	Details	
1.	1-Methylimidazole	CAS No.	: 616-47-7
		Make	: Alfa Aesar
		Purity	: 99 %
		B.P.	: 195 ^{o}C
		Density	: 1.031 g/mL
2.	1-Chlorobutane	CAS No.	: 109-69-3
		Make	: Alfa Aesar
		Purity	: 99 %
		B.P.	: 78 ^{o}C
		Density	: 0.886 g/mL
3.	1-Chlorohexane	CAS No.	: 544-10-5
		Make	: Sigma Aldrich
		Purity	: 99 %
		B.P.	: 134 ^{o}C
		Density	: 0.879 g/mL
4.	1-Chlorohexadecane	CAS No.	: 4860-03-1
		Make	: Sigma Aldrich
		Purity	: 95 %
		B.P.	: 149 ^{o}C/1mm Hg
		Density	: 0.865 g/mL
5.	1-Butyl-3-methylimidazolium chloride	CAS No.	: 79917-90-1
		Make	: Otto Chemie
		Purity	: 98 %
6.	1-Butyl-3-methylimidazolium tetrafluoroborate	CAS No.	: 74501-65-6
		Make	: Otto Chemie
		Purity	: 98 %
7.	1-Decyl-3-methylimidazolium chloride	CAS No.	: 171058-18-7
		Make	: Otto Chemie
		Purity	: 96 %
8.	Sodium montmorillonite clay (Cloisite-Na^{+})	CAS No.	: 1318-93-0
		Make	: Southern Clay Inc.
		d-spacing	: 12.09 Å
9.	Cloisite-10A	CAS No.	: 71011-24-0
		Modifier	:dimethyl, benzyl, hydrogenated tallow, quaternary ammonium
		d-spacing	: 19.20 Å
10.	Cloisite-15A	CAS No.	: 68953-58-2
		Modifier	: dimethyl, dihydrogenated tallow, quaternary ammonium
		d-spacing	: 31.50 Å

11.	Cloisite-20A	CAS No.	: 68953-58-2
		Modifier	: dimethyl, dihydrogenated tallow, quaternary ammonium
		d-spacing	: 24.20 Å
12.	Cloisite-25A	CAS No.	: 68953-58-2
		Modifier	: dimethyl, hydrogenated tallow, 2-ethylhexyl quaternary ammonium
		d-spacing	: 18.60 Å
13.	Hydrochloric acid	CAS No.	: 7647-01-0
		Make	: Merck Chemicals
		Purity	: 37 %
14.	Ammonium perchlorate AR	CAS No.	: 7790-98-9
		Make	: In house
		Purity	: 99.9 %
15.	Colloidal silica	CAS No.	: 7631-86-9
		Make	: Sigma-Aldrich
		Purity	: 30 % suspension
16.	Poly (vinylidene fluoride)	CAS No.	: 24937-79-9
		Make	: Alfa Aesar
17.	N,N'-Dimethylacetamide	CAS No.	: 127-19-5
		Make	: Spectrochem
		Purity	: 99.9 %

2.2.2 Characterization techniques

2.2.2.1 Fourier transform infrared spectroscopy

Fourier transform infrared spectroscopy (FTIR) is a fast and easy analytical technique for the identification of functional groups. It is based on the interaction of molecules with IR radiation. Certain frequencies characteristics of the vibrational energy levels are absorbed by the molecule and the rest is transmitted. Thus the absorption pattern will be characteristic of the chemical structure of the molecule.

The FTIR spectrum of the samples in the present work are recorded using Perkin Elmer Spectrum GX FTIR spectrometer and ThermoScientific Nicolet iS50 FTIR spectrometer equipped with attenuated total reflectance (ATR) accessory and variable temperature cell accessory. The instrumental source is Nernst glower and detector used is deuterated triglycine sulphate (DTGS). FTIR spectra of powder samples were recorded using the KBr pellet method, liquid samples on the NaCl crystal and films/composites in the ATR mode.

2.2.2.2 Raman spectroscopy

Raman spectroscopy is based on the inelastic scattering of monochromatic light when the frequency of photons changes upon interaction with a sample. The photons of the laser light are absorbed by the sample and subsequently re-emitted. Frequency of the reemitted photons is shifted up or down in comparison with the original monochromatic frequency, which is known as the Raman Effect. The Raman shift provides information about vibrational and rotational energies of molecular bonds. It is a non-destructive technique.

The Raman spectrum of the samples in the present work are recorded using WITec alpha 300R confocal Raman microscope. A 532 nm Nd:YAG laser source was used for excitation and a charge coupled device (CCD) was used as the detector. Five spectra were accumulated with an integration time of 1 sec to obtain a single spectrum, plotted as intensity *vs.* wave number.

2.2.2.3 Nuclear magnetic resonance spectroscopy

Nuclear magnetic resonance spectroscopy (NMR) is used for the characterization of materials based on the magnetic property of atomic nuclei present in the sample. The NMR has a probe placed in a strong magnetic field and the sample placed in the probe is irradiated with radiofrequency leading to nuclear level transitions. Depending on the atomic nuclei, the excitation frequency ranges and the excited nuclei emit a signal called free induction decay (FID) which is recorded. The FID generated in the time domain is converted to frequency domain by Fourier transformation resulting in the NMR spectrum output.

NMR analysis was done using Bruker Avance-III, 400 MHz spectrometer operated at 400 MHz for ^{1}H and 100.2 MHz for ^{13}C nuclei. The field strength was 9.4 T. The samples were dissolved in deuterated solvents and the spectrum was recorded. Chemical shifts are expressed in ppm and tetramethylsilane (TMS) was used as internal standard.

2.2.2.4 Atomic absorption spectroscopy

Atomic absorption spectroscopy (AAS) involves the study of the absorption of radiation by neutral atoms in the gaseous state. The sample is first converted into an atomic vapour and then the absorption of atomic vapour is measured at a selected

wavelength which is characteristic of each individual element. The source is a hollow cathode lamp and detector used is a photo multiplier tube. The atoms of a particular element can only absorb radiation of their own characteristic wavelength and separate lamp source is required for each element to be determined. AAS experiments were carried out using Varian AA280FS spectrometer.

2.2.2.5 X-Ray diffraction

X-ray diffraction (XRD) is the most important technique for crystal structure analysis. The interaction of X-ray radiation with the crystalline sample is governed by Bragg's law,

$$n\lambda = 2d\ \text{Sin}\theta \quad \text{--- (2.12)}$$

where λ is the wavelength of the X-ray, n is an integer representing the order of diffraction peak, d is the interplanar spacing and θ is the half of the angle between incident beam and diffracted beam.

In this work, XRD analysis was performed using Bruker D8 Discover diffractometer using CuKα radiation source (1.5418 A°) and solid state detector (Lynx Eye). Crystallite size determination based on Scherrer equation was performed using the Diffrac Plus Eva software.

2.2.2.6 Ion chromatography

Ion chromatograph (IC) is an excellent separation and detection technique for the simultaneous analysis of different anions and different cations. In this technique an ion exchange process takes place between the mobile phase and the exchange group which are covalently bound to the stationary phase. Different ions elute at different intervals of time depending upon their affinity to the stationary phase and are detected by a conductivity detector. A chromatogram is recorded by plotting time verses conductivity of the eluted ions. Conductivity of an ion is directly proportional to concentration of the ion.

In this work, IC analysis was performed using Dionex ICS 2000 ion chromatograph equipped with AS16 column, AG16 Guard column, ASRS 300 Suppressor column and a conductivity detector. Chromeleon chromatographic software was used for the data analysis.

2.2.2.7 Gas chromatograph-mass spectrometer

Gas chromatograph-mass spectrometer (GC-MS) is a hyphenated technique in which a gas chromatograph is connected to a mass spectrometer. Gas chromatography is a separation technique in which the compounds of a vaporized sample are separated and fractionated as a consequence of partition between a mobile gaseous phase and a stationary phase held in column. In GC-MS, gas chromatograph separates the mixture into its components and individual components are detected and identified by the mass spectrometer from mass spectrum obtained.

GC-MS analysis was performed using a Thermo Electron Trace ultra GC directly coupled to a Thermo Electron PolarisQ (Quadrupole ion trap) mass spectrometer and SGE pyrolyser. The *m/z* range used was 20-600 amu. The ionization technique chosen is electron ionization (EI).

2.2.2.8 Atomic force microscopy

Atomic force microscopy (AFM) works by scanning a tip over a surface. The cantilever is typically silicon or silicon nitride with a tip radius of curvature on the order of nanometers. When the tip is brought into proximity of a sample surface, forces between the tip and the sample lead to a deflection of the cantilever to which the tip is attached. Typically, the deflection is measured using a laser spot reflected from the top surface of the cantilever into an array of photodiodes. The vertical movement of the scanner follows the surface profile and is recorded as the surface topography. The AFM can be operated either in static mode (also called contact mode) or dynamic (non-contact or "tapping") modes.

In this work, AFM images were taken using Agilent 5500 scanning probe microscope in contact mode.

2.2.2.9 Field emission scanning electron microscope

A scanning electron microscope (SEM) is a type of electron microscope that produces images of a sample by scanning it with a focused beam of electrons. The electrons interact with atoms in the sample, producing various signals that can be detected and that contain information about the sample's surface topography and composition. The types of signals produced by a SEM include secondary electrons, back-scattered electrons, characteristic X-rays and transmitted electrons. In the most

common or standard detection mode, secondary electron imaging, the SEM can produce very high-resolution images of a sample surface, revealing details less than 1 nm in size. A wide range of magnifications is possible, from about 10 times to more than 500,000 times. Field emission (FE) is emission of electrons induced by an electrostatic field. The most common context is field emission from a solid surface into vacuum. In FESEM, the interaction of electrons with atoms in the sample surface, producing various signals that contain information about the sample's surface topography as well as elemental composition.

FESEM images and EDS spectra of gold-coated samples were recorded using a Carl Zeiss, Supra 55 model field emission scanning electron microscope equipped with an Oxford Inca (UK) energy dispersive X-ray spectrometer.

Energy-dispersive X-ray spectroscopy (EDS) is an analytical technique used for the elemental analysis or chemical characterization of a sample. Characteristic X-rays are emitted when the electron beam removes an inner shell electron from the sample, causing a higher energy electron to fill the shell and release energy. The number and energy of the X-rays emitted from a specimen can be measured by an energy-dispersive spectrometer. As the energy of the X-rays are characteristic of the difference in energy between the two shells, and of the atomic structure of the element from which they were emitted, this allows the elemental composition of the specimen to be measured.

2.2.2.10 CHN analyzer

The CHN (carbon, hydrogen, nitrogen) elemental analyzer employs a combustion method to convert the sample elements to simple gases. The sample is first oxidized in a pure oxygen environment to form CO_2, H_2O and oxides of nitrogen. The oxides of nitrogen are reduced to nitrogen. The resulting gases are homogenized and are separated in a stepwise manner and detected as a function of their thermal conductivities.

The analysis was carried out using Perkin Elmer 2400 CHNS analyzer with thermal conductivity detector.

2.2.2.11 Thermogravimetric analysis

Thermogravimetric analysis (TGA) measures the mass change associated with materials as a function of temperature and time. Thermocouples located within the

sample platforms detect the changes in the reference and sample temperature and gives heat flow/temperature difference as a function of temperature/time.

TA Instruments SDT Q600 TGA was used for thermal analysis. Kinetic parameters for the thermal decomposition process were studied using (i) Kissinger method (ii) Ozawa-Flynn-Wall method and (iii) Coats-Redfern method.

Kissinger method [Kissinger 1957] is a multiple heating rate method based on the following equation (Eqn. 2.13).

$$\ln \frac{\beta}{T_\alpha^2} = ln[\frac{AR}{g(\alpha)E_a})] - \frac{E_a}{RT_\alpha} \qquad \text{--- (2.13)}$$

Where β is the heating rate, T_α is the temperature in Kelvin corresponding to a fixed degree of conversion α, A is the pre-exponential factor, R is the gas constant, E_a is the activation energy at a given degree of conversion and g(α) is the integral form of kinetic model function. E_a for a given degree of conversion is obtained from the slope of the linear fit of the plot $\ln \frac{\beta}{T_\alpha^2}$ versus $1/T_\alpha$.

Ozawa-Flynn-Wall (FWO) method [Ozawa 1965; Flynn and Wall 1966] for determination of kinetic parameters is based on the assumption that the decomposition obeys first order kinetics using a point of constant conversion from a series of decomposition curves obtained at different heating rates. It helps in calculating the E_a for a desired conversion (Eqn.2.14).

$$E_a = \left(\frac{R}{b}\right) * \left(\frac{\Delta log[\beta]}{\Delta(1/T)}\right) \qquad \text{--- (2.14)}$$

Where R is the universal gas constant, β is the heating rate, b = 0.457 initially and it depends on the value of E/RT.

First order reaction and random nucleation (F1 function) is generally used for thermal degradation kinetic study of nanocomposite films. The Coats-Redfern for F1 function is given as,

$$\ln \frac{-\ln (1-\alpha)}{T^2} = \ln \frac{AR}{\beta E_a} - \frac{E_a}{RT} \qquad \text{--- (2.15)}$$

where, E_a is the activation energy for decomposition, A is the pre-exponential factor, R is the universal gas constant, β is the heating rate, α is the degree of conversion and T is the maximum decomposition temperature (K) corresponding to each α. The plot of

$\ln \dfrac{-\ln (1-\alpha)}{T^2}$ versus 1/T, result in a linear plot whose slope gives the value of activation energy.

2.2.2.12 Differential scanning calorimetry

Differential scanning calorimetry (DSC) measures the differential heat flow associated with material transitions as a function of time and temperature. DSC works on heat flux principle. The sample and reference are kept in a temperature programmed furnace. The temperature of the furnace is raised in a linear fashion and the resultant differential heat flow to the sample and reference is monitored by thermocouples and recorded against temperature/time.

TA Q20 Differential Scanning Calorimeter was used in this work for melting, crystallisation characteristics and phase analysis.

2.2.2.13 Universal testing machine

Universal testing machine (UTM) Instron 5569 was used for the mechanical property evaluation. For measuring loads, Load cells are being used which are precision force-transducers that contain a full strain gauge bridge bonded to an ultra-high stiffness elastic element. When the element is subjected to a force, the electrical resistance of the gauges changes, which results in an output signal proportional to the applied force. Mechanical properties such as tensile strength, elongation at break and Young's modulus were measured using UTM. Tensile strength is the maximum stress that a material can withstand while being stretched or pulled before failing or breaking. Young's modulus is the ratio of stress (force per unit area) to strain (ratio of deformation over initial length) within elastic limits.

$$\text{Tensile strength (MPa)} = \frac{\text{Load at failure (N)x } 10^{-6}}{\text{Cross sectional area (m}^{2)})} \quad \text{--- (2.16)}$$

$$\text{Elongation (\%)} = \frac{\text{Increase in length (m) x 100}}{\text{Original length (m)}} \quad \text{--- (2.17)}$$

$$\text{Young's modulus (MPa)} = \frac{\text{Stress (MPa)}}{\text{Strain}} \quad \text{--- (2.18)}$$

Computational studies on ionic liquids

Part A- Energetic ionic liquids
&
Part B- Screening of ILs for clay modification
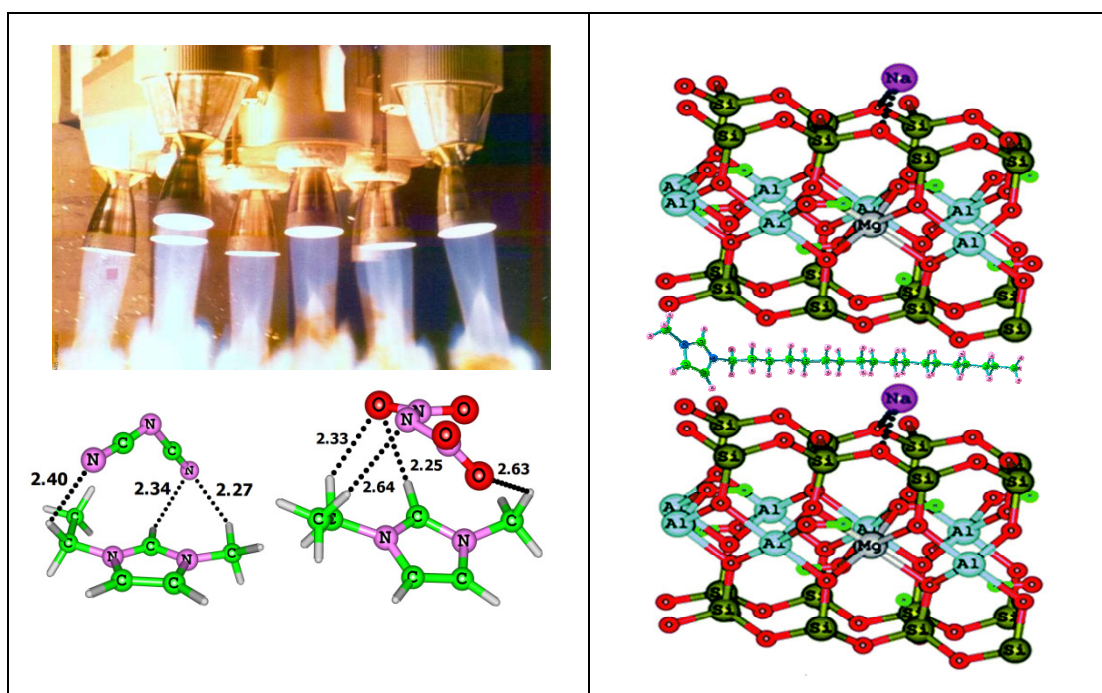
Imidazolium based energetic ionic liquids for monopropellant applications: a theoretical study†

Eapen Thomas, Kunduchi Periya Vijayalakshmi* and Benny Kattikkanal George

Part A - Energetic ionic liquids

Abstract

Energetic properties of 1-ethyl-3-methylimidazolium based ionic liquids were investigated by suitably selecting the pairing anions containing energetic groups. The key property to determine the specific impulse, the molar heat of formation, was computed. The accuracy of the method was proved with compounds of known heat of formation values. Based on the studies new ionic liquids were predicted with equivalent or better specific impulse than the commonly used hydrazine monopropellant.

3.1 Introduction

Hydrazine is one of the most widely used monopropellants for spacecraft application due to its good combustion, decomposition and storage properties [Sutton and Biblarz 2010]. However, owing to high toxic and carcinogenic character of this compound, development of new energetic and green compounds which show higher propellant performance than hydrazine is necessary. Ionic salts are attractive for this purpose as they are essentially non-volatile and thermally stable under normal conditions [Drake *et al.* 2003; Trohalaki *et al.* 2005; Coleman and Gathergood 2010]. The energetic salts such as, hydroxyl ammonium nitrate (HAN), ammonium dinitramide (ADN) and hydrazinium nitroformate were proposed as a substitute for hydrazine. However, they have melting points above room temperature, and can be used only in an aqueous solution to produce a storable liquid propellant. Ionic Liquids (ILs) have been anticipated, as the new generation green propellant fuels [Schneider *et al.* 2008; Zhang *et al.* 2011, 2013; Sebastiao *et al.* 2014; McCrary *et al.* 2014]. ILs are more attractive than ionic salts as they show low melting points, thus potentially combining the useful characteristics of salt systems with the advantage of handling liquid systems. Their low sensitivity to external stimuli such as impact, friction, shock, and electrostatic discharge further add to the credit [Zhang and Shreeve 2014].

Among various ILs in use, imidazolium based ILs are known for their chemical stability and fluid properties. The unique properties of these cations stem from the electronic structure of the aromatic cations. The electronic structure of imidazolium cations is characterized by 3-center-4-electron configuration across the N1-C2-N2

bonds, and a double bond between C3 and C4. The C2 is positively charged owing to the electron scarcity in the C=N bond, imparting slight acidity to the C2-H hydrogen atom (Figure 3.1). Hence the C2-H···anion interactions play an important role in the overall chemical and physical properties of the compound. The liquescent features of imidazolium based ILs are also well explained with these C2-H···anion interactions [Ludwig and Paschek 2009] and are relevant to the use of these compounds as propellants. Apart from fluidity parameters, heat of formation ($\Delta_f H°$) turns out to be a decisive factor for propellant properties. The energy release during combustion of a high energy material is given by the difference between the heat of formation of the compound and that of the combustion products which increases with increasing positive heat of formation of the compound.

[C₂MIm]⁺	[BF₄]⁻	[PF₆]⁻	[tz]⁻
	[dc]⁻	[mtz]⁻	[trz]⁻
	[dtrz]⁻	[dn]⁻	[CNtz]⁻
	[NH₂tz]⁻	[NO₂tz]⁻	[NO₂Otz]⁻
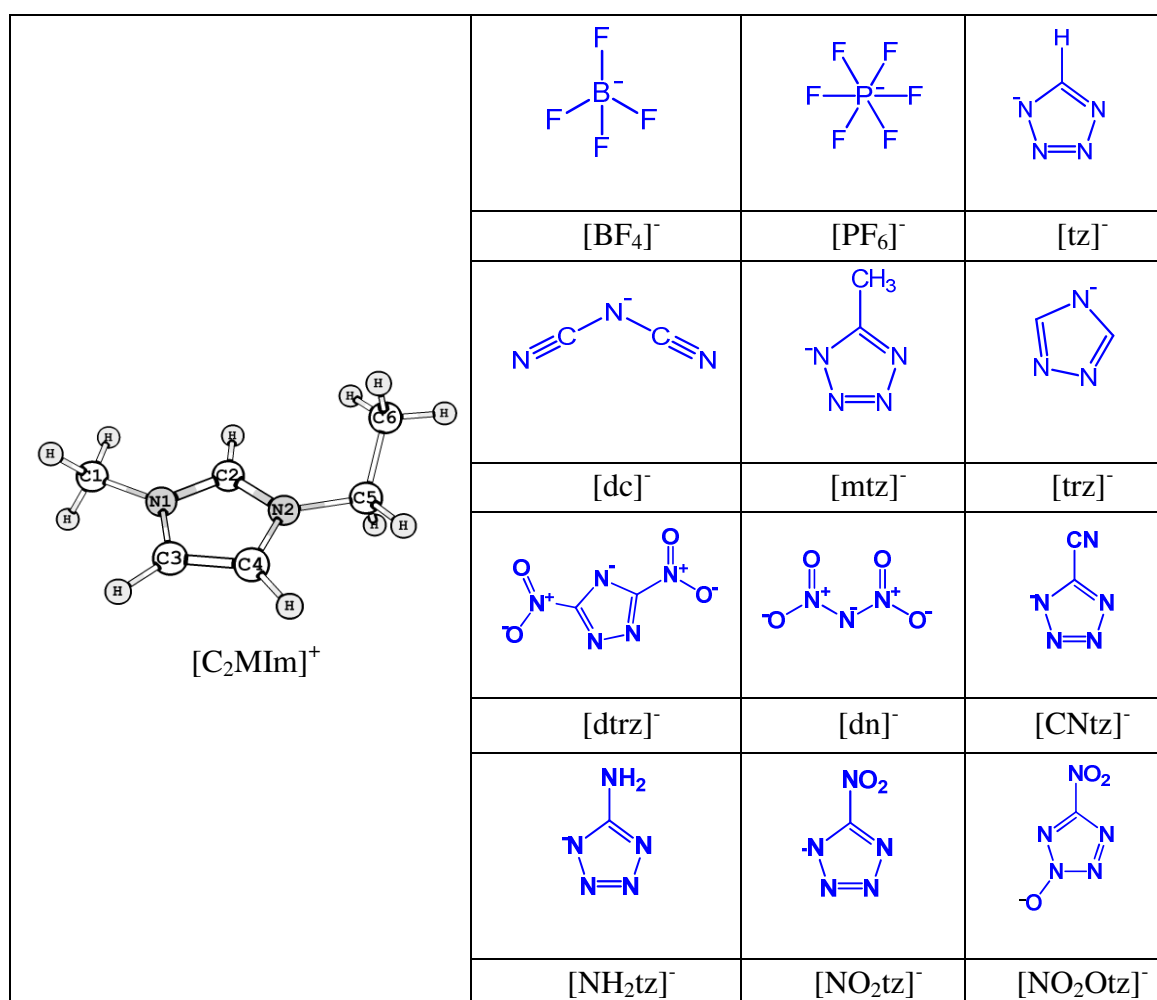
Figure 3.1 Chemical structures of imidazolium cation and the selected counter anions. The abbreviations used to name these systems are also given.

In spite of the numerous reports on structure-physical property correlation of ILs [Zorn *et al.* 2006; Ueno *et al.* 2010; Erdmenger *et al.* 2008], studies on the thermo chemical properties are very limited. Ab initio methods have been employed for accurate calculation of heat of formation parameters of energetic salts [Emelyanenko *et al.* 2009; Gutowski *et al.* 2007]. Vladimir *et al.* [2007] studied heat of formation of the ionic liquid 1-butyl-3-methylimidazolium dicyanamide using atomization reaction and isodesmic reactions and observed a concurrence between theoretical and experimental results.

3.2 Methodology

1-ethyl-3-methylimidazolium cation ([C$_2$MIm]$^+$) is selected as the cationic portion of the IL and twelve different anions are selected to form ion-pair complexes with the cation (Figure 3.1). Among the anions, tetrafluoroborate (BF$_4$$^-$) and hexafluorophosphate (PF$_6$$^-$) are conventionally used anions while the rest of them are nitrogen rich energetic anions. Among the nitrogen rich anions, the tetrazolate anions [tz]$^-$ and its derivatives are given prime importance as they possess high heats of formation resulting from the nitrogen-nitrogen bonds, ring strain and high energy density. In addition, the aromatic ring of [tz]$^-$ provides the required thermal stability for its ion pairs. To improve the oxygen balance in [tz]$^-$, the NO$_2$ substitution is useful. The study also includes the anion 5-nitrotetrazolate-2N-oxide ([NO$_2$Otz]$^-$) synthesized by Klapötke *et al.* [2009] as a superior energetic anion than nitrotetrazole.

The dispersion included Minnesota DFT method M06L [Zhao *et al.* 2006] as implemented in *Gaussian09* [Frisch *et al.* 2009] is used in conjunction with 6-311+G(d,p) basis set for optimizing all the molecular geometries in their gas phase. A benchmark study by Remya and Suresh [2013] showed that this method is the most effective to reproduce coupled cluster single and double (CCSD(T)) level geometry and binding energy (E_b) of noncovalently bonded molecular dimers of organic molecules. Since the focus of this study is on the propellant applications of energetic ionic liquids (EILs) and considering that the process of ignition and combustion of EILs takes place in the gas phase, the gas phase results are expected to be reliable. Several orientations of the anion-cation pairs were considered to locate the most stable IL structure (Figure 3.2). Normal modes of vibrations were analyzed for all the optimized geometries to ensure that every structure is a minimum on the potential energy surface. Basis set

superposition error corrected E_b of the ion pair $[C_2MIm]^+[X]^-$ formation in the gas phase (eqn. 3.1) was calculated at M06L/6-311+G(d,p) level.

$$[C_2MIm]^+ + [X]^- \rightleftharpoons [C_2MIm]^+[X]^- \qquad\qquad --- (3.1)$$

3.2.1 Conformation analysis of 1-ethyl-3-methylimidazolium cation

Conformations of 1-ethyl-3-methylimidazolium cation, $[C_2MIm]^+$ was done by rotating the ethyl group around the C-N bond (Figure 3.2). This was done by varying the dihedral angle (θ) defined by the four atoms in the order CH_3-CH_2-N(ring)-CH(ring). The angle θ is varied from 0.0^o to 360.0^o in increments of 10°. Because of the planar symmetry of the molecule at $θ = 0.0^o$ and $θ = 180.0^o$, the energy profile for the rotation values in the range 180.0^o - 360.0^o is same as that in the range 180° to 0.0^o. Imidazolium cation exists in two different conformations. The methyl group always showed a fixed orientation wherein a cis-arrangement of one of its CH bond with respect to the CH bond of the ring juxtaposed with the two nitrogen atoms.
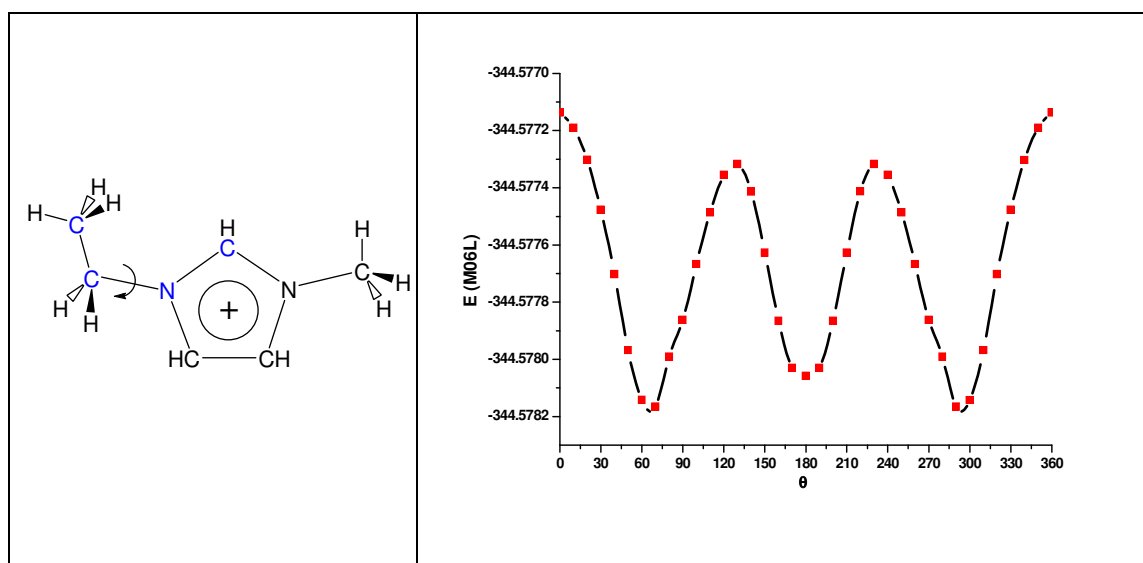
Figure 3.2 (a) Structure of $[C_2MIm]^+$ cation and (b) the energy profile for the rotation of the C-N bond (energy values in au and angle in degrees).

3.2.2 The strategy used to locate various configurations of cation-anion complex

The schematic shown in Figure 3.3 (blue is cation and red is anion) is useful to explain the conformational space scanned for the cation-anion complex. The illustration is based on $[C_2MIm]^+[dtrz]^-$ complex. To generate an initial structure of the cation-anion complex, we used the Chemcraft program to place the cation above the π-region of the anion to obtain a parallel orientation of its ring with respect to the ring of the

anion while the distance between the centres of the two rings is selected close to 3.5 Å. While selecting this orientation, one of the ring atoms of the anion is oriented close to the C2 carbon of the cation. The initial geometry of another configuration is made in a similar manner but the nearest ring atom of the anion from C2 is changed. This way we can generate 5 initial structures (a-e) so that N⁻ atom of anion will be facing the 5 different atoms of imidazolium ring. Also we used four different orientations for the in-plane configuration of the cation-anion complex as shown in (f-i). This exercise is done for all the tetrazolate and triazolate anions with both conformations obtained for the cation. For the open structures, viz. [dc]⁻ and [dn]⁻, the conformational space is scanned by orienting the central nitrogen towards the π-region of the cation or that nitrogen orienting away from the π-region. Also the in plane configurations are considered.
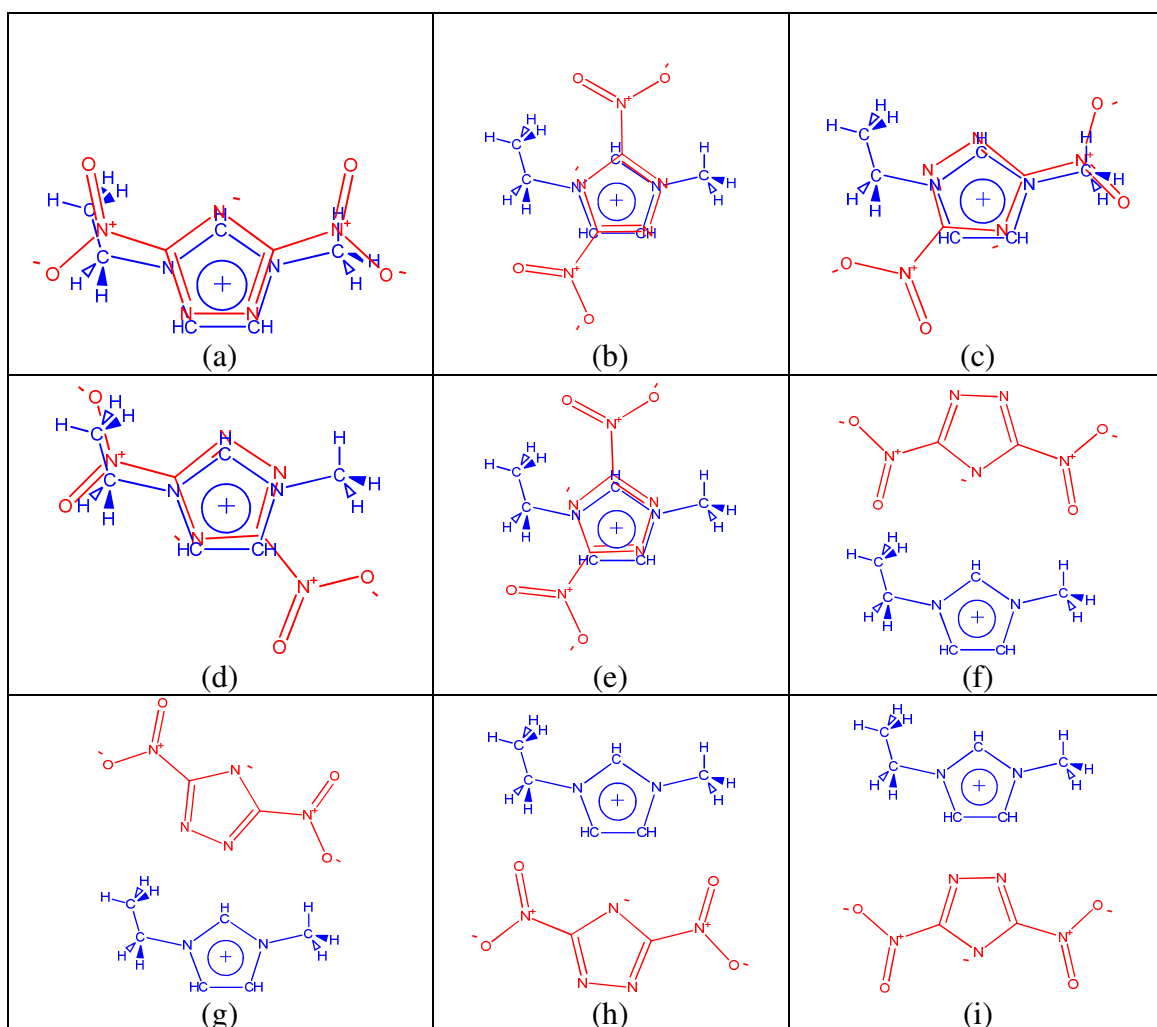
Figure 3.3 The schematics showing the strategy used to search for the conformational space of the cation-anion complex. The illustration is based on [C$_2$MIm]$^+$[dtrz]$^-$ complex.

3.2.3 Calculation of heat of formation

In the present study, atomization data obtained from the literature along with the G3MP2 level thermodynamic data is used to calculate the heat of formation for all IL systems. The G3MP2 is one of the popular high accuracy methods for calculating enthalpy quantities which is based on complex energy computations involving several pre-defined calculations on the specified molecular system [Curtiss *et al*. 1999]. Calculating enthalpies of formation of the molecule at 298K, $\Delta_f H^o_{(M,298K)}$ can be split into a couple of steps which is given below.

(a) Atomization energy of the molecule, $\sum D_o(M)$

$$\sum Do(M) = \sum n.X(\varepsilon_o) - M(\varepsilon_{o+ZPE}) \qquad \text{--- (3.2)}$$

M stands for the molecule and X to represent each element which makes up M, n is the number of atoms of X in M. ε_o is the electronic energy and ZPE is the zero-point energy.

(b) Heat of formation of the molecule at 0K, $\Delta_f H^o_{(M,0K)}$

$$\Delta_f H^o_{(M,OK)} = \sum n.\Delta_f H^o_{(X,OK)} - \sum Do(M) \qquad \text{--- (3.3)}$$

Table 3.1: Experimental enthalpies of formation of elements (kcal/mol) and enthalpy correction taken for elements in their standard states.

Element	$\Delta_f H^o_{(X,0K)}$[Chase *et al*. 1985]	H^o(298 K) - H^o(0 K)
H	51.63	1:01
Li	37.69	1.10
Be	76.48	0.46
B	136.20	0.29
C	169.98	0.25
N	112.53	1.04
O	58.99	1.04
F	18.47	1.05
Na	25.69	1.54
Mg	34.87	1.19
Al	78.23	1.08
Si	106.6	0.76
P	75.42	1.28
S	65.66	1.05
Cl	28.59	1.10

The experimental values of $\Delta_f H^o_{(X, 0K)}$ of the first and second row atomic elements at 0K are tabulated in Table 3.1.

(c) Enthalpy correction for the molecule, $H^o_M(298\ K)$ - $H^o_M(0\ K)$

$$H^o_M\ (298\ K) - H^o_M\ (0\ K) =\ H_{corr}\ -\ M(\varepsilon_{ZPE}) \qquad\qquad \text{--- (3.4)}$$

The enthalpy corrections, $H^o\ (298\ K)$ - $H^o(0\ K)$ is used to convert the atomic heats of formation at 0 K to those at 298.15 K, which is obtained from Gaussian output as "thermal correction to enthalpy".

 (d) Heat of formation of the molecule at 298K, $\Delta_f H^o_{(M,298\ K)}$.

$$\Delta_f H^o_{(M,298\ K)} = \Delta_f H^o_{(M,0K)} + [H^o_M\ (298\ K) - H^o_M\ (0\ K)] - [\sum n.\ (H^o\ (298K) - H^o(0K)]$$

$$\text{--- (3.5)}$$

   To estimate the accuracy of the proposed methods, an error function based on the normalized standard deviation is calculated as follows (eqn.3.6),

$$\Delta q(\%) = \sqrt{\frac{\sum[(\Delta_f H^o_{(exp)} - \Delta_f H^o_{(cal)})/\ \Delta_f H^o_{(exp)}]^2}{(N-1)}} \qquad\qquad \text{--- (3.6)}$$

where $\Delta q(\%)$ is the normalized standard deviation. The $\Delta_f H^o_{(exp)}$ and $\Delta_f H^o_{(cal)}$ are the experimental and calculated heat of formation. N is the number of data points available. The gaseous heat of formation, $\Delta_f H^o$ is also calculated using B3LYP/6-311+G(d,p), M06L/6-311+G(d,p), M05-2X/6-311+G(d,p) and M06-2X/6-311+G(d,p) levels of DFT.

3.2.4 Specific impulse

        The term 'specific impulse' (Isp) is used in rocket propulsion to define the impulse created per unit weight of propellant. It is equal to the number of pounds of thrust produced per pound of propellant burned per second. Isp is usually expressed in "seconds". Using the G3MP2 level heat of formation of the molecule, rocket performance analysis is done to determine the capability of the selected ILs (combination of $[C_2MIm]^+$ and any of the selected anions) to function as chemical monopropellants. Equilibrium combustion analysis is done by using the NASA Chemical equilibrium with applications (CEA) computer code [Gordon 1996]. Isp was calculated using conditions similar to on orbit engines with Nozzle area ratio (i.e., Area of exit: Area of throat) of 50:1 and combustion chamber pressure of 300 psi. CEA is employed for 100 % fuel and then with a shifting equilibrium assumption for binary

mixture, fuel and oxidiser. In the binary mixture of IL with HAN, Isp is calculated as a function of % oxidiser by weight.

3.3 Results and discussion

3.3.1 Electronic structure and properties
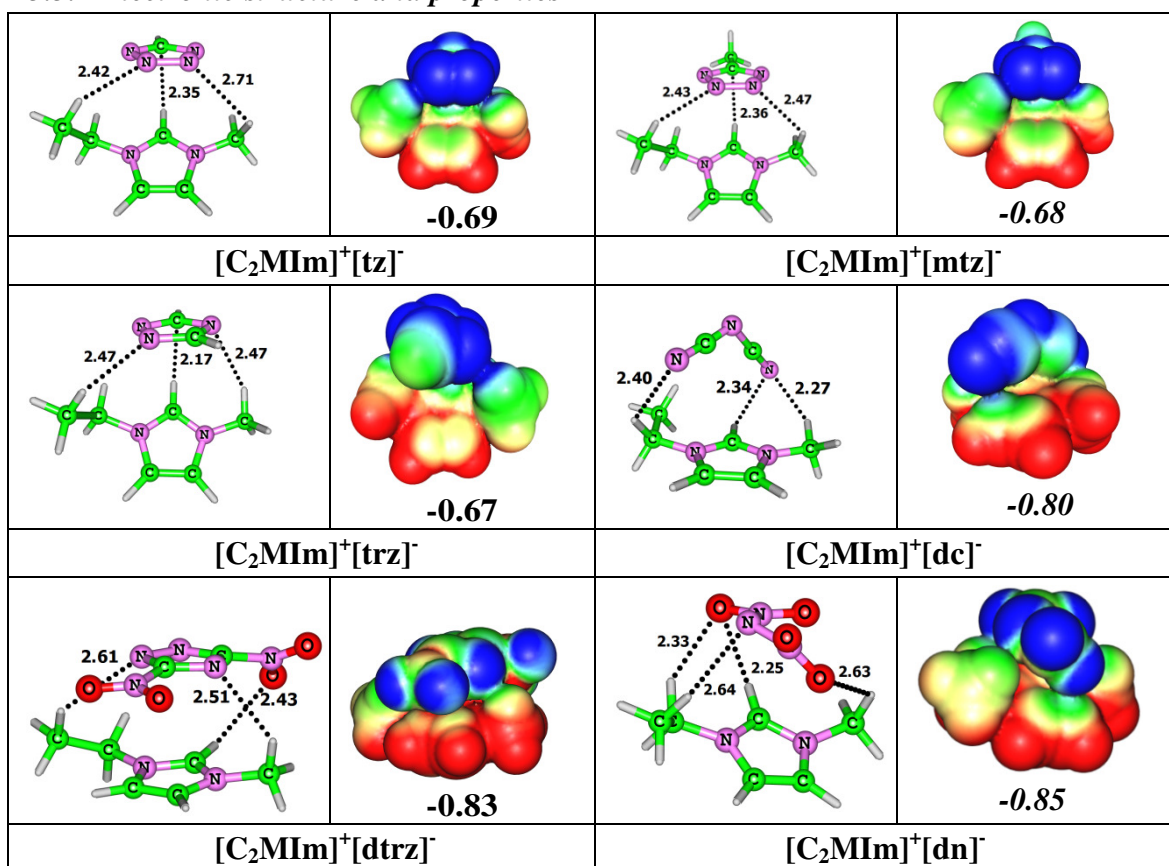
Figure 3.4 The optimized structures (left) of the representative set of EILs predicted for propellant applications and MESP plots (right). MESP-derived charge on anion is also depicted. Colour coding, ▬▬▬▬ blue -0.05 au. to red 0.05 au. Distances in Å.

The $[C_2MIm]^+$ showed two distinct nearly isoenergetic conformations with energy difference 0.30 kJ/mol. Hence, both the conformers are used for generating initial structures of ion-pair complexes. The most stable structures of the representative energetic ion pairs $[C_2MIm]^+[X]^-$ are reported in Figure 3.4. All of them exhibit non-covalent C-H⋯C/C-H⋯N/C-H⋯O interactions in the range 2.17 Å – 2.64 Å. Normally, if uncharged systems are involved, such non-covalent distances would suggest very weak E_b in the range 10 – 20 kJ/mol. In sharp contrast to this, the non-covalent E_b computed for IL systems are very high, in the range 336 – 400 kJ/mol (Table 3.2) indicating that strong electrostatic interactions prevail in all the charge separated ion-pairs.

The cation-anion charge separation is significant in all the cases which is well evident in the molecular electrostatic potential (MESP) plots given in Figure 3.4, where the anion has the MESP-derived Merz-Singh-Kollman (MK) charge in the range of -0.68 to -0.86 (Table 3.2) and cation has the counter positive values. The MK charge can be considered as a measure of the amount of charge transfer from the anion to the cation. The charge transfer (29–34 %) is clearly more dominant in four energetic anions, *viz.* [trz]⁻, [tz]⁻, [mtz]⁻ and [NH₂tz]⁻ which show E_b in the range 388 – 400 kJ/mol while the rest of the energetic anion show E_b in the range 336 – 370 kJ/mol with charge transfer 20 ± 5 %.

Table 3.2 Binding energy E_b, ΔE^* and MK charge of ion pairs computed at M06L/6-311+G level of DFT.

IL	E_b (kJ/mol)	ΔE^* (eV)	MK charge
$[C_2MIm]^+ [BF_4]^-$	370.0	5.38	-0.86
$[C_2MIm]^+ [PF_6]^-$	351.2	5.54	-0.85
$[C_2MIm]^+ [dc]^-$	361.9	2.83	-0.80
$[C_2MIm]^+ [trz]^-$	398.7	3.31	-0.67
$[C_2MIm]^+ [dtrz]^-$	335.5	3.14	-0.83
$[C_2MIm]^+[dn]^-$	355.9	3.30	-0.85
$[C_2MIm]^+[tz]^-$	388.0	3.68	-0.69
$[C_2MIm]^+[mtz]^-$	389.7	3.62	-0.68
$[C_2MIm]^+[CNtz]^-$	351.5	3.83	-0.77
$[C_2MIm]^+[NH_2tz]^-$	399.8	2.94	-0.72
$[C_2MIm]^+[NO_2tz]^-$	353.6	3.12	-0.78
$[C_2MIm]^+ [NO_2Otz]^-$	347.2	2.39	-0.82

The stability of compounds are also examined based on the energy gap (ΔE^*) between the highest occupied molecular orbital (HOMO) and the lowest unoccupied molecular orbital (LUMO). Conventional ILs (first two entries in Table 3.2) possess ΔE^* of ~5.5 eV while energetic ILs (EILs) are characterized with a lower band gap energy (2 - 4 eV). In general, a small ΔE^* helps the electrons to cross the band gap easily, leading to poor compound stability [Zhao and Lu 2012; Ravi *et al.* 2012] as this process destroys charge separation in the ion-pair. The derivatives of tetrazolate anions show good stability in terms of the predicted band gap. Among different derivatives of tetrazolate based EILs, ΔE^* predicts $[C_2MIm]^+[CNtz]^-$ as the most stable as it possesses the highest ΔE^* value of 3.83 eV. The very high E_b (398.7 kJ/mol) obtained for

$[C_2MIm]^+[trz]^-$ was decreased to 335.5 kJ/mol by dinitro substitution in the triazolate anion ($[C_2MIm]^+[dtrz]^-$). The electronic structural features have successfully been employed to tailor thermodynamic properties such as melting point of ILs. Generally, highly delocalised charge in the anion and shielded positive charge in the cation assist the formation of low melting ILs. In the given set of ion pairs, the best delocalization is observed for highly symmetric anions like $[dc]^-$ and $[dtrz]^-$ as revealed from the MESP plot given in Figure 3.4. There are many strategies reported to fluidize imidazolium based ionic liquids. Introducing weakly polar anions generally reduce the interaction energy between cations and anions resulting in reduced melting points and decreased viscosities [Krossing *et al*. 2006]. Another strategy is to introduce asymmetry into the imidazolium cation by using different substituents at the N1 and N3 positions [Fredlake *et al*. 2004]. Strong, directional and localized hydrogen bonds are also reported to enhance the fluid properties of imidazolium based ILs [Fumino *et al*. 2008].

        We have considered all these factors while designing the compounds and sought possible correlation between computed E_b and melting points of known compounds. Generally higher E_b correlates to higher melting point which suggest that the melting points of energetic ILs could be higher than the traditional ILs (first two entries in Table 3.2) and among them the $[C_2MIm]^+[NH_2tz]^-$ is expected to possess the highest melting point. Organic salts of $[dc]^-$ anions, in general are known to possess relatively lower melting points [MacFarlane *et al*. 2001] and reported melting point of $[C_2MIm]^+[dc]^-$ is -27 ^{o}C. Among the named EILs, $[C_2MIm]^+[CNtz]^-$, $[C_2MIm]^+[dn]^-$, $[C_2MIm]^+[dtrz]^-$, $[C_2MIm]^+[NO_2tz]^-$ and $[C_2MIm]^+[NO_2Otz]^-$ possess lower E_b than the $[C_2MIm]^+[dc]^-$ and indicate their existence in liquid state.

3.3.2 Thermochemical properties

        It is important to determine the thermochemical properties of ILs in the vapor phase as the process of ignition and combustion take place in the gas phase. The thermochemical calculations using DFT methods (B3LYP, M06L, M05-2X, M06-2X) and ab initio method (G3MP2) are compared for compounds of known experimental heat of formation, $\Delta_f H^o$ in Table 3.3. Compared to the DFT methods, the G3MP2 results are very close to the experimental values. For the fourteen known compounds in Table 3.3, the error function Δq values are 20.6, 28.4, 48.7, 23.8 and 4.0 %, respectively observed for B3LYP, M06L, M05-2X, M06-2X and G3MP2 methods.

Table 3.3 Experimentally reported $\Delta_f H^o$ (kJ/mol) values of known systems along with calculated DFT and ab initio values.

| Compound | $\Delta_f H^o$ (kJ/mol) | | | | | Ab initio | Experimental | Reference |
| | DFT | | | | | G3MP2 | | |
	B3LYP	M06L	M05-2X	M06-2X				
1,3-H-imidazolium cation	758.8	749.5	716.5	752.8		725.8	719.8	[Dixon et al. 2006]
1,4-H-1,2,4-triazolium cation	867.0	869.3	908.1	877.7		847.3	836.0	[Gutowski et al. 2006]
Tetrazolate anion	192.4	202.4	222.4	228.3		186.1	200.2	[Gutowski et al. 2006]
1,2,4-triazolate anion	120.6	121.2	142.3	135.1		100.8	102.8	[Gutowski et al. 2006]
[C4MIm]+[dc]-	499.7	404.0	592.1	445.7		360.9	363.4	[Vladimir et al. 2007]
[C2MIm]+[dc]-	510.3	422.2	576.8	466.4		404.1	391.7	[Verevkin et al. 2010]
Hydrazine	91.9	151.6	158.5	124.2		92.1	90.0, 95.0	[Schmidt et al. 2001; Chase Jr. et al. 1998]
Monomethyl hydrazine	104.0	158.1	185.3	128.2		82.9	92.0	[Schmidt et al. 2001]
Pyridine	193.4	141.1	219.8	177.3		133.5	140.0	[Lias et al. 1988]
Pyridazine	322.7	285.9	356.9	325.1		277.4	278.3	[Lias et al. 1988]
Pyrazine	245.2	210.5	276.0	243.0		201.8	196.0	[Lias et al. 1988]
1,2,3-triazine	435.9	411.5	455.6	477.4		403.3	416.0	[Lias et al. 1988]
1,2,4-triazine	368.1	348.9	404.6	382.6		337.1	334.0	[Lias et al. 1988]
1,3,5-triazine	256.8	239.8	282.9	263.4		226.4	226.0	[Lias et al. 1988]

Table 3.4 The $\Delta_f H^o$, % (N + O) and Isp values of ion-pairs of ILs and hydrazine at G3MP2 level.

Compound	Molecular formula	$\Delta_f H^o$ (kJ/mol)	(N+O) (Wt%)	Isp (s)	% HAN with IL for Isp=263 s	Isp (s) maximum (% HAN)
Hydrazine	N_2H_4	90.0	87.5	263	-	-
$[C_2MIm]^+[BF_4]^-$	$C_6N_2H_{11}BF_4$	-1692.2	14.2	-*	68	295 (80%)
$[C_2MIm]^+[PF_6]^-$	$C_6N_2H_{11}PF_6$	-1909.2	10.8	105	63	287 (80%)
$[C_2MIm]^+[tz]^-$	$C_7N_6H_{12}$	441.9	46.7	221	54	317 (80%)
$[C_2MIm]^+[dc]^-$	$C_8N_5H_{11}$	401.3	39.5	208	58	314 (80%)
$[C_2MIm]^+[mtz]^-$	$C_8N_6H_{14}$	404.2	43.3	213	57	315 (80%)
$[C_2MIm]^+[trz]^-$	$C_8N_5H_{13}$	346.9	39.1	207	59	314 (80%)
$[C_2MIm]^+[dtrz]^-$	$C_8N_7H_{11}O_4$	305.9	60.2	241	34	315 (70%)
$[C_2MIm]^+[dn]^-$	$C_6N_5H_{11}O_4$	166.9	61.7	252	23	319 (70%)
$[C_2MIm]^+[CNtz]^-$	$C_8N_7H_{11}$	558.6	47.8	221	54	316 (80%)
$[C_2MIm]^+[NH_2tz]^-$	$C_7N_7H_{13}$	444.8	50.3	219	53	317 (80%)
$[C_2MIm]^+[NO_2tz]^-$	$C_7N_7H_{11}O_2$	418.8	57.7	239	40	315 (80%)
$[C_2MIm]^+[NO_2Otz]^-$	$C_7N_7H_{11}O_3$	387.1	60.6	246	33	316 (70%)
HAN	$N_2H_4O_4$	-198.2	95.8	238	-	-

* A condensed species H_3BO_3 is formed.

Vikram Sarabhai Space Centre

The high accuracy of G3MP2 results is obvious from this data. Moreover, for the $\Delta_f H^o$ of hydrazine, two different experimental values are known and between them, the smaller value 90 kJ/mol is closer to G3MP2 value of 92.1 kJ/mol. Therefore, only G3MP2 data are used for calculating the propellant property of ILs. For EILs to be used for propellant applications, they require high energy density which is often associated with large positive heat of formation. This in turn results in high combustion chamber temperature and hence a higher Isp. Conventional ILs, *viz.* $[C_2MIm]^+[BF_4]^-$ and $[C_2MIm]^+[PF_6]^-$ have negative heat of formation suggesting a lower energy content. The heat of formation increases from -1692.2 to +558.6 kJ/mol when the anionic part is substituted by energetic groups (Table 3.4). The computed $\Delta_f H°$ of all the nitrogen rich energetic ILs possess much higher heat of formation than hydrazine and suggests their use for propellant applications. The highest value of $\Delta_f H°(g)$ is obtained for CNtz (558.6 kJ/mol) derivative. The lower values of $\Delta_f H°(g)$ for $[C_2MIm]^+[trz]^-$, $[C_2MIm]^+[Mtz]^-$ and $[C_2MIm]^+[dc]^-$ can be attributed to their higher carbon content.

Oxygen balance is another significant index of energetic materials which is a measure of oxygen deficiency or excess of oxygen in a compound required to convert all the carbon into carbon dioxide and all the hydrogen into water. Generally oxygen rich compounds have higher Isp as all elements gets converted to gaseous product resulting in increased thrust. In the present set of EILs, the absence of oxygen content leads to relatively lower Isp for $[C_2MIm]^+[dc]^-$, $[C_2MIm]^+[NH_2]^-$, $[C_2MIm]^+[CNtz]^-$, $[C_2MIm]^+[tz]^-$, $[C_2MIm]^+[mtz]^-$ and $[C_2MIm]^+[trz]^-$ in spite of their higher values of $\Delta_f H°(g)$ (> 400 kJ/mol).
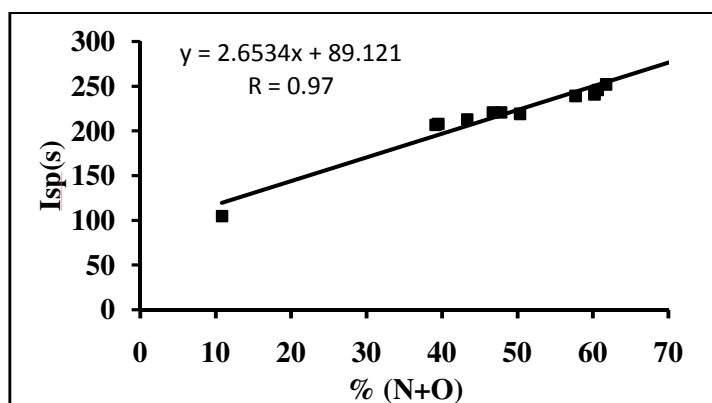
Figure 3.5 Correlation between % (N+O) and predicted Isp of $[C_2MIm]^+$ ion pairs with 11 different anions given in Table 3.4.

The highest Isp of 252 s is obtained for $[C_2MIm]^+[dn]^-$ with two $N-NO_2$ groups in the anion. In fact a linear correlation of Isp with total $(N + O)$ weight % is observed for all the ILs studied in the present work (Figure 3.5). The low oxygen balance of imidazolium based EILs can be overcome by using suitable oxidizer such as HAN and solvent properties of ILs can beneficially exploited to form binary-monopropellant mixtures [Freemantle *et al*. 2010]. ILs has been tested for hypergolicity with HAN oxidizer and it showed no visible signs of reactivity at room temperature [Dambach *et al*. 2008; Berg and Rovey 2013]. Hence a monopropellant mixture of IL with varying percentage of HAN is analyzed using CEA, which would be thermally stable at room temperature and ignited thermally or catalytically.

The Isp gradually increases with increase in the oxidizer concentration. This change is rapid in the 20 – 50 % concentration and reaches the peak region around 60 – 80 % concentration (Figure 3.6). These results clearly suggest that Isp tuning can be achieved by mixing ILs with suitable amount of HAN and these ILs may find use as fuel component in a binary propellant system. The ILs with oxygen rich anions, *viz*. $[dn]^-$, $[dtrz]^-$ and $[NO_2Otz]^-$ attain the Isp of currently used propellant hydrazine (263 s) at 23 - 34% of HAN concentration (Table 3.4). An enhancement of 56 units in Isp is obtained for $[C_2MIm]^+[dn]^-$ for 70 % HAN mixtures which provide the limit of Isp that can be achieved using the derivatives of imidazolium based ionic liquids (Table 3.4).
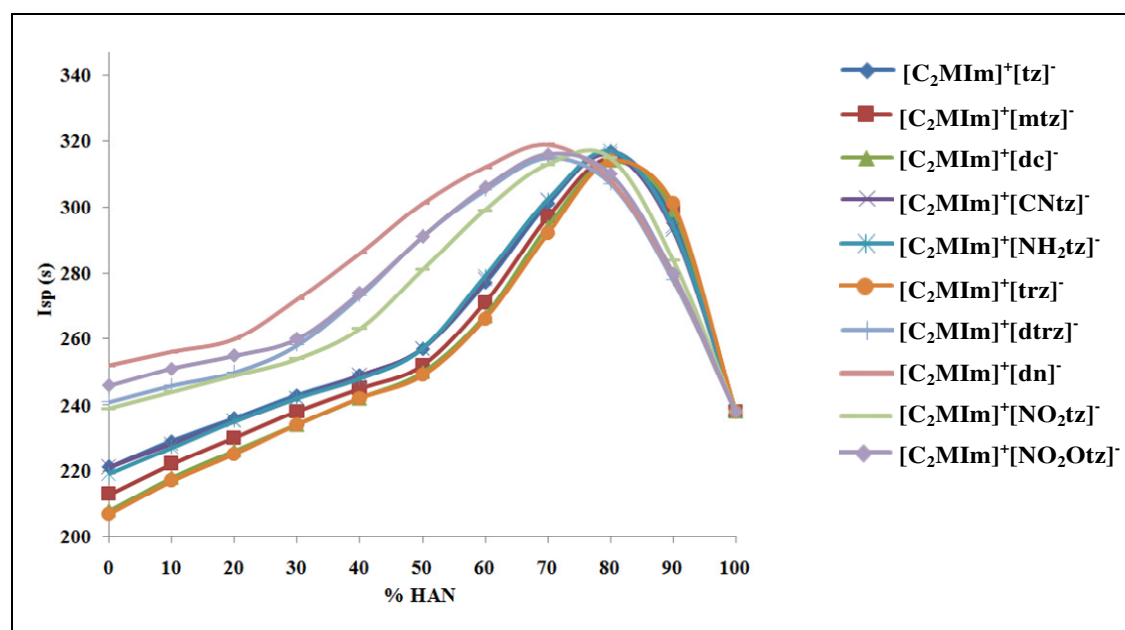
Figure 3.6 Variation of Isp with increasing HAN concentration.

3.4 Conclusions

In summary, thermochemistry of a variety of imidazolium based ILs were predicted accurately using quantum chemical computational studies. The high binding energy suggests ILs exist as ion-pairs in gaseous phase. The computed heats of formation of all the EILs of 1-ethyl-3-methylimidazolium cation and tetrazolide derivatives, dicyanamide, triazolide, dinitrotriazine, and dinitramide as anions are higher than that of hydrazine. ILs with a suitable oxidizer can be considered as a binary monopropellant due to the ILs solvent properties. Among the 12 imidazolium based EILs studied, $[C_2MIm]^+[dtrz]^-$, $[C_2MIm]^+[dn]^-$ and $[C_2MIm]^+[NO_2Otz]^-$ provided the best energetic performance in combination with HAN proposing the title compounds as potential green substitute for hydrazine. The Isp correlation with (N+O) content reveal the limit of Isp that can be achieved using imidazolium based ILs.

Part B - Screening of ILs for clay modification

Abstract

The structure and stability of 1-alkyl-3-methylimidazolium based ionic liquids were investigated using *Gaussian09* software. The effect of alkyl chain length and pairing anions on IL stability was explored using computed parameters like HOMO-LUMO energy gap (ΔE^*), Mulliken charge on the ring and charge transfer features from molecular electrostatic potential mapping at B3LYP level of density functional theory. Clay modification involves a cation exchange reaction and hence the stability of 1-alkyl-3-methylimidazolium cations were assessed using computed ΔE^* values. A decrease in ΔE^* was observed for 1-alkyl-3-methylimidazolium cations with increase in alkyl chain length and consequently 1-buyl-3-methylimidazolium based ionic liquids with highest cation stability are selected for experimental studies. As the d-spacing of modified clays play significant role in the final application, long chain 1-hexadecyl-3-methylimidazolium based ionic liquids were also selected for experimental studies. 1-hexyl-3-methylimidazolium substituted derivatives were selected to investigate the influence of medium chain length as the ΔE^* values start decreasing sharply after C_6. The effect of pairing anions was investigated using monatomic chloride ions and complex anion tetrafluoroborate. The frontier molecular orbital plot of 1-alkyl-3-methylimidazolium based ionic liquids reveal that the HOMO is always located in the anions for chloride derivatives while it is distributed between the anion and cation in the case of 1-alkyl-3-methylimidazolium tetrafluoroborate. Further Merz–Singh–Kollman (MK) charge parameters computed from molecular electrostatic potential mapping show that chloride anions have better charge transfer features than tetrafluoroborate anions.

3.5 Introduction

The invention of nylon/clay nanocomposites by Toyota researchers in the 1990s [Usuki *et al*. 1993; Kojima *et al*. 1993], triggered the use of nanoclay reinforced polymer composites in various applications. The easy availability and environment friendly nature of clay and layered silicates make them a potential candidate among all other nanocomposite precursors. The poor dispersion of polar clay into a non polar

polymer matrix restricts its wider use in nanocomposite field. Hence, organic modification of nanoclay is done to enhance the dispersion, wetting and compatibility in organic media.

Commercial organophilic clays used in polymer nanocomposites are often prepared from sodium montmorillonite (MMT-Na$^+$) clay by ion exchange of its interlayer sodium cations with long chain alkylammonium based ions (Figure 3.7). Their low thermal stability (<180 ^{o}C) results in degradation by Hoffmann elimination and limits its use in nanocomposite processing at higher temperatures [Cope and Trumbull 1960; Lee *et al*. 2005]. Thus, to increase the thermal stability of organically modified clays, the use of thermally stable imidazolium based ionic liquids (ILs) are envisaged as an alternative to ammonium salts [Xie *et al*. 2002; Awad *et al*. 2004; Mittal 2007; Livi *et al*. 2011].
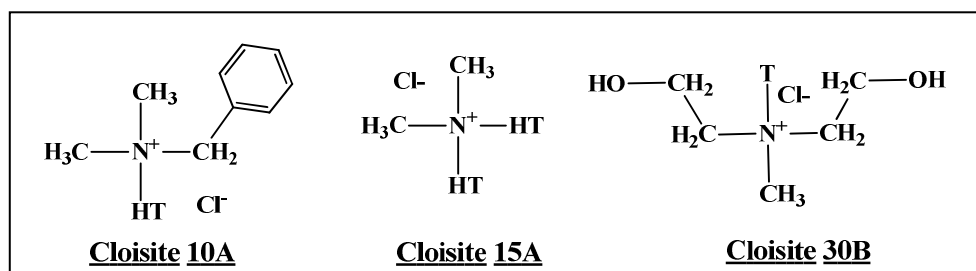
Figure 3.7 Typical quaternary ammonium modifiers for MMT nanoclay. T represents tallow and HT represents hydrogenated tallow.
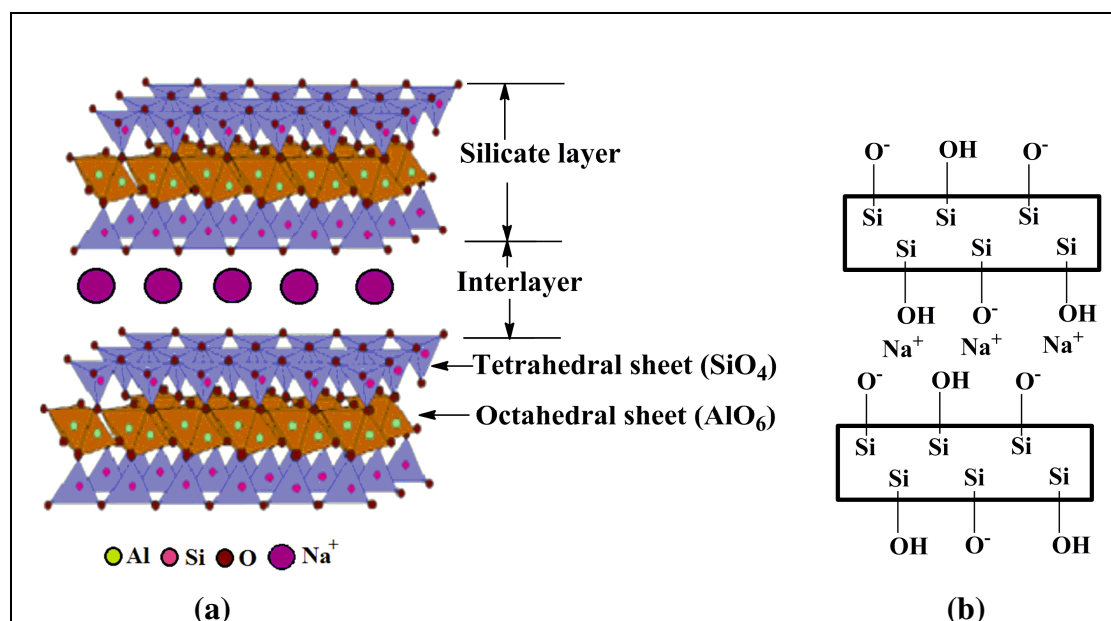
Figure 3.8 (a) Molecular structure of MMT containing exchangeable sodium ion (MMT-Na$^+$) and (b) Schematic representation of side view between layers.

Depending on the number of layers, clays are broadly classified as kaolinites and phyllosilicates. Kaolinites have 1:1 layered structures with tetrahedral sheet fused with an octahedral sheet, whereby the oxygen atoms are shared [Miranda Trevino and Coles 2003]. On the other hand, phyllosilicates consist of the crystal lattice of 2:1 layered silicates with two-dimensional layers where a central octahedral sheet of alumina fused to silica tetrahedra as shown in Figure 3.8 [Kato *et al*. 2000; Ray and Okamoto 2003].

Cationic nanoclays are exemplified by smectites, a group of 2:1 layer minerals that includes the hydrated aluminium silicate, montmorillonite (MMT). In such minerals the anionic charge of the aluminosilicate layer is neutralized by the intercalation of compensating, exchangeable cations (e.g. Na^+, Ca^{2+} and Mg^{2+}) and their coordinated water molecules. MMT consists of thin platelets of less than 1 nm in thickness. Each aluminum octahedral layer is linked together by oxygen and is sandwiched between silicon tetrahedral layers. These layers are linked together by Vander Waals forces and are formed as stacks of plates. Each platelet has a large surface area and a high aspect ratio of over 200. MMT clays having expandable interlayer spacing are known to be highly reactive to polar compounds containing exchangeable ions and, hence, are ideal candidates for modification with organic cations. The cation exchange capacity of MMT clay ranges between 80 and 150 meq/100 g [Lagaly *et al*. 2006], which makes clay modification possible through a cation exchange mechanism. In the modification of MMTs by ion exchange, the interlayer accessible compensating cations can be exchanged with a wide variety of hydrated inorganic cations or organic cations including those of amines or quaternary ammonium salts, phosphonium, pyridinium and more complex cationic species [Singla *et al*. 2012; Vaia *et al*. 1994; Xie *et al*. 2002; Calderon *et al*. 2008].

ILs being organic salts can be used in ion-exchange processes. The choice of 1-alkyl-3-methylimidazolium based ILs as organic modifier was based on its stability and high ionic conductivity. Use of 1-alkyl-3-methylimidazolium chlorides for cation exchange helps in easier processing by detection of chloride traces with silver nitrate solution. The first report on use of 1-alkyl-3-methylimidazolium based ionic liquid for clay modification was by Awad *et al.* in 2004 and the modified, 1-ethyl-3-methylimidazolium montmorillonite clay showed improved basal spacing and thermal stability. In addition to the high temperature polymer composite applications [Ding *et*

al. 2006; Kim *et al*. 2006; Ha *et al*. 2009; Montano *et al*. 2017], 1-alkyl-3-methylimidazolium modified clays were also used for contaminant removal from water [Sun *et al*. 2017; Ladino *et al*. 2016; Lawal *et al*. 2015; Li *et al*. 2014], in chromatographic columns [Yalcinkaya *et al*. 2014], as catalyst [Huang *et al*. 2010] and so on.

This work aims to select 1-alkyl-3-methylimidazolium cations for thermally stable and organophilic clay preparation. The properties of 1-alkyl-3-methylimidazolium cations are studied systematically using computational techniques and the cations are selected for experimental studies based on the stability, alkyl chain length and charge transfer features.

3.6 Methodology

The geometries of 1-alkyl-3-methylimidazolium cations and its ion-pairs with chloride and tetrafluoroborate anions were optimized at B3LYP level [Lee *et al*. 1988; Becke 1993] of DFT using 6-311+G(d,p) basis set as implemented in Gaussian 09 software [Frisch *et al*. 2009]. The alkyl chain length was selected from methyl ($[C_1MIm]^+$) to hexadecyl ($[C_{16}MIm]^+$). The computed parameters include HOMO-LUMO energy gap (ΔE^*), Mulliken charge analysis and charge transfer features from molecular electrostatic potential mapping.

HOMO-LUMO gap gives a direct correlation of chemical and radiation stability in ILs [Zhan *et al*. 2003; Ilawe *et al*. 2016]. A large HOMO-LUMO gap implies low chemical reactivity since it hinders adding electrons to a high-lying LUMO or extracting electrons from a low-lying HOMO and prevents the formation of the activated complex of any further reaction [Aihara 1999]. Zhou and Parr [1990] discussed the chemical reactivity of cyclic conjugated systems using the HOMO-LUMO gaps of the reactant and the transition state. The kinetic stability of fullerenes has also been discussed in terms of the HOMO-LUMO energy gap [Schmalz *et al*. 1988; Liu *et al*. 1992; Aihara *et al*. 1996]. Mulliken charge analysis was used to calculate individual charge contributions at the N2-C_nH_{2n+1}, imidazolium ring and N1-CH_3 sites and the total charge contribution to binding energy (E_b) in ILs. The MESP-derived Merz–Singh–Kollman (MK) charge gives a measure of the amount of charge transfer from the anion to the cation.

3.7 Results and discussion

3.7.1 1-alkyl-3-methylimidazolium cation

The optimized structures and HOMO-LUMO plot of 1-alkyl-3-methylimidazolium cations with different alkyl chain lengths are shown in Figure 3.9.
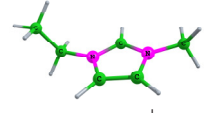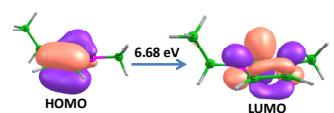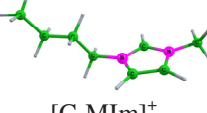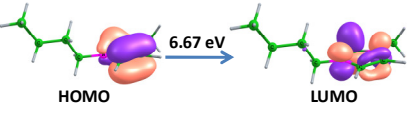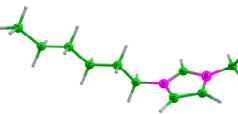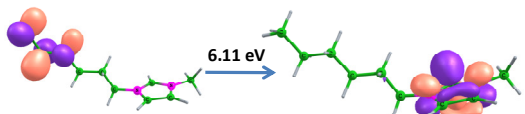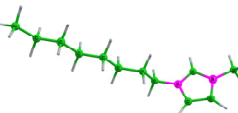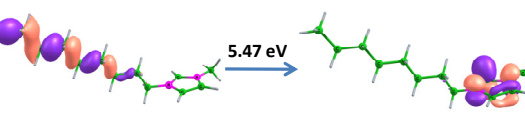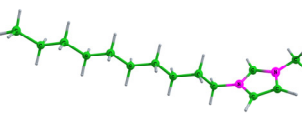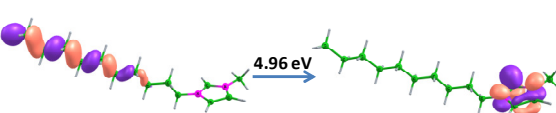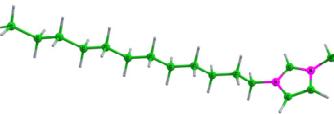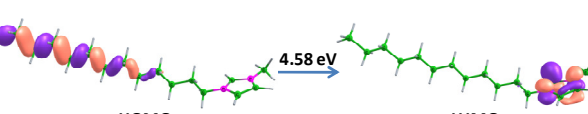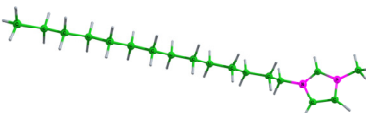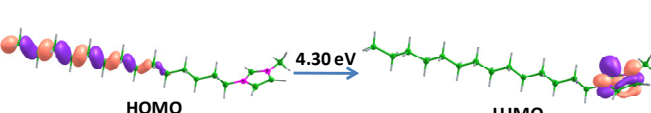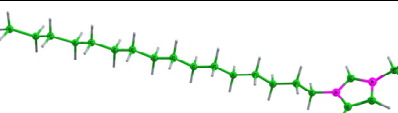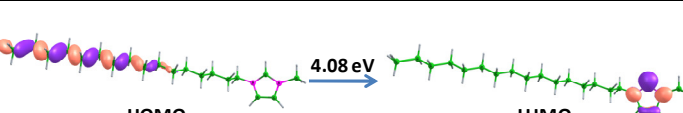
Optimized structure	HOMO-LUMO plot
 $[C_2MIm]^+$	
 $[C_4MIm]^+$	
 $[C_6MIm]^+$	
 $[C_8MIm]^+$	
 $[C_{10}MIm]^+$	
 $[C_{12}MIm]^+$	
 $[C_{14}MIm]^+$	
 $[C_{16}MIm]^+$	

Figure 3.9 The optimized structures (left) of the representative set of $[C_nMIm]^+$ and orbital plots (right). The abbreviations used to name the system are also shown.

In 1-alkyl-3-methyl imidazolium cations, as the alkyl chain length increases from methyl (C_1) to hexadecyl (C_{16}), there is significant changes in the HOMO plot,

where as LUMO is always located at the imidazolium ring. In 1,3-dimethylimidazolium cation (C_1MIm^+), HOMO is located on the imidazolium ring and the same trend is followed till 1-butyl-3-methylimidazolium cation (C_4MIm^+) with constant HOMO-LUMO gap (6.7 eV). From 1-methyl-3-pentylimidazolium cation (C_5MIm^+) onwards, the HOMO is shifted to the alkyl chain with decrease in HOMO-LUMO gap, indicating a decrease in stability and easy degradation of alkyl chain. The change in HOMO-LUMO gap with increase in alkyl chain length is shown in Figure 3.10. A steady decrease was observed after C_4MIm^+ cation and the energy gap falls below 4.0 eV after $C_{16}MIm^+$.
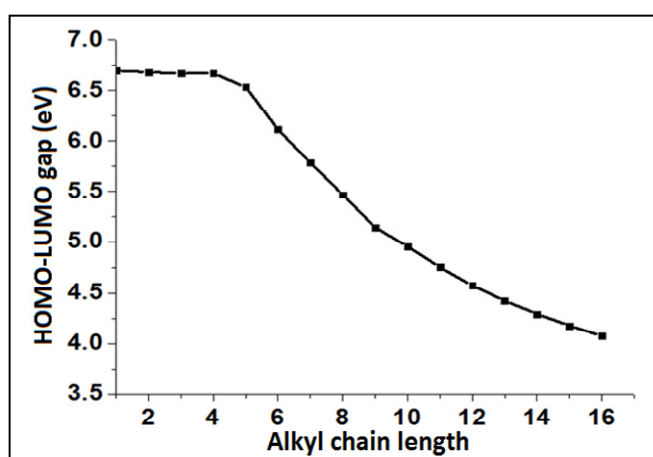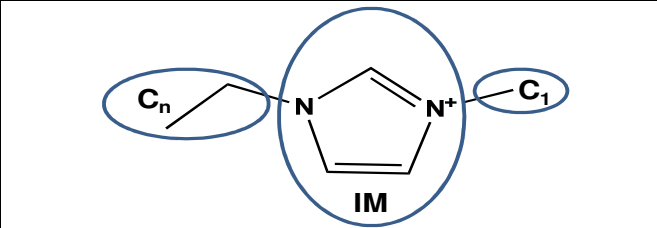
Figure 3.10 HOMO-LUMO gap *vs* alkyl chain length of $[C_nMIm]^+$ cations.

The effect of alkyl chain length on imidazolium ring charge was calculated from Mulliken charge analysis. The effective charge on the alkyl chain (C_n) and imidazolium ring (IM) are shown in Table 3.5. Mulliken charge on $N1-CH_3(C_1)$ showed no prominent change (0.385 - 0.421) on alkyl substitution at N2, but the charges on IM (0.230 - 0.567) and C_n (0.385 - 0.013) showed significant changes. The total charge on IM and C_n (0.579 - 0.615) remained constant suggesting the charge transfer from alkyl group at N2. Since the species as such is a cation with a single positive charge, the charge delocalization properties are dominant over the electron donating nature of alkyl groups. Hence an unexpected decrease in positive charge from 0.385 to 0.013 a.u. at the alkyl (C_n) side is observed with increasing chain length. Corresponding increase in positive charge is observed at the imidazolium ring as aromatic delocalization stabilizes the cation.

Table 3.5 Mulliken charge distribution in 1-alkyl-3-methylimidazolium cations.

Cation	C_n	IM	C_1	Total
$[C_1MIm]^+$	0.385	0.230	0.385	1
$[C_2MIm]^+$	0.331	0.273	0.396	1
$[C_3MIm]^+$	0.184	0.405	0.411	1
$[C_4MIm]^+$	0.154	0.435	0.411	1
$[C_5MIm]^+$	0.145	0.441	0.414	1
$[C_6MIm]^+$	0.173	0.410	0.417	1
$[C_7MIm]^+$	0.062	0.519	0.419	1
$[C_8MIm]^+$	0.042	0.538	0.420	1
$[C_9MIm]^+$	0.043	0.537	0.420	1
$[C_{10}MIm]^+$	0.032	0.548	0.420	1
$[C_{11}MIm]^+$	0.032	0.548	0.420	1
$[C_{12}MIm]^+$	0.017	0.562	0.421	1
$[C_{13}MIm]^+$	0.013	0.566	0.421	1
$[C_{14}MIm]^+$	0.017	0.563	0.420	1
$[C_{15}MIm]^+$	0.015	0.565	0.420	1
$[C_{16}MIm]^+$	0.013	0.567	0.420	1

From the electronic structure analysis, it can be concluded that lower alkyl group up to C_4 are preferable for the clay modification in terms of stability. At the same time to introduce a higher d-spacing in nanoclays longer alkyl chains are desirable. For thermally stable IL modified organoclay, $[C_nMIm]^+$ with $\Delta E^* > 4$ eV was selected and $[C_{16}MIm]^+$ with ΔE^* of 4.1 eV was the longest alkyl chain selected for the study. To study the effect of medium chains C_6 derivatives are chosen as the sharp decrease in ΔE^* begins at C_6. Hence effect of pairing anions described in the following sessions are restricted to C_4, C_6 and C_{16} derivatives of $[C_nMIm]^+$.

3.7.2 1-alkyl-3-methylimidazolium chloride

The optimized structures and the HOMO-LUMO plots of representative sets of $[C_nMIm]^+[Cl]^-$ ion-pairs are shown in Figure 3.11. The C2-H··Cl distances ranges from 1.983 Å - 2.008 Å, which is longer than the covalent bond distance of H-Cl (1.31 Å) and shorter than the van der Waals distance of H··Cl (2.95 Å). The higher E_b value

(373.4 - 382.8 kJ/mol) suggests strong electrostatic interactions along with hydrogen bonding.
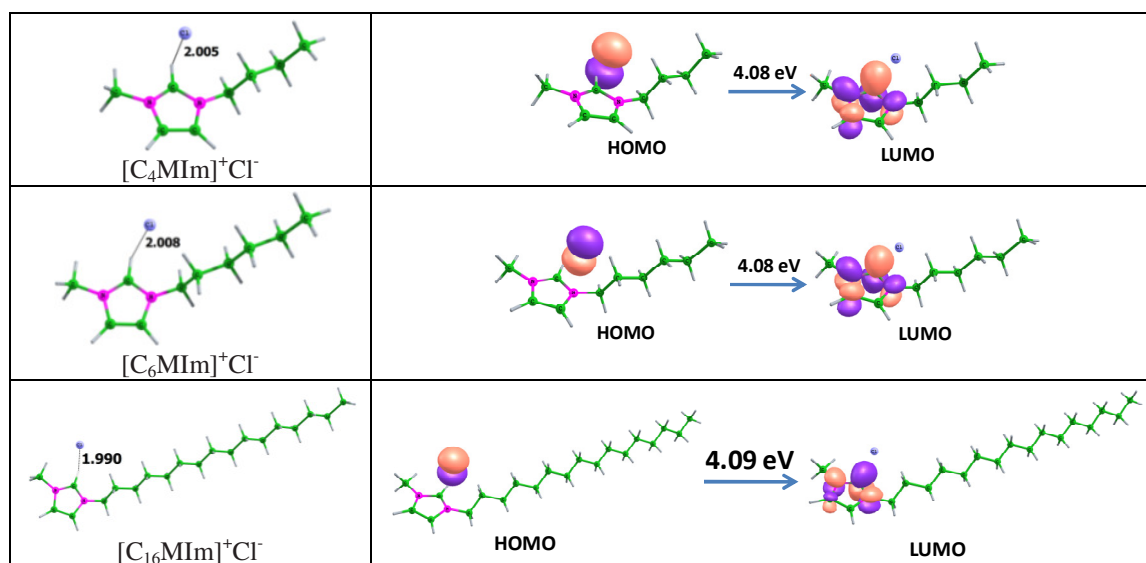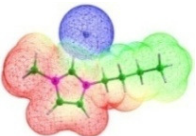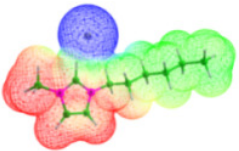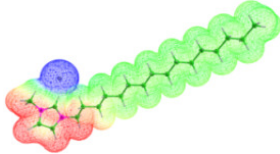
Figure 3.11 The optimized structures (left) of the representative set of $[C_nMIm]^+[Cl]^-$ and HOMO-LUMO plots (right). Distances in Å.

The cation–anion charge separation is well evident in the molecular electrostatic potential (MESP) plots given in Table 3.6. In $[C_nMIm]^+[Cl]^-$, the HOMO is located on the chloride anion and LUMO is located on the imidazolium ring irrespective of the alkyl chain at N2 with constant HOMO-LUMO gap (4.1 eV). This suggests the higher reactivity of Cl^- and hence the cation exchange in MMT-Na^+ will be favoured by the formation of NaCl and MMT-$[C_nMIm]^+$.

In the MESP plot, anionic charge (represented by blue region) is spherically distributed around the chloride ion, where as cationic charge (red region) is concentrated around the imidazolium cation with a short range. The Cl^- anion has the MK charge of -0.77 (Table 3.6) and cation has the counter positive values, which suggests a charge transfer of 23 % in $[C_nMIm]^+[Cl]^-$. The Mulliken charge analysis showed a total charge of 0.69 - 0.71 and remaining 0.31- 0.29 (31- 29 %) contribution is attributed to the sum of electrostatic interaction (23 %) and H-bonding. Considering MK charge for electrostatic contributions, the hydrogen bonding of 6 - 8 % contributes 77- 96 kJ/mol and electrostatic interaction contributes 287- 296 kJ/mol in the total interaction energy of 373-383 kJ/mol. The hydrogen bonding energy values computed by this method is comparable with the reported values [Hunt *et al*. 2015].

Table 3.6 MESP plots of $[C_4MIm]^+[Cl]^-$, $[C_6MIm]^+[Cl]^-$ and $[C_{16}MIm]^+[Cl]^-$ with MESP-derived charge on anion and Mulliken charge. Colour coding, ▬▬▬▬ blue -0.05 au. to red 0.05 au.

IL	MESP plot	MK charge on $[Cl]^-$	Mulliken charge			
			C_n	IM	C_1	Total
$[C_4MIm]^+[Cl]^-$		-0.77	0.19	0.13	0.38	0.70
$[C_6MIm]^+[Cl]^-$		-0.77	0.15	0.17	0.39	0.71
$[C_{16}MIm]^+[Cl]^-$		-0.77	0.13	0.18	0.38	0.69

3.7.3 1-alkyl-3-methylimidazolium tetrafluoroborate

The optimized structures and the HOMO-LUMO plots of representative sets of $[C_nMIm]^+[BF_4]^-$ ion-pairs are shown in Figure 3.12. The C2-H⋯F distances ranges from 2.039 Å - 2.268 Å, it is longer than the covalent bond distance of H-F (1.07Å) and shorter than the van der Waals distance of H⋯F (2.67 Å). Higher E_b values (340- 353 kJ/mol), suggesting existence of strong electrostatic interactions along with hydrogen bonding. $[C_nMIm]^+[BF_4]^-$ molecule have two hydrogen bonds each at C2H⋯F and C5-H⋯F respectively [Dong *et al*. 2006].

In $[C_nMIm]^+[BF_4]^-$, the HOMO is distributed between the BF_4^- anion and imidazolium ring and LUMO is located on the imidazolium ring. As the chain length increases, from $[C_{14}MIm]^+[BF_4]^-$, the N2-C_nH_{2n+1} side chain also contributes to HOMO and in $[C_{16}MIm]^+[BF_4]^-$, mostly the side chain alone contributes to HOMO. The higher HOMO-LUMO gap (6.9 eV), suggests a higher stability for $[C_nMIm]^+[BF_4]^-$ than $[C_nMIm]^+[Cl]^-$. In the MESP plot shown in Table 3.7, the BF_4^- anion has the MK charge of -0.88 and cation has the counter positive values, which suggests a charge transfer of 12 % in $[C_nMIm]^+[BF_4]^-$. The Mulliken charge analysis showed a total charge of 0.77 and remaining 0.23 (23 %) contribution to electrostatic interaction (12 %) and H-bonding. In $[C_nMIm]^+[BF_4]^-$, hydrogen bonding of 11 % (C2H⋯F and C5-H⋯F)

contribute 78-82 kJ/mol and electrostatic interaction contribute 184-189 kJ/mol in the total interaction energy of 340-353 kJ/mol.
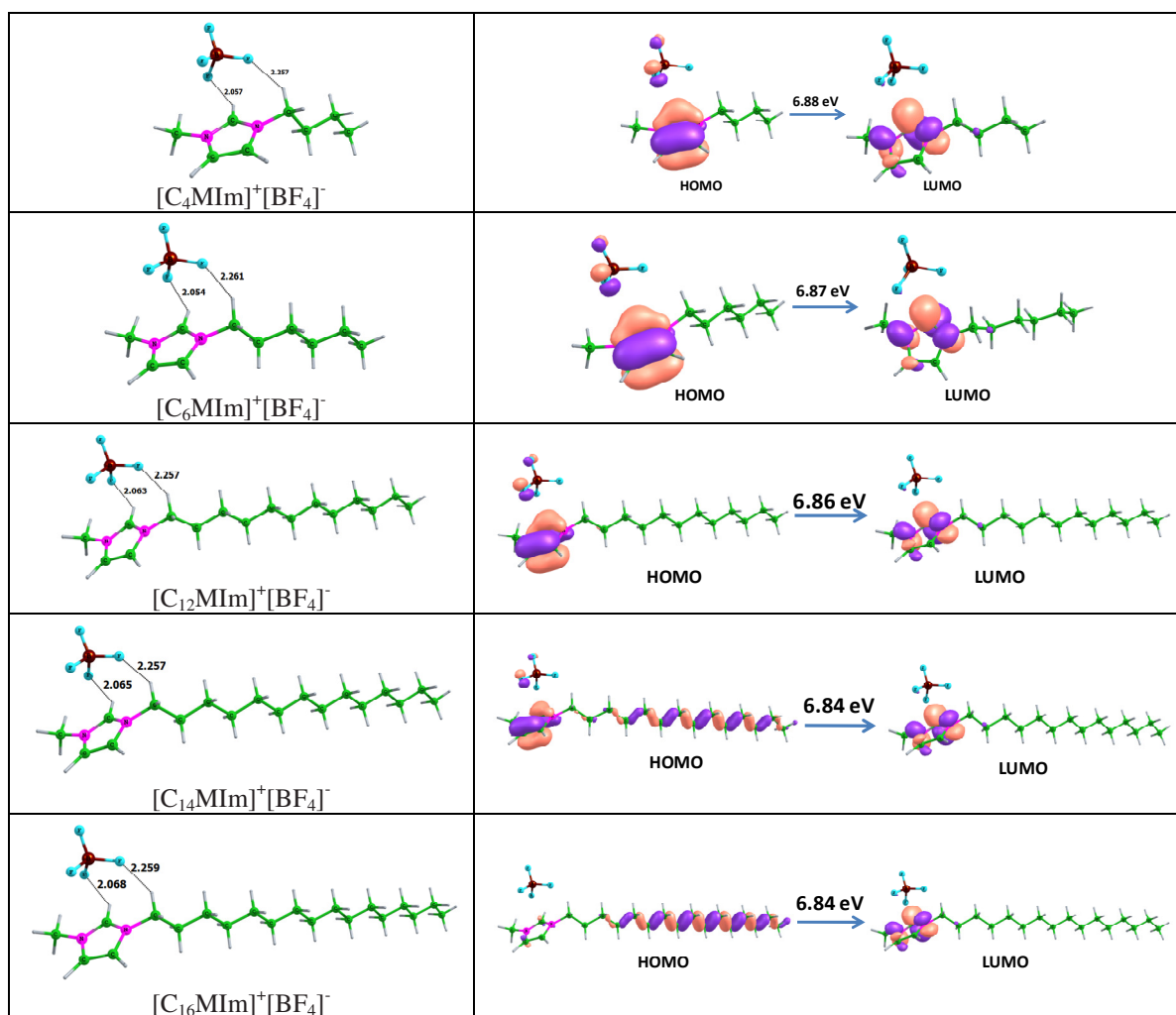
Figure 3.12 The optimized structures (left) of the representative set of $[RMIm]^+[BF_4]^-$ and HOMO-LUMO plots (right). Distances in Å.

A comparative analysis of ΔE^*, E_b, MK charge and H-bonding features between $[C_nMIm]^+[Cl]^-$ and $[C_nMIm]^+[BF_4]^-$ are given in Table 3.8. ΔE^* shows a decrease in stability for $[C_nMIm]^+$ with increase in alkyl chain length, where as alkyl chain length has no effect on stability of ion-pairs. Stability of $[C_nMIm]^+[BF_4]^-$ is higher than $[C_nMIm]^+[Cl]^-$ due to higher ΔE^* value. Higher E_b for $[C_nMIm]^+[Cl]^-$ than $[C_nMIm]^+[BF_4]^-$ suggest a higher dissociation energy for $[C_nMIm]^+[Cl]^-$. MK charge shows higher charge transfer features for chloride derivatives and HOMO-LUMO plots of $[C_nMIm]^+[Cl]^-$ suggest that Cl^- has a better reactivity, the HOMO being located

always in anion. In clay modification, $[C_nMIm]^+[Cl]^-$ favours cation exchange reactions by the formation of C_nMIm/MMT and NaCl.

Table 3.7 MESP plots of $[C_4MIm]^+[BF_4]^-$, $[C_6MIm]^+[BF_4]^-$ and $[C_{16}MIm]^+[BF_4]^-$ with MESP-derived charge on anion and Mulliken charge. Colour coding, ▬ blue -0.05 au. to red 0.05 au.
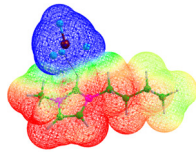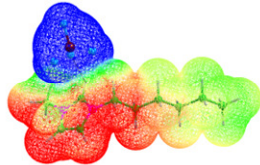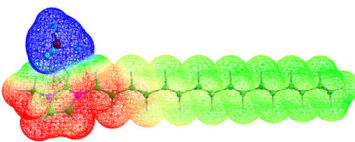
IL	MESP plot	MK charge on $[BF_4]^-$	Mulliken charge			
			C_n	IM	C_1	Total
$[C_4MIm]^+[BF_4]^-$		-0.88	0.07	0.38	0.33	0.78
$[C_6MIm]^+[BF_4]^-$		-0.88	0.01	0.43	0.33	0.77
$[C_{16}MIm]^+[BF_4]^-$		-0.88	-0.08	0.51	0.34	0.77

Table 3.8 ΔE^*, E_b, MK charge and H-bonding features of $[C_nMIm]^+$, $[C_nMIm]^+[Cl]^-$ and $[C_nMIm]^+[BF_4]^-$.

Property	n	$[C_nMIm]^+$	$[C_nMIm]^+[Cl]^-$	$[C_nMIm]^+[BF_4]^-$
ΔE^* (eV)	4	6.67	4.08	6.88
	6	6.11	4.08	6.87
	16	4.08	4.09	6.84
E_b (kJ/mol)	4	-	375.8	345.4
	6	-	374.5	344.0
	16	-	373.5	343.3
MK charge (% Charge transfer)	4	-	23.0	12.0
	6	-	23.0	12.0
	16	-	23.0	12.0
H-bonding (% E_b)	4	-	7.0	10.0
	6	-	6.0	11.0
	16	-	8.0	11.0

3.8 Conclusions

1-alkyl-3-methylimidazolium ILs are proposed as a replacement for alkyl ammonium salts in clay modification for high temperature applications. Screening of ILs for cation exchange with MMT-Na$^+$ was done based on computed parameters like HOMO-LUMO energy gap for stability studies, Mulliken charge analysis and MK charge analysis for charge contribution to electrostatic and hydrogen bonding interactions. Since clay modification involves cation exchange reactions, the stability of $[C_nMIm]^+$ cations are assessed based on HOMO-LUMO energy gap ΔE^*. The aim of organic modification of clay is to achieve higher organic content and higher d-spacing for better clay dispersion in organic media and studies are extended up to C_{16} chain length though ΔE^* shows drastic decrease in stability after $[C_4MIm]^+$ (ΔE^*= 6.7 eV). This change in stability is attributed to shift in HOMO from imidazolium ring to alkyl chain after C4. Chain length of $[C_nMIm]^+$ in this study is limited to C_{16} for thermally stable IL modified organoclay ($\Delta E^* > 4$ eV).

$[C_nMIm]^+[Cl]^-$ and $[C_nMIm]^+[BF_4]^-$ ILs were studied for cation exchange reaction with MMT-Na$^+$. HOMO-LUMO analysis illustrates higher stability for $[C_nMIm]^+[BF_4]^-$ (6.8 eV) than $[C_nMIm]^+[Cl]^-$ (4.1 eV). In $[C_nMIm]^+[BF_4]^-$, HOMO is diffused between BF_4^- and imidazolium ring and shifted to N2-alkyl group on increasing chain length beyond C14, where as HOMO is located on the Cl$^-$ anion irrespective of the N2-alkyl chain length in $[C_nMIm]^+[Cl]^-$.

Based on the results, $[C_4MIm]^+$, $[C_6MIm]^+$ and $[C_{16}MIm]^+$ based ILs are selected for experimental studies.

Synthesis of ionic liquids for clay modification and experimental validation
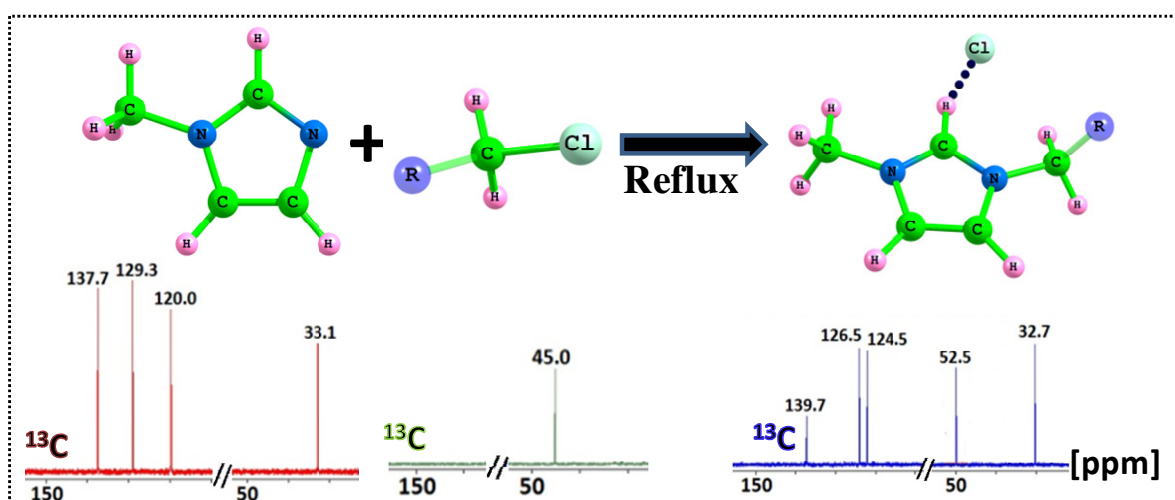
1-Hexadecyl-3-methylimidazolium chloride: Structure, thermal stability and decomposition mechanism

Eapen Thomas, Deepthi Thomas, S. Bhuvaneswari, K. P. Vijayalakshmi,* Benny K. George

Analytical and Spectroscopy Division, Analytical, Spectroscopy and Ceramics Group, Propellants, Polymers, Chemicals and Materials Entity, Vikram Sarabhai Space Centre, Thiruvananthapuram- 695022, India

Abstract

Ionic liquids selected for clay modification, $[C_6MIm]^+[Cl]^-$ and $[C_{16}MIm]^+[Cl]^-$ were synthesized by refluxing 1-methylimidazole with 1-chloro hexane and 1-chloro hexadecane respectively with 95 % yield. Commercially available $[C_4MIm]^+[Cl]^-$ and $[C_4MIm]^+[BF_4]^-$ were also used for experimental validation of computational results. Thermal stability of ILs were analyzed using TG, decomposition products were identified using Py-GC-MS and activation energy for thermal decomposition was computed by Kissinger method and Flynn-Wall-Ozawa method. The experimental results were remarkably conforming to the theoretical studies described in chapter 3.

4.1 Introduction

Derivatives of 1,3-dialkylimidazolium cation associated with various anions are among the most investigated class of ionic liquids (ILs).This is due to their ease of synthesis, stability and the possibility of tuning their physico-chemical properties by choice of the N-alkyl substituents and/or anions [Dupont 2004]. The majority of these ILs are prepared by alkylation of N-methylimidazole with an alkyl halide to give the corresponding 1-alkyl-3-methylimidazolium halide followed by anion metathesis (Scheme 4.1)[Wilkes and Zaworotko1992; Suarez *et al*. 1996; Huddleston *et al*. 1998].
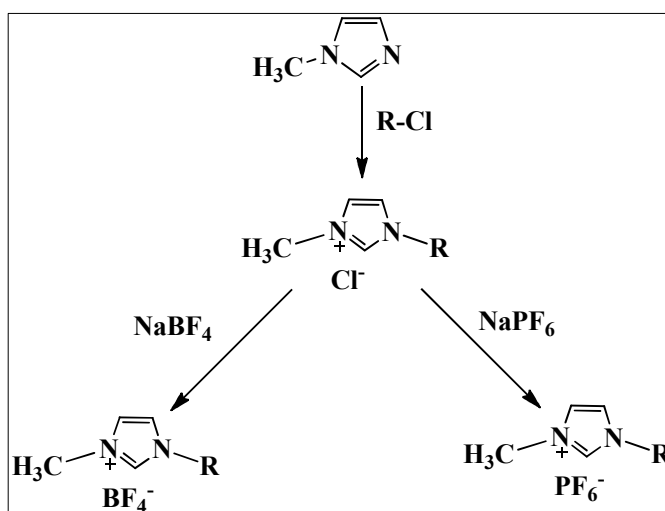
Scheme 4.1 General reaction scheme for the synthesis of 1-alkyl-3-methylimidazolium ILs.

4.2 Experimental section

4.2.1 Materials

1-Methylimidazole from Alfa Aesar, England, 1-chlorohexane and 1-chlorohexadecane from Sigma Aldrich, USA were used for synthesis of 1-hexyl-3-methylimidazolium chloride and 1-hexadecyl-3-methylimidazolium chloride. 1-butyl-3-methylimidazolium chloride and 1-butyl-3-methylimidazolium tetrafluoroborate from M/s Otto Chemie Pvt. Ltd, Mumbai, India were used for experimental validation.

4.2.2 Synthesis of 1-hexyl-3-methylimidazolium chloride, $[C_6MIm]^+[Cl]^-$

In a 250 mL round bottom flask connected with a reflux condenser, 1-methylimidazole (12.30 g, 0.150 mol) and 1-chlorohexane (19.30 g, 0.160 mol) were added simultaneously. The mixture was heated from room temperature to 120 ^{o}C with magnetic stirring and the reaction was continued at 120 ^{o}C for 120 min. The progress of reaction was monitored by analyzing the reaction mixture every 30 minutes by ^{13}C NMR spectroscopy till the CH$_2$-Cl peak in 1-chlorohexane at 45.0 ppm disappeared and a new quaternary N-CH$_2$ peak appeared at 52.5 ppm (Figure 4.1). The product purified by phase separation in ethyl acetate resulted in a slightly yellowish liquid with 95 % yield.
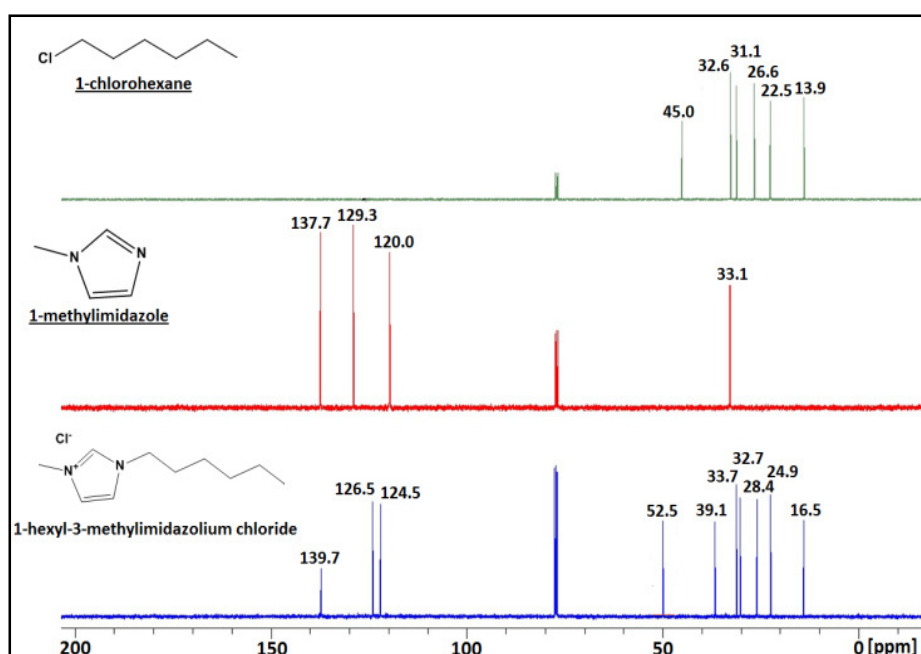
Figure 4.1 Overlaid ^{13}C NMR spectra of 1-chlorohexane, 1-methylimidazole and $[C_6MIm]^+[Cl]^-$.

4.2.3 Synthesis of 1-hexadecyl-3-methylimidazolium chloride, [C₁₆MIm]⁺[Cl]⁻

4.2.3 Synthesis of 1-hexadecyl-3-methylimidazolium chloride, [C$_{16}$MIm]$^+$[Cl]$^-$

In a 250 mL round bottom flask connected with a reflux condenser, 1-methylimidazole (12.30 g, 0.150 mol) and 1-chlorohexadecane (41.74 g, 0.160 mol) were added simultaneously. The mixture was heated from room temperature to 140 ^{o}C with magnetic stirring and the reaction was continued at 140 ^{o}C for 120 min. The progress of reaction was monitored by analyzing the reaction mixture by ^{13}C NMR spectroscopy till the CH$_2$-Cl peak in 1-chlorohexadecane at 45.17 ppm disappeared and a new quaternary N-CH$_2$ peak appeared at 50.25 ppm (Figure 4.2). The non equivalent C4 (129.27 ppm) and C5 (120.01 ppm) in 1-methylimidazole was shifted to 123.31 and 121.55 ppm respectively in [C$_{16}$MIm]$^+$[Cl]$^-$ due to the formation of new N-CH$_2$ bond and presence of Cl$^-$ anion. The mixture was cooled to room temperature (30 ^{o}C) and the product was purified by recrystallization in ethyl acetate. Vacuum drying of the recrystallised material for 4 hours resulted in a white powder with 95 % yield.
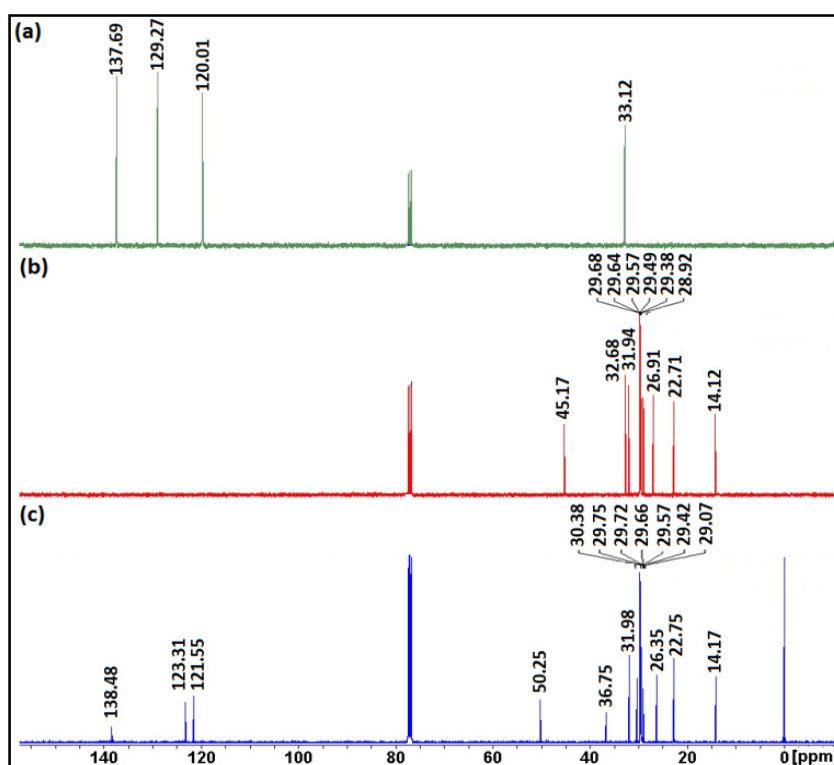
Figure 4.2 ^{13}C NMR spectra of (a) 1-methylimidazole, (b) 1-chlorohexadecane and (c) [C$_{16}$MIm]$^+$[Cl]$^-$.

4.2.4 Instrumental

4.2.4 Instrumental

Synthesis of ILs were followed using ^{13}C NMR analysis using a Bruker Avance-III, 400 MHz spectrometer at 100.2 MHz for ^{13}C nucleus. ILs were characterized using

ThermoScientific Nicolet iS50 FTIR spectrometer equipped with PIKE GladiATR accessory in the wavelength region 4000-525 cm^{-1} with a spectral resolution of 4 cm^{-1}. CHN analysis was done using Perkin Elmer 2400 CHNS analyzer with thermal conductivity detector. Thermal stability of ILs was studied using TA Instruments SDT Q600 TGA from room temperature to 600 ^{o}C at a heating rate of 10 ^{o}C/min. in nitrogen atmosphere. Melting point and phase changes of solid $[C_{16}MIm]^{+}[Cl]^{-}$, were determined using TA Q20 Differential Scanning Calorimeter (DSC) at a rate of 10 °C/min. from -20 ^{o}C to 100 °C in nitrogen atmosphere followed by cooling at the same rate and repeating the cycle for 4 times. FTIR heating experiments (30 -170 ^{o}C) and X-ray diffraction analysis using Bruker D8 Discover diffractometer were also carried out for $[C_{16}MIm]^{+}[Cl]^{-}$. Decomposition products of ILs were identified using pyrolysis GC-MS. The GC/MS system consists of a Thermo Electron trace Ultra GC directly coupled to a Thermo Electron PolarisQ (Quadrupole ion trap) mass spectrometer and SGE pyrolyser and the pyrolysis was carried out at 350 ^{o}C.

4.3 Results and discussion

4.3.1 FTIR analysis
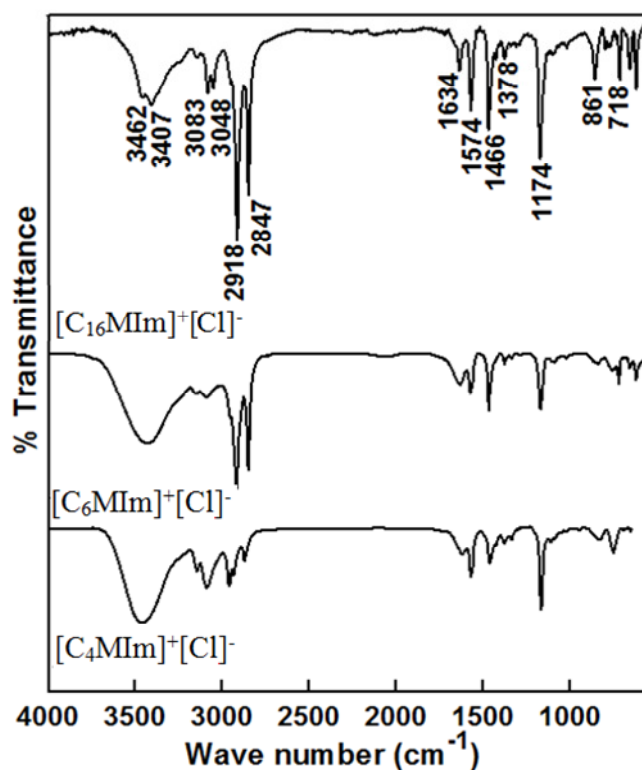
Figure 4.3 FTIR spectrum of $[C_{4}MIm]^{+}[Cl]^{-}$, $[C_{6}MIm]^{+}[Cl]^{-}$ and $[C_{16}MIm]^{+}[Cl]^{-}$.

FT-IR spectra of $[C_4MIm]^+[Cl]^-$, $[C_6MIm]^+[Cl]^-$ and $[C_{16}MIm]^+[Cl]^-$ are shown in Figure 4.3. The peaks at 3083 and 3048 cm^{-1} were due to the aromatic C-H stretching vibrations of imidazolium ring. Strong absorption bands in the region 2800-3000 cm^{-1} represent alkyl C-H stretching vibrations. Peaks at 1574 cm^{-1} and 1466 cm^{-1} are due to C=C and C=N vibrations respectively. Presence of water is confirmed from the peaks at 3462 cm^{-1} and 1634 cm^{-1}. In $[C_{16}MIm]^+[Cl]^-$, peak at 3407 cm^{-1} suggests O-H stretching (H-bonded), which may be due to presence of water of hydration.
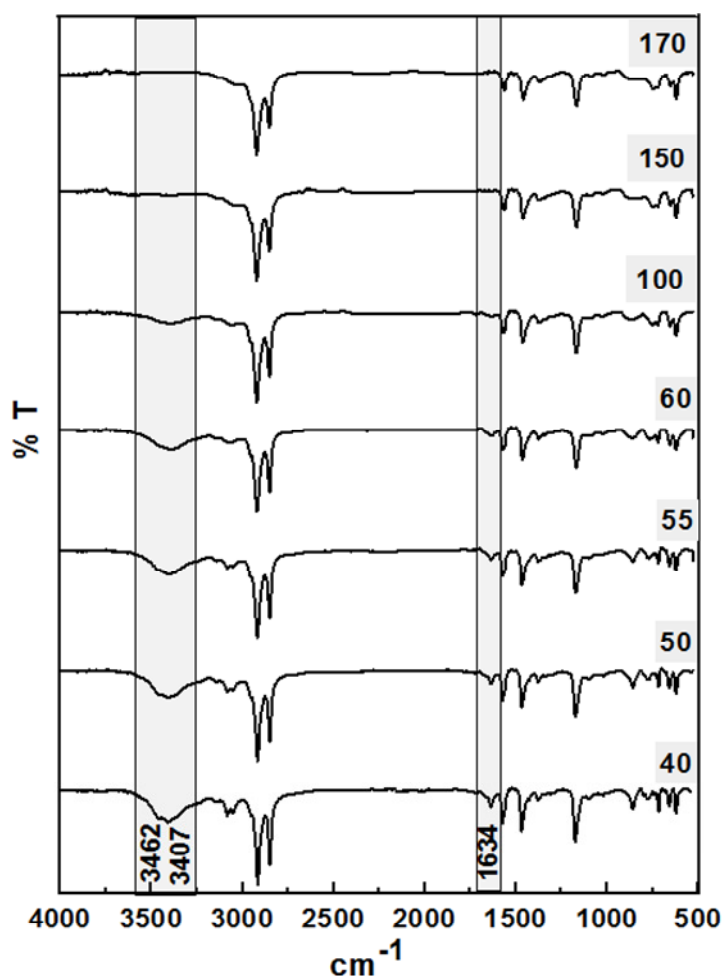
Figure 4.4 FTIR spectra of $[C_{16}MIm]^+[Cl]^-$ at 40, 50, 55, 60, 100, 150 and 170 ^{o}C.

Figure 4.4 shows the FTIR spectrum of $[C_{16}MIm]^+[Cl]^-$ at different temperatures; 40, 50, 55, 60, 100, 150 and 170 ^{o}C. The intensity of characteristic alkyl C-H stretching vibrations (2800-3000 cm^{-1}), C=C (1574 cm^{-1}) and C=N (1466 cm^{-1}) vibrations of imidazolium ring, were unaffected on heating from 30 -170 ^{o}C. The peaks at 3462 cm^{-1} (free hydroxyl) and 3407 cm^{-1} (H-bonded) merged to a single peak (3430

cm^{-1}) on heating between 60 ^{o}C to 150 ^{o}C with reduction in intensity and finally disappeared above 170 ^{o}C indicating the presence of water of hydration in [C$_{16}$MIm]$^{+}$[Cl]$^{-}$.

The water of hydration possibility in [C$_{16}$MIm]$^{+}$[Cl]$^{-}$ was theoretically verified using DFT at B3LYP/6-311+G(d,p) level of DFT. Figure 4.5 shows the optimized structures and molecular electrostatic potential (MESP) plots of [C$_{16}$MIm]$^{+}$[Cl]$^{-}$, C$_{16}$MImCl.H$_2$O and C$_{16}$MImCl.2H$_2$O. The distances of the C2-H$^{…}$Cl were 1.99 Å, 2.17 Å and 2.19 Å respectively in [C$_{16}$MIm]$^{+}$[Cl]$^{-}$, C$_{16}$MImCl.H$_2$O andC$_{16}$MImCl.2H$_2$O, which was longer than the covalent bond distance of H-Cl (1.31 Å) and shorter than the van der Waals distance of H$^{…}$Cl (2.95 Å). Existence of strong electrostatic interactions in [C$_{16}$MIm]$^{+}$[Cl]$^{-}$ ion pair was revealed from its BSSE corrected binding energy of 371.1 kJ/mol. The bond lengths and bond angles of [C$_{16}$MIm]$^{+}$[Cl]$^{-}$, C$_{16}$MImCl.H$_2$O and C$_{16}$MImCl.2H$_2$O are compared with reported values of [C$_{16}$MIm]$^{+}$ cation in Table 4.1. These values show that hydration has no significant effect on the structural parameters of [C$_{16}$MIm]$^{+}$[Cl]$^{-}$.

(a) [C$_{16}$MIm]$^{+}$[Cl]$^{-}$

(b) C$_{16}$MImCl.H$_2$O
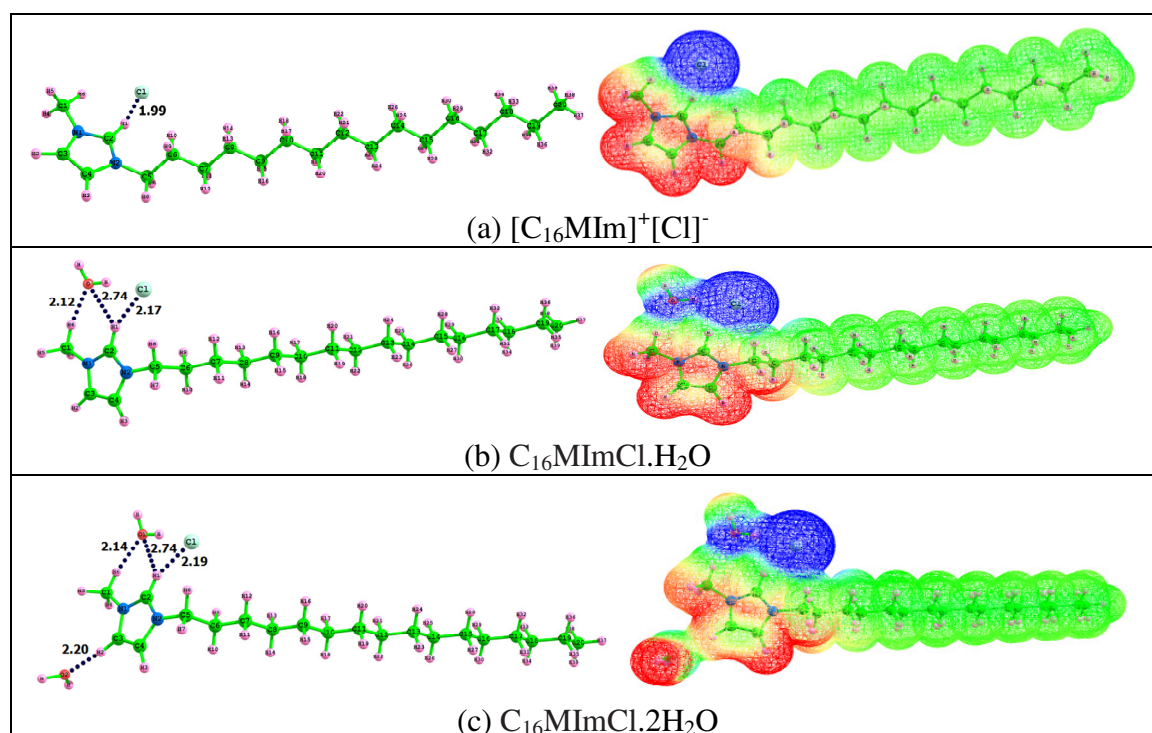
(c) C$_{16}$MImCl.2H$_2$O

Figure 4.5 Optimized structures and MESP plots of [C$_{16}$MIm]$^{+}$[Cl]$^{-}$, C$_{16}$MImCl.H$_2$O and C$_{16}$MImCl.2H$_2$O at B3LYP level of DFT. Distance in Å. Colour coding, ▬▬▬ blue -0.05 au. to red 0.05 au.

Table 4.1 Selected bond lengths (Å) and angles (°) of [C$_{16}$MIm]$^+$[Cl]$^-$, C$_{16}$MImCl.H$_2$O and C$_{16}$MImCl.2H$_2$O. Experimental values for [C$_{16}$MIm]$^+$ cation is shown.

	Computed			Experimental [Zhao *et al.* 2010]
	[C$_{16}$MIm]$^+$[Cl]$^-$	C$_{16}$MImCl.H$_2$O	C$_{16}$MImCl.2H$_2$O	[C$_{16}$MIm]$^+$
N(1)–C(1)	1.470	1.469	1.468	1.471
N(1)–C(2)	1.337	1.338	1.338	1.324
N(1)–C(3)	1.384	1.385	1.386	1.375
N(2)–C(4)	1.385	1.382	1.383	1.356
N(2)–C(5)	1.478	1.480	1.478	1.474
N(2)–C(2)	1.339	1.337	1.337	1.327
C(3)–C(4)	1.361	1.361	1.361	1.347
C(5)–C(6)	1.529	1.529	1.529	1.498
C(6)–C(7)	1.533	1.533	1.532	1.516
C(19)–C(20)	1.531	1.531	1.532	1.503
C(2)–N(1)–C(1)	123.3	124.9	124.9	125.1
C(2)–N(1)–C(3)	109.3	108.8	109.0	108.7
C(2)–N(2)–C(4)	109.0	108.9	108.8	108.4
C(2)–N(2)–C(5)	124.0	124.0	124.0	125.2
C(4)–N(2)–C(5)	126.9	127.1	127.2	126.3
C(4)–C(3)–N(1)	106.8	107.0	106.6	106.2
C(3)–C(4)–N(2)	107.0	107.0	107.2	108.1
C(3)–N(1)–C(1)	127.4	126.3	126.1	126.3
N(1)–C(2)–N(2)	108.0	108.4	108.3	108.6
N(2)–C(5)–C(6)	112.4	112.2	112.2	113.4
C(5)–C(6)–C(7)	111.7	111.4	111.5	110.6
C(18)–C(19)–C(20)	113.3	113.3	113.3	115.0

The stabilization energy computed was 59.9 kJ/mol on monohydration (C$_{16}$MImCl.H$_2$O) and 18.8 kJ/mol on dihydration (C$_{16}$MImCl.2H$_2$O). The value of MESP at electrostatic minimum (V$_{min}$) [Gadre *et al.* 1992; Pathak and Gadre 1990; Neetha *et al.* 2014] for [C$_{16}$MIm]$^+$[Cl]$^-$, C$_{16}$MImCl.H$_2$O and C$_{16}$MImCl.2H$_2$O were 0.1230, 0.1118 and 0.1170 a.u. respectively. In [C$_{16}$MIm]$^+$[Cl]$^-$, the anionic charge is spherically distributed around Cl$^-$ and cationic charge is concentrated around the imidazolium ring. The long alkyl chain (green region) showed lower interaction with the anion. In C$_{16}$MImCl.H$_2$O, the anionic charge is dispersed between Cl- and H$_2$O molecule. In C$_{16}$MImCl.2H$_2$O, the second water molecule at C3 position shows more of cationic character due to the utilization of water lone pair for hydrogen bond formation [Neetha *et al.* 2014]. The HOMO-LUMO gap increases on hydration, in the order

$[C_{16}MIm]^+[Cl]^-$ (4.09 eV) < $C_{16}MImCl.H_2O$ (4.44 eV) < $C_{16}MImCl.2H_2O$ (4.53 eV). Generally increased HOMO-LUMO gap suggest increased stability especially in the case of ionic liquids [Ilawe *et al.* 2016].

4.3.2 CHN analysis

Theoretical elemental composition for $[C_4MIm]^+[Cl]^-$, $[C_6MIm]^+[Cl]^-$ and $[C_{16}MIm]^+[Cl]^-$ with the observed values are shown in Table 4.2. Purity of standard $[C_4MIm]^+[Cl]^-$ was 99 % and the elemental analysis showed a purity of 99.4 % for $[C_4MIm]^+[Cl]^-$ and 99.3 % for $[C_6MIm]^+[Cl]^-$. In the case of $[C_{16}MIm]^+[Cl]^-$, elemental analysis suggests the formation of $C_{16}MImCl.2H_2O$. The formation of dihydrate is further supported by TG/DSC analysis (section 4.3.4.4).

Table 4.2 Theoretical and observed elemental composition.

Compound	Theoretical (%)					Observed (%)				
	C	H	N	O	Cl	C	H	N	O	Cl
$[C_4MIm]^+[Cl]^-$	55.0	8.7	16.0	0	20.3	53.9	9.2	15.5	0	21.4
$[C_6MIm]^+[Cl]^-$	59.2	9.5	13.8	0	17.5	58.8	10.0	13.9	0	17.3
$[C_{16}MIm]^+[Cl]^-$	70.0	11.5	8.2	0	10.3					
$C_{16}MImCl.H_2O$	66.5	11.4	7.8	4.5	9.8	63.1	12.2	8.1	8.4	8.2
$C_{16}MImCl.2H_2O$	63.4	11.4	7.4	8.4	9.3					

4.3.3 DSC analysis of $[C_{16}MIm]^+[Cl]^-$

The melting point of $[C_{16}MIm]^+[Cl]^-$ was analyzed using DSC (Figure 4.6) and observed a broad endothermic peak at 56.9 ^{o}C, suggesting the existence as IL with different phases. DSC heat cool method was done to identify the phases present in synthesized $C_{16}MImCl$ (Figure 4.6).
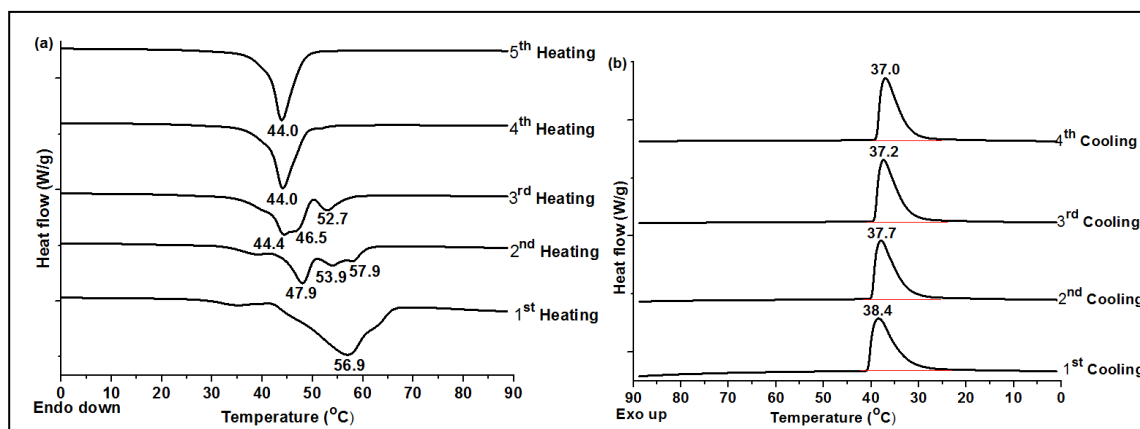
Figure 4.6 DSC heating (a) and cooling (b) profiles of $[C_{16}MIm]^+[Cl]^-$.

A broad endothermic transition at 56.9 ^{o}C on first cycle of heating represents the crystal-mesophase transition and a crystallization peak was observed at 38.4 ^{o}C on subsequent cooling at the same rate (-10 ^{o}C/min) [Goujon *et al*. 2015; Bradley *et al*. 2002]. The enthalpy of endothermic crystal to mesophase transition is in the range of 20-50 kJ/mol [Downard *et al*. 2004] and $[C_{16}MIm]^+[Cl]^-$ possess enthalpy of 21.2 kJ/mol. Multiple endothermic transitions were observed on second and third cycle of heating representing the melting of various crystal phases in to smectic phase with slight variation in hydration levels. The cooling curves showed only one crystallization peak at every event. Repeated heating resulted in single endotherm at 44 ^{o}C, suggests that water is more evenly incorporated into the system.

4.3.4 Thermal stability

4.3.4.1 Effect of anion

Computational studies revealed that the anion has a significant effect on thermal stability and decomposition mechanism of ILs. Figure 4.7 shows the TG/DTG curves of $[C_4MIm]^+[Cl]^-$ and $[C_4MIm]^+[BF_4]^-$ with maximum decomposition temperatures (T_s) of 284 and 427 ^{o}C respectively. The change of Cl^- to BF_4^- with $[C_4MIm]^+$ resulted in an increase of T_s by 143 ^{o}C. The reason for higher reactivity of Cl^- was attributed to the presence of HOMO on the Cl^- anion in $[C_4MIm]^+[Cl]^-$, where as HOMO was diffused between BF_4^- and imidazolium ring in $[C_4MIm]^+[BF_4]^-$. The decomposition mechanism of $[C_4MIm]^+[Cl]^-$ and $[C_4MIm]^+[BF_4]^-$ were analysed to clarify the concepts further.
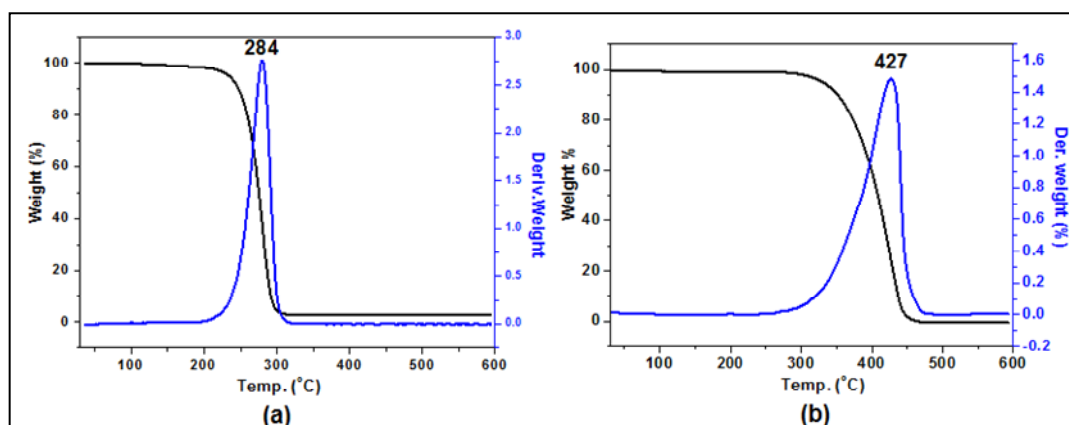
Figure 4.7 TG and DTG curves of (a) $[C_4MIm]^+[Cl]^-$ and (b) $[C_4MIm]^+[BF_4]^-$

4.3.4.2 Decomposition mechanism of [C₄MIm]⁺[Cl]⁻

Time (min)	1.63	2.60	7.81	10.79
Product	CH₃Cl	C₄H₉Cl		
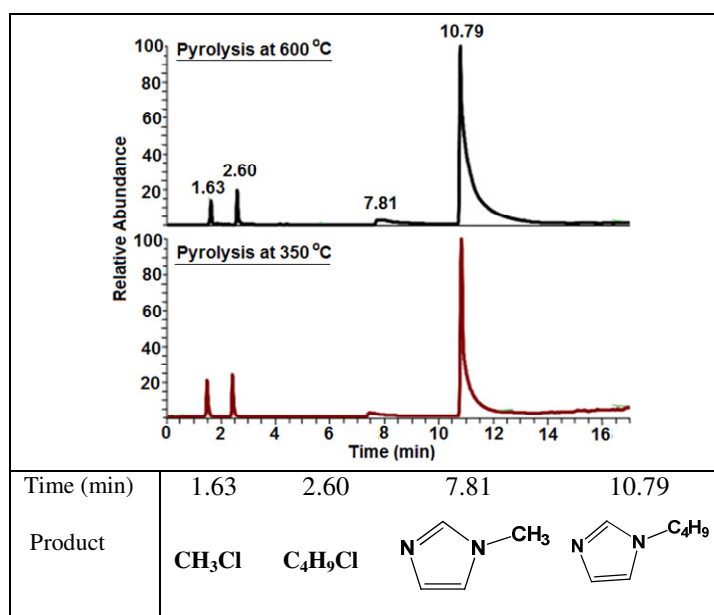
Figure 4.8 Pyrogram and decomposition products of [C₄MIm]⁺[Cl]⁻ at 350 and 600 °C.

Figure 4.8 shows the pyrogram of [C₄MIm]⁺[Cl]⁻ at 350 and 600 °C. The decomposition products were 1-chloromethane ($m/z = 50$), 1-chlorobutane ($m/z = 92$), 1-methylimidazole ($m/z = 82$) and 1-butylimidazole ($m/z = 124$). A decomposition mechanism based on the products obtained on pyrolysis is shown in Scheme 4.2. The dealkylation reaction is initiated by the nucleophilic attack of Cl⁻ anion at the alkyl group of imidazolium cation which passes through the bimolecular nucleophilic (S$_N$2) transition state.
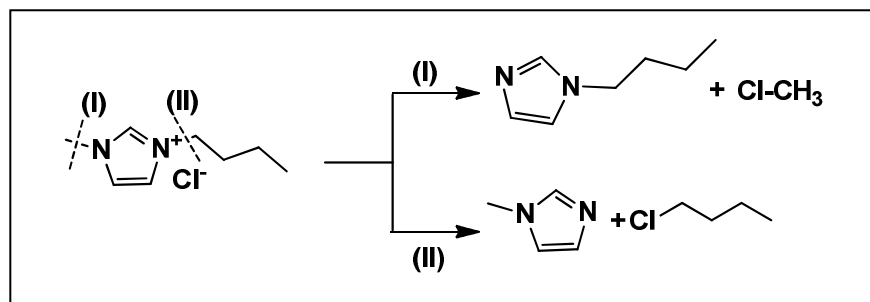
Scheme 4.2 Decomposition route of [C₄MIm]⁺[Cl]⁻.

A semi-quantitative estimation of products formed during pyrolysis was done using standard solutions (1 ppm) of 1-methylimidazole (C₁Im) and 1-butylimidazole (C₄Im) in analytical grade methanol. 1 μL of standard solutions were injected and the area ratio of C₁Im to C₄Im was taken. From the C₁Im to C₄Im area ratio, the actual ratio

of C1Im and C_4Im were quantified as shown in Table 4.3. Based on this, S_N2 reaction by pathway-I (Scheme 4.2) proceed by 89.9 % and pathway-II by 10.1 %.

Table 4.3 Semi-quantitative estimation of 1-methylimidazole and 1-butylimidazole from area of respective peaks in the pyrogram.

		Area	Area ratio (C_1Im : C_4Im)
Standard (1 ppm)	1-methylimidazole (C_1Im)	1439687	1 : 1.46
	1-butylimidazole (C_4Im)	2101943	
Sample ([C_4MIm]$^+$[Cl]$^-$)	C_1Im	26225477	1 : 12.97
	C_4Im	340105531	
	Actual ratio		1 : (12.97/1.46)
			1 : 8.88
	Ratio for 100 % of the reaction		10.12 : 89.88
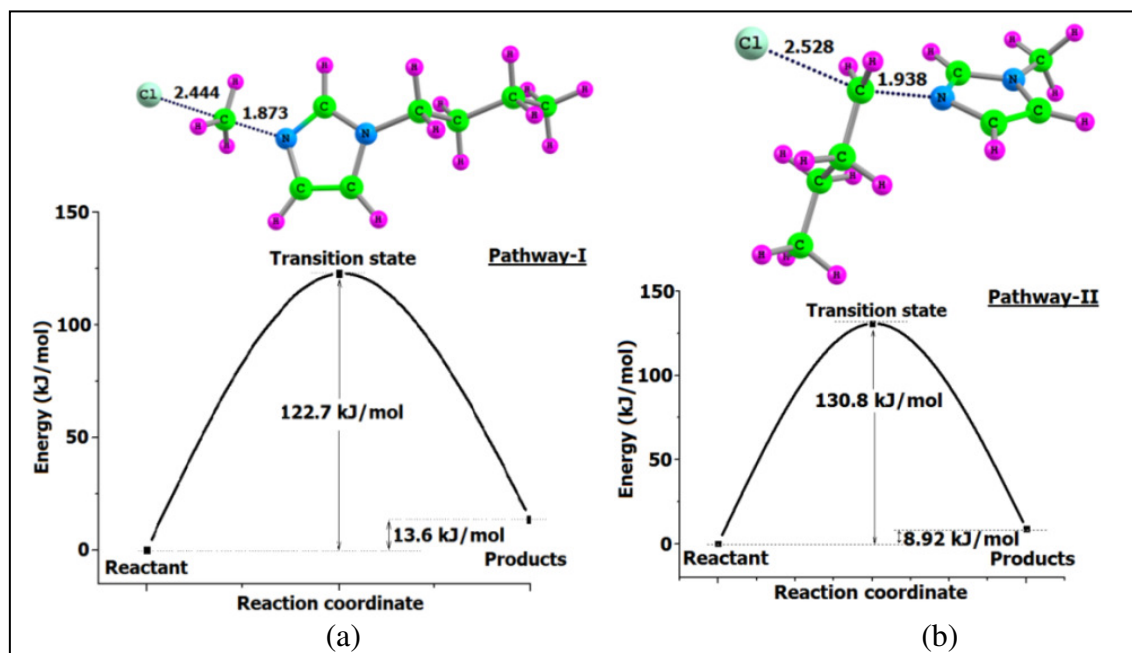
Figure 4.9 Energy profile and transition states of [C_4MIm]$^+$[Cl]$^-$ decomposition shown in Scheme 4.2. (a) Pathway-I and (b) Pathway-II. Bond lengths in Å.

The activation energy (E_a) of reaction pathways shown in scheme 4.2 was calculated at B3LYP/6-311+G(d,p) level of DFT. Transition states identified and energy profile are shown in Figure 4.9. Demethylation reaction (pathway-I) proceed with an E_a
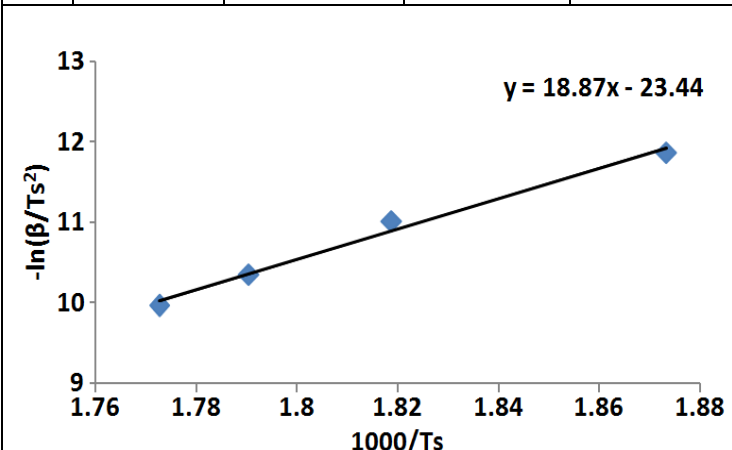
of 122.7 kJ/mol while debutylation reaction proceed with an E_a of 130.8 kJ/mol (Figure 4.9). These results show the preference for pathway-I with decrease in E_a of 8 kJ/mol over pathway II and the higher percentage of 1-butylimidazole is accounted. The easy accessibility of Cl^- in the sterically favoured methyl side can also be attributed to the presence of higher percentage of 1-butylimidazole in the pyrolysis products.

Table 4.4 Computed activation energy of $[C_4MIm]^+[Cl]^-$.

	S_N2 (I)		S_N2 (II)		Avg. E_a (kJ/mol)
	E_a (kJ/mol)	Rn. (%)	E_a (kJ/mol)	Rn. (%)	
$[C_4MIm]^+[Cl]^-$	122.7	89.88	130.8	10.12	123.5

Table 4.5 Activation energy by Kissinger method.

Kissinger method				
β	Ts (K)	$β/Ts^2$	1000/Ts	$\ln(β/Ts^2)$
2	533.8	7.02E-06	1.873	-11.8669
5	549.8	1.65E-05	1.819	-11.0097
10	557.2	3.21E-05	1.791	-10.3479
15	564.1	4.71E-05	1.773	-9.9624

Slope				18.87
E_a(kJ/mol) = slope x R				156.8

The net E_a for the reaction was calculated from E_a of pathway-I and pathway-II and C_1Im: C_4Im area ratio. The average E_a was 123.5 kJ/mol (Table 4.4). Experimental values for E_a were calculated using Kissinger method and FWO methods as shown in Table 4.5 and Table 4.6 respectively.

Table 4.6 Activation energy by FWO method.

FWO method									
β	Temp. (°C) for Conversion								
	10%	20%	30%	40%	50%	60%	70%	80%	90%
2	502	512	518	523	527	531	534	538	542
5	515	526	533	538	543	547	550	554	558
10	522	535	543	548	552	556	560	563	569
15	529	542	549	555	559	563	567	572	577
Calculations									
log β	1000/Ts								
0.301	1.992	1.953	1.930	1.912	1.897	1.883	1.873	1.859	1.845
0.699	1.942	1.901	1.876	1.859	1.842	1.828	1.818	1.805	1.792
1.000	1.916	1.869	1.842	1.825	1.812	1.799	1.786	1.776	1.757
1.176	1.890	1.845	1.821	1.802	1.789	1.776	1.764	1.748	1.733

	10%	20%	30%	40%	50%	60%	70%	80%	90%
Slope	-8.791	-8.193	-8.021	-7.995	-8.132	-8.252	-8.079	-8.094	-7.891
Constant, b	0.457	0.457	0.457	0.457	0.457	0.457	0.457	0.457	0.457
E_a(kJ/mol) $= (\frac{-\text{Slope x R}}{b})$	159.93	149.05	145.92	145.45	147.94	150.13	146.98	147.25	143.56
Avg. E_a = 148.5 kJ/mol									

E_a calculated using Kissinger method and FWO methods were 156.8 kJ/mol and 148.5 kJ/mol respectively. The difference between computed and experimental E_a is due to the lattice energy change in experiments unlike gas phase calculations in computational methods, however computational studies provide more insight in to the mechanism and difference in E_a among various reaction mechanisms.

4.3.4.3 Decomposition mechanism of [C₄MIm]⁺[BF₄]⁻

4.3.4.3 Decomposition mechanism of $[C_4MIm]^+[BF_4]^-$

Pyrogram of $[C_4MIm]^+[BF_4]^-$ at 600 °C is shown in Figure 4.10. Major peaks in the pyrogram are identified as 1-butene (m/z = 56), 1-methylimidazole (m/z = 82) and 1-butylimidazole (m/z = 124). Owing to the steric bulkiness of $[BF_4]^-$ compared to Cl⁻, the S_N2 reactions are likely to happen only at the N3-CH₃ site (Scheme 4.3) and it is unambiguous with the presence of butylimidazole as the major product in the pyrogram.
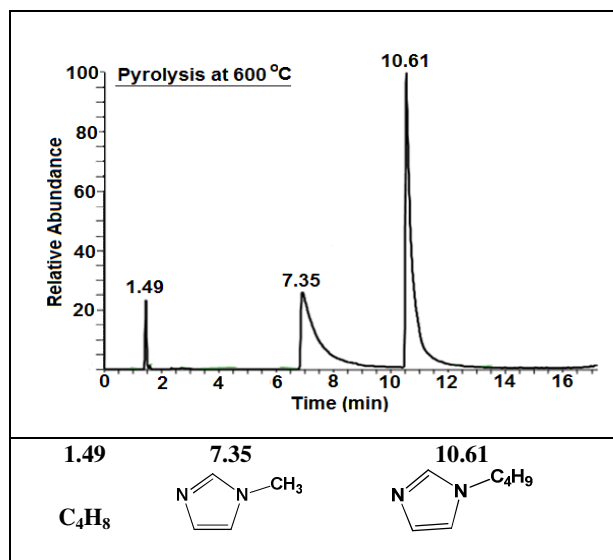
Figure 4.10 Pyrogram and decomposition products of $[C_4MIm]^+[BF_4]^-$ at 600 °C.
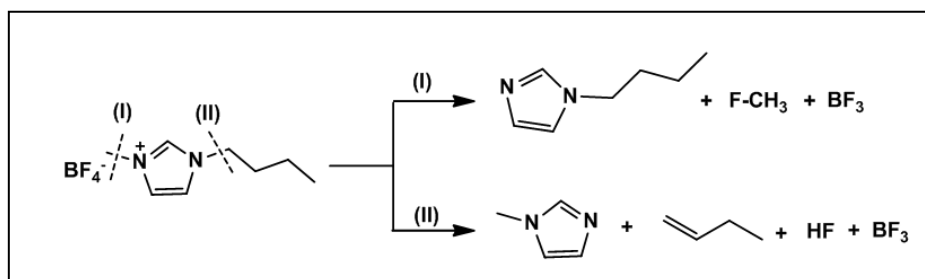
Scheme 4.3 Decomposition routes of $[C_4MIm]^+[BF_4]^-$.

Table 4.7 Semi quantitative estimation exemplified for $[C_4MIm]^+[BF_4]^-$.

		Area	Area ratio ($C_1Im : C_4Im$)
Standard (1 ppm)	1-methylimidazole	1439687	1 : 1.46
	1-butylimidazole (C_4Im)	2101943	
Sample ($[C_4MIm]^+[BF_4]^-$)	C_1Im	51652142	1 : 1.54
	C_4Im	79814872	
	Actual ratio		1 : (1.54/1.46)
			1 : 1.05
	Ratio for 100 % of the reaction		48.78 : 51.22

Differing from $[C_4MIm]^+[Cl]^-$, the presence of 1-butene in the pyrogram suggests existence of competitive elimination reactions in the thermal decomposition of $[C_4MIm]^+[BF_4]^-$ and transition state was identified for E2 elimination (pathway-II). Higher concentration of 1-butene and 1-methylimidazole in the pyrogram suggest the possibility of interplay of both the mechanisms in decomposition of $[C_4MIm]^+[BF_4]^-$. The ratio of 1-methylimidazole to 1-butylimidazole was determined by a semi quantitative method and observed both reactions proceed equally (1:1) (Table 4.7).
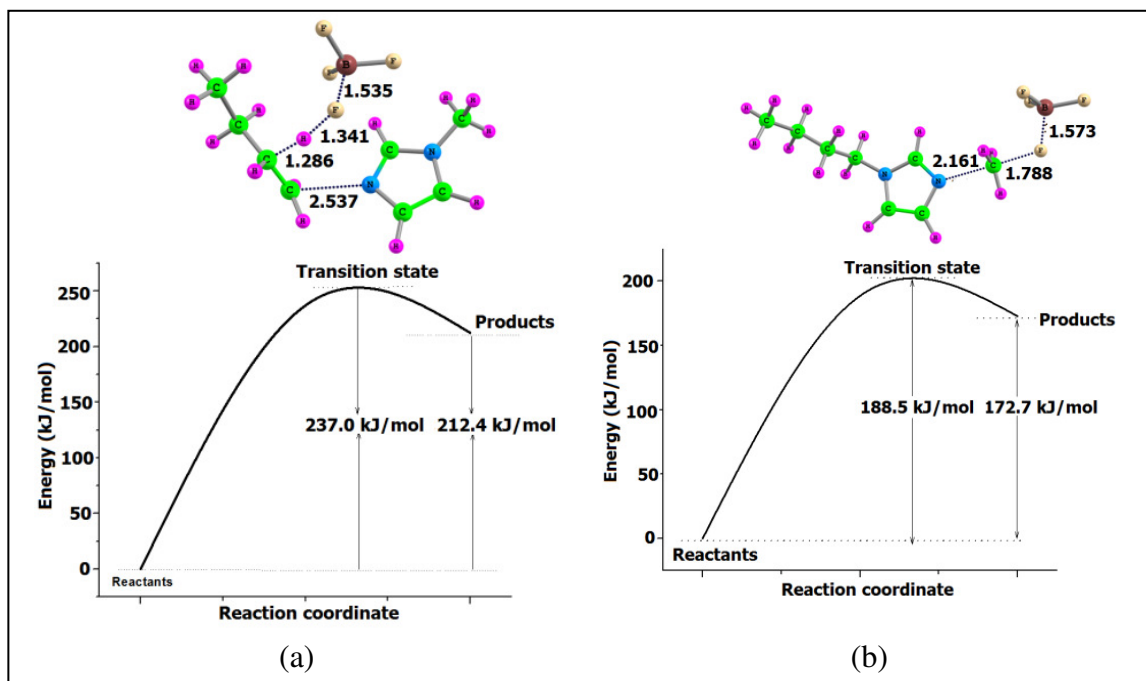
Figure 4.11 Energy profile and transition states of $[C_4MIm]^+[BF_4]^-$ decomposition shown in Scheme 2. (a) Pathway-I (S_N2)and (b) Pathway-II (E2). Bond lengths in Å.

Computed activation barrier for the formation of butylimidazole (Figure 4.11) is 188.5 kJ/mol and is higher than the corresponding value for $[C_4MIm]^+[Cl]^-$ (122.7 kJ/mol). Transition state for E2 elimination was characterized by a four membered ring with breaking of C-N bond at C···N distance 2.537 Å and simultaneous β-hydrogen shift. The activation barrier for this reaction was 237 kJ/mol (Figure 4.11). The average E_a predicted using DFT was 212.1 kJ/mol and using Kissinger method and FWO methods were 236.8 kJ/mol and 258.0 kJ/mol respectively.

4.3.4.4 Effect of alkyl chain length on thermal stability

Computational studies showed that alkyl chain length have no effect on thermal stability of ILs with similar anions. Figure 4.12 shows the TG/DTG curves of

$[C_4MIm]^+[Cl]^-$, $[C_6MIm]^+[Cl]^-$ and $[C_{16}MIm]^+[Cl]^-$. It was observed that the maximum decomposition temperatures were 284, 285 and 296 ^{o}C respectively for $[C_4MIm]^+[Cl]^-$, $[C_6MIm]^+[Cl]^-$ and $[C_{16}MIm]^+[Cl]^-$. The DTG curve of $[C_{16}MIm]^+[Cl]^-$ showed two distinct exothermic peaks below 200 ^{o}C with weight loss of 10.6 % equivalent to two moles of water ($C_{16}MImCl.2H_2O$). This is in agreement with the elemental analysis and computed parameters.
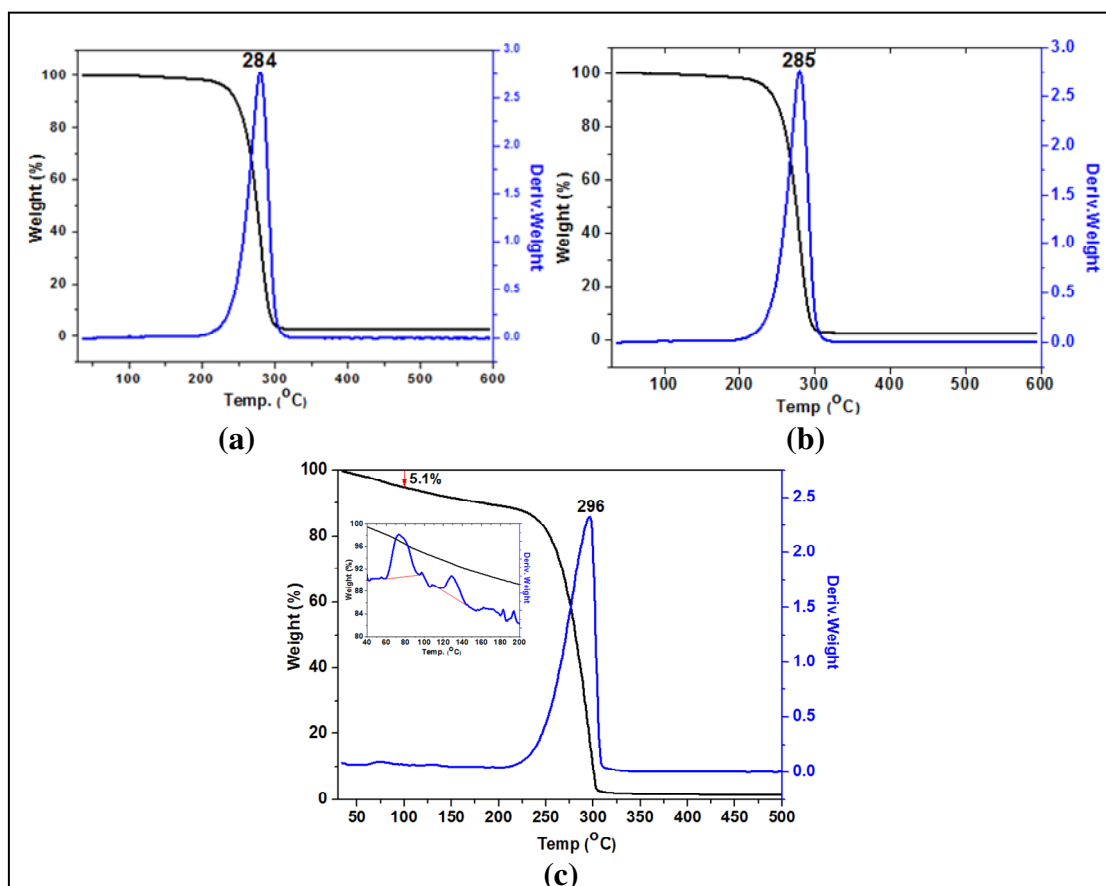
Figure 4.12 TG/DTG curves of (a) $[C_4MIm]^+[Cl]^-$, (b) $[C_6MIm]^+[Cl]^-$ and (c) $[C_{16}MIm]^+[Cl]^-$. The enlarged TG/DSC curve below 200 ^{o}C is shown as inset for $[C_{16}MIm]^+[Cl]^-$.

4.4 Conclusions

Ionic liquids selected for clay modification, $[C_6MIm]^+[Cl]^-$ and $[C_{16}MIm]^+[Cl]^-$ were synthesized with 95 % yield. The effect of anion on thermal stability of ILs were established using $[C_4MIm]^+[Cl]^-$(T_s = 284 ^{o}C) and $[C_4MIm]^+[BF_4]^-$(T_s = 427 ^{o}C), and conform to the computed parameters based on HOMO-LUMO energy gap. The decomposition products identified using pyrolysis GC-MS and transition states using

DFT method established the higher reactivity of $[C_4MIm]^+[Cl]^-$ over $[C_4MIm]^+[BF_4]^-$ as predicted from the charge transfer analysis. The non-dependency of alkyl chain length on stability of ILs were confirmed by analysing $[C_4MIm]^+[Cl]^-$, $[C_6MIm]^+[Cl]^-$ and $[C_{16}MIm]^+[Cl]^-$. The dihydrate formation in $[C_{16}MIm]^+[Cl]^-$ was analysed using DFT method and confirmed using elemental analysis, FT-IR high temperature studies and DSC analysis. The experimental results were complimenting to the theoretical studies described in chapter 3.

Chapter 5

Modification of clay using ILs

Abstract

Sodium montmorillonite clay (MMT-Na$^+$) was modified using cation exchange reaction of Na$^+$ with [C$_n$MIm]$^+$. The modification was followed using FTIR analysis, improved d-spacing in XRD, CHN analysis and TG analysis. The cation exchange efficiency was 60 - 64%. The modified clay showed decrease in thermal stability with respect to increase in alkyl chain length complimenting the theoretical prediction. The decomposition product of C$_4$MIm/MMT was identified using pyrolysis GC-MS and activation energy was calculated using FWO method. The predicted carbene mechanism was established by identifying 1-butyl-3-methylimidazol-2-ylidine using ^{13}C NMR spectroscopy.

5.1 Introduction

Awad *et al.* for the first time in 2004, used 1-alkyl-3-methylimidazolium based ionic liquid for clay modification. The modified, 1-ethyl-3-methylimidazolium montmorillonite clay (C$_2$MIm/MMT) showed an improved basal spacing of 1.2 Å and thermal stability with onset temperature (5 % weight loss, T$_{5\%}$) of 325 ^{o}C. Later, Ding *et al.* [2006] used 1-methyl-3-tetradecylimidazolium modified clay (C$_{14}$MIm/MMT) with increased d-spacing of 7.5 Å, as a filler (5 wt %) for polyolefin-clay composite and observed an improvement in thermal stability of composite material (T$_s$ = 484 ^{o}C) over neat polypropylene (T$_s$ = 318 ^{o}C). Table 5.1 shows the reported 1-alkyl-3-methylimidazolium modified MMT clays (C$_n$MIm/MMT) with d-spacing values. In reported C$_n$MIm/MMT systems, TGA data was used for organic content estimation [Ha *et al.* 2009; Huang *et al.* 2010; Yalcinkaya *et al.* 2014] and multiple maximum decomposition temperatures due to side chain degradation and adsorbed IL in unwashed clays were reported [Lv *et al.* 2015; Montano *et al.* 2017]. Only few literatures gives a quantitative information on thermal stability of C$_n$MIm/MMT [Awad *et al.* 2004; Reinert *et al.* 2012].

The initial studies were focused on the use of C$_n$MIm/MMT as a filler for polymer-clay nanocomposites [Ding *et al.* 2006; Kim *et al.* 2006; Ha *et al.* 2009]. Various applications and modification process of C$_n$MIm/MMT are shown in Table 5.1.

Table 5.1 Reported 1-alkyl-3-methylimidazolium modified clays.

C_nMIm/MMT	d-spacing increase (Å)	Application	Method/ References
C_2MIm/MMT	1.2	Thermal degradation studies	Aq. suspension of MMT and IL mixture stirred for 5 h at 60 °C. [Awad *et al.* 2004]
$C_{14}MIm/MMT$	7.5	Polyolefin clay nano-composites	Magnetic stirring for 5 h at 50 °C. [Ding *et al.* 2006]
C_2MIm /MMT C_6MIm/MMT	0.9 2.4	Polypropylene clay nano- composites/	Stirring at 80 °C for 6 h. [Kim *et al.*2006; Ha *et al.* 2009]
C_4MIm/MMT C_8MIm/MMT $C_{16}MIm/MMT$	2.0 3.0 4.0	Clay-supported chloro-aluminate ionic liquid catalyst	Stirring at 80 °C for 5 h. [Huang *et al.* 2010]
C_4MIm/MMT C_8MIm/MMT	1.6 1.7	Adsorption of ILs on to MMT	Agitation at 55 °C for 30 min. [Reinert *et al.* 2012]
C_4MIm/MMT	4.2	Electrically conducting thin film	Mixing MMT and IL in the weight ratio 1:10. [Takahashi *et al.* 2012]
C_8MIm/MMT $C_{12}MIm/MMT$ $C_{18}MIm/MMT$	2.5 4.9 9.6	Chromatographic applications	Stirring overnight. [Yalcinkaya *et al.* 2014]
$C_{12}MIm/MMT$ $C_{16}MIm/MMT$	4.0 6.6	Ionic liquids in Ca-MMT for chromate removal	Shaken for 24 h at 150 rpm. [Li *et al.* 2014]
$C_{16}MIm/MMT$	8.2	IL concentration on process of intercalation	Centrifuged for 60 min at 150 rpm. [Wu *et al.* 2014]
$C_{16}MIm/MMT$	2.1	Removal of amaranth dye	Stirring overnight. [Lawal *et al.* 2015]
$C_{12}MIm/MMT$ $C_{16}MIm/MMT$	4.0 6.6	Ionic liquids in Ca-MMT	Shaken on a reciprocal shaker at 150 rpm for 24 h. [Lv *et al.* 2015]
C_4MIm/MMT	1.5	Thermal degradation of organoclay	Probe sonication for 15 min. [Eapen *et al.* 2016 (This Thesis)]
C_6MIm/MMT $C_{16}MIm/MMT$	1.9 6.5	Perchlorate removal from water	Probe sonication for 15 min. [Eapen *et al.* 2016 (This Thesis)]
C_4MIm/MMT C_8MIm/MMT $C_{16}MIm/MMT$	2.2 3.3 6.4	Extraction of low-polarity organic compounds from water	Stirred for 1 h at room temperature. [Ladino *et al.* 2016]
C_4MIm/MMT C_8MIm/MMT $C_{16}MIm/MMT$	1.9 2.9 6.3	Functionalization of MMT with ILs	Stirred for 1 h at room temperature. [Montano *et al.* 2017]
$C_{16}MIm/MMT$	8.5	Removal of chloramph-enicol from water	Mixed on a shaker table at 150 rpm for 24 h. [Sun *et al.* 2017]

Processing of C_nMIm/MMT involves time consuming stirring methods with or without heating (Table 5.1). Wu *et al.* [2014] studied the effect of IL concentration on efficiency of clay intercalation and observed no further improvement in d-spacing above 5000 ppm concentration of IL. Ladino *et al.* [2016] studied the effect of counter anion on IL intercalation in MMT clay by selecting ILs with Br^-, OH^- and BF_4^- anions and no significant changes in d-spacing ($\pm$ 0.3 Å) were observed.

In this work, the proposed ILs *viz.* C_4MIm/MMT, C_6MIm/MMT and $C_{16}MIm$/MMT for clay modification, together with unexplored 1-decyl-3-methylimidazolium modified MMT ($C_{10}MIm$/MMT) were prepared using a probe sonication method with the lowest processing time (15 min.) reported. Thermal stability of prepared C_nMIm/MMT was compared quantitatively with commercial alkyl ammonium clays for 1 % decomposition ($T_{1\%}$) and 50 % decomposition ($T_{50\%}$). The conformation of $[C_nMIm]^+$ inside the clay gallery was analysed using Raman spectroscopy and the microstructural environment of C_nMIm/MMT is also depicted. Thermal decomposition mechanism of C_4MIm/MMT was established using pyrolysis GC-MS analysis, ^{13}C NMR analysis and computational studies.

5.2 Experimental section

5.2.1 Materials

Sodium montmorillonite clay (MMT-Na^+), Cloisite 10A, Cloisite 15A, Cloisite 20A and Cloisite 25A from Southern Clay Products, Inc., USA; 1-butyl-3-methylimidazolium chloride, 1-butyl-3-methylimidazolium tetrafluoroborate and 1-decyl-3-methylimidazolium chloride from Otto Chemie, India; Methanol from Fisher Scientific, India; 1-hexyl-3-methylimidazolium chloride and 1-hexadecyl-3-methylimidazolium chloride synthesized were used for clay modification.

5.2.2 Modification of clay

Aqueous suspension of MMT-Na^+ in distilled water (2%) was prepared by sonicating for 10 minutes using Hielscher-UIP1000hd probe sonicator at amplitude of 80 %. To this IL diluted in methanol was added and the exchange reactions were carried out by sonicating for 15 minutes. It was allowed to settle and filtered. The residue was repeatedly (5–8 times) washed with distilled water until no chloride traces were detected with silver nitrate solution. The residue (C_nMIm/MMT) was dried at room

temperature for 4 h and then at 100 ^{o}C for 2 hour under vacuum. Table 5.2 shows the list of modified clays.

Table 5.2 Modifier and abbreviations for modified clays.

Modifier/cation	Modified clay
1-butyl-3-methylimidazolium	C_4MIm/MMT
1-hexyl-3-methyl imidazolium	C_6MIm/MMT
1-decyl-3-methyl imidazolium	C_{10}MIm/MMT
1-hexadecyl-3-methylimidazolium	C_{16}MIm/MMT

5.3 Results and discussion

5.3.1 FTIR analysis

Figure 5.1 shows the FTIR spectrum of C_{16}MIMCl, MMT-Na$^+$ and C_{16}MIm/MMT. In [C_{16}MIM]$^+$[Cl]$^-$, The peaks at 3154, 3083 and 3048 cm^{-1} were due to the aromatic C-H stretching vibrations of imidazolium ring. Strong absorption bands in the region 2800-3000 cm^{-1} represent alkyl C-H stretching vibrations. Peaks at 1574 cm^{-1} and 1466 cm^{-1} are due to C=C and C=N vibrations respectively. Presence of water is confirmed from the peaks at 3462 and 1634 cm^{-1}. In MMT-Na$^+$, The stretching signals for the silicon-oxygen and aluminum-oxygen bonds are observed at 1047 cm^{-1} and 915 cm^{-1} respectively. The bands at 1636 cm^{-1} and 3630 cm^{-1} are assigned to absorbed water, while peak at 3430 cm^{-1} is assigned to the stretching of hydroxyl group. The modification of MMT-Na$^+$ is clearly evident in C_{16}MIm/MMT from the appearance of peaks characteristic of [C_{16}MIM]$^+$[Cl]$^-$.
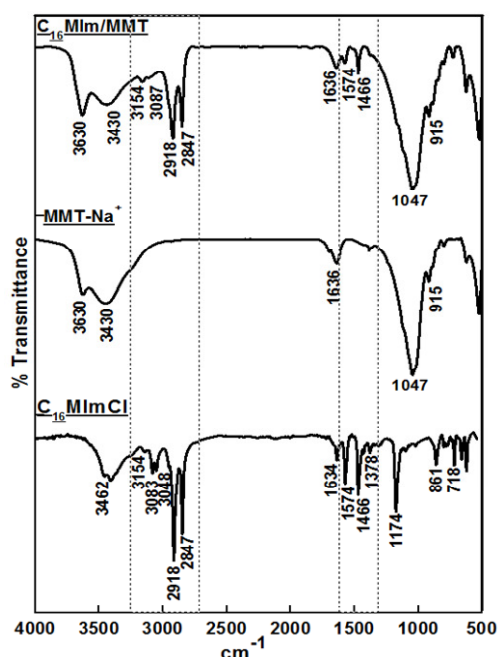
Figure 5.1 FTIR spectra of [C_{16}MIM]$^+$[Cl]$^-$, MMT-Na$^+$ and C_{16}MIm/MMT.

5.3.2 XRD analysis

XRD analysis was performed to observe the basal spacing between layers after exchanging sodium ions with the imidazolium cation (Figure 5.2). X-ray diffraction pattern of MMT-Na$^+$ exhibits 001 peak centred at $2\theta = 7.30^o$ corresponding to a basal d-spacing of 12.09 Å. For the modified clays, the characteristic peak of the clay was shifted to lower 2θ value leading to an increase of the interlayer spacing. This shift is a clear signature of the intercalation of the imidazolium cation between the layers of MMT. The d-spacing values of modified clays are shown in Figure 5.2.

Clay	d-spacing (Å)
MMT-Na$^+$	12.09
C$_4$MIm/MMT	13.64
C$_6$MIm/MMT	13.97
C$_{10}$MIm/MMT	14.38
C$_{16}$MIm/MMT	18.55
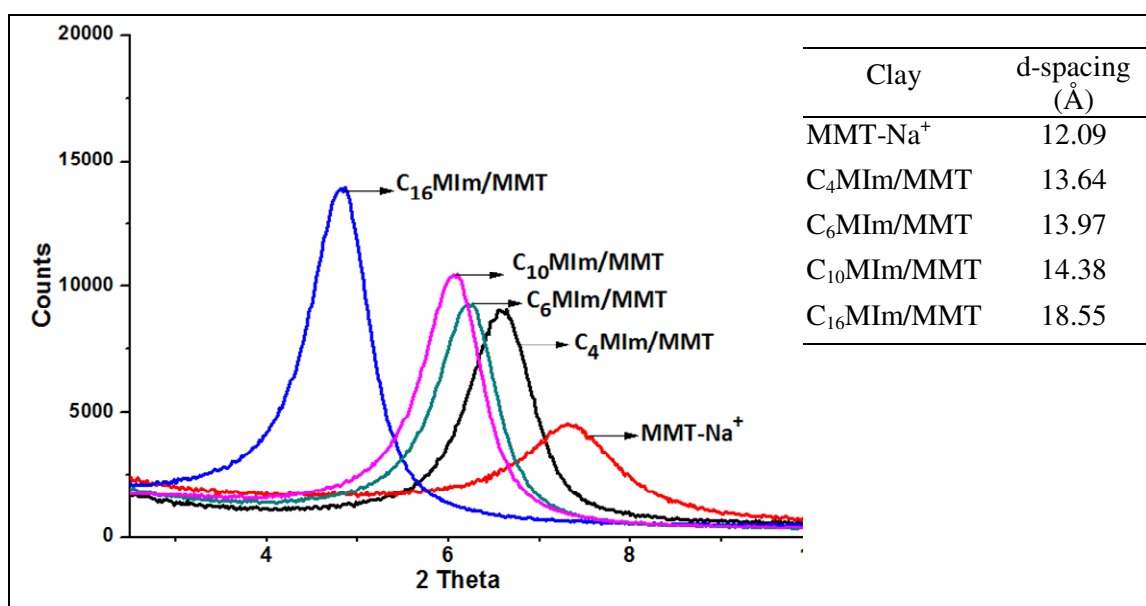
Figure 5.2 XRD spectra of MMT-Na$^+$, C$_4$MIm/MMT, C$_6$MIm/MMT, C$_{10}$MIm/MMT and C$_{16}$MIm/MMT. The d-spacing values are shown as inset.

5.3.3 Sodium estimation

Table 5.3 shows the sodium content in MMT-Na$^+$ and modified clays. The ion exchange efficiency was calculated from the amount of Na$^+$ exchanged on clay modification. An ion exchange efficiency of 60-63 % was observed in modified clays.

Table 5.3 Sodium (Na) content in clays and ion exchange efficiency.

Clay	Na (%)	Na exchanged (%)	Ion exchange efficiency (%)
MMT-Na$^+$	3.03	-	-
C$_4$MIm/MMT	1.12	1.91	63
C$_6$MIm/MMT	1.21	1.82	60
C$_{10}$MIm/MMT	1.11	1.92	63
C$_{16}$MIm/MMT	1.12	1.91	63

5.3.4 CHN analysis

1-alkyl-3-methylimidazolim cation with general formula $[C_{n+4}H_{2n-1}N_2]^+$ in modified clays were estimated using CHN analysis (Table 5.4). The total %(C+H+N) gave the organic content in modified clays.

Table 5.4 CHN analysis of modified clays.

Clay	C (%)	H (%)	N (%)	Total (%)
C_4MIm/MMT	7.9	1.4	2.2	11.5
C_6MIm/MMT	9.3	1.9	2.0	13.2
$C_{10}MIm/MMT$	14.0	2.4	2.2	18.6
$C_{16}MIm/MMT$	20.1	3.4	2.1	25.6

5.3.5 Thermal stability of clays

Thermal stability of clays were analysed using TG from room temperature to 600 ^{o}C. MMT-Na$^+$ has a mass loss of 2.6 % between 500 and 600 °C assigned to the loss of condensation water of silanol groups on the clay mineral surface (Figure 5.3).
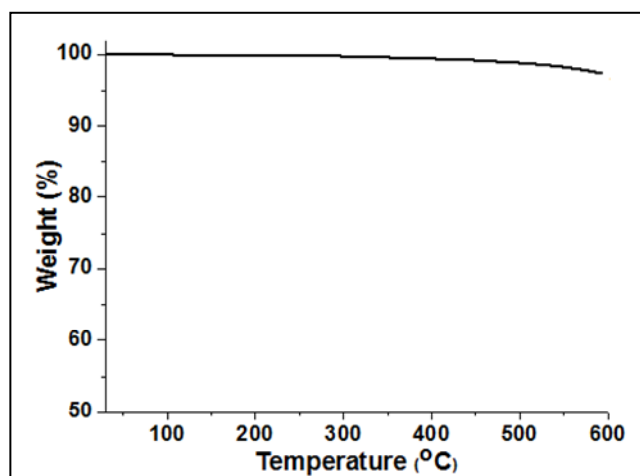
Figure 5.3 TG curve for MMT-Na$^+$

Figure 5.4 shows the TG/DTG curves for C_4MIm/MMT, C_6MIm/MMT, $C_{10}MIm/MMT$, $C_{16}MIm/MMT$ and commercial alkyl ammonium modified clays. The temperature for 1 % decomposition ($T_{1\%}$) and 50 % decomposition ($T_{50\%}$) are shown in Table 5.5. Among selected C_nMIm/MMT clays, C_4MIm/MMT showed maximum $T_{1\%}$ of 423 ^{o}C and the stability decreased with increase in alkyl chain length to 266 ^{o}C for $C_{16}MIm/MMT$. The $T_{50\%}$ also showed similar trend. Thermal stability of $[C_nMIm]^+$ followed the same trend predicted using computed HOMO-LUMO gap.
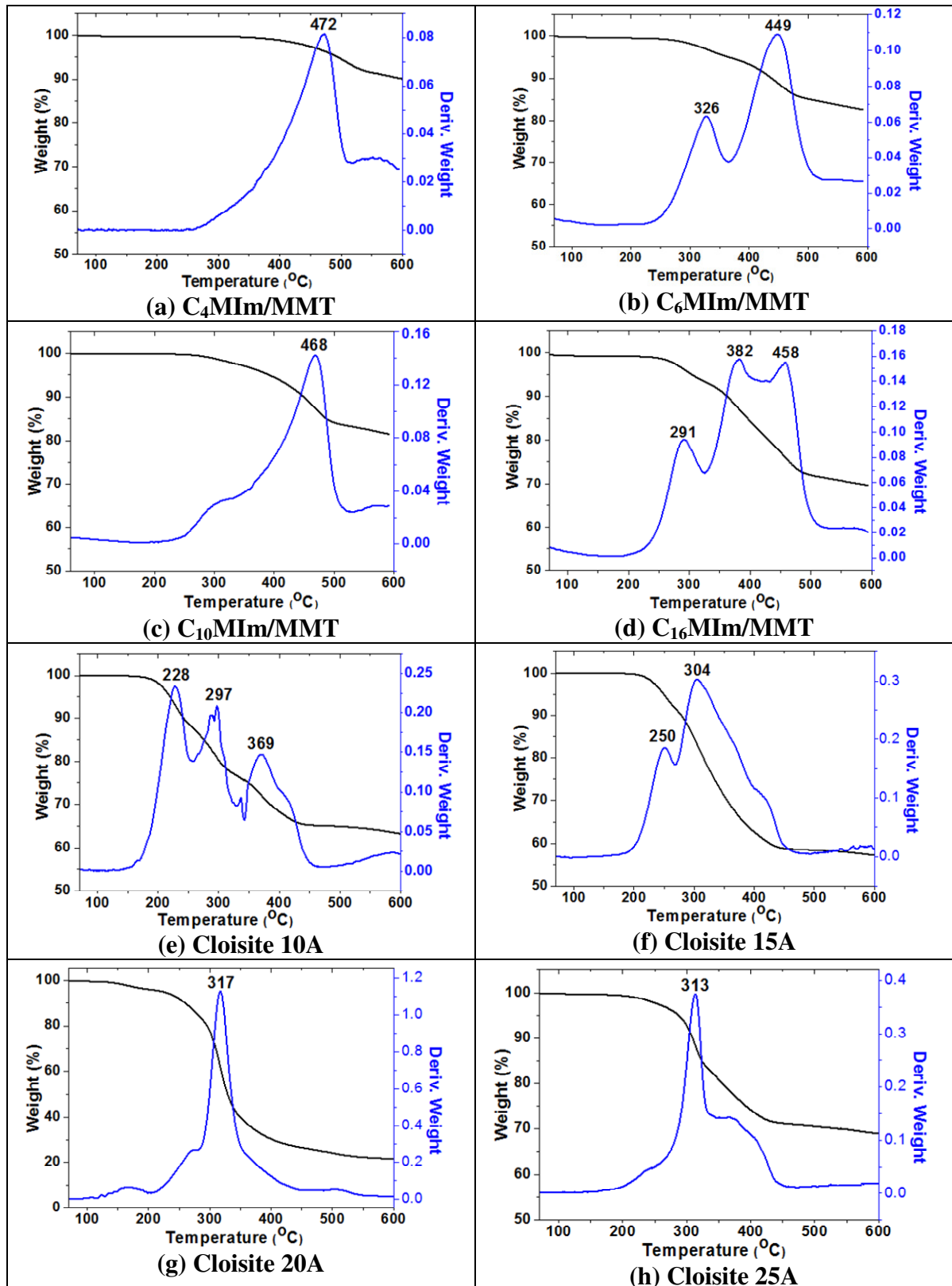
Figure 5.4 TG/DTG curves for C$_n$MIm/MMT clays and commercial alkylammonium modified clays.

Cloisite 25A showed the highest thermal stability among selected alkylammonium modified clays with $T_{1\%}$ of 214 ^{o}C. The $T_{1\%}$ of C_{16}MIm/MMT showed an increase of 52 ^{o}C than Cloisite 25A. All C_nMIm/MMT clays showed higher thermal stability than conventional alkyl ammonium clays (Table 5.5).

Table 5.5 Thermal stability of C_nMIm/MMT clays and Cloisite clays. The d-spacing values are also shown.

Clay	$T_{1\%}$	$T_{50\%}$	d-spacing (Å)
C_4MIm/MMT	423	467	13.64
C_6MIm/MMT	307	425	13.97
C_{10}MIm/MMT	290	411	14.38
C_{16}MIm/MMT	266	396	18.55
Cloisite 10A	181	284	19.20
Cloisite 15A	208	317	31.50
Cloisite 20A	154	318	24.20
Cloisite 25A	214	321	18.60

(a) C_4MIm/MMT   (b) C_{16}MIm/MMT
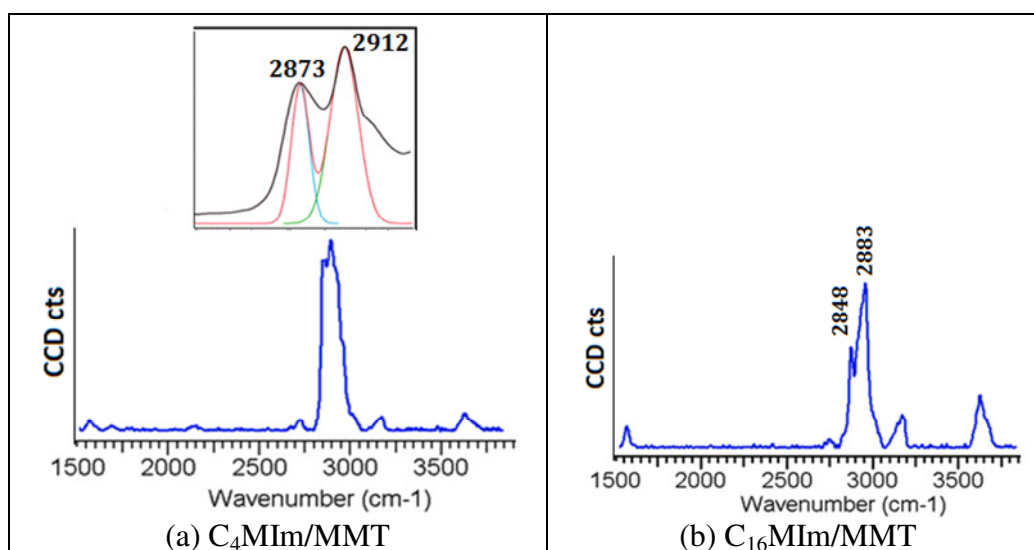
Figure 5.5 Raman spectra of C_4MIm/MMT and C_{16}MIm/MMT. The deconvoluted spectrum is shown in inset.

5.3.6 Raman spectral analysis

Figure 5.5 shows the Raman spectrum of C_{16}MIm/MMT and C_4MIm/MMT. Peak position and intensities of -CH_2 indicates the conformational state and local environment of imidazolium ionic liquids. Higher intensity for -CH_2 asymmetric stretching (2878 cm^{-1}) than symmetric stretching (2847 cm^{-1}) indicates a trans

conformer [Prokhorov *et al*. 2005]. $C_{16}MIm/MMT$ possess $-CH_2$ asym. (2883 cm^{-1}) and sym. (2848 cm^{-1}) stretching with peak intensities 0.74 and 0.19 respectively, the value of 3.9 for intensity ratio of asymmetric to symmetric confirms trans conformation for $[C_{16}MIm]^+$ inside the clay gallery. In C_4MIm/MMT, $-CH_2$ asymmetric stretching appears at 2912 cm^{-1} and symmetric stretching at 2873 cm^{-1} with peak intensities 0.56 and 0.45 respectively. All modified clays showed higher intensity for $-CH_2$ asymmetric stretching than symmetric stretching and exist as trans conformer (Table 5.6). A shift in peak position was observed as the alkyl chain length increased.

Table 5.6 Conformation analysis of $[C_nMIm]^+$ inside the clay gallery.

C_nMIm/MMT	*-CH$_2$- sym str.*		*-CH$_2$- asym str.*		$\frac{I_{asym.}}{I_{sym.}}$	Conformation
	Peak position (cm^{-1})	Intensity	Peak position (cm^{-1})	Intensity		
C_4MIm/MMT	2873	0.45	2912	0.56	1.2	T
C_6MIm/MMT	2867	0.74	2906	0.86	1.2	T
$C_{10}MIm/MMT$	2856	0.50	2903	0.51	1.0	T
$C_{16}MIm/MMT$	2848	0.19	2883	0.74	3.9	T

5.3.7 Thermal decomposition of C₄MIm/MMT

Pyrolysis GC-MS analysis was done to identify the decomposition products of C_4MIm/MMT (Figure 5.6). The decomposition products were 1-butene (m/z = 56) and methylimidazole (m/z = 82).
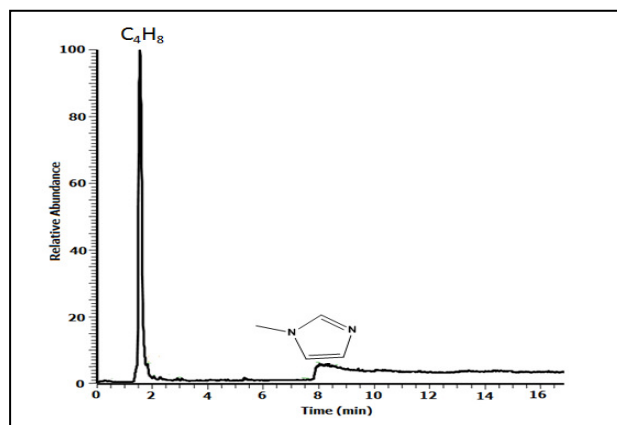
Figure 5.6 Pyrogram of C_4MIm/MMT at 600 ^{o}C.

The possible reactions were analyzed using computational method, B3LYP at 6-311+G(d,p) level of DFT (Figure 5.7). From the model of MMT-Na$^+$ given in Figure 5.7 (a), it is clear that the ions in the interlayer gallery face SiO$_4$ tetrahedral unit as their immediate neighbour [Cadars *et al*. 2012]. In C_4MIm/MMT (Figure 5.7 (b)), sodium ions are replaced by $[C_4MIm]^+$ cation. Considering the possible CH/O–Si interactions

from $[C_4MIm]^+$ to the clay, the use of the anionic moiety $Si(OH)_3O^-$ to model the decomposition reaction of $[C_4MIm]^+$ in the clay is proposed. $[C_4MIm]^+[Si(OH)_3O]^-$ ion pair is found to be marginally higher in energy (9.1 kJ/mol) than the neutral complex of imidazole-2-ylidene–$Si(OH)_4$ (Figure 5.7(e)). Therefore the DFT results suggest that the intercalated imidazolium cations can easily form the 1-butyl-3-methylimidazole-2-ylidene through a barrier less pathway.

(a) MMT-Na$^+$

(b) C_4MIm/MMT^+

(c) $[C_4MIm]^+$

(d) $[C_4MIm]^+[Si(OH)_3O]^-$

(e) $[C_4MIm]$-2-ylidene-$[Si(OH)_4]$

(f) $[C_4MIm]$-2-ylidene

(g) Transition state
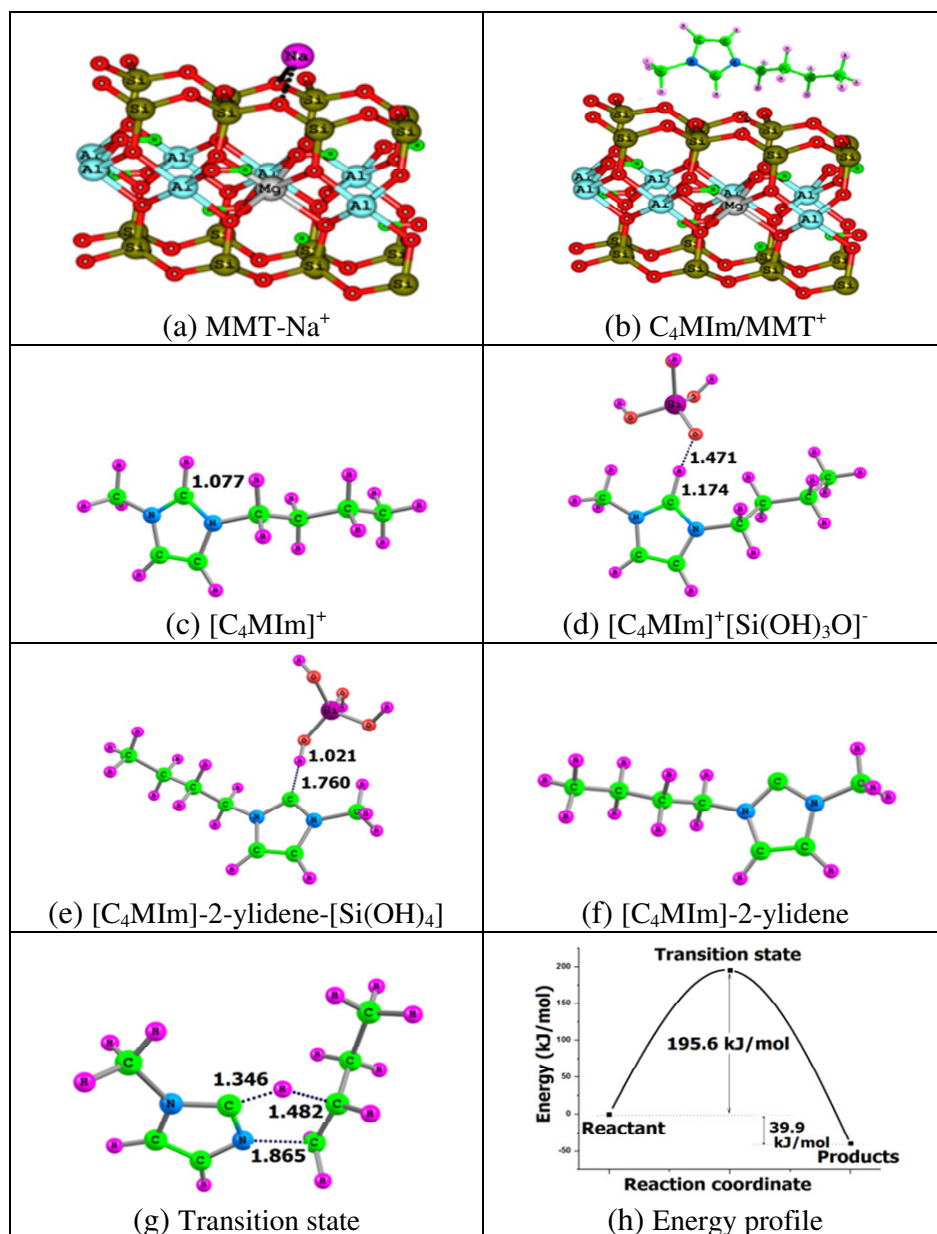
(h) Energy profile

Figure 5.7 (a) Model structure of MMT-Na$^+$, (b) C_4MIm/MMT, (c-h) Optimized structures of species involved in decomposition of C_4MIm/MMT with transition state and energy profile.

The singlet carbenes thus formed on heating can undergo elimination reactions involving β hydrogen shift from the butyl substituent at N1 to the carbenic centre followed by bond breaking at the quaternary nitrogen. Such a transition state was located in the DFT analysis with single imaginary frequency corresponding to the bond shifting process which is shown in Figure 5.7(g). The activation energy for the decomposition was 195.6 kJ/mol (Figure 5.7(h)) and the reaction is exothermic by 39.9 kJ/mol. The summarized decomposition mechanism is shown in Scheme 5.1. Anions with high basicity is capable of deprotonating imidazolium cation at C2 position, resulting in the formation of neutral carbon bases with nucleophilic singlet carbenes that are stabilized by the two neighbouring nitrogen atoms at the carbenic centre.
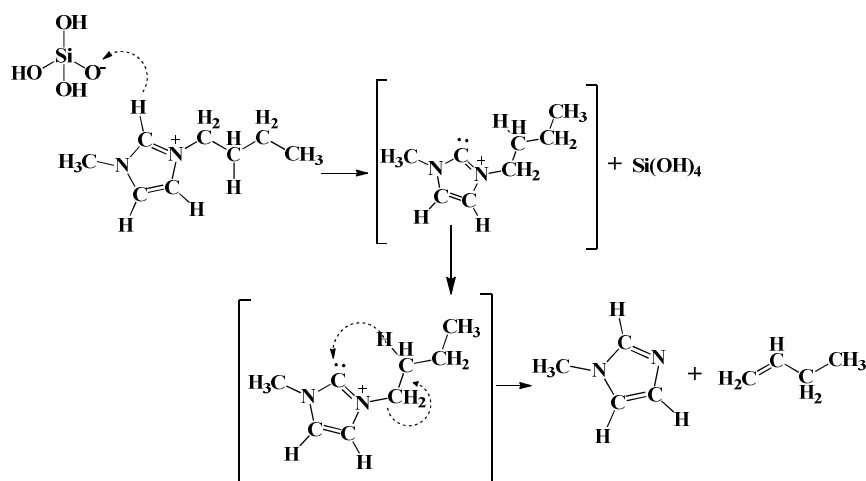
Scheme 5.1 Mechanism of C_4MIm/MMT decomposition through 1-butyl-3-methylimidazole-2-ylidene route.

The formation of carbene from $[C_4MIm]^+$ cation on heating was confirmed by the NMR analysis of C_4MImCl in D_2O solvent in presence of colloidal silica. Colloidal silica is 30 % suspension of SiO_2 in water, which contains –SiOH species similar to the model compound $Si(OH)_3O^-$ used in DFT study. ^{13}C NMR spectra of C_4MImCl and C_4MImCl with colloidal silica heated at 90 ^{o}C for 5 minutes are shown in Figure 5.8. The additional NMR signal observed at 187.64 ppm is attributed to singlet carbene carbon in imidazolium ring.
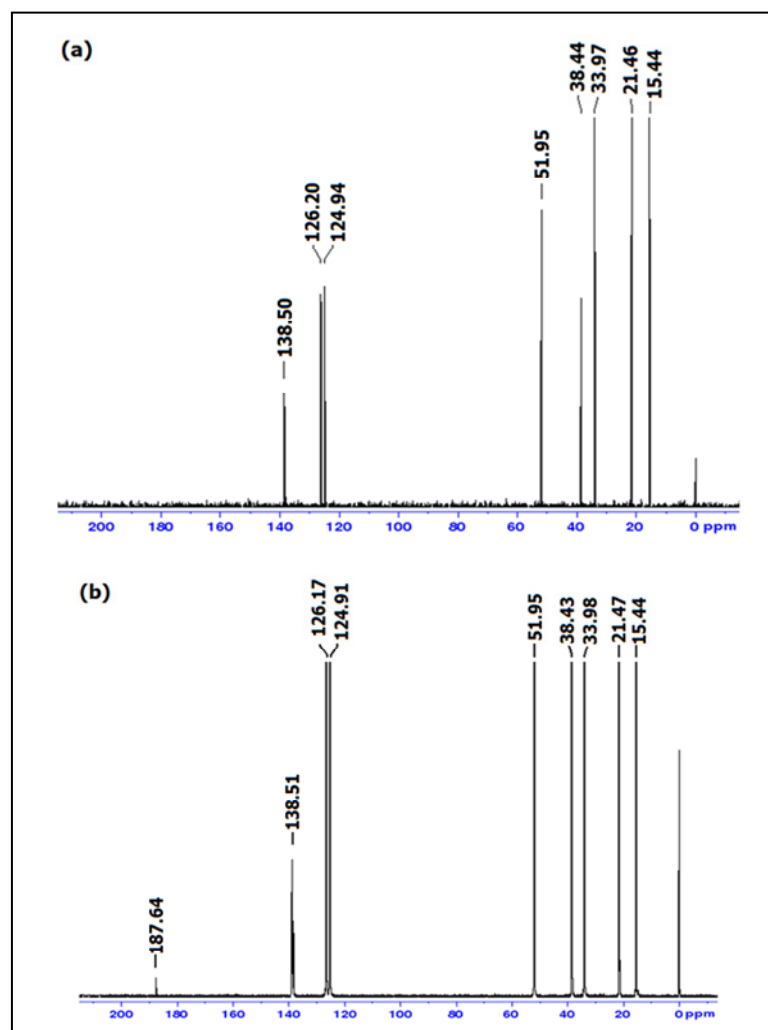
Figure 5.8 ^{13}C NMR spectrum of (a) [C$_4$MIm]$^+$[Cl]$^-$ in D$_2$O and (b) [C$_4$MIm]$^+$[Cl]$^-$ with colloidal silica in D$_2$O after heating.

Pyrolysis GC-MS analysis of C$_6$MIm/MMT, C$_{10}$MIm/MMT and C$_{16}$MIm/MMT also showed 1-methylimidazole and alkene as major product, in addition side chain decomposition products were also observed.

5.4 Conclusions

Modification of MMT-Na$^+$ was achieved with the lowest processing time of 15 minutes using a probe sonication method. The modification was confirmed using FTIR analysis, improved d-spacing in XRD, CHN analysis and TG analysis. The amount of [C$_n$MIm]$^+$ inside the clay gallery was quantified using CHN analysis. The cation exchange efficiency was estimated to be 60 - 63% from sodium estimation and CHN analysis. The C$_n$MIm/MMT showed improved thermal stability than conventional alkyl ammonium modified clays. C$_{16}$MIm/MMT with d-spacing of 18.55 Å and T$_{1\%}$ of 266

^{o}C is proposed as a replacement for Cloisite 25A with d-spacing of 18.65 Å and $T_{1\%}$ of 214 ^{o}C. For the first time the thermal degradation of ionic liquid modified clay was elucidated using DFT and experimentally rationalized using Pyrolysis GC-MS and ^{13}C-NMR experiments. The predicted carbene mechanism was established by identifying 1-butyl-3-methylimidazol-2-ylidine using ^{13}C NMR spectroscopy. The experimental results on stability of $[C_nMIm]^+$ cations were in parallel to the theoretical studies described in chapter 3.

Perchlorate removal from water using IL modified clay
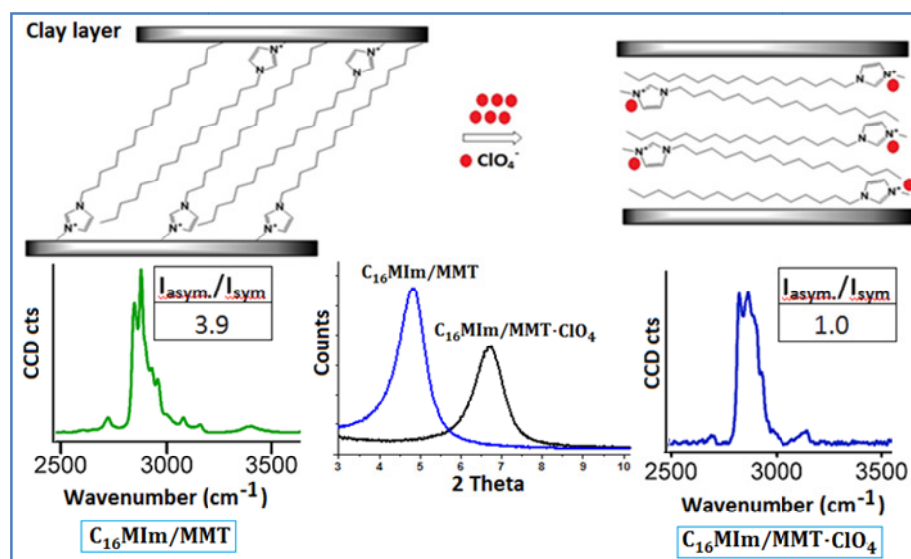
Eapen Thomas, Krishnan G. Rekha, Soundiraraju Bhuvaneswari, Kunduchi P. Vijayalakshmi* and Benny K. George

Abstract

C_nMIm/MMT was used for perchlorate adsorption from water. $MMT-Na^+$ showed negligible adsorption whereas C_nMIm/MMT showed an increase in adsorption with increase in chain length of the exchanged cation. $C_{16}MIm/MMT$ showed the highest adsorption of 15.6 mg/g from 1000 ppm perchlorate solution at pH =2 and contact time of 15 min. The adsorption followed the Freundlich isotherm with pseudo second order kinetics. The d-spacing of $C_{16}MIm/MMT$ (18.55 Å) decreased to 13.70 Å on perchlorate adsorption and observed a conformational change in $[C_{16}MIm]^+$ inside the clay gallery from trans to gauche, suggesting the possible formation of $[C_{16}MIm]^+[ClO_4]^-$ inside the clay gallery. The adsorbed clays were regenerated by heating to $175 \pm 5\ ^oC$ in air and 95 % regenerability was observed.

6.1 Introduction

Perchlorate ion detected in soil, water and food originates mainly from different salts used in solid propellants for rockets and oxidizer components in various military and industrial processes [Kannan *et al*. 2009; Kosaka *et al*. 2007; Ye *et al*. 2012; Chitrakar *et al*. 2012]. Perchlorates are highly soluble in water and it enters human body through drinking water or food chain and causes hypothyroidism by interfering with the ability of the thyroid gland to process iodine [Urbansky 1998; Wolff 1998]. The persistent and toxic nature of perchlorates with its unusual physical and chemical properties makes it difficult to remove. Different methods like adsorption, ion-exchange, membrane methods, biological treatment, chemical reduction, electrochemical reduction and so on were studied and a reliable, repeatable, recyclable system is yet to be established for perchlorate removal from water [Rekha *et al*. 2017; Srinivasan and Sorial 2009; Parette and Cannon 2005; Luo *et al*. 2016; Kim *et al*. 2011; Komarneni *et al*. 2010; Seliem *et al*. 2010, 2011, 2013; Hutchison and Zilles 2015].

Among alternatives for perchlorate removal, ion-exchange is apparently the most efficient method. However, it is costly and not efficient to deal with small concentration of perchlorate in water. Adsorption methods are promising and widely studied method for perchlorate removal. The first choice for adsorption, virgin activated carbon, was not effective for perchlorate adsorption, however surface modification made it comparative to ion exchange [Parette and Cannon 2005]. Considering the

availability, low cost and thermal stability, clays were studied for perchlorate removal but no improvements were observed. The use of organoclay to 'selective' uptake of perchlorate from water marked the changing phase in terms of perchlorate removal systems [Chitrakar *et al*. 2012; Kim *et al*. 2011; Komarneni *et al*. 2010; Seliem *et al*. 2010, 2011, 2013; Wu *et al*. 2016]. Alkyl ammonium and alkyl pyridinium modified clays were extensively used for perchlorate removal and no regenerable system was reported.

Luo *et al*. [2015, 2016] used benzyloctadecyldimethylammonium modified and hexadecylpyridinium modified montmorillonite clay to achieve perchlorate removal efficiency of 0.90 and 0.09 mmol/g respectively. Kim *et al.* [2011] used octadecyltrimethylammonium, dodecyltrimethylammonium and hexadecyltrimethyl-ammonium modified clays with perchlorate uptake of 0.07, 0.02 and 0.04 mmol/g respectively. Seliem *et al.* [2011] used commercially available clays, Cloisite 10A, Cloisite 15A and Cloisite 20A for perchlorate removal with 0.26, 0.16 and 0.09 mmol/g perchlorate uptake efficiency respectively. Bagherifam *et al*. [2014] used hexadecylpyridinium modified montmorillonite clay and achieved perchlorate removal of 1.11 mmol/g. Al-pillared montmorillonite by Komarneni *et al*. [2013] showed perchlorate removal capacity of 0.01 mmol/g.

In this work, a new class of modified clays using thermally stable 1-alkyl-3-methylimidazolium based ILs with varying chain lengths were explored for perchlorate removal from water. The adsorption mechanism, isotherms, kinetics and regeneration studies are reported.

6.2 Methodology

6.2.1 Materials

Sodium montmorillonite, MMT-Na$^+$ from Southern Clay Products, Inc., USA, Hydrochloric acid (purity > 36-38 %) from Merck, C_4MIm/MMT, C_6MIm/MMT, C_{10}MIm/MMT, C_{16}MIm/MMT and ammonium perchlorate AR (99.9 %) prepared in house were used.

6.2.2 Perchlorate adsorption studies

0.5 g of C_nMIm/MMT was dispersed in 25 mL each of 50, 100, 250, 500 and 1000 mg/L perchlorate solution and the mixture was equilibrated at 30 ^{o}C for 1, 2, 5, 10, 15, 30, 60, 120 and 180 min. using a shaker. After equilibration, the suspension was

centrifuged and the solution was analysed for perchlorate content using Ion Chromatograph (IC). The experiment was repeated with different pH from 2 to 8. The amount of sorbed perchlorate per gram of clay was calculated using eqn. 6.1,

$$\mathbf{ClO_4 \ (mg/g)} = \frac{(C_i - C_e)V}{m} \qquad \text{--- (6.1)}$$

where, C_i is the initial perchlorate solution concentration, V is the volume of perchlorate solution, m is the weight of adsorbent in g and C_e is the concentration of perchlorate after adsorption calculated from IC analysis.

6.2.3 Kinetic studies

The experiments were conducted at pH = 2 and various time intervals, *viz.* 1, 2, 5, 10, 15, 30 and 60 min. The experimental data were fitted with pseudo-first order (eqn. 6.2), pseudo-second order (eqn. 6.3) and intra-particle diffusion process (eqn. 6.4),

$$\mathbf{log(q_e - q_t)} = \mathbf{log q_e} - \frac{k_1 t}{2.303} \qquad \text{--- (6.2)}$$

$$\frac{t}{q_t} = \frac{1}{k_2 q_e^2} + \frac{t}{q_e} \qquad \text{--- (6.3)}$$

$$q_t = k_p t^{1/2} + C \qquad \text{--- (6.4)}$$

where q_e and q_t are the amount of perchlorate (mg/g) adsorbed at equilibrium and time t (min) respectively. The first order rate constant, k_1 is obtained from the slope of the log $(q_e - q_t)$ *versus* t plot. k_2 is the second order rate constant obtained from the plot of t/q_t *versus* t. k_p is the rate constant of intra-particle diffusion determined from the slope of q_t *versus* $t^{1/2}$ plot. The value of C relates to the thickness of the boundary layer. Larger the intercept, greater is the boundary layer effect [Vimonses *et al*. 2009]. If the plot passes through the origin (C = 0), the intra-particle diffusion is regarded as the only rate controlling step [Demiral and Gunduzoglu 2010].

6.2.4 Isotherm studies

It is essential to establish the most suitable adsorption equilibrium correlation for reliable prediction of adsorption parameters and quantitative comparison. Langmuir model (eqn. 6.5) (based on the assumption that monolayer adsorption on a homogeneous adsorbent takes place with no interacting forces between adsorbed

molecules) and heterogeneous models, *viz.* Freundlich (eqn. 6.6) and Tempkin (eqn. 6.7) were used to fit the adsorption of perchlorate onto modified clay,

$$\text{Langmuir model} \qquad \frac{C_e}{q_e} = \frac{1}{Q_0 b} + \frac{C_e}{Q_0} \qquad \text{--- (6.5)}$$

$$\text{Freundlich model} \qquad \log q_e = \log k_F + \frac{1}{n} \log C_e \qquad \text{--- (6.6)}$$

$$\text{Tempkin model} \qquad q_e = B \ln A + B \ln C_e \qquad \text{--- (6.7)}$$

where C_e (mg/L) is the concentration of perchlorate solution at equilibrium, q_e (mg/g) is the amount of perchlorate adsorbed per unit mass of the adsorbent at equilibrium and Q_0 (mg/g) is the amount of adsorbate at complete coverage, which gives the maximum adsorption capacity and b (L/mg) is the Langmuir constant reflecting the energy of adsorption. k_F is the Freundlich constant, n is a constant related to energy of adsorption and its magnitude is an indication of the favourability of adsorption. A and B are the Tempkin constants.

6.2.5 Computational method

Geometries of gaseous ion pairs were optimized at B3LYP level of density functional theory using 6-311+G(d,p) basis set as implemented in *Gaussian 09*. BSSE corrected binding energy for the ion-pairs ([RMIm]$^+$[X]$^-$) was calculated using eqn. (6.8).

$$[RMIm]^+ + [X]^- \rightleftharpoons [RMIm]^+[X]^- \qquad \text{--- (6.8)}$$

6.2.6 Regeneration

The perchlorate adsorbed clays were regenerated by heating at different temperatures; 170, 175, 180 and 190 ^{o}C. The *% regenerability* was analysed by comparing the perchlorate adsorption efficiency of regenerated clay and parent modified clay.

6.2.7 Instrumental

Perchlorate was estimated using a Dionex model ICS 2000 Ion Chromatograph (IC) equipped with AS16 column, AG16 Guard column, ASRS 300 Suppressor column and a conductivity detector using 35 mM NaOH as eluent with a flow rate of 1 mL/min. Chromeleon chromatographic software was used for the data analysis. XRD analysis

was done using Bruker D8 Discover diffractometer. CHN analysis using Perkin Elmer 2400 CHNS analyzer with thermal conductivity detector. Thermal analysis using TA instruments SDT Q600 TGA from room temperature to 600 $^{\circ}$C at a heating rate of 10 $^{\circ}$C/min. in nitrogen atmosphere for modified clay and in air for regeneration study and Raman spectral studies using WiTec alpha 300R confocal Raman microscope were also done.

6.3 Results and discussion

6.3.1 Effect of solution pH on adsorption

Figure 6.1 shows the variation of adsorption capacity of modified clays with pH. pH was limited to 8 due to the enhanced solubility of clay in alkaline medium [McBride 1994]. Higher rate of adsorption was observed at lower pH and pH = 2 was selected for experiment. At low pH levels H^{+} ions dominate the surface of the clay. Perchlorate ions with negative charge at low pH results in electrostatic attraction with the positive charge on the clay resulting in an increased adsorption at the surface.
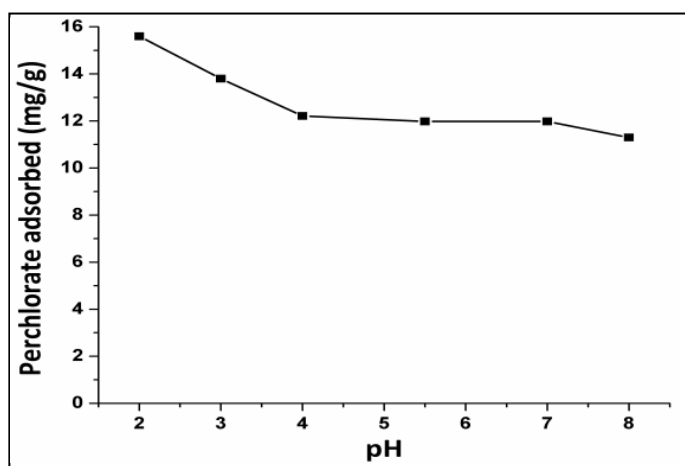
Figure 6.1 Effect of pH on perchlorate adsorption using C$_{16}$MIm/MMT.

When pH is increased, the excess of OH^{-} ions present in the solution lead to competition of adsorption sites with perchlorate ions which results in lower adsorption. If there is still significant amount adsorbed onto modified clay surface at higher pH values, it can be attributed to chemisorption [Lawal and Moodley 2015]. From Figure 6.1, at pH = 8, higher perchlorate adsorption capacity is retained (11.3 mg/g) by C$_{16}$MIm/MMT suggest chemisorption.

6.3.2 Effect of contact time

The effect of contact time on adsorption at room temperature (303 K) was studied at various time intervals from 1 to 180 min. Figure 6.2 shows the perchlorate adsorption by C_{16}MIm/MMT. Maximum adsorption was observed at 15 min. and equilibrium was reached. Lower equilibration time is advantageous in its practical applications.
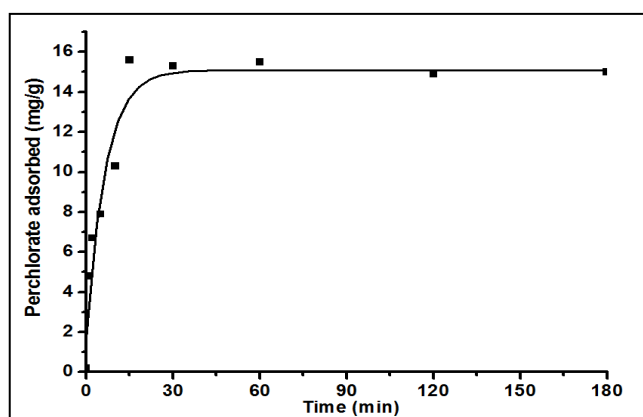
Figure 6.2 Effect of contact time on perchlorate adsorption using C_{16}MIm/MMT.

6.3.3 Effect of perchlorate concentration

Adsorption studies were done using different concentrations of perchlorate solutions from 50 mg/L to 1000 mg/L and the adsorption increased linearly ($R^2 = 0.98$) with increasing concentrations of perchlorate solutions (Figure 6.3).
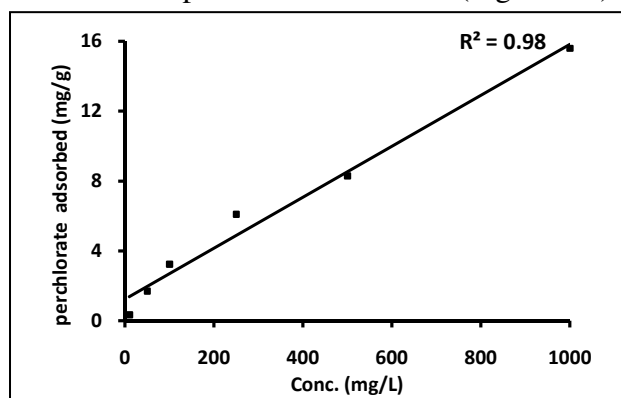
Figure 6.3 Effect of initial concentration on adsorption using C_{16}MIm/MMT.

Table 6.1 d-spacing of clay and its adsorption capacity (q_e).

Clay	d-spacing (Å)	q_e (mg/g)	d-spacing after ClO_4^- adsorption (Å)
MMT-Na$^+$	12.09	0.1	12.10
C_4MIm/MMT	13.64	0.7	13.08
C_6MIm/MMT	13.97	1.1	13.43
C_{10}MIm/MMT	14.38	12.4	14.20
C_{16}MIm/MMT	18.55	15.6	13.70

6.3.4 Perchlorate adsorption by C_nMIm/MMT

Adsorption studies were carried out using MMT-Na$^+$, C$_4$MIm/MMT, C$_6$MIm/MMT, C$_{10}$MIm/MMT and C$_{16}$MIm/MMT with 1000 mg/L perchlorate solution at pH = 2 and contact time of 15 min. The adsorption capacity (q$_e$) and d-spacing of clays before and after adsorption are tabulated in Table 6.1. The value of q$_e$ showed the same trend as d-spacing of modified clays; MMT-Na$^+$ < C$_4$MIm/MMT < C$_6$MIm/MMT < C$_{10}$MIm/MMT < C$_{16}$MIm/MMT (Table 6.1). C$_{16}$MIm/MMT showed maximum perchlorate adsorption of 15.6 mg/g (0.16 mmol/g) of clay. d-spacing of C$_{16}$MIm/MMT decreased from 18.55 Å to 13.70 Å on adsorption of perchlorate (Figure 6.4) with composition unchanged while all other modified clays showed negligible change (Table 6.1). The increased adsorption of perchlorate with increasing d-spacing is attributed to the enhanced access of perchlorate ions on to the clay surface.
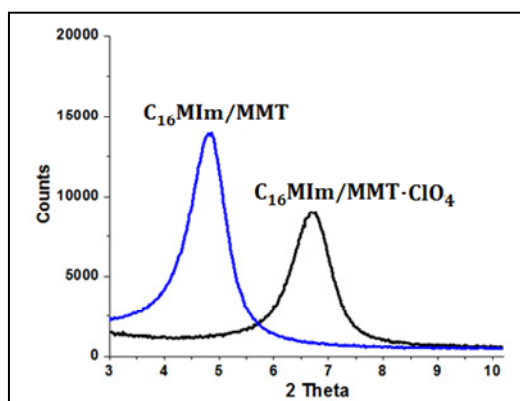
Figure 6.4 XRD spectra of C$_{16}$MIm/MMT and perchlorate adsorbed C$_{16}$MIm/MMT (C$_{16}$MIm/MMT-ClO$_4$)

Raman spectroscopy was used for conformational analysis to account for the decreased d-spacing on adsorption by measuring the intensity of symmetric (2847 cm^{-1}) and asymmetric (2878 cm^{-1}) stretching vibrations of methylene groups present [Prokhorov *et al*. 2005]. Trans conformer shows higher intensity for asymmetric stretching than symmetric stretching and in gauche conformer symmetric stretching is reported to possess higher intensity. Figure 6.5 shows the Raman spectra of C$_{16}$MImCl, C$_{16}$MIm/MMT and C$_{16}$MIm/MMT-ClO$_4$ with intensity of methylene stretching vibrations. C$_{16}$MIm/MMT showed an increase in intensity ratio of asymmetric to symmetric stretching vibrations, suggesting more of trans conformer. The C$_{16}$MIm/MMT-ClO$_4$ showed a decrease in intensity ratio of asymmetric to symmetric C-H stretching vibrations compared to C$_{16}$MIm/MMT, an indication of change in

conformation from trans to gauche. This accounts for the large decrease (4.85 Å) in d-spacing observed for $C_{16}MIm/MMT$ on perchlorate adsorption. The analysis reveals the possibility of formation of a new ion pair, $[C_{16}MIm]^+[ClO_4]^-$ within the clay layer between imidazolium cation and perchlorate anion. From the Figure 6.5, it is clear that the CH_2 stretching pattern in free ionic liquid $[C_{16}MIm]^+[Cl]^-$ and newly formed ion pair within the clay layers are comparable.

IL/Clay	$I_{sym.}$	$I_{asym.}$	$\dfrac{I_{asym.}}{I_{sym.}}$
$[C_{16}MIm]^+[Cl]^-$	0.66	0.80	1.21
$C_{16}MIm/MMT$	0.19	0.74	3.89
$C_{16}MIm/MMT-ClO_4$	0.95	0.99	1.04
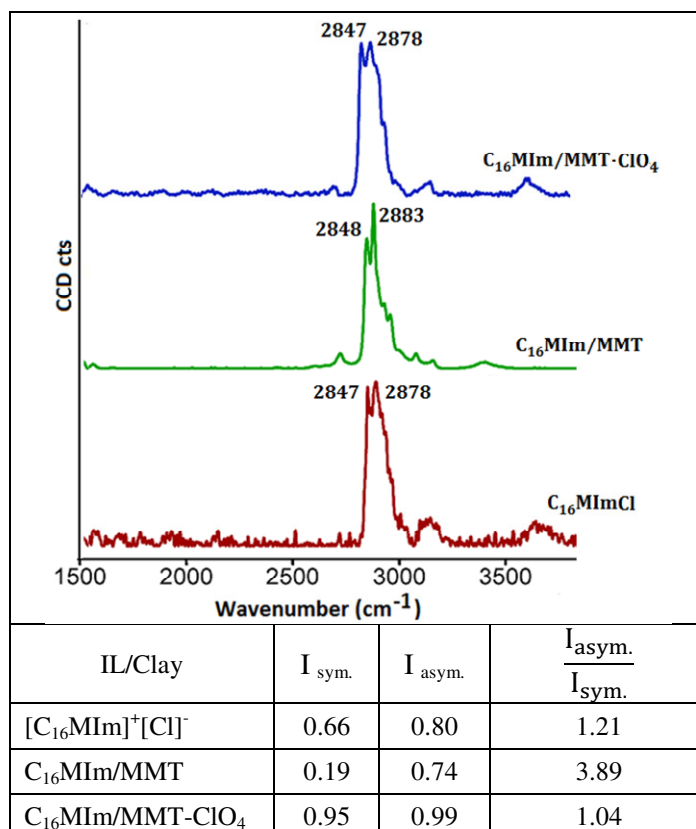
Figure 6.5 Raman spectra of $[C_{16}MIm]^+[Cl]^-$, $C_{16}MIm/MMT$ and $C_{16}MIm/MMT-ClO_4$. The table shows the intensity of C-H str. vibrations.

The $[C_{16}MIm]^+[ClO_4]^-$ ion-pair formation possibility was studied using B3LYP/6-311+G(d,p) method. $[C_{16}MIm]^+[Si(OH)_3O]^-$ represent the model structure of $C_{16}MIm/MMT$ used for computational studies as depicted in Figure 6.6, where the $[C_{16}MIm]^+$ represent the intercalated imidazolium cation and $[SiO_4H_3]^-$ represent the anionic clay layer. $C_{16}MIm/MMT$ in acidic medium (pH = 2) weakens the cation clay layer interaction due to the presence of excess H^+ ions, which is supported by the increase in C2H··O bond distance from 1.476 Å to 2.077 Å in the optimized model structures given in Figure 6.6(a) and 6.6(b) respectively. The free imidazolium cations

thus generated on acidification, can also interact with perchlorate anions to form 1-hexadecyl-3-methylimidazolium perchlorate, $[C_{16}MIm]^+[ClO_4]^-$ (Figure 6.6(c) as substantiated by Raman spectroscopic analysis.

(a) $[C_{16}MIm]^+[Si(OH)_3O]^-$

(b) $[C_{16}MIm]^+[Si(OH)_4]$
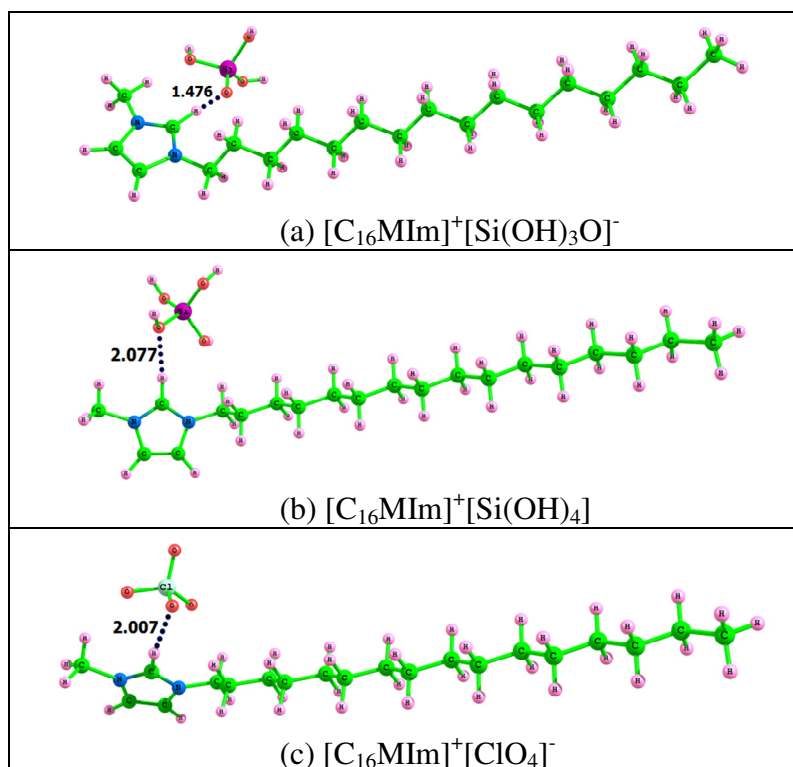
(c) $[C_{16}MIm]^+[ClO_4]^-$

Figure 6.6 Optimized structures of species involved in perchlorate adsorption mechanism, (a) $[C_{16}MIm]^+[Si(OH)_3O]^-$, (b) $[C_{16}MIm]^+[Si(OH)_4]$ and (c) $[C_{16}MIm]^+[ClO_4]^-$.
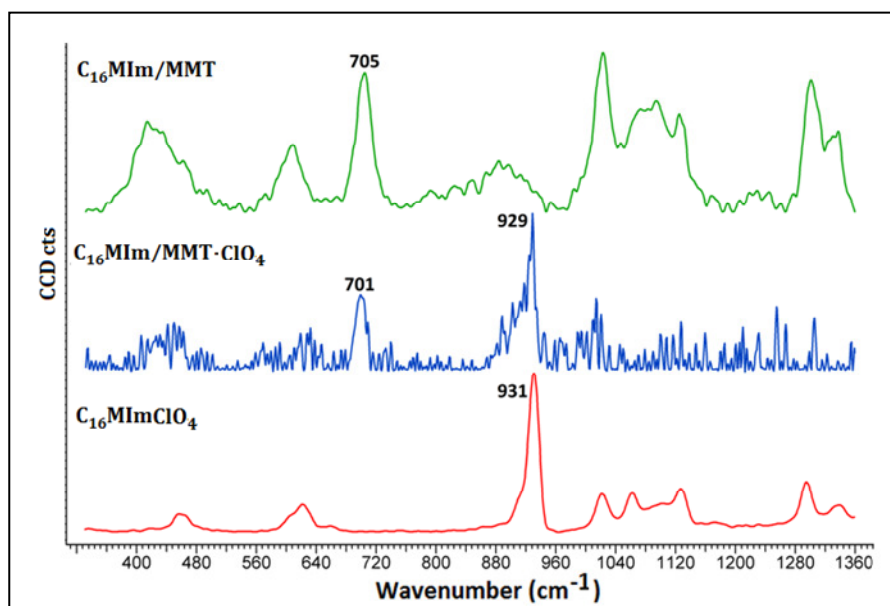
Figure 6.7 Raman spectra of $[C_{16}MIm]^+[ClO_4]^-$, $C_{16}MIm/MMT$-ClO_4 and $C_{16}MIm/MMT$.

The $[C_{16}MIm]^+[ClO_4]^-$ ion-pair formation inside the clay gallery was further confirmed by comparing the Raman spectra of $C_{16}MIm/MMT$ and $C_{16}MIm/MMT-ClO_4$ with $[C_{16}MIm]^+[ClO_4]^-$ (Figure 6.7). $[C_{16}MIm]^+[ClO_4]^-$ was synthesized using reported procedure by Wang *et al.* [2014]. The characteristic peak of perchlorate anion at 931 cm^{-1} is seen in Raman spectra of $[C_{16}MIm]^+[ClO_4]^-$ (Figure 6.7). Clay shows a characteristic vibration of Si-O$_b$-Si at 705 cm^{-1} (O$_b$- bridging oxygen atoms that connects the SiO$_4$ tetrahedra which makes up the layers in clay). Raman spectra of $C_{16}MIm/MMT-ClO_4$, shows the presence of characteristic peaks due to Si-O$_b$-Si and ClO_4^- with a peak shift. i.e. the peak due to Si-O$_b$-Si at 705 cm^{-1} shifted to 701 cm^{-1} indicating the change in inter gallery spacing and the peak due to ClO_4^- at 931 cm^{-1} is downshifted to 929 cm^{-1}. This further confirms the formation of $[C_{16}MIm]^+[ClO_4]^-$ in the clay gallery.

6.3.5 Adsorption kinetics
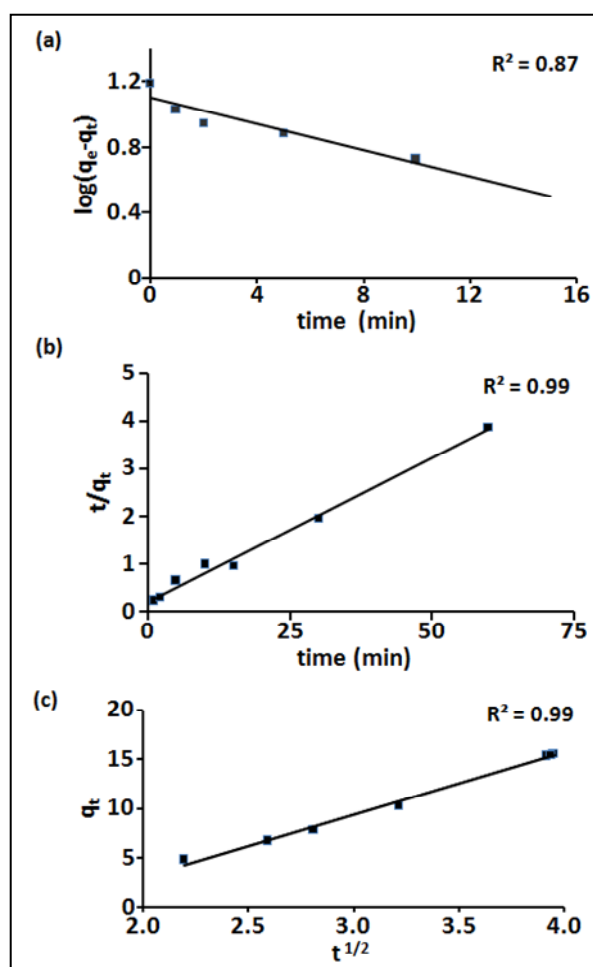
Figure 6.8 (a) Pseudo-first order model (b) Pseudo-second order model and (c) Intra-particle diffusion model for perchlorate uptake by $C_{16}MIm/MMT$.

Pseudo-second order and intra-particle diffusion models were best fitted for perchlorate adsorption with $R^2 = 0.99$. The pseudo-second order linear plot (Figure 6.8) suggests that the rate limiting step is chemisorption including valence force through sharing and exchange of electrons between ClO_4^- and modified MMT [Ho 2006]. In Figure 6.8 (c), the intercept not passing through the origin ($C \neq 0$) suggests that intra-particle diffusion is not the rate controlling step [Demiral and Gunduzoglu 2010]. The conformational change and thereby fluidic property observed may be the reason for higher correlation of intra-particle diffusion kinetics.

6.3.6 Adsorption isotherm study

The experimental data were fitted in eqn. 6.5 - 6.7 and adsorption isotherms were plotted. Freundlich adsorption describes the most favourable adsorption process with $R^2 = 0.98$ (Figure 6.9). The value of n > 1 in Freundlich adsorption isotherm indicates a favourable adsorption process and $1/n = 0.54$, a value below unity implies chemisorption [Haghseresht and Lu 1998].
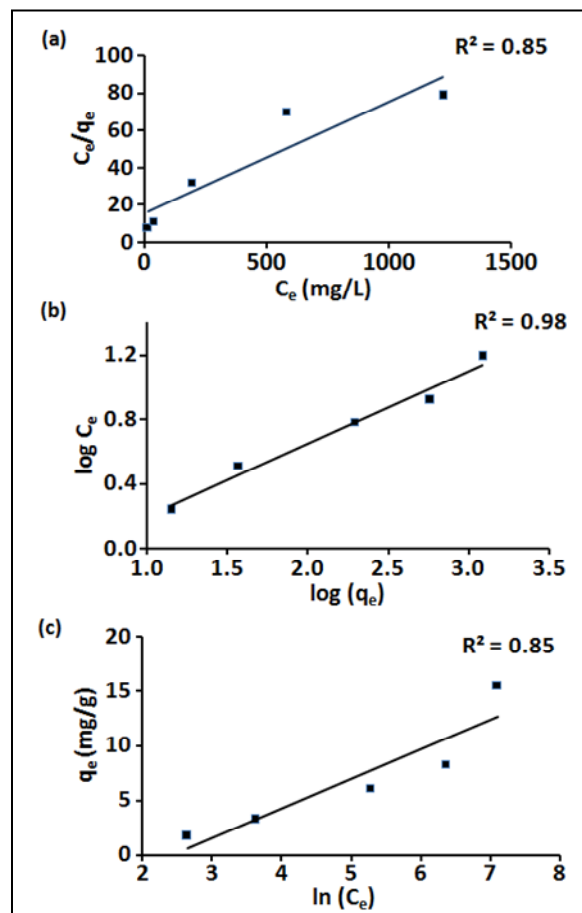
Figure 6.9 (a) Langmuir plot (b) Freundlich plot and (c) Tempkin plot for perchlorate uptake by $C_{16}MIm/MMT$.

6.3.7 Regeneration studies

The formation of $HClO_4$ on heating $C_{16}MIm/MMT-ClO_4$ was analysed using B3LYP/6-311+G(d,p) method due to the presence of excess H^+ ions (pH = 2) during adsorption process. Figure 6.10 shows the optimized structure of $[C_{16}MIm]^+[HClO_4]$. The C2H···O bond distance in $[C_{16}MIm]^+[HClO_4]$ (2.183 Å) was higher than $[C_{16}MIm]^+[ClO_4]^-$ (2.007 Å). The binding energy for $[C_{16}MIm]^+[Si(OH)_3O]^-$ (409.8 kJ/mol) and $[C_{16}MIm]^+[ClO_4]^-$ (337.3 kJ/mol) suggest imidazolium cation-silicate interaction is much stronger than the imidazolium cation-perchlorate interaction. Hence, on thermal activation of the perchlorate adsorbed system, reversal of cation interaction from perchlorate to silicate is feasible with the elimination of $HClO_4$. The peak decomposition temperature of $HClO_4$ was 173 ^{o}C from TG/DTG analysis (Figure 6.10(b)).

(a) $[C_{16}MIm]^+[HClO_4]$

(b)
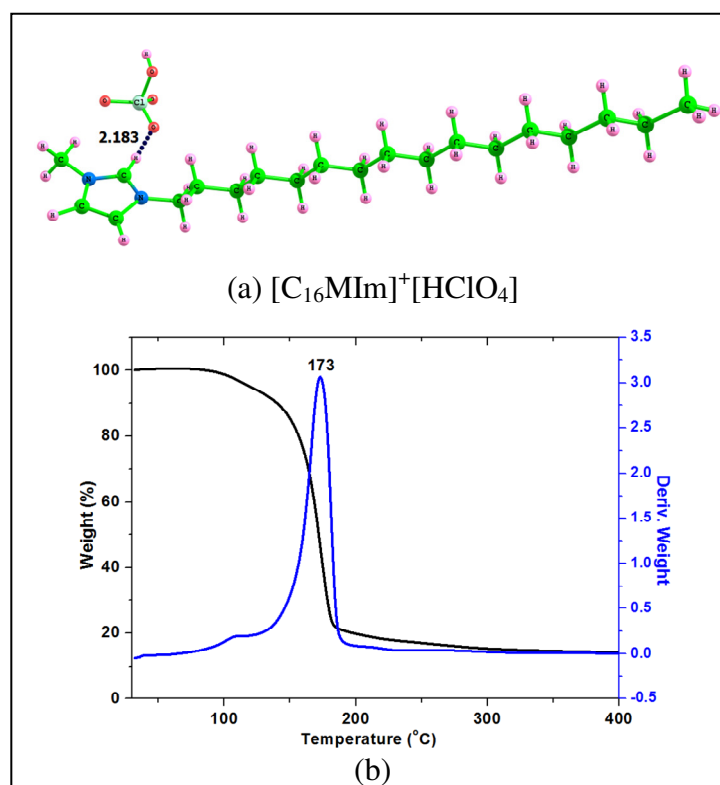
Figure 6.10 (a) Optimized structure of $[C_{16}MIm]^+[HClO_4]$ and TG/DTG curve of $HClO_4$ in air.

Thermal regeneration of perchlorate adsorbed clays were done at different temperatures from 170 to 190 ^{o}C (Table 6.2). The initial $C_{16}MIm/MMT$ perchlorate adsorption of 15.6 mg/g is taken as 100 % (Cycle-I) and it is compared with perchlorate adsorption after regeneration at different temperatures (Cycle-II). Maximum

regenerability of 95 % was achieved at 175 ^{o}C. This confirms the regeneration mechanism proposed using computational studies, where the H^{+} ions accelerated the elimination of HClO$_4$ by weakening the imidazolium cation-perchlorate bonding. Above 175 ^{o}C regeneration capacity decreased due to initiation of alkyl chain degradation of intercalated imidazolium cation.

Table 6.2 Regeneration of modified clays at different temperatures.

Temp. (^{o}C)	Regeneration (adsorption capacity in %)	
	Cycle-I	Cycle-II
170	100	87
175	100	95
180	100	82
190	100	72

4. Conclusions

1-alkyl-3-methylimidazolium modified clays were used for perchlorate adsorption from water. C$_{16}$MIm/MMT with maximum d-spacing showed highest adsorption and the conformational changes associated with adsorption were studied using Raman spectroscopy. Experimental data fitted with different adsorption isotherms and kinetic models revealed Freundlich adsorption and pseudo second order kinetics for the adsorption process. On thermal activation 95 % regeneration of clay was observed at 175 ^{o}C and regeneration mechanism involving perchloric acid removal was proposed based on DFT studies. The organoclay prepared represents a potential adsorbent for perchlorate with advantage of very low contact time and regenerability of the system.

PVDF- IL modified clay nanocomposite
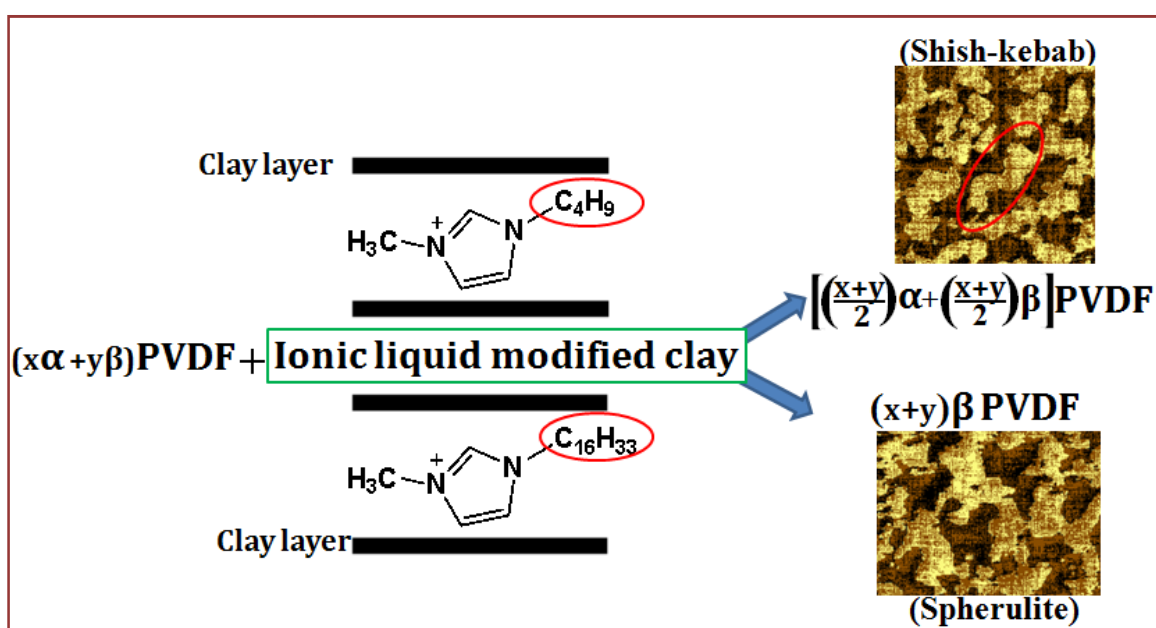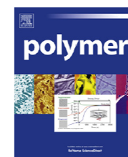
PVDF-ionic liquid modified clay nanocomposites: Phase changes and shish-kebab structure

Eapen Thomas, C. Parvathy, Nisha Balachandran, S. Bhuvaneswari, K.P. Vijayalakshmi[*], Benny K. George

Analytical and Spectroscopy Division, Analytical, Spectroscopy and Ceramics Group, Propellants, Polymers, Chemicals and Materials Entity, Vikram Sarabhai Space Centre, Thiruvananthapuram 695022, India

Abstract

Crystalline behaviour of PVDF nanocomposite with 1-alkyl-3-methylimidazolium modified montmorillonite clay was analyzed. The phase change from α to β increased with alkyl chain length of the organic modifier in the filler, 1-alkyl-3-methylimidazolium clay, and maximum conversion (99 %) was observed for PVDF-1-hexadecyl-3-methylimidazolium modified clay composite with 2 % loading. The phase conversion was evident from X-ray diffraction, DSC analysis and improved electrical properties. AFM analysis of PVDF-1-butyl-3-methylimidazolium montmorillonite clay composite (PVDF-C4) showed a shish-kebab structure while pristine PVDF and all other composites showed spherulite structures. Computational studies revealed that the extended chain α-phase forms the 'shish', the back bone and folded chain β-phase forms the 'kebab'. This was further supported by the superior mechanical properties for PVDF-C4 composite. Present work shows that introducing ionic liquid modified MMT-clay within the PVDF matrix enables nucleation of electroactive β phase and the presence of equal content of α to β can leads to the formation of self reinforced shish-kebab structures in PVDF.

7.1 Introduction

Poly(vinylidene fluoride) (PVDF) is a semi-crystalline polymer known for its electrical properties [Kawai 1969; da-Silva *et al*. 2014; Wang *et al*. 2009]. Among the polymorphs of PVDF *viz*., α-phase (TGTG' conformation), β-phase (TTT), γ-phase (T3GT3G′) and δ-phase (two TGTG' chains parallel), PVDF exists mainly in the stable non-polar α-phase along with polar β-phase (Figure 7.1) [Bohlen and Bolton 2014; Lovinger 1981]. β-phase is responsible for electrical properties and finds wide application in polymer sensors, actuators, etc., [Zhu *et al*. 2012; Lee *et al*. 2004; Khanna *et al*. 2004; Martins *et al*. 2012]. Several methodologies were adopted to improve the β-phase in PVDF such as melt crystallization under high pressure from solution [Rinaldo and Borges 2008], fast quenching from the melt [Ke *et al*. 2014], uniaxial or biaxial stretching of PVDF film [Sajkiewicz *et al*. 1999; Li *et al*. 2014; Gebrekrstos *et al*. 2016; Satyanarayana and Bolton 2012], addition of nanofillers [Byelov *et al*. 2008; Huo *et al*. 2004; Patil *et al*. 2010; Fillery *et al*. 2012] etc.
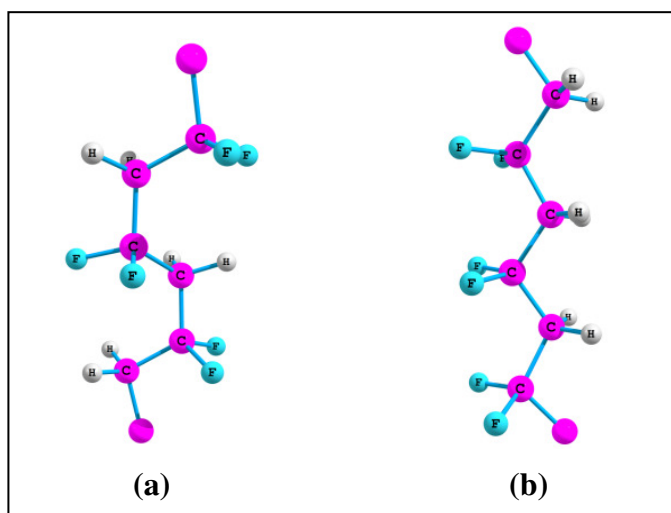
Figure 7.1 (a) α- phase and (b) β-phase with 3 repeating units in PVDF. The end atoms represent the head and tail atoms.

The most convenient and vast studied method to improve the β-phase is the nanofiller addition since it acts as nucleation sites and thus influencing crystallization kinetics and final morphology of the polymer. Nanofillers with high aspect ratio are beneficial for large electric break down field and permittivity [Fillery *et al*. 2012]. The combined effects of addition of particles and the shear have been suggested to yield an increase in the number of active nuclei, increasing crystallization rates higher than their individual contribution [Byelov *et al*. 2008; Huo *et al*. 2004]. Nanofillers with stronger chain-particle interaction and retarding the relaxation of extended chains are known to form "shish-kebab" structure with molecular orientation composed of an extended chain crystal called 'shish' and folded chain crystal called 'kebab' [Patil *et al*. 2010]. Shish-kebab structures are important as it shows improved mechanical property and thermal stability.

Various PVDF nanocomposites were studied using $BaTiO_3$ [Dang *et al*. 2010; Hao *et al*. 2015], TiO_2 [Li *et al*. 2009] silver nanoparticles [Manna *et al*. 2006 ; Audoit *et al*. 2015] copper oxide nanoparticles [Dutta *et al*. 2015], $CoFe_2O_4$ nanoparticles [Martins *et al*. 2012], carbon nanotubes [Sharma *et al*. 2015; Kim *et al*. 2009; Mandal and Nandi 2011; Yu *et al*. 2014, Zhao *et al*. 2009], graphene or graphene oxide [Layek *et al*. 2010; Achaby *et al*. 2012; Maity *et al*. 2015], ionic liquids [Wang *et al*. 2012; Xing *et al*. 2013; Okada *et al*. 2015; Mejri *et al*. 2015], clay and organically modified clays, [Wang *et al*. 2015; Priya *et al*. 2002; Dillon *et al*. 2006; Buckley *et al*. 2006; Patro *et al*. 2008] etc. Organically modified clays were preferred over pristine clay as fillers due to its better dispersion with polymers. The trend of PVDF to crystallize in the

β-phase is higher in organically modified clays [Patro *et al*. 2008], however few reports indicate that electrically active γ-phase also can be nucleated in the presence of organoclays [Martins *et al*. 2014; Ince-Gunduz *et al*. 2010; Lopes *et al*. 2011]. It was suggested that the matching of crystal lattice of the clay with that of the β-phase of PVDF is probably responsible for the formation and stabilization of the β-phase.

In this work, C_nMIm/MMT was used for PVDF-clay nanocomposite preparation. The effect of alkyl chain length of IL cation on the crystallization behaviour and orientation of PVDF structure was investigated. Xing *et al*. [2013] used ionic liquid, 1-butyl-3-methylimidazolium tetrafluoroborate for PVDF modification and more of γ-phase was observed. The colloidal crystallization of PVDF (46 % α-phase and 54 % amorphous phase) in presence of ionic liquid, 1-ethyl-3-methylimidazolium nitrate by Okada *et al*. [2015] resulted in partial conversion to β-phase (32 %). Mejri *et al*. [2015] reported the effect of ionic liquid anion and cation on the properties of PVDF/ionic liquid blends and observed that the average size of the spherulites depend on both the anion and cation (spherulite size increases with chain length of cation for a specific anion). Lopes *et al*. [2013] reported the nucleating effect of MMT on the crystallization of PVDF, incorporation of MMT fillers resulted in increased number of spherulites with decreased spherulite size. All reported PVDF-clay composites describe crystallization into spherulite morphology [Sencadas *et al*. 2011; Xing *et al*. 2013; Lopes *et al*. 2013].

7.2 Experimental section

7.2.1 Materials

PVDF (CAS No. 24937-79-9, product No.44080) from Alfa Aesar and HPLC grade N,N'-Dimethylacetamide (DMAc) from Spectrochem were used for the preparation of casting solution. Distilled water was used in coagulation bath as non solvent.

7.2.2 Nanocomposite preparation

PVDF-clay nanocomposite films were prepared by phase inversion method using MMT-Na^+, C_4MIm/MMT, C_6MIm/MMT, C_{10}MIm/MMT and C_{16}MIm/MMT. PVDF powder was dried at 100 °C for 2 hour prior to processing. Clay (1, 2, 3 and 5 wt % w.r.t PVDF) were dispersed in 50 mL DMAc by bath sonication (10 min.) and the clay dispersions were maintained at 50 °C using a water bath. 5 g PVDF powder was

added to the clay dispersion, the mixture was stirred for 30 min. and the solution was kept at room temperature for 24 hours. PVDF–clay nanocomposite films were casted on a glass plate using doctor blade (set at 30 rotations for films of ~100 micron thickness) and the casted films on glass plate was immersed in water (T=25 ^{o}C). Selection of coagulation bath (water) temperature was based on report by Buonomenna *et al*. [2007]. Films peeled off from the glass plates were washed thoroughly with water to remove any solvent traces present and dried at 100 ^{o}C for 2 hour in an air oven. Table 7.1 shows the list of PVDF-clay composites.

Table 7.1 List of clays and PVDF-clay composites.

Clay	PVDF-clay composite
MMT-Na$^+$	PVDF-MMT
C$_4$MIm/MMT	PVDF-C4
C$_6$MIm/MMT	PVDF-C6
C$_{10}$MIm/MMT	PVDF-C10
C$_{16}$MIm/MMT	PVDF-C16

7.2.3 Instrumental

PVDF films were characterized using Perkin Elmer Spectrum GX FTIR spectrometer in ATR mode in the wavelength region 4000-550 cm^{-1} with a spectral resolution of 4 cm^{-1}. For systems containing α and β–phases, the relative fraction of the β-phase, F(β), was calculated from FTIR spectra by measuring the absorbance at 763 cm^{-1} (CF$_2$ bending and skeletal bending, A$_α$) and 840 cm^{-1} (CH$_2$ rocking mode, A$_β$) respectively using Eqn.7.1 [Salimi and Yousefi 2004].

$$F_{(\beta)} = \frac{A_\beta}{(\frac{k_\beta}{k_\alpha}) A_\alpha + A_\beta} \quad ...(7.1)$$

where, A$_α$ and A$_β$ are the absorbance of the peaks corresponding to α and β respectively in the FTIR spectrum. The absorption coefficients of α-phase (k$_α$) and β-phase (k$_β$) were 6.1 x 10^4 cm^2/mol and 7.7 x 10^4 cm^2/mol respectively.

XRD studies were carried out using Bruker D8 Discover diffractometer with 2θ ranges between 10-30°. Thermal stability of PVDF-clay nanocomposite films were studied using TA Instruments SDT Q600 TGA from room temperature to 600 ^{o}C at a heating rate of 10 ^{o}C/min. in nitrogen atmosphere. Percentage crystallinity of PVDF in the nanocomposite films were determined using TA Q20 Differential Scanning Calorimeter (DSC) by heating at a rate of 5 °C/min. from room temperature to 200 °C

in nitrogen atmosphere and followed by cooling at the same rate to obtain the crystallization peak. Percentage crystallinity, X_c (%) of PVDF was calculated from its enthalpy of crystallization (ΔH_c) using Eqn. 7.2.

$$X_{(c)}(\%) = \frac{\Delta H_c}{\Delta H_p} \times 100 \quad \ldots (7.2)$$

where, ΔH_p = 104.7 J/g, heat of fusion for 100 % crystalline PVDF [Thakur *et al*. 2011].

Morphology was studied using AFM in contact mode using Agilent 5500 scanning probe microscope. FESEM was performed using a Carl Zeiss, Supra 55 model field emission scanning electron microscope with an acceleration voltage of 15 kV to evaluate the morphology and microstructure. Mechanical properties of PVDF-modified clay composites were measured using UTM INSTRON 5569 in tensile mode with cross head speed of 50 mm/min. and gauge length of 80 mm. At least 3 samples of each type of films were tested as per ASTM D-882. Capacitance of the films were measured using TEGAM 3550 LCR meter at temperature of 23 ^{o}C ± 2 ^{o}C and relative humidity of 60 % ± 5 % at 1 KHz frequency using ASTM D-257 method.

The activation energy (E_a) for thermal decomposition of PVDF and PVDF-clay nanocomposites were studied using Coats-Redfern method. First order reaction and random nucleation (F1 function) is generally used for thermal degradation kinetic study of nanocomposite films. The Coats-Redfern for F1 function is given as,

$$\ln \frac{-\ln(1-\alpha)}{T^2} = \ln \frac{AR}{bE_a} - \frac{E_a}{RT} \quad \ldots (7.3)$$

where, E_a is the activation energy for decomposition, A is the pre-exponential factor, R is the universal gas constant, b is the heating rate (10 ^{o}C/min.), α is the degree of conversion and T is the maximum decomposition temperature (K) corresponding to each α. The plot of $\ln \frac{-\ln(1-\alpha)}{T^2}$ versus 1/T, result in a linear plot whose slope gives the value of activation energy.

7.2.4 Computational studies

PVDF was constructed using 'build polymer' tool in Materials Studio 4.0 (Accelrys Inc.) software with single chain of PVDF in α-phase or β-phase [Accelrys 2006; Wang *et al*. 2010]. Amorphous cell calculation was done using the polymer

consistent force field (PCFF), Ewald electrostatic summation with accuracy = 0.0001 kcal/mol and temperature = 298 K with 20 monomer units.

7.3 Results and discussion

7.3.1 Phase changes

Organically modified clays facilitate the formation of β-phase in PVDF composites. In this study highly stable imidazolium cations were used as clay modifier and the phase transformation with increasing alkyl chain length was quantified using FTIR spectroscopy. Figure 7.2 shows the FTIR spectra of pristine PVDF, PVDF-C16 and C_{16}MIm/MMT in the spectral range of 1800 to 600 cm^{-1}. The characteristic peaks of the α-phase occur at 763, 974 and 1181 cm^{-1}. In β-phase (TTT) and γ-phase (T3GT3G'), due to the similar polymer chain conformation the absorption bands appear at similar wave numbers [Boccaccio et al. 2002]. The β-phase is associated with absorptions at 840 and 1275 cm^{-1}. The quantification of γ-phase has been more difficult, as exclusive FTIR bands (776, 833 and 1234 cm^{-1}) corresponding to the γ-phase appear as shoulders [Martins et al. 2014].
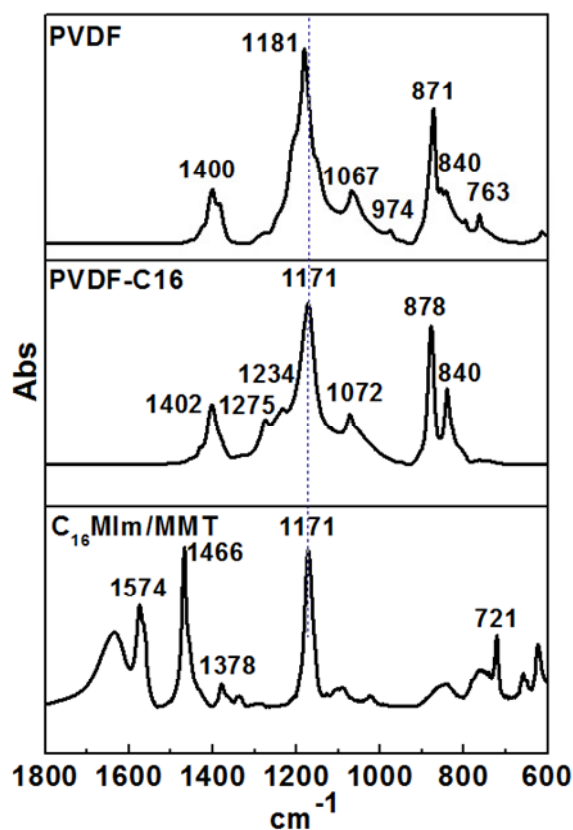
Figure 7.2 FTIR spectra of pristine PVDF, PVDF-C16 and C_{16}MIm/MMT.

In C_{16}MIm/MMT, the characteristic imidazolium ring absorption peak is at 1171 cm^{-1}. The peak at 1181 cm^{-1} corresponding to CF_2-CH_2 stretching vibration in pristine PVDF was shifted to 1171 cm^{-1} in PVDF-C16, suggesting the specific interaction of PVDF chains with the imidazolium ring in the cation. CF_2-CH_2 bending vibration at 871 cm^{-1} in PVDF was shifted to 878 cm^{-1} in PVDF-C16. These results suggest that the β-phase formation was driven through the coulombic interaction between the imidazolium cations in the clay interface and the negatively polarized CF_2 groups in PVDF.

In PVDF-modified clay composites, the relative fraction of β-phase was calculated from FTIR absorption spectra using Eqn.1 assuming that the crystalline phase content of the polymer is either in the α or β-phase, with no or small traces of γ-phase. The variation of β-phase in PVDF with MMT-Na$^+$ and C_nMIm/MMT were represented graphically in Figure 7.3. The relative fraction of β-phase in pristine PVDF (0.43) was increased to 0.99 in PVDF-C16. PVDF-MMT showed a relative β-phase of 0.57 and PVDF-C4 showed equal proportion of both phases (α=0.49 and β=0.51). Due to the high surface to volume ratio of nanofillers, the interfacial interactions between the nanofiller and the polymer matrix increases in general. Higher conversion to β-phase in PVDF-C16 is attributed to the maximum d-spacing of C_{16}MIm/MMT (18.55 Å) which enhance the interaction of PVDF with imidazolium cation. The phase conversion was constant above 2 % filler, IL modified clay and 2 % IL modified clay was used for PVDF- clay composite preparation in this study.
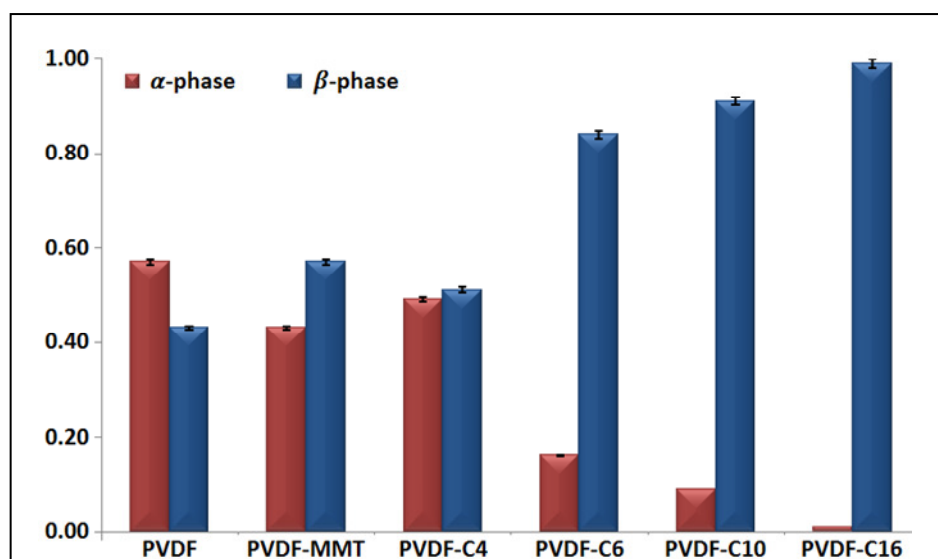
Figure 7.3 Variations of α and β-phase content in PVDF with the addition of MMT and C_nMIm/MMT. Error bars are shown for the selected chart series with 1 % value.
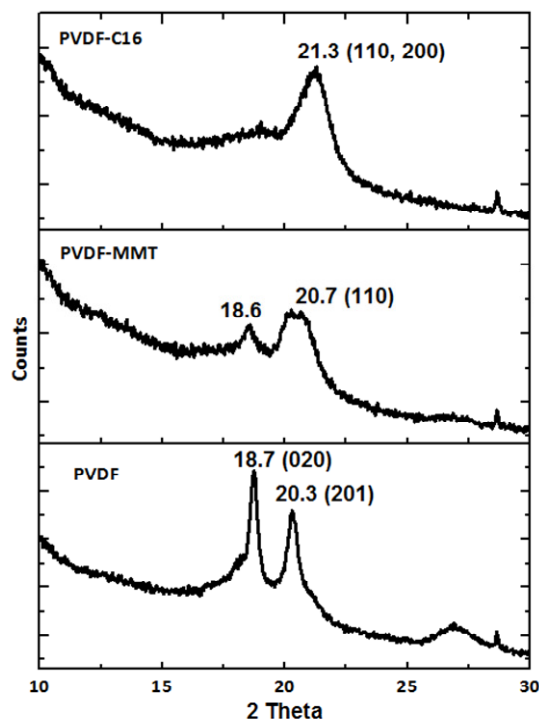
Figure 7.4 XRD pattern of PVDF, PVDF-MMT and PVDF-C16.

The phase change was further studied using XRD and the XRD spectra of PVDF, PVDF-MMT and PVDF-C16 are given in Figure 7.4. For PVDF films, the peaks corresponding to the 2θ values of 18.1, 18.7 and 20.3^o are assigned to the diffraction in (100), (020), and (201) planes, belong to α-phase. On addition of MMT-Na$^+$ clay, intensity of peak corresponding to α-phase decreases and a merged broad peak is observed at $2\theta = 20.7^o$, corresponding to (110) reflection of β-phase. In PVDF-C16, the broad peak at 21.3^o refers to the sum of the diffraction in (110) and (200) planes characteristic of β-phase.
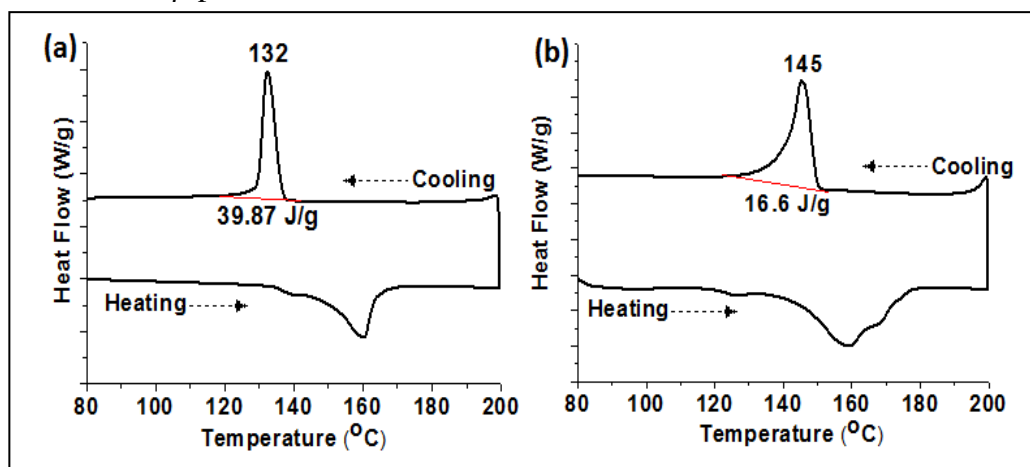
Figure 7.5 DSC heating and cooling curve for (a) PVDF and (b) PVDF-C16.

The enthalpy change associated with α to β-phase change was estimated using DSC analysis. DSC heating and cooling curve of PVDF and PVDF-C16 are shown in Figure 7.5. The enthalpy changes for crystallization were calculated using eqn. 7.2. Addition of modified clay in PVDF results in lowering of enthalpy of crystallization and percentage crystallinity (Table 7.2). An increase in crystallization temperature was also observed on addition of modified clay filler in PVDF (Table 7.2), which is also an indication for the formation of β-phase as reported by Patro *et al.* [2008].

Table 7.2 Crystallization temperature (T_c), enthalpy of crystallization (ΔH_c) and percentage crystallinity (X_c using eqn.7.2) of PVDF clay nanocomposite films.

Sl. No.	Film	T_c (^{o}C)	ΔH_c (J/g)	X_c (%)
1	PVDF	132	39.87	38.1
2	PVDF-MMT	137	32.99	31.5
3	PVDF-C4	141	30.53	29.2
4	PVDF-C6	143	29.69	28.4
5	PVDF-C10	144	28.12	26.9
6	PVDF-C16	145	16.60	15.8

7.3.2 Electrical properties

In PVDF, β-phase having an all trans conformation as shown in Figure 7.1 is responsible for its electrical properties. The electrical properties are likely to increase with the β-phase content. Figure 7.6 shows the variation of capacitance with increasing β content in PVDF films. The capacitance of PVDF with relative β fraction of 0.43 was 45.1 pF and showed an increase of 36.4 % (61.5 pF) in PVDF-C16 (β fraction = 0.99). A linear plot with $R^2 = 0.95$ suggests the dependence of electrical properties on β-phase content.
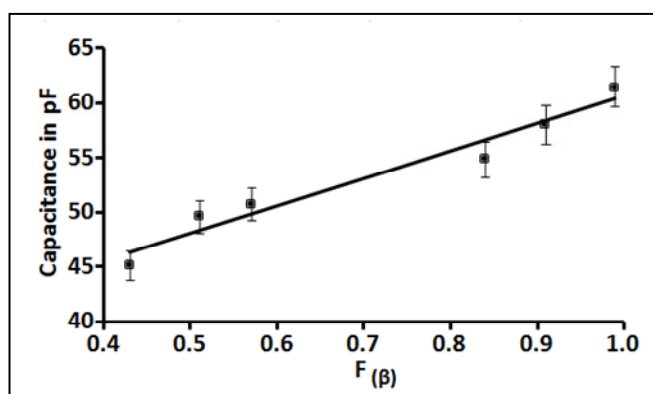
Figure 7.6 Plot of capacitance of PVDF-clay nanocomposite at 1 KHz with β-phase content. Error bars are shown for the selected chart series with 3 % value.
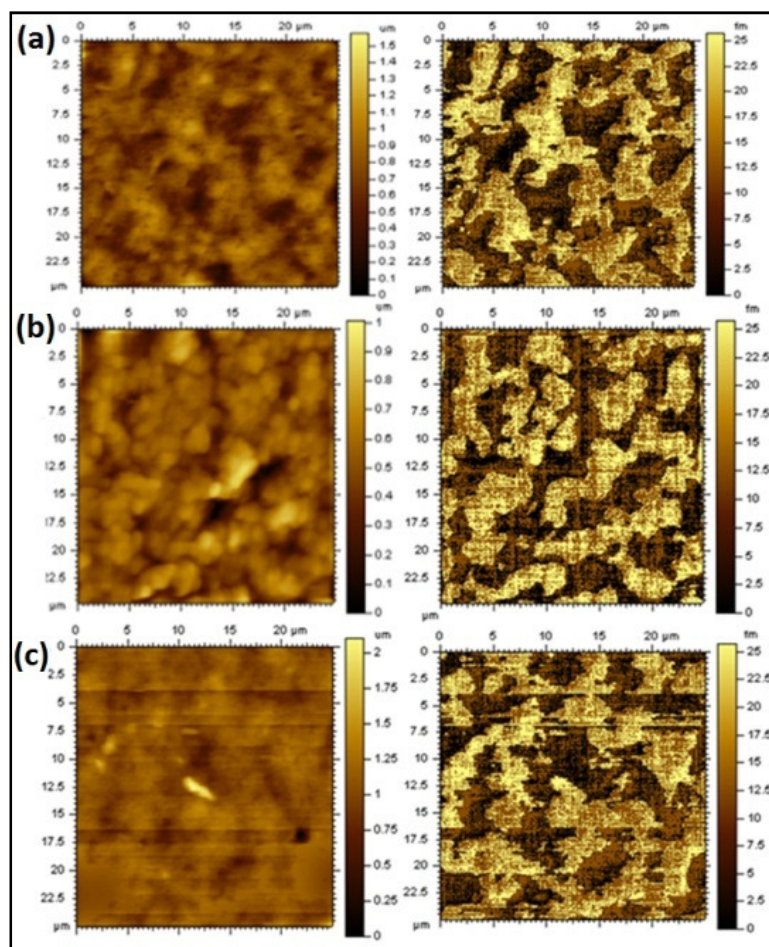
Figure 7.7 Topography images of (a) pristine PVDF, (b) PVDF-C4 and (c) PVDF-C16 (left) with motifs (right).

7.3.3 Molecular orientations

The change in molecular orientation was studied using AFM technique (Figure 7.7). The texture aspect ratio (Str) of the surface was calculated from the image to find the structural orientation. AFM images of pristine PVDF, PVDF-C6, PVDF-C10 and β-phase rich PVDF-C16 films possessed spherulite morphology with isotropic nature (Str = 0.77) and are devoid of oriented molecular structure. The spherulite morphology of PVDF was transformed to shish-kebab in PVDF-C4 due to stress induced during crystallinity change (Str = 0.58). Stress induced in PVDF-C4 is evident from the equal proportion of α-phase (0.49) and β-phase (0.51) estimated from FTIR analysis.

FESEM images of pristine PVDF and PVDF/clay nanocomposites are shown in Figure 7.8. FESEM images show a uniform distribution of C_nMIm/MMT within the polymer matrix with porous microstructure. PVDF-C4 (Figure 7.8c) showed a difference in microstructure complimenting the formation of shish-kebab as revealed in

the AFM images shown in Figure 7.7. The EDX spectra of PVDF-C16 (Figure 7.8f) confirms the presence of C, F (from PVDF) and Si (from MMT) which serves as an evidence for the exfoliation of clay in PVDF. The dispersion of C_{16}MIm/MMT in PVDF-C16 was confirmed using EDX analysis at various sites.
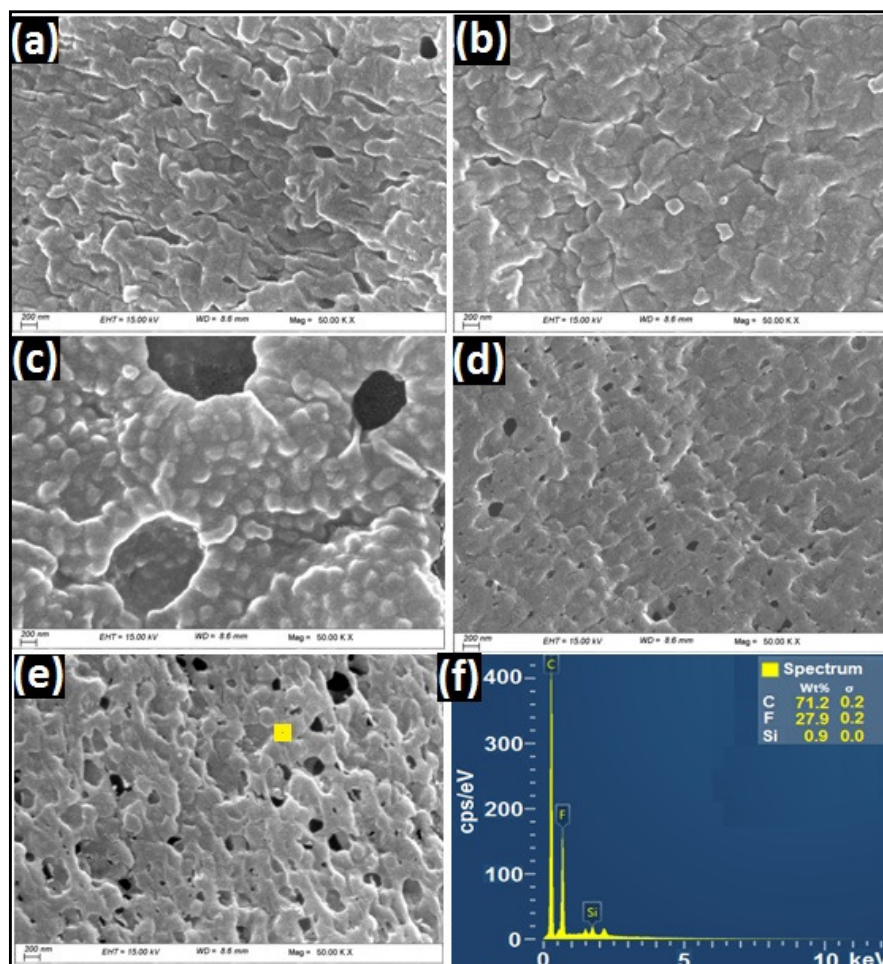
Figure 7.8 FESEM images of (a) pristine PVDF, (b) PVDF-MMT, (c) PVDF-C4, (d) PVDF-C6 and (e) PVDF-C16 at scale bar = 200 nm, and 50 Kx magnification, (f) EDX spectra of PVDF-C16.

Nagasawa *et al.* [1974] used polyethylene to study the mechanism of shish-kebab formation and observed that gradual and undisturbed cooling of polyethylene solution resulted in single crystals while gradual cooling with ultrasonication produced shish-kebab structures. The methodology followed in this work was also similar to the reported studies with ultrasonication and undisturbed cooling. PVDF-clay composite was prepared by bath sonication for 10 min. at 50 ^{o}C and kept at room temperature for 24 hours before casting the film. In PVDF-clay composites, unlike the reported mechanism, the interplay of phase changes and molecular orientation was observed as

evidenced from the AFM imaging. The ratio of two dominant phases in PVDF, α and β in the mixture has a great importance in the formation of its final morphology. The shish-kebab formation was further supported by computational studies and improved mechanical properties.

7.3.4 Computational studies

The polymer chain was constructed with 20 repeating units initially and observed a linear structure for α-phase and a bent structure for β-phase as shown in Figure 7.9. As the number of repeating VDF units in β-phase was increased, with 160 repeating units the folded chain is converted to a circle, (Figure 7.9c) whereas α-phase remained as linear molecule under similar condition.

(a)   **(b)**   **(c)**   **(d)**
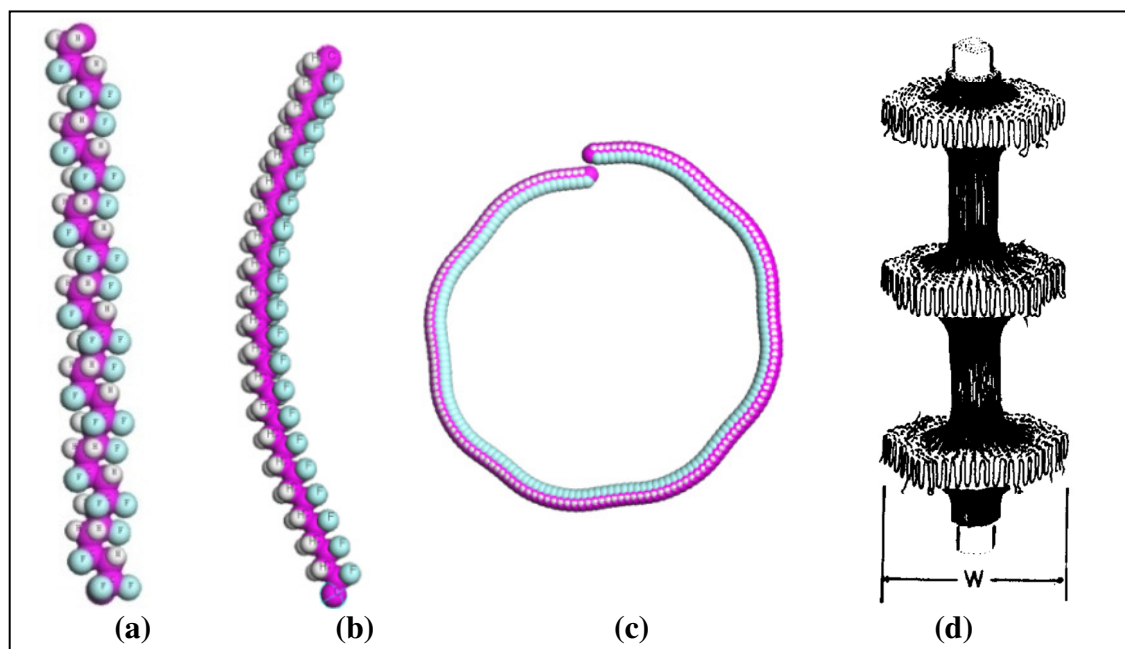
Figure 7.9 Structure of PVDF (a) α-phase with 20 repeating units (b) β-phase containing 20 repeating units, (c) β-phase containing 160 repeating units and (d) Penning's model for shish-kebab structure.

Equal ratio of α-chains and β-chains results in a symmetrical shish-kebab structure as explained by Penning's model. Alternatively, extended chain 'α-phase' forms the shish, the back bone and folded chain 'β-phase' forms the kebab. Among the studied PVDF-clay composites, only PVDF-C4 falls in this category and shows shish-kebab structure as evidenced in the AFM analysis. PVDF containing 20 monomer units of both α-phase and β-phase were used to construct the amorphous cell (Figure 7.10). The α-phase was lower in energy by 9.06 kJ/mol than β-phase.
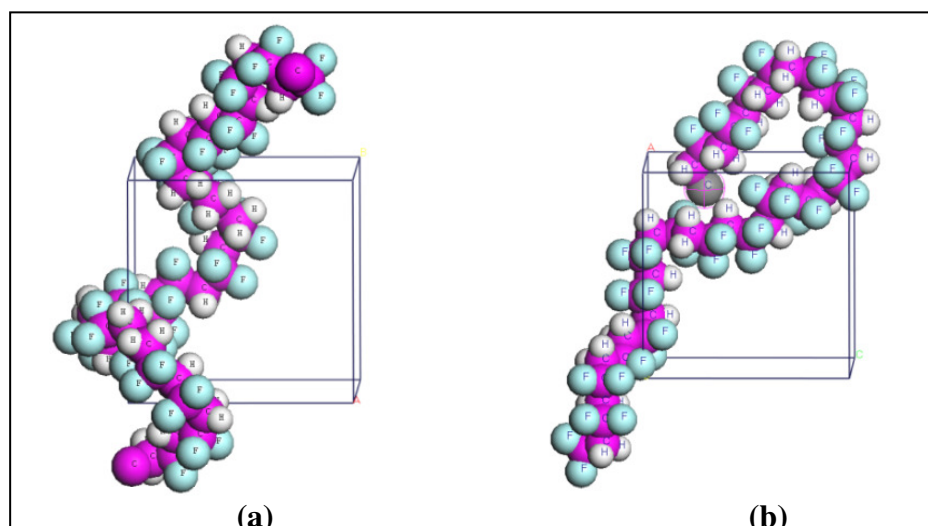
Figure 7.10 Optimized Structure of PVDF using amorphous cell with dimensions (Å) 12.9 x 12.9 x 12.9 (a) α-phase and (b) β-phase containing 20 monomer units.

7.3.5 Mechanical properties

The shish-kebab formation in polymers leads to improved mechanical properties, especially elongation as evident from the Penning's model. Mechanical properties of pristine PVDF and PVDF-clay composites are listed in Table 7.3. PVDF-C4 showed 8 % improvement in tensile strength, 77 % improvement in elongation and 17 % improvement in modulus than pristine PVDF film. The toughness of the polymer calculated as area under the stress-strain curve, also showed 117 % improvement for PVDF-C4 than pristine PVDF. This clearly supports the shish-kebab formation in PVDF-C4 nanocomposites. PVDF-MMT, PVDF-C6, PVDF-C10 and PVDF-C16 showed an increase in modulus and decrease in elongation, tensile strength and toughness as similar to reported PVDF-functionalized multiwalled carbon nanotube composite by Mandal *et al*. [2011].

Table 7.3 Mechanical properties of pristine PVDF film and PVDF-clay composites.

Film	Tensile Strength (MPa)	Elongation (%)	Modulus (MPa)	Toughness (MPa)
PVDF	2.21 ± 0.02	5.6 ± 0.6	108 ± 3	9.2
PVDF-MMT	1.66 ± 0.04	4.4 ± 0.5	109 ± 5	5.4
PVDF-C4	**2.40 ± 0.06**	**9.9 ± 0.7**	**126 ± 6**	**20.1**
PVDF-C6	1.50 ± 0.10	4.7 ± 0.5	113 ± 6	5.9
PVDF-C10	1.62 ± 0.10	5.1 ± 0.6	113 ± 5	6.1
PVDF-C16	1.72 ± 0.10	5.2 ± 0.6	115 ± 5	7.2

7.3.6 Thermal properties

Thermal stability of PVDF decreased on addition of modified clay filler, an evidence for the phase conversion. The interaction of CH_2-CF_2 with the imidazolium ring leads to lower thermal stability (10 to 23 ^{o}C). Figure 7.11 shows the TG/DTG curves of pristine PVDF, PVDF-C4 and PVDF-C16. The peak decomposition temperature (T_s) for pristine PVDF was 480 ^{o}C and PVDF-C16 showed the lowest thermal stability (457 ^{o}C) among the studied PVDF-clay nanocomposites (Table 7.4). The results agree with the lower degradation temperatures of PVDF-nanocomposites reported by Manna et al. [2006].
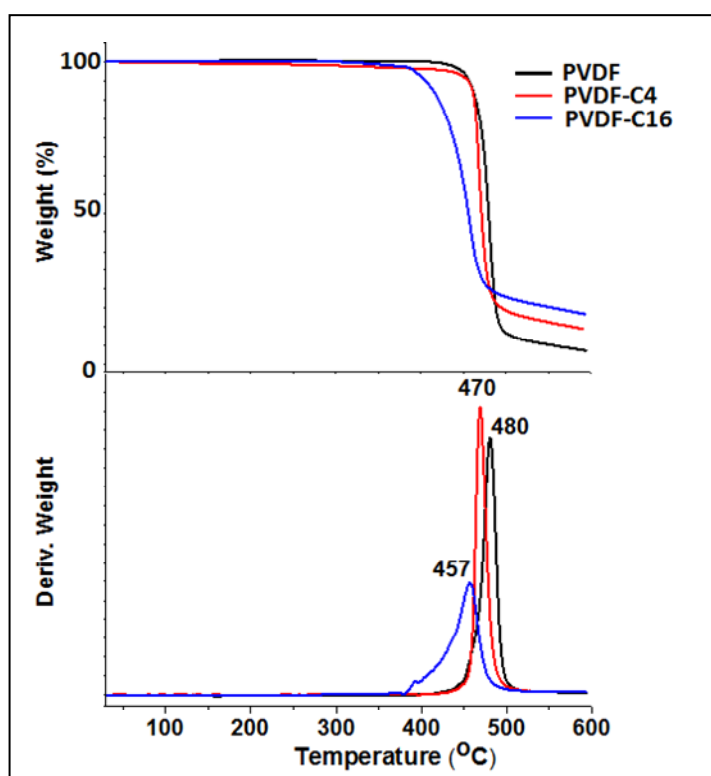
Figure 7.11 TG and DTG curves of pristine PVDF, PVDF-C4 and PVDF-C16.

PVDF-C4 with T_s of 470 ^{o}C showed higher thermal stability than PVDF-MMT (T_s = 467 ^{o}C) and all other nanocomposites. The higher stability of PVDF-C4 is due to its oriented and self reinforced structural features. Dutta et al. [2015] reported an E_a of 545.6 kJ/mol for pristine PVDF and a comparable value of 524.2 kJ/mol is obtained in the present work. Coats-Redfern plot for pristine PVDF is shown in Table 7.4. Generally the activation energy of thermal decomposition of polymer composites decreases with addition of fillers [Kar et al. 2015]. The same trend is followed here with exception to PVDF-C4 (Table 7.5) due to self reinforced shish-kebab structure.

Table 7.4 Activation energy of PVDF by Coats-Redfern method.

α	T (^{o}C)	T (K)	1000/T	$\ln[\{-\ln(1-\alpha)\}/T^2]$
0.1	461.83	734.83	1.3609	-15.4496
0.2	469.32	742.32	1.3471	-14.7195
0.3	473.59	746.59	1.3394	-14.2620
0.4	476.54	749.54	1.3341	-13.9106
0.5	478.9	751.90	1.3300	-13.6117
0.6	481.04	754.04	1.3262	-13.3383
0.7	483.21	756.21	1.3224	-13.0710
0.8	485.72	758.72	1.3180	-12.7874
0.9	489.35	762.35	1.3117	-12.4388

y = -63.05x + 70.26
R² = 0.996

E_a (kJ/mol) = -slope x R	524.2 kJ/mol

Table 7.5 Peak decomposition temperature (T_s) and E_a for thermal decomposition of pristine PVDF and PVDF-modified clay composites.

Film	Ts (^{o}C)	E_a (kJ/mol)
PVDF	480	524.2
PVDF-MMT	467	382.8
PVDF-C4	470	711.9
PVDF-C6	458	283.3
PVDF-C10	458	264.1
PVDF-C16	457	232.0

7.4 Conclusions

The microstructural changes induced in PVDF by ionic liquid modified clay was investigated in the present study. Enhancement of electro active β-phase crystallization was observed with increased alkyl chain length of the organic modifier, 1-alkyl-3-methylimidazolium cations in the nanoclay. The PVDF-C4 composite with a self

reinforced shish-kebab structure showed superior mechanical properties and retained the thermal stability of pristine PVDF. This work reports a way to prepare PVDF/organoclay composites with enhanced electrical and mechanical properties by adjusting the alkyl chain length of the ionic liquid which offers potential applications in the field of sensors, actuators and batteries.

Chapter 8

Summary and future perspectives

8.1 Summary

The main objectives and the outcomes of the thesis are shown below:

➢ Design of imidazolium based energetic ionic liquids using computational chemistry tools.

Thermochemistry of a variety of imidazolium based ILs were predicted accurately using quantum chemical computational studies. The computed heats of formation of all the EILs of 1-ethyl-3-methylimidazolium cation and tetrazolide derivatives, dicyanamide, triazolide, dinitrotriazine, and dinitramide as anions were higher than that of hydrazine. Considering ILs with a suitable oxidizer as a binary monopropellant, Isp of different EILs with varying concentration of HAN was computed. Among the 12 imidazolium based EILs studied, $[C_2MIm]^+[dtrz]^-$, $[C_2MIm]^+[dn]^-$ and $[C_2MIm]^+[NO_2Otz]^-$ provided the best energetic performance in combination with HAN proposing the title compounds as potential green substitute for hydrazine.

➢ Structural studies of ionic liquids using computational methods for organic modification of clay.

1-alkyl-3-methylimidazolium ILs were proposed as a replacement for alkyl ammonium salts in clay modification for high temperature applications. Screening of ILs for cation exchange with MMT-Na$^+$ was done based on computed parameters like HOMO-LUMO energy gap for stability studies, Mulliken charge analysis and MK charge analysis for charge contribution to electrostatic and hydrogen bonding interactions. The stability of $[C_nMIm]^+$ cations were assessed based on HOMO-LUMO energy gap (ΔE^*). ΔE^* shows drastic decrease in stability after $[C_4MIm]^+$ ($\Delta E^* = 6.7$ eV). This change in stability is attributed to shift in HOMO from imidazolium ring to alkyl chain after C4. Chain length of $[C_nMIm]^+$ in this study is limited to C_{16} for thermally stable IL modified organoclay ($\Delta E^* > 4$ eV). ΔE^* analysis illustrates higher stability for $[C_nMIm]^+[BF_4]^-$ (6.8 eV) than $[C_nMIm]^+[Cl]^-$ (4.1 eV). In $[C_nMIm]^+[BF_4]^-$, HOMO is diffused between BF_4^- and imidazolium ring and shifted to N2-alkyl group on increasing chain length beyond C14, where as HOMO is located on the Cl$^-$ anion irrespective of the N2-alkyl chain length in $[C_nMIm]^+[Cl]^-$. Compiling all results, $[C_4MIm]^+$, $[C_6MIm]^+$ and $[C_{16}MIm]^+$ based ILs were selected for experimental studies.

- Synthesis of ionic liquids and experimental validation of predicted properties.

  Ionic liquids selected for clay modification, $[C_6MIm]^+[Cl]^-$ and $[C_{16}MIm]^+[Cl]^-$ were synthesized with 95 % yield. The effect of anion on thermal stability of ILs were established using $[C_4MIm]^+[Cl]^-$ ($T_s = 284$ ^oC) and $[C_4MIm]^+[BF_4]^-$ ($T_s = 427$ ^oC), and conform to the computed parameters based on HOMO-LUMO energy gap. The decomposition products identified using pyrolysis GC-MS and transition states using DFT method established the higher reactivity of $[C_4MIm]^+[Cl]^-$ over $[C_4MIm]^+[BF_4]^-$ as predicted from the charge transfer analysis. The non-dependency of alkyl chain length on stability of ILs were confirmed by analysing $[C_4MIm]^+[Cl]^-$, $[C_6MIm]^+[Cl]^-$ and $[C_{16}MIm]^+[Cl]^-$. Modification of MMT-Na^+ with IL was achieved with the lowest processing time of 15 minutes using probe sonication method. The modification was confirmed using FTIR analysis, improved d-spacing in XRD, CHN analysis and TG analysis. The C_nMIm/MMT showed improved thermal stability than conventional alkyl ammonium modified clays. $C_{16}MIm$/MMT with d-spacing of 18.55 Å and $T_{1\%}$ of 266 ^oC is proposed as a replacement for Cloisite 25A with d-spacing of 18.65 Å and $T_{1\%}$ of 214 ^oC. Thermal degradation mechanism of ionic liquid modified clay was elucidated using DFT and experimentally rationalized using pyrolysis GC-MS and ^{13}C NMR experiments. For the first time, the predicted carbene mechanism was established by identifying 1-butyl-3-methylimidazol-2-ylidine using ^{13}C NMR spectroscopy. The experimental results were conforming to the theoretical studies.

- Application of ionic liquid modified clay in the removal of perchlorate ion from water.

  1-alkyl-3-methylimidazolium modified clays were used for perchlorate adsorption from water. $C_{16}MIm$/MMT showed highest adsorption of perchlorate ions (15.6 mg/g of clay) and the conformational changes associated with adsorption were studied using Raman spectroscopy. Experimental data fitted with different adsorption isotherms and kinetic models revealed Freundlich adsorption and pseudo second order kinetics for the adsorption process. On thermal activation 95 % regeneration of clay was observed at 175 ^oC and regeneration mechanism involving perchloric acid removal was proposed based on DFT studies. The organoclay prepared represents a potential adsorbent for perchlorate with advantage of very low contact time and regenerability of the system.

➤ Preparation and property evaluation of IL modified clay nanocomposites.

The microstructural changes induced in PVDF by ionic liquid modified clay was investigated. Enhancement of electro active β-phase crystallization was observed with increased alkyl chain length of the organic modifier, 1-alkyl-3-methylimidazolium cations in the nanoclay. The PVDF-C4 composite with a self reinforced shish-kebab structure showed superior mechanical properties and retained the thermal stability of pristine PVDF. This work reported a way to prepare PVDF/organoclay composites with enhanced electrical and mechanical properties by adjusting the alkyl chain length of the ionic liquid which offers potential applications in the field of sensors, actuators and batteries.

8.2 Future perspectives

The present investigations extend ample scope for further investigations and future developments, especially to realize ionic liquid based green propellant in space application. Synthesis and characterization of long chain ionic liquid $C_{16}MImCl$ provides, scope for their application as surfactant/soft template in polymerization reactions. The initial studies using $C_{16}MImCl$ as a soft template for copolymerization of aniline and pyrrole resulted in uniform spherical particles with particle size less than 40 nm. AFM images of copolymer of aniline and pyrrole (APC) with and without $C_{16}MImCl$ are shown in Figure 8.1. This opens a promising route for APC synthesis with improved property, especially for sensor application. The use of IL modified clays as thermally stable filler for preparation of different polymer composites are also appealing.

(a)   (b)
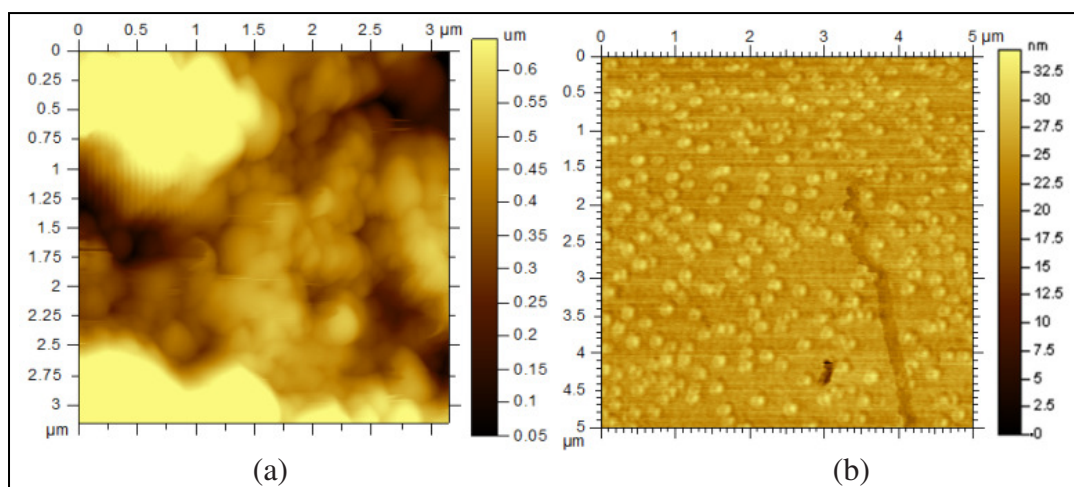
Figure 8.1 Topography images of (a) APC and (b) APC in presence of $[C_{16}MIm]^{+}[Cl]^{-}$.

References

Accelrys, Material Studio 4.0, Accelrys Software, Inc.: San Diego, **2006**.

Achaby, M. E.; Arrakhiz, F. Z.; Vaudreuil, S.; Essassi, E. M.; Qaiss, A. Piezoelectric β-polymorph formation and properties enhancement in graphene oxide – PVDF nanocomposite films, *Appl. Surf. Sci.* **2012**, 258, 7668−7677.

Ahmaruzzaman, M. Adsorption of phenolic compounds on low-cost adsorbents: A review, *Adv. Colloid Interface Sci.* **2008,** 143, 48-67.

Aihara, J. Reduced HOMO−LUMO gap as an index of kinetic stability for polycyclic aromatic hydrocarbons, *J. Phys. Chem. A* **1999**, 103, 7487−7495.

Aihara, J.; Oe, S.; Yoshida, M.; Osawa, E. Further test of the isolated pentagon rule: Thermodynamic and kinetic Stabilities of C_{84} fullerene isomers, *J. Comput. Chem.* **1996**,17, 1387-1394.

Aki, S. N. V. K.; Mellein, B. R.; Saurer, E. M.; Brennecke, J. F. High pressure phase behavior of carbon dioxide with imidazolium based ionic liquids, *J. Phys. Chem. B* **200**4, 108, 20355−20365.

Allen, L. C.; Karo, A. M. Basis functions for Ab initio calculations, *Rev. Modern Phys.***1960**, 32, 275-284.

Audoit, J.; Laffont, L.; Lonjon, A.; Dantras, E.; Lacabanne, C. Percolative silver nanoplates/PVDF nanocomposites: Bulk and surface electrical conduction, *Polymer* **2015,** 78, 104−110.

Awad, W. H.; Gilman, J. W.; Nyden, M.; Harris, R. H.;Sutto, T. E.; Callahan, J.; Trulove, P. C.; DeLong,H. C.; Fox, D. M. Thermal degradation studies of alkyl-imidazolium salts and their application in nanocomposites, *Thermochim. Acta* **2004**, 409, 3-11.

Bagherifam, S.; Komarneni, S.; Lakzian, A.; Fotovat, A.; Khorasani, R.; Huang, W.; Ma, J.; Hong, S.; Cannon, F. S.; Wang, Y. Highly selective removal of nitrate and perchlorate by organoclay, *Appl. Clay Sci.* **2014**, 95, 126–132.

Becke, A. D. Density functional thermochemistry. III. The role of exact exchange, *J. Chem. Phys.* **1993**, 98, 5648-5652.

Berg, S. P.; Rovey, J. L. Decomposition of monopropellant blends of hydroxylammonium nitrate and imidazole based ionic liquid fuels, *J. Propul. Power* **2013**, 29, 125–135.

Berthod, A.; Ruiz-Angel, M. J.; Carda-Broch, S. Ionic liquids in separation techniques, *J. Chromatogr. A* **2008**, 1184, 6–18.

Blesic, M.; Marques, M. H.; Plechkova, N. V.; Seddon, K. R.; Rebelo, L. P. N.; Lopes, A. Self-aggregation of ionic liquids: Micelle formation in aqueous solution, *Green Chemistry* **2007**, 9, 481-490.

Boccaccio, T.; Bottino, A.; Capannelli, G.; Piaggio, P. Characterization of PVDF membranes by vibrational spectroscopy, *Journal of Membrane Science* **2002**, 210, 315-329.

Bockris, J. O. M.; Reddy, A. K.; Modern electrochemistry, *Springer*, New York, **1970**.

Bohlen, M.; Bolton, K. Conformational studies of poly(vinylidene fluoride), poly(trifluoroethylene) and poly(vinylidene fluoride-co-trifluoroethylene) using density functional theory*, Phys. Chem. Chem. Phys*. **2014**, 16, 12929–12939.

Bonhôte, P.; Dias, A. P.; Papageorgiou, N.; Kalyanasundaram, K.; Gratzel, M. Hydrophobic, highly conductive ambient temperature molten salts, *Inorg. Chem*. **1996**, 35, 1168-1178.

Boon, J. A.; Levisky, J. A.; Pflug, J. L.; Wilkes, J. S. Friedel-Crafts reactions in ambient-temperature molten salts, *J. Org. Chem*. **1986**, 51, 480–483.

Born, M.; Oppenheimer, J. R. Zur quantentheorie der molekeln, *Ann. Phys*. **1927**, 84, 457-484.

Boys, S. F. Electronic wave functions. 1. A general method of calculation for the stationary states of any molecular systems, *Proc. Roy. Soc*. **1950**, 200, 542-554.

Boys, S. F.; Bernardi, F. The calculation of small molecular interactions by the differences of separate total energies. Some procedures with reduced errors, *Mol. Phys*. **1970**, 19, 553-566.

Bowen, J. P.; Allinger, N. L. Molecular mechanics: the art and science of parameterization, *Rev. Comp. Chem*. **1991**, 2, 81-97.

Boyd, D. B.; Lipkowitz, K. B. Molecular mechanics: The method and its underlying philosophy, *J. Chem. Educ*. **1982**, 59, 269-274.

Bradley, A. E.; Hardacre, C.; Holbrey, J. D.; Johnston, S.; McMath, S. E. J.; Nieuwenhuyzen, M. Small angle X-ray scattering studies of liquid crystalline 1-alkyl-3-methylimidazolium salts, *Chem. Mater*. **2002**, 14, 629-635.

Branco, L. C.; Rosa, J. N.; Ramos, J. J. M.; Afonso, C. A. M. Preparation and characterization of new room temperature ionic liquids, *Chem. Eur. J.* **2002**, 8, 3671-3677.

Buckley, J.; Cebe, P.; Cherdack, D.; Crawford, J.; Ince, B. S.; Jenkins, M.; Pan, J.; Reveley, M.; Washington, N.; Wolchover, N. Nanocomposites of poly(vinylidene fluoride) with organically modified silicate, *Polymer* **2006**, 47, 2411-2422.

Buonomenna, M. G.; Macchi, P.; Davoli, M.; Drioli, E. Poly(vinylidene fluoride) membranes by phase inversion: the role the casting and coagulation conditions play in their morphology, crystalline structure and properties, *Eur. Polym. J.* **2007**, 43, 1557–1572.

Buzzeo, M. C.; Evans, R. G.; Compton, R. G. Examination of the potential of ionic liquids for gas separations, *Sep. Sci. Technol.* **2005**, 40, 525–541.

Buzzeo, M. C.; Evans, R. G.; Compton, R. G. Non-haloaluminate room-temperature ionic liquids in electrochemistry-A review, *Chem. Phys. Chem.* **2004**, 5, 1106–1120.

Byelov, D.; Panine, P.; Remerie, K.; Biemond, E.; Alfonso, G. C.; de Jeu, W. H. Crystallization under shear in isotactic polypropylene containing nucleators, *Polymer* **2008**, 49, 3076–3083.

Cadars, S.; Guegan, R.; Garaga, M. N.; Bourrat, X.; Forestier, L. L.; Fayon, F.; Huynh, T. V.; Allier, T.; Nour, Z.; Massiot, D. *Chem. Mater.* **2012**, 24, 4376–4389.

Calderon, J. U.; Lennox, B.; Kamal, M. R.; Thermally stable phosphonium-montmorillonite organoclays, *Applied Clay Science* **2008**, 40, 90-98.

Chase Jr., M. W. NIST-JANAF Thermochemical Tables, *J. Phys. Chem. Ref. Data Monograph* **1998**, 9 (4), 1–1951.

Chase Jr., M. W.; Davies, C. A.; Downey Jr., J. R.; Frurip, D. J.; McDonald, R. A.; Syverud, A. N. JANAF Thermochemical tables, Third Edition, *J. Phys. Chem. Ref. Data* **1985**, 14(1), 1-1856.

Chiappe, C.; Pieraccini, D. Ionic liquids: solvent properties and organic reactivity, *J. Phys. Org. Chem.* **2005**, 18, 275-297.

Chitrakar, R.; Makita, Y.; Hirotsu, T.; Sonoda, A. Montmorillonite modified with hexadecylpyridinium chloride as highly efficient anion exchanger for perchlorate ion, *Chem. Eng. J.* **2012**, 191, 141–146.

Chun, S.; Dzyuba, S. V.; Bartsch, R. A. Influence of structural variation in room-temperature ionic liquids on the selectivity and efficiency of competitive alkali metal salt extraction by a crown ether, *Anal. Chem.* **2001**, 73, 3737-3741.

Coleman, D.; Gathergood, N. Biodegradation studies of ionic liquids, *Chem. Soc. Rev.* **2010**, 39, 600-637

Comelles, F.; Ribosa, I.; González, J. J.; Garcia, M. T. Micellization of sodium laurylethoxysulfate (SLES) and short chain imidazolium ionic liquids in aqueous solution, *Journal of Colloid and Interface Science* **2014**, 425, 44-51.

Cope, A. C.; Trumbull, E. R. Organic reactions.vol. 11, *John Wiley and Sons*, New York **1960**, 317–487.

Curtiss, L. A.; Redfern, P. C.; Raghavachari, K.; Rassolov V.; Pople, J. A. Gaussian-3 theory using reduced Moller-Plesset order, *J. Chem. Phys.* **1999**, 110, 4703–4709.

Dadi, A. P.; Schall, C. A.; Varanasi, S. Mitigation of cellulose recalcitrance to enzymatic hydrolysis by ionic liquid pretreatment, *Appl. Biochem. Biotechnol.* **2007**, 137, 407–421.

Dambach, E.; Heister, S.; Ismail, I.; Schneider, S.; Hawkins, T. An investigation into the hypergolicity of dicyanamide based ionic liquid fuels with common oxidizers, *U.S. Air Force Research Lab Rept.* **2008**.

Dang, Z.M.; Yao, S.H.; Yuan, J.K.; Bai, J. Tailored dielectric properties based on microstructure change in $BaTiO_3$-carbon nanotube/polyvinylidene fluoride three-phase nanocomposites, *J. Phys. Chem. C* **2010**, 114, 13204–13209.

Davis, J. H. Task-specific ionic liquids, *Chem. Lett.* **2004**, 33, 1072-1077.

da-Silva, A. B.; Arjmand, M.; Sundararaj, U.; Bretas, R. E. S. Novel composites of copper nanowire/PVDF with superior dielectric properties, *Polymer* **2014**, 55, 226–234.

Demiral, H; Gunduzoglu, G. Removal of nitrate from aqueous solutions by activated carbon prepared from sugar beet bagasse, *Bioresour. Technol.* **2010**, 101, 1675–1680.

de Souza, R. F.; Padilha, J. C.; Goncalves, R. S.; Dupont, J. Room temperature dialkylimidazolium ionic liquidbased fuel cells, *Electrochemistry Communications* **2003**, 5, 728–731.

Derecskei, B.; Kovacs, A. D. Molecular modelling simulations to predict density and solubility parameters of ionic liquids. *Mol. Simul.* **2008**, 34(10–15), 1167–1175.

Dewar, M. J. S.; Zoebisch, E. G.; Healy, E. F.; Stewart, J. J. P. Development and use of quantum mechanical molecular models. 76. AM1: a new general purpose quantum mechanical molecular model, *J. Am. Chem. Soc.* **1985**, 107, 3902-3909.

Dillon, D. R.; Tenneti, K. K.; Li, C. Y.; Ko, F. K.; Sics, I.; Hsiao, B. S. On the structure and morphology of polyvinylidene fluoride–nanoclay nanocomposites, *Polymer* **2006**, 47, 1678–1688.

Ding, Y.; Guo, C.; Dong, J. Y.; Wang, Z. Novel organic modification of montmorillonite in hydrocarbon solvent using ionic liquid type surfactant for the preparation of polyolefin–clay nanocomposites, *Journal of Applied Polymer Science* **2006**, 102, 4314–4320.

Dinur, U.; Hagler, A. T. New approaches to empirical force fields, *Rev. Comp. Chem.* **1991**, 2, 99-164.

Dixon, R. N. Approximate self-consistent field molecular orbital calculations for valence shell electronic states, *Mol. Phys.* **1967**, 12, 83-90.

Dixon, D. A.; Arduengo, A. J. Accurate heats of formation of the "Arduengo-Type" carbene and various adducts including H_2 from ab initio molecular orbital theory, *J. Phys. Chem. A* **2006**, 110, 1968–1974.

Domanska, U.; Bogel-Łukasik, E.; Bogel-Łukasik, R. 1-Octanol/water Partition coefficients of 1-alkyl-3-methylimidazolium chloride, *Chem. Eur. J.* **2003**, 9, 3033-3041.

Dong, K.; Zhang, S.; Wang, D. Hydrogen bonds in imidazolium ionic liquids, *J. Phys. Chem. A* **2006**, 110, 9775–9782.

Downard, A.; Earle, M.; Hardacre, C.; McMath, S.; Nieuwenhuyzen, M.; Teat, S. Structural studies of crystalline 1-alkyl-3-methylimidazolium chloride salts, *Chem. Mater.* **2004**, 16, 43–48.

Drake, G.; Hawkins, T.; Brand, A.; Hall, L.; McKay, M. Energetic low melting salts of simple heterocycles, *Propellants, Explos. Pyrotech*. **2003**, 28, 174-180.

Dupont, J. On the solid, liquid and solution structural organization of imidazolium ionic liquids, *J. Braz. Chem. Soc.* **2004**, 15, 341 – 350.

Durga1, G.; Mishra, A. Ionic liquids: Industrial applications, *Encyclopedia of Inorganic and Bioinorganic Chemistry* **2016**, 1-13.

Dutta, B.; Kar, E.; Bose, N.; Mukherjee, S. Significant enhancement of the electroactive β- phase of PVDF by incorporating hydrothermally synthesized copper oxide nanoparticles, *RSC Adv*. **2015**, 5, 105422−105434.

Dzyuba, S. V.; Bartsch, R. A. Influence of structural variations in 1-alkyl(aralkyl)-3-methylimidazolium hexafluorophosphates and bis(trifluoromethylsulfonyl) imides on physical properties of the ionic liquids, *Chem. Phys. Chem.* **2002**, 3, 161-166.

Elaiwi, A.; Hitchcock, P. B.; Seddon, K. R.; Srinivasan, N.; Tan, Y. M.; Welton, T.; Zora, J. A. Hydrogen bonding in imidazolium salts and its implicationsfor ambient temperature halogenoaluminate(III) ionic liquids*, J. Chem. Soc. Dalton Trans.* **1995**, 1, 3467-3471.

Emelyanenko, V. N.; Verevkin, S. P.; Heintz, A.; Voss, K.; Schulz, A. Imidazolium-based ionic liquids: Methylimidazolium nitrate: Thermochemical measurements and ab initio calculations, *J. Phys. Chem. B* **2009**, 113, 9871–9876.

Erdmenger, T.; Vitz, F. J; Wiesbrock, F.; Schubert, U. S. Influence of different branched alkyl side chains on the properties of imidazolium-based ionic liquids, *J. Mater. Chem*. **2008**, 18, 5267-5273.

Erfurt, K.; Wandzik, I.; Walczak, K.; Matuszek, K.; Chrobok, A. Hydrogen bond rich ionic liquids as effective organo catalysts for Diels–Alder reactions, *Green Chem*. **2014**, 16, 3508–3514.

Evans, R. G.; Klymenko, O. V.; Hardacre, C.; Seddon, K. R.; Compton, R. G. Oxidation of N,N,N′,N′-tetraalkyl para phenylenediamines in a series of room temperature ionic liquids incorporating the bis(trifluoromethylsulfonyl)imide anion, *J. Electroanal. Chem.***2003**, 556, 179-188.

Fan, X. H.; Chen, Y. P.; Su, C. S. Density and viscosity measurements for binary mixtures of 1-ethyl-3-methylimidazolium tetrafluoroborate ([Emim][BF$_4$]) with

dimethylacetamide, dimethylformamide, and dimethyl Sulfoxide, *J. Chem. Eng. Data* **2016**, 61, 920-927.

Fannin, A. A.; Floreani, D. A.; King, L. A.; Landers, J. S.; Piersma, B. J.; Stech, D. J.; Vaughn, R. L.; Wilkes, J. S.; Williams, J. L. Properties of 1,3-dialkylimidazolium chloride-aluminum chloride ionic liquids. 2. Phase transitions, densities, electrical conductivities, and viscosities, *J. Phys. Chem.* **1984**, 88, 2614-2621.

Feller, D.; Davidson, E. R. Basis sets for ab initio molecular orbital calculations and intermolecular interactions. In reviews in computational chemistry, Lipkowitz, K. B.; Boyd, D. B., Eds. VCH, New York, **1990**, Vol. 1.

Fermi, E. Un metodo statistice per la determinazione di alcune oroprieta dell atomo, *Rend. Accad. Lincei* **1927**, 6, 602-607.

Fermi, E. Eine statistiche methode zur bestimmung einiger eigenschaften des atmoes und ihre anwendung auf die theorie des periodischen systems der elemente, *Z. Phys.* **1928**, 48, 73-79.

Fillery, S. P.; Koerner, H.; Drummy, L.; Dunkerley, E.; Durstock, M. F.; Schmidt, D. F.; Vaia, R. A. Nanolaminates: Increasing dielectric breakdown strength of composites, *ACS Appl. Mater. Interfaces* **2012**, 4, 1388−1396.

Flynn, J. H.; Wall, L. A. A quick, direct method for the determination of activation energy from thermogravimetric data, *Polymer Letters*, **1966**, 4, 323-328.

Fock, V. Näherungs methode zur lösung des quantenmechanischen mehrkörper problems, *Z. Phys.* **1930**, 61, 126-148.

Formentin, P.; Garcia, H.; Leyva, A. Assessment of the suitability of imidazolium ionic liquids as reaction medium for base-catalysed reactions: Case of Knoevenagel and Claisen-Schmidt reactions. *J. Mol. Catal. A Chem.* **2004**, 214, 137−142.

Fredlake, C. P.; Crosthwaite, J. M.; Hert, D. G.; Aki, S. N. V. K.; Brennecke, J. F. Thermophysical properties of imidazolium-based ionic liquids, *J. Chem. Eng. Data* **2004**, 49, 954−964.

Freemantle, M. Designer Solvents: Ionic liquids may boost clean technology development, *Chem. Eng. News* **1998**, 76, 32−37.

Freemantle, M. An Introduction to ionic liquids, *RSC Publishing*, London, **2010**.

Freire, M. G.; Carvalho, P. J.; Fernandes, A. M.; Marrucho, I. M.; Queimada, A. J.; Coutinho, J. A. P. Surface tensions of imidazolium based ionic liquids: Anion, cation, temperature and water effect, *Journal of Colloid and Interface Science* **2007**, 314, 621–630

Frisch, M. J.; Trucks, G. W.; Schlegel, H. B.; Scuseria, G. E.; Robb, M. A.; Cheeseman, J. R.; Scalmani, G.; Barone, V.; Mennucci, B.; Petersson, G. A.;Nakatsuji, H.; Caricato, M.; Li, X.; Hratchian, H. P.;Izmaylov, A. F.;Bloino, J.; Zheng, G.; Sonnenberg, J. L.;Hada, M.; Ehara, M.; Toyota, K.; Fukuda, R.; Hasegawa, J.; Ishida, M.; Nakajima, T.; Honda, Y.; Kitao, O.; Nakai, H.; Vreven, T.; Montgomery Jr, J. A.; Peralta, J. E.;Ogliaro, F.; Bearpark, M.;Heyd, J. J.; Brothers, E.; Kudin, K. N.; Staroverov, V. N.; Kobayashi, R.; Normand, J.; Raghavachari, K.; Rendell, A.;Burant, J. C.; Iyengar, S. S.;Tomasi, J.;Cossi, M.; Rega, N.; Millam, J. M.;Klene, M.; Knox, J. E.; Cross, J. B.; Bakken, V.; Adamo, C.; Jaramillo, J.; Gomperts, R.;Stratmann, R. E.; Yazyev, O.; Austin, A. J.;Cammi, R.; Pomelli, C.; Ochterski, J. W.; Martin, R. L.;Morokuma, K.; Zakrzewski, V. G.; Voth, G. A.; Salvador, P.; Dannenberg, J. J.; Dapprich, S.; Daniels, A. D.; Farkas, O.; Foresman, J. B.; Ortiz, J. V.; Cioslowski, J.; Fox, D. J. *Gaussian 09*, *Revision A.1*, Gaussian, Inc., Wallingford CT, **2009**.

Fuller, J.; Carlin, R. T.; Osyteryoung, R. A. The room temperature ionic liquid 1-ethyl-3-methylimidazolium tetrafluoroborate: Electrochemical couples and physical properties *J. Electrochem. Soc*. **1997**, 144, 3881-3886.

Fuller, J.; Carlin, R. T.; De Long, H. C.; Haworth, D. Structure of 1-ethyl-3-methylimidazolium hexafluorophosphate: model for room temperature molten salts, *J. Chem. Soc., Chem. Commun*. **1994**, 299-300.

Fumino, K.; Wulf, A.; Ludwig, R. The cation–anion interaction in ionic liquids probed by far-infrared spectroscopy, *Angew. Chem*. **2008**, 120, 8859–8862.

Gabriel S., Weiner J.: Ueber einige Abkömmlinge des Propylamins. *Ber. Dtsch. Chem. Ges.* **1888**, 21, 2669–2679.

Gadre, S. R.; Bhadane, P. K.; Pundlik, S. S.; Pingale, S. S. Molecular recognition via electrostatic potential topography, in Molecular electrostatic potentials: Concepts and applications, Murray, J. S.; Sen, S. Eds. *Elsevier*, Amsterdam, **1996**.

Gadre, S. R.; Kulkarni, S.A.; Shrivastava, I.H. Molecular electrostatic potentials: A topographical study, *J. Chem. Phys*. **1992**, 96, 5253-5260.

Gadre, S. R.; Pathak, R. K. Maximal and minimal characteristics of molecular electrostatic potentials*, J. Chem. Phys*. **1990**, 93, 1770-1773.

Gadre, S. R.; Pathak, R. K. Nonexistence of local maxima in molecular electrostatic potential maps, *Proc. Ind. Acad. Sci.* (*Chem. Sci.*) **1990**, 102, 189-192.

Gadre, S. R.; Shirsat, R. N. Electrostatics of atoms and molecules, *Universities press*, Hyderabad, India, **2000**.

Gardas, R. L.; Costa, H. F.; Freire, M. G. Densities and derived thermodynamic properties of imidazolium, pyridinium, pyrrolidinium, and piperidinium based ionic liquids. *J. Chem. Eng. Data* **2008**, 53(3), 805–811.

Gebrekrstos, A.; Sharma, M.; Madras, G.; Bose, S. New physical insights into shear history dependent polymorphism in PVDF, *Cryst. Growth Des*. **2016**, 16 (5), 2937–2944.

Goujon, N.; Forsyth, M.; Dumee, L. F.; Bryant, G.; Byrne, N. Characterization of the phase behaviour of a novel polymerizable lyotropic ionic liquid crystal, *Phys. Chem. Chem. Phys*. **2015**, 17, 23059-23068.

Guan, W.; Tong, J.; Chen, S. P. Density and surface tension of amino acid ionic liquid 1-alkyl-3-methylimidazolium glutamate, *J. Chem. Eng. Data*. **2010**, 55(9), 4075–4079.

Gupta, S. S.; Bhattacharyya, K. G. Adsorption of heavy metals on kaolinite and montmorillonite: a review, *Phys. Chem. Chem. Phys*. **2012**, 14, 6698–6723.

Gutowski, K. E.; Rogers, R. D.; Dixon, D. A. Accurate thermochemical properties for energetic materials applications. II. Heats of formation of imidazolium-1,2,4-triazolium, and tetrazolium based energetic salts from isodesmic and lattice energy calculations, *J. Phys. Chem. B* **2007**, 111, 4788-4800.

Ha, J. U.; Xanthos, M., Functionalization of nanoclays with ionic liquids for polypropylene composites, *Polym. Compos*. **2009**, 30, 534–542.

Haghseresht, F.; Lu, G. Adsorption characteristics of phenolic compounds onto coal-reject-derived adsorbents, *Energy Fuels* **1998**, **12**, 1100-1107.

Han, X.; Armstrong, D. W. Ionic liquids in separations, *Acc. Chem. Res*. **2007**, 40, 1079–1086.

Hao, Y. N.; Wang, X. H.; OBrien, S.; Lombardi, J.; Li, L. T. Flexible BaTiO$_3$/PVDF gradated multilayer nanocomposite film with enhanced dielectric strength and high energy density, *J. Mater. Chem. C* **2015**, 3, 9740−9747.

Hardacre, C.; Holbrey, J. D.; Katdare, S. P.; Seddon, K. R. Alternating copolymerisation of styrene and carbon monoxide in ionic liquids, *Green Chem.* **2002**, 4, 143-146.

Hartree, R. R. The wave mechanics of an atom with a non-coulomb central field, Part-1: Theory and methods, *Proc. Cambridge Phil. Soc.* **1928**, 24, 89-110.

He, L.; Zhang, W.; Zhao, L.; Liu, X.; Jiang, S. Effect of 1-alkyl-3-methylimidazoliumbased ionic liquids as the eluent on the separation of ephedrines by liquid chromatography, *Journal of Chromatography A*, **2003**, 1007, 39–45.

Hehre, W. J.; Stewart, R. F.; Pople, J. A. Self consistent molecular orbital methods. 1. Use of gaussian expansions of slater type atomic orbitals, *J. Chem. Phys.* **1969**, 51, 2657-2664.

Ho, Y. Review of second-order models for adsorption systems, *J. Hazard. Mater.* **2006**, 136, 681-689.

Hohenberg, P.; Kohn, W. Inhomogeneous electron gas, *Phys. Rev. B* **1964**, 136, B864-B871.

Holbrey, J. D.; Seddon, K. R. Ionic liquids, *Clean Prod. Proc.* **1999**, 1, 223−236.

Hough, W. L.; Smiglak, M.; Rodriguez, H.; Swatloski, R. P.; Spear, S. K.; Daly, D. T.; Pernak, J.; Grisel, J. E.; Carliss, R. D.; Soutullo, M. D.; Davis Jr., J. H.; Rogers, R. D. The third evolution of ionic liquids: active pharmaceutical ingredients, *New J. Chem.* **2007**, 31, 1429–1436.

Huang, M. Y.; Wu, J. C.; Shieu, F. S.; Lin, J. J. Isomerization of endo tetrahydro dicyclopentadiene over clay supported chloroaluminate ionic liquid catalysts, *Journal of Molecular Catalysis A: Chemical* **2010**, 315, 69–75.

Huddleston, J. G.; Willauer, H. D.; Swatloski, R. P.; Visser, A. E.; Rogers, R. D. Room temperature ionic liquids as novel media for clean liquid-liquid extraction, *Chem. Commun.* **1998**, 1765–1766.

Huddleston, J. G.; Visser, A. E.; Reichert, W. M.; Willauer, H. D.; Broker, G. A.; Rogers, R. D. Characterization and comparison of hydrophilic and hydrophobic

room temperature ionic liquids incorporating the imidazolium cation, *Green Chem.* **2001**, 3, 156-164.

Hunt, P. A.; Ashworth, C. R.; Matthews, R. P.; Hydrogen bonding in ionic liquids, **2015**, 44, 1257-1288.

Huo, H.; Jiang, S.; An, L. Influence of shear on crystallization behavior of the β-phase in isotactic polypropylene with β-nucleating agent, *Macromolecules* **2004**, 37, 2478–2483.

Hutchison, J. M.; Zilles, J. L. Biocatalytic perchlorate reduction: kinetics and effects of groundwater characteristics, *Environ. Sci.: Water Res. Technol.* **2015**, 1, 913–921.

Ilawe, N. V.; Ramanathan, S.; Wong, B. M.; Wu, J.; Fu, J. Chemical and radiation stability of ionic liquids – A computational screening study, *J. Phys. Chem. C*, **2016**, 120, 27757-27767.

Ince-Gunduz, B. S.; Alpern, R.; Amare, D.; Crawford, J.; Dolan, B.; Jones, S.; Kobylarz, R.; Reveley, M.; Cebe, P. Impact of nanosilicates on poly(vinylidene fluoride) crystal polymorphism: Part 1. Melt-crystallization at high supercooling, *Polymer* **2010**, 51, 1485-1493.

Jimenez, A. E.; Bermudez, M.D.; Iglesias, P.; Carrion, F.J.;Martinez-Nicolas, G. 1-N-alkyl-3-methylimidazolium ionic liquids as neat lubricants andlubricant additives in steel–aluminium contacts, *Wear* **2006**, 260, 766–782.

Kannan, K.; Praamsma, M. L.; Oldi, J. F.; Kunisue, T.; Sinha, R. K. Occurrence of perchlorate in drinking water, groundwater, surface water and human saliva from India, *Chemosphere* **2009**, 76(1), 22–26.

Kar, E.; Bose, N.; Das, S.; Mukherjee, N.; Mukherjee, S. Enhancement of electroactive β phase crystallization and dielectric constant of PVDF by incorporating GeO_2 and SiO_2 nanoparticles, *Phys. Chem. Chem. Phys.* **2015**, 17, 22784-22798.

Katsyuba, S. A.; Zvereva, E. E.; Vidis, A.; Dyson, P. J. Application of density functional theory and vibrational spectroscopy toward the rational design of ionic liquids, *J. Phys. Chem. A* **2007**, 111, 352-370.

Kato, M.; Usuki, A. in: Pinnavaia, T.J.; Beall G.W. (Eds.), Polymer clay nanocomposites, John Wiley & Sons Ltd., New York, **2000**.

Katritzky, A. R.; Lomaka, A.; Petrukhin, R. Correlation of the melting point for pyridinium bromides, potential ionic liquids, *J. Chem. Inf. Comput. Sci.* **2002**, 42, 71–74.

Katritzky, A. R.; Singh, S.; Kirichenko, K.; Holbrey, J. D.; Smiglak, M.; Reichert, W. M.; Rogers, R. D. "β-cis-SAr effect" on decarbonylation from α,β-unsaturated acyl and aroyl complexes, *Chem. Commun.* **2005**, 868–870.

Kawai, H. The Piezoelectricity of Poly (vinylidene Fluoride), *Japan. J. Appl. Phys.* **1969**, 8, 975–976.

Ke, K.; Potschke, P.; Jehnichen, D.; Fischer, D.; Voit, B. Achieving β-phase poly(vinylidene fluoride) from melt cooling: Effect of surface functionalized carbon nanotubes, *Polymer* **2014**, 55, 611–619.

Khanna, P. K.; Hornbostel, B.; Grimme, R.; Schaefer, W.; Dorner, J. Miniature pressure sensor and micromachined actuator structure based on low-temperature-cofired ceramics and piezoelectric material, *J. Mater. Chem. Phys.* **2004**, 87, 173–178.

Kilaru, P.; Baker, G. A.; Scovazzo, P. Density and surface tension measurements of imidazolium, quaternary phosphonium, and ammonium based room-temperature ionic liquids: data and correlations, *J. Chem. Eng. Data.* **2007**, 52(6), 2306–2314.

Kim, J. Y.; Komarneni, S.; Parette, R.; Cannon, F.; Katsuki, H. Perchlorate uptake by synthetic layered double hydroxides and organoclay minerals, *Appl. Clay Sci.* **2011**, 51, 158–164.

Kim, G. H.; Hong, S. M.; Seo, Y. Piezoelectric properties of poly(vinylidene fluoride) and carbon nanotube blends: β-phase development, *Phys. Chem. Chem. Phys.* **2009**, 11, 10506–10512.

Kim, N. H.; Malhotra, S. V.; Xanthos, M. Modification of cationic nanoclays with ionic liquids, *Microporous and Mesoporous Materials* **2006**, 96, 29–35.

King, L. A.; Brown, A. D.; Frayer, F. H. *Proceedings OAR Research Applications Conference* **1968**, J-1–J-16.

Kissinger, H. E. Reaction Kinetics in Differential Thermal Analysis, *Analytical Chemistry* **1957**, 29, 1702-1706.

Klamt, A. Conductor-like screening model for real solvents – a new approach to the quantitative calculation of solvation phenomena. *J. Phys. Chem.* **1995**, 99(7), 2224–2235.

Klapötke, T. M.; Miŕo Sabaté,C.; Rasp, M. Synthesis and properties of 5-nitrotetrazole derivatives as new energetic materials, *J. Mater. Chem.* **2009**, 19, 2240–2252.

Koch, V. R.; Nanjundiah, C.; Appetecchi, G. B.; Scrosati, B. The interfacial stability of Li with two new solvent free ionic liquids: 1,2-dimethyl-3-propyl imidazolium imide and methide, *J. Electrochem. Soc.* **1995**, 142, L116-L118.

Kohn, W.; Sham, L. J. Self-consistent equations including exchange and correlation effects, *Phys. Rev. A* **1965**, 140, A1133-A1138.

Kojima, Y.; Usuki, A.; Kawasumi, M.; Okada, A. Mechanical properties of nylon 6-clay hybrid, *J. Mater. Res.* **1993**, 8, 1185-1189.

Kojima, Y.; Usuki, A.; Kawasumi, M.; Okada, A.; Kurauchi, T.;Kamigaito, O. Sorption of water in nylon 6-clay hybrid, *J. Appl. Polym. Sci.* **1993**, 49, 1259-1264.

Komarneni, S.; Kim, j. Y.; Parette, R.; Cannon, F. S. As-synthesized MCM-41 silica: new adsorbent for perchlorate, *J. Porous Mater.* **2010**, 17, 651–656.

Komarneni, S.; Aref, A R.; Hong, S.; Noh, Y. D.; Cannon, F. S.; Wang, Y. Organoclays of high-charge synthetic clays and alumina pillared natural clays: Perchlorate uptake, *Appl. Clay Sci.* **2013**, 80–81, 340–345.

Kosaka, K.; Asami, M.; Matsuoka, Y.; Kamoshita, M.; Kunikane, S. Occurrence of perchlorate in drinking water sources of metropolitan area in Japan, *Water Res.* **2007**, 41(15), 3474–3482.

Krossing, I.; Slattery, J.; Gaguenet, C.; Dyson, P.; Oleinikova, A.; Weingrtner, H. Why Are Ionic Liquids Liquid? A Simple Explanation Based on Lattice and Solvation Energies, *J. Am. Chem. Soc.* **2006**, 128, 13427–13434.

Ladino, J. A. F.; Ceballos, M. O.; Moreano, M. R.; Montano, D. F.; Cardona, W.; Giraldo, L. F.; Richter, P. Ionic liquids intercalated in montmorillonite as the sorptive phase forthe extraction of low-polarity organic compounds from water by rotating-disk sorptive extraction, *Analytica Chimica Acta* **2017**, 953, 23-31.

Lagaly, G.; Ogawa, M.; Dekany, I. Clay mineral organic interactions, Handbook of clay science edited by Bergaya, F.; Theng, B.K.G.; Lagaly, G. Developments in clay science, *Elsevier* **2006**, 1, 309-377.

Lawal, I. A.; Moodley, B. Synthesis, characterisation and application of imidazolium based ionic liquid modified montmorillonite sorbents for the removal of amaranth dye, *RSC Adv.* **2015**, 5, 61913-61924.

Lawal, I. A.; Chetty, D.; Akpotu, S. O.; Moodley, B. Sorption of congo red and reactive blue on biomass and activated carbonderived from biomass modified by ionic liquid, *Environmental Nanotechnology, Monitoring & Management* **2017**, 8, 83–91.

Layek, R. K.; Samanta, S.; Chatterjee, D. P.; Nandi, A. K. Physical and mechanical properties of poly(methylmethacrylate)-functionalized graphene/ poly(vinylidine fluoride) nanocomposites: Piezoelectric β polymorph formation, *Polymer* **2010**, 51, 5846−5856.

Lee, C. S.; Joo, J.; Han, S.; Koh, S. K. Multifunctional transducer using poly(vinylidene fluoride) active layer and highly conducting poly (3,4-ethylenedioxythiophene) electrode: Actuator and generator. *Applied Physics Letters* **2004**, 85, 1841−1843.

Lee, C. T.; Yang, W. T.; Parr, R. G. Development of the Colle-Salvetti correlation-energy formula into a functional of the electron density, *Phys. Rev. B* **1988**, *37*, 785-789.

Lee, S. Y.; Cho, W. J.; Kim, K. J.; Ahn, J. H.; Lee, M. Interaction between cationic surfactants and montmorillonites under non equilibrium condition, *J. Colloid Interface Sci.* **2005**, 284, 667-673.

Letcher, T. M.; Deenadayalu, N. Ternary liquid–liquid equilibria for mixtures of 1-methyl-3-octyl-imidazolium chloride + benzene + an alkane at T=298.2 K and 1 atm, *J. Chem. Thermodyn.* **2002**, 35, 67-76.

Lewandowski, A.; Mocek, A. S. Ionic liquids as electrolytes for Li-ion batteries—An overview of electrochemical studies, *J. Power Sources* **2009**, 194, 601–609.

Li, J.; Seok, S.I.; Chu, B.; Dogan, F.; Zhang, Q.; Wang, Q. Nanocomposites of ferroelectric polymers with TiO_2 nanoparticles exhibiting significantly enhanced electrical energy density, *Adv. Mater.* **2009**, 21, 217−221.

Li, L.; Zhang, M.; Rong, M.; Ruan, W. Studies on the transformation process of PVDF from α to β phase by stretching, *RSC Adv*. **2014**, 4, 3938−3943.

Lias, S. G.; Bartmess, J. E.; Liebman, J. F.; Holmes, J. L.; Levin, R. D.; Mallard, W. G. Gas-phase ion and neutral thermochemistry, *J. Phys. Chem. Ref. Data* **1988**, 17(suppl. 1), 1–861.

Liu, X.; Schmalz, T. G.; Klein, D. Favorable structures for higher fullerenes, *J. Chem. Phys. Lett*. **1992**, 188, 550-554.

Liu, J.; Jiang, G. B.; Chi, Y.; Cai, Y.; Zhou, Q.; Hu, J. Use of ionic liquids for liquid-phase microextraction of polycyclic aromatic hydrocarbons, *Anal. Chem.* **2003**, 75, 5870-5876.

Livi, S.; Duchet-Rumeau, J.; Geŕard, J. F. Tailoring of interfacial properties by ionic liquids in a fluorinated matrix based nanocomposites, *Eur. Polym. J.* **2011**, 47, 1361-1369.

Livi, S.; Duchet-Rumeau, J.; Pham, T. N.; Geŕard, J. F. Synthesis and physical properties of new surfactants based on ionic liquids: Improvement of thermal stability and mechanical behaviour of high density polyethylene nanocomposites, *J. Colloid Interface Sci.* **2011**, 354, 555-562.

Livi, S.; Duchet-Rumeau, J.; Gérard, J. F. Effect of ionic liquid modified synthetic layered silicates on thermal and mechanical properties of high density polyethylene nanocomposites, *Macromol. Symp.* **2014**, 342, 46–55

Lopes, A. C.; Ferreira, J. C.; Costa, C. M; Lanceros-Mendez, S. Crystallization kinetics of montmorillonite/ poly(vinylidene fluoride) composites and its correlation with the crystalline polymer phase formation, *Thermochimica Acta* **2013**, 574, 19-25.

Lovinger, A. J. Unit Cell of the γ Phase of Poly(viny1idene fluoride), *Macromolecules* **1981**, 14, 322−325.

Łuczak,J.; Jungnickel, C.; Łącka, I.; Stoltec, S.; Hupka, J. Antimicrobial and surface activity of 1-alkyl-3-methylimidazolium derivatives, *Green Chem.* **2010**, 12, 593-601.

Ludwig, R.; Paschek, D. Applying the inductive effect for synthesizing low melting and low viscosity imidazolium based ionic liquids, *Chem. Phys. Chem.* **2009**, 10, 516 – 519.

Luo, W.; Hirajima, T.; Sasaki, H. Optimization of hexadecylpyridinium modified montmorillonite for removal of perchlorate based on adsorption mechanisms, *Appl. Clay Sci.* **2016**, 123, 29–36.

Luo, W.; Sasaki, K.; Hirajima, T. Surfactant modified montmorillonite by benzyloctadecyldimethylammonium chloride for removal of perchlorate, *Colloids Surf. A* **2015**, 481, 616–625.

Luque, F. J.; Orozco, M.; Bhadane, P. K.; Gadre, S. R. Effect of solvation on the shapes, sizes and anisotropies of polyatomic anions *via* molecular electrostatic potential topology: An *ab* initio self consistent reaction field approach, *J. Chem. Phys.* **1994**, 100, 6718-6726.

Lv, G.; Li, Z.; Jiang, W. T.; Chang, P. H.; Liao, L. Interlayer configuration of ionic liquids in a Ca-montmorillonite as evidenced by FTIR, TG-DTG, and XRD analyses, *Materials Chemistry and Physics* **2015**, 162, 417-424.

Ma, H.; Wan, X.; Chen, X.; Zhou, Q. F. Reverse atom transfer radical polymerization of methyl methacrylatein imidazolium ionic liquids, *Polymer* **2003**, 44, 5311–5316.

MacFarlane, D. R.; Golding, J.; Forsyth, S.; Forsyth, M.; Deacon, G. B. Low viscosity ionic liquids based on organic salts of the dicyanamide anion, *Chem. Commun.* **2001**, 16, 1430-1431.

MacFarlane, D. R.; Forsyth, M.; Howlett, P. C.; Pringle, J. M.; Sun, J.; Annat, G.; Neil, W.; Izgorodina, E. Ionic liquids in electrochemical devices and processes: Managing interfacial electrochemistry, *Acc. Chem. Res.* **2007**, 40, 1165–1173.

Maity, N.; Mandal, A.; Nandi, A. K. Interface engineering of ionic liquid integrated graphene in poly(vinylidene fluoride) matrix yielding magnificent improvement in mechanical, electrical and dielectric properties, *Polymer* **2015**, 65, 154−167.

Mandal, A.; Nandi, A. K. Physical properties of poly(vinylidene fluoride) composites with polymer functionalized multiwalled carbon nanotubes using nitrene chemistry, *J. Mater. Chem.* **2011**, 21, 15752−15763.

Manna, S.; Batabyal, S. K.; Nandi, A. K. Preparation and characterization of silver-poly(vinylidene fluoride) nanocomposites: Formation of piezoelectric polymorph of poly(vinylidene fluoride), *J. Phys. Chem. B* **2006**, 110, 12318−12326.

Mantz, R. A.; Fox, D. M.; Green, J. M.; Fylstra, P. A.; De Long, H. C.; Trulove, P. C.; Z. Dissolution of Biopolymers Using Ionic Liquids, *Naturfors. Sect. A* **2007**, 62, 275–280.

Martins, P.; Caparros, C.; Goncalves, R.; Martins, P.M.; Benelmekki, M.; Botelho, G.; Lanceros-Mendez, S. Role of nanoparticle surface charge on the nucleation of the electroactive β-poly(vinylidene fluoride) nanocomposites for sensor and actuator applications, *J. Phys. Chem. C* **2012**, 116, 15790−15794.

Martins, P.; Lopes, A.C.; Lanceros-Mendez, S. Electroactive phases of poly(vinylidene fluoride): Determination, processing and applications, *Progress in Polymer Science* **2014**, 39, 683–706.

Martins, P.; Caparros, C.; Goncalves, R.; Martins, P.M.; Benelmekki, M.; Botelho, G.; Lanceros-Mendez, S. Role of nanoparticle surface charge on the nucleation of the electroactive β-poly(vinylidene fluoride) nanocomposites for sensor and actuator applications, *J. Phys. Chem. C* **2012**, 116, 15790−15794.

Matsumoto, H.; Kageyama, H.; Miyazaki, Y.; Molten salts XIII, *The Electrochemical Society*, Pennigton, NJ, **2002**, 19, 1057.

Matsumoto, H.; Yanagida, M.; Tanimoto, K.; Nomura, M.; Kitagawa, Y.; Miyazaki, Y. Highly conductive room temperature molten salts based on small trimethylalkylammonium cations and bis(trifluoromethylsulfonyl)imide, *Chem. Lett.* **2000**, 8, 922-923.

Mattsson, A. E. In pursuit of the "divine" functional, *Science* **2002**, 298, 759-760.

McBride, M. B. *Environmental Chemistry of Soils*, Oxford University Press, **1994.**

McCrary, P. D.; Chatel, G.; Alaniz, S. A.; Cojocaru, O. A.; Beasley, P. A.; Flores, L. A.; Kelley, S. P.; Barber, P. S.; Rogers, R. D. Evaluating ionic liquids as hypergolic fuels: Exploring reactivity from molecular structure, *Energy & Fuels* **2014,** 28 (5), 3460-3473.

Mejri, R.; Dias, J. C.; Lopes, A. C.; Hentati, S. B.; Silva, M. M.; Botelho, G.; de Ferro, A. M.; Esperanca, J. M. S. S.; Maceiras, A.; Laza, J. M.; Vilas, J. L.; Leon, L. M.; Lanceros-Mendez, S. Effect of ionic liquid anion and cation on the physico-chemical properties of poly(vinylidene fluoride)/ionic liquid blends, *European Polymer Journal* **2015**, 71, 304–313.

Mirmohamadsadeghi, S.; Kaghazchi, T.; Soleimani, M.; Asasian, N. An efficient method for clay modification and its application for phenol removal from waste water, Applied Clay Science **2012**, 59–60, 8–12.

Miranda-Trevino, J. C.; Coles, C. A. Kaolinite properties, structure and influence of metal retention on pH, *Appl. Clay Sci.* **2003**, 23, 133–139.

Mittal, V. Gas permeation and mechanical properties of polypropylene nanocomposites with thermally stable imidazolium modified clay, *Eur. Polym. J.* **2007**, 43, 3727-3736.

Montano, D. F.; Casanova, H.; Cardona, W. I.; Giraldo, L. F. Functionalization of montmorillonite with ionic liquids based on 1-alkyl-3-methylimidazolium: Effect of anion and length chain, *Materials Chemistry and Physics* **2017**, 198, 386-392.

Nagasawa, T.; Shimomura, Y. Mechanism of formation of shish-kebab structures, *J. Polym. Sci.: Polymer Physics* **1974**, 12, 2291-2308.

Nandwani, S. K.; Malek, N. I.; Lad, V.N.; Chakraborty, M.; Gupta, S. Study on interfacial properties of Imidazolium ionic liquids assurfactant and their application in enhanced oil recovery, *Colloids and Surfaces A: Physicochem. Eng. Aspects* **2017**, 516, 383–393.

Nanjundiah, C.; McDevitt, F.; Koch, V. R. Differential capacitance measurements in solvent free ionic liquids at Hg and C interfaces, *J. Electrochem. Soc.* **1997**, 144, 3392-3397.

Neetha, M.; Suresh, C. H.; A molecular electrostatic potential analysis of hydrogen, halogen, and dihydrogen bonds, *J. Phys. Chem. A* **2014**, 118, 1697–1705.

Nevskaia, D. M.; Castillejos-Lopez, E.; Guerrero-Ruiz, A.; Muñoz, V. Effects of the surface chemistry of carbon materials on the adsorption of phenol–aniline mixtures from water, *Carbon* **2004**, 42, 653-665.

Ngo, H. L.; LeCompte, K.; Hargens, L.; McEwen, A. B. Thermal properties of imidazolium ionic liquids, *Thermochim. Acta* **2000**, 357, 97-102.

Nishida, T.; Tashiro, Y.; Yamamoto, M. Physical and electrochemical properties of 1-alkyl-3-methylimidazolium tetrafluoroborate for electrolyte, *J. Fluorine Chem.* **2003**, 120, 135-141.

Noda, A.; Hayamizu, K.; Watanabe, M. Pulsed gradient spin echo ^{1}H and ^{19}F NMR ionic diffusion coefficient, viscosity, and ionic conductivity of non-

chloroaluminate room temperature ionic liquids, *J. Phys. Chem. B* **2001**,105, 4603−4610.

Okada, D.; Kaneko, H.; Kato, K.; Furumi, S.; Takeguchi, M.; Yamamoto, Y. Colloidal crystallization and ionic liquid induced partial β-phase transformation of poly(vinylidene fluoride) nanoparticles, *Macromolecules* **2015**, 48, 2570−2575.

Olivier-Bourbigoum, H.; Magna, L.; Morvan, D. Ionic liquids and catalysis: Recent progress from knowledge to applications, *Appl. Catal. A* **2010**, 373, 1−56.

Ozawa, T. A new method of analyzing thermogravimetric data, *Bulletin of the Chemical Society of Japan* **1965**, 88, 1881-1886.

Palomar, J.; Ferro, V. R.; Torrecilla, J. S. Density and molar volume predictions using COSMO-RS for ionic liquids. An approach to solvent design. *Ind. Eng. Chem. Res*. **2007**, 46 (18), 6041–6048.

Parette, R.; Cannon, F. S. The removal of perchlorate from groundwater by activated carbon tailored with cationic surfactants, *Water Res*. **2005**, 39, 4020–4028.

Pariser, R; Parr, R. G. A Semi-Empirical Theory of the Electronic Spectra and Electronic Structure of Complex Unsaturated Molecules. I. *J. Chem. Phys.* **1953**, 21, 466-471.

Parvulescu, V. I.; Hardacre, C. Catalysis in Ionic Liquids, *Chem. Rev*. **2007**, 107, 2615–2665.

Patil, N.; Balzano, L.; Portale, G.; Rastogi, S. A Study on the chain-particle interaction and aspect ratio of nanoparticles on structure development of a linear polymer, *Macromolecules* **2010**, 43, 6749–6759.

Patro, T.U.; Mhalgi, M.V.; Khakhar, D.V.; Misra, A. Studies on poly(vinylidene fluoride)–clay nanocomposites: Effect of different clay modifiers, *Polymer* **2008**, 49, 3486-3499.

Perdew, J. P.; Schmidt, K. Jacob's ladder of density functional approximations for the exchange correlation energy. In *Density functional theory and its applications to materials*, Van Doren, V. E.; Van Alseoy, K; Geerlings, P. Eds. AIP Press, New York, **2001**.

Politzer, P.; Truhlar, D. G. Chemical applications of atomic and molecular electrostatic potentials, *Plenum press*, New York, **1981**.

Pople, J. A.; Duncan, A. B. F. The structure of some simple molecules with lone pair electrons, *Trans Faraday Soc.* **1953**, 49, 217-224.

Pople, J. A.; Santry, D. P.; Segal, G. A. Approximate self consistent molecular orbital theory. I. Invariant procedures, *J. Chem. Phys.* **1965**, 43, S129- S135.

Pople, J. A.; Segal, G. A. Approximate Self-Consistent Molecular Orbital Theory. II. Calculations with Complete Neglect of Differential Overlap, *J. Chem. Phys.* **1965**, 43, S136-S151.

Pople, J. A.; Segal, G. A. Approximate self consistent molecular orbital theory. III. CNDO results for AB_2 and AB_3 systems *J. Chem. Phys.* **1966,** 44, 3289-3296.

Pople, J. A.; Beveridge, D. L.; Dobosh, P. A. Approximate self consistent molecular orbital theory. V. Intermediate neglect of differential overlap, *J. Chem. Phys.* **1967**, 47, 2026-2033.

Priya, L.; Jog, J. P. Poly(vinylidene fluoride)/clay nanocomposites prepared by melt intercalation: Crystallization and dynamic mechanical behavior studies, *J. Poly. Sci. B. Polym. Phys.* **2002**, 40, 1682-1689.

Prokhorov, K. A.; Saguitova, E. A.; Yu. Nikolaeva, G.; Kozlov, D. N.; Pashinin, P. P.; Antipov, E. M.; Gerasin, V. A.; Bakhov, F. N.; Guseva, M. A. Characterization of the structure of modified clay by Raman spectroscopy, *Laser Phys. Lett.* **2005**, 2, 285-291.

Ravi, P.; Gore, G. M.; Tewari, S.P.; Sikder, A.K. A DFT study of aminonitroimidazoles. *J. Mol. Model.* **2012**, 18, 597–605.

Ray, S. S.; Okamoto, M. Polymer/layered silicate nanocomposites: a review from preparation to processing, *Progr. Polym. Sci.* **2003**, 28 (11) 1539-1641.

Reinert, L.; Batouche, K.; Lévêque, J. M.; Muller, F.; Bény, J. M., Kebabi, B.; Duclaux, L. Adsorption of imidazolium and pyridinium ionic liquids onto montmorillonite: Characterisation and thermodynamic calculations, *Chemical Engineering Journal* **2012**, 209, 13–19.

Rekha, K. G.; Radhika, R.; Jayalatha, T.; Salu, J.; Rajeev, R.; Benny, K. G.; Anjali, B. R. Removal of perchlorate from drinking water using granular activated carbon modified by acidic functional group: Adsorption kinetics and equilibrium studies, *Process Safety and environmental protection* **2017**, 109, 158-171.

Remya, K.; Suresh, C. H. Which density functional is close to CCSD accuracy to describe geometry and interaction energy of small non-covalent dimers? A benchmark study using Gaussian09, *J. Comput. Chem.* **2013**, 34, 1341-1353.

Rinaldo Jr., G.; Borges, D. S. Effect of crystallization rate on the formation of the polymorphs of solution cast poly(vinylidene fluoride), *Polymer* **2008**, 49, 4009–4016.

Roszak, R.; Trzeciak, A. M.; Pernak, J.; Borucka, N. Effect of chiral ionic liquids on palladium-catalyzed Heck arylation of 2,3-dihydrofuran, *Appl. Catal. A: Gen.* **2011**, 409–410, 148–155.

Safaei-Ghomi, J.; Emaeili, M. Mild and efficient method for oxidation of alcohols in ionic liquid media,*Journal of Nanomaterials and Biostructures*, 2010, 5(4), 865-871.

Saha, S.; Hamaguchi, H. Effect of water on the molecular structure and arrangement of Nitrile functionalized ionic liquids, *J. Phys. Chem. B*. **2006**, 110, 2777-2781.

Sajkiewicz, P.; Wasiak, A.; Goclowski, Z. Phase transitions during stretching of poly(vinylidene fluoride), *Eur. Polym. J.* **1999**, 35, 423–429.

Salimi, A.; Yousefi, A. A. Conformational changes and phase transformation mechanisms in PVDF solution-cast films, *J. Polym. Sci. Part B: Polym. Phys.* **2004**, 42, 3487-3495.

Sanmamed, Y. A.; Gonzalez-Salgado, D.; Troncoso, J.; Cerdeirina, C. A.; Romani, L. Viscosity induced errors in the density determination of room temperature ionic liquids using vibrating tube densitometry, *Fluid Phase Equilib.* **2007**, 252, 96–102.

Sarac, B.; Medos, Z.; Cognigni, A.; Bica, K.; Chen, L. J.; Rogac, M. B. Thermodynamic study for micellization of imidazolium based surface active ionic liquids in water: Effect of alkyl chain length and anions, *Colloids and Surfaces A: Physicochem. Eng. Aspects* **2017**, 7, 41144-41151.

Sarkar, A.; Roy, S. R.; Parikh, N.; Chakraborti, A. K. Non-solvent application of ionic liquids: Organo catalysis by 1-Alkyl-3-methylimidazolium cation based room temperature ionic liquids for chemoselective N-tert-Butyloxycarbonylation of amines and the influence of the C2-Hydrogen on catalytic efficiency, *The Journal of Organic Chemistry*, **2011**, 76 (17), 7132-7140.

Satyanarayana, K. C.; Bolton, K. Molecular dynamics simulations of α- to β-poly(vinylidene fluoride) phase change by stretching and poling, *Polymer* 2012, 53, 2927−2934.

Schmalz, T. G.; Seitz, W. A.; Klein, D. J.; Hite, G. E. Elemental carbon cages, *J. Am. Chem. Soc.* **1988**, 110, 1113-1127.

Schmidt, E. W. Hydrazine and its derivatives – Preparation, properties, application, *Wiley*, New York, **2001**.

Schneider, S.; Hawkins, T.; Rosander, M.; Vaghjiani, G.; Chambreau, S.; Drake, G. Ionic liquids as hypergolic fuels, *Energy Fuels* **2008**, 22, 2871-2872.

Scrocco, E.; Tomasi, J. Electronic molecular structure, reactivity and intermolecular forces: An euristic interpretation by means of electrostatic molecular potentials, *Adv. Quantum Chem.* **1978**, 11, 115-193.

Sebastiao, E; Cook, C.; Hu, A.; Murugesu, M. Recent developments in the field of energetic ionic liquid,*J. Mater. Chem. A* **2014**, 2, 8153-8173.

Seddon, K. R. Ionic liquids for clean technology, *J. Chem. Tech. Biotechnol*. **1997**, 68, 351-356.

Seddon, K. R.; Bowlas, C. J.; Bruce, D. W. Liquid crystalline ionic liquids, *Chem. Commun*. **1996**, 1625-1626.

Seddon, K. R.; Stark, A.; Torres, M. J. Influence of chloride, water, and organic solvents on the physical properties of ionic liquids, *Pure Appl. Chem*. **2000**, 72, 2275-2287.

Seliem, M. K.; Komarneni, S.; Parette, R.; Katsuki, H.; Cannon, F. S.; Shahien, M. G.; Khalil, A. A.; El-Gaid, I. M. A. Composites of MCM-41 silica with rice husk: hydrothermal synthesis, characterisation and application for perchlorate separation, *Mater. Res. Innovations* **2010**, 14, 351–354.

Seliem, M. K.; Komarneni, S.; Parette, R.; Katsuki, H.; Cannon, F. S.; Shahien, M. G.; Khalil, A. A.; El-Gaid, I. M. A. Perchlorate uptake by organosilicas, organo-clay minerals and composites of rice husk with MCM-48, *Appl. Clay Sci*. **2011**, 53, 621–626.

Seliem, M. K.; Komarneni, S.; Byrne, T.; Cannon, F. S.; Shahien, M. G.; Khalil, A. A.; El-Gaid, I. M. A. Removal of perchlorate by synthetic organosilicas and organoclay: Kinetics and isotherm studies, *Appl. Clay Sci*. **2013**, 71, 21–26.

Sencadas, V.; Martins, P.; Pitaes, A.; Benelmekki, M.; Ribelles, J.L.G.; Mendez, S.L. Influence of ferrite nanoparticle type and content on the crystallization kinetics and electroactive phase nucleation of poly(vinylidene fluoride), *Langmuir* **2011**, 27, 7241-7249.

Sharma, M.; Madras, G.; Bose, S. Unusual fragility and co-operativity in glass forming and crystalline PVDF/PMMA blends in the presence of multiwall carbon nanotubes, *Macromolecules* **2015**, 48, 2740−2750.

Shavitt, I. *Methods in Computational Physics*, Academic press, New York, **1963**.

Sheldon, R. Catalytic reactions in ionic liquids, *Chem. Commun.* **2001**, 23, 2399–2407.

Shirsat, R. N.; Bapat, S. V.; Gadre, S. R. Molecular electrostatics: A comprehensive topographical approach, *Chem. Phys. Lett*. **1992**, 200, 373-378.

Singla, P.; Mehta, R.; Upadhyay, S. N. Clay modification by the use of organic cations, *Green and Sustainable Chemistry* **2012**, 2, 21-25.

Slater, J. C. Note on Hartree's method, *Phys. Rev*. **1930**, 35, 210-211.

Srinivasan, R.; Sorial, G. A. Treatment of perchlorate in drinking water: A critical review, *Sep. Purif. Technol*. **2009**, 69, 7–21.

Stegemann, H.; Rhode, A.; Reiche, A. Room temperature molten polyiodides, *Electrochim. Acta* **1992**, 37, 379-383.

Suarez, P. A. Z.; Selbach,V. M.; Dullius, J. E. L.; Einloft, S.; Platnicki, C. M. S.; Azambuja, D. S.; de Souza, R. F.; Dupont, J. Enlarged electrochemical window in dialkyl-imidazolium cation based room-temperature air and water-stable molten salts, *Electrochim. Acta* **1997**, 42, 2533-2535.

Suarez, P. A. Z.; Dullius, J. E. L.; Einloft, S.; DeSouza, R. F.; Dupont, J. The use of new ionic liquids in two-phase catalytic hydrogenation reaction by rhodium complexes, *Polyhedron* **1996**, 15, 1217 – 1219.

Suarez, P. A. Z.; Einloft, S.; Dullius, J. E. L.; Souza, R. F.; Dupont, J. Synthesis and physical-chemical properties of ionic liquids based on 1-n-butyl-3-methylimidazolium cation, *J. Chim. Phys. Phys.Chim. Biol.* **1998**, 95, 1626-1639.

Sun, K.; Shi, Y.; Xu, W.; Potter, N.; Li, Z.; Zhu, J. Modification of clays and zeolites by ionic liquids for the uptake of chloramphenicol from water, *Chemical Engineering Journal* **2017**, 313, 336–344.

Sun, N.; Swatloski, R. P.; Maxim, M. L.; Rahman, M.; Harland, A. G.; Haque, A.; Spear, S. K.; Daly, D. T.; Rogers, R. D. Magnetite-embedded cellulose fibers prepared from ionic liquid, *J. Mater. Chem.* **2008**, 18, 283–290.

Sutton, G. P.; Biblarz, O. Rocket propulsion elements, 8th Ed., Wiley, New York, **2010**.

Swatloski, R. P.; Spear, S. K.; Holbrey, J. D.; Rogers, R. D. Dissolution of cellulose with ionic liquids, *J. Am. Chem. Soc.* **2002**, 124, 4974-4975.

Takahashi, C.; Shirai, T.; Fuji, M. Study on intercalation of ionic liquid into montmorillonite and its property evaluation, *Materials Chemistry and Physics* **2012**, 135, 681- 686.

Thakur, V. K.; Tan, E. J.; Lin, M. F.; Lee, P. S. Polystyrene grafted poly(vinylidenefluoride) copolymers with high capacitive performance, *Polym. Chem.* **2011**, 2, 2000-2009.

Thomas, L. H. The calculation of atomic fields, *Proc. Cambridge Phil. Soc.* **1927**, 23, 542-548.

Trohalaki, S.; Pachter, R.; Drake, G. W.; Hawkins, T. Quantitative structure property relationships for the melting points and densities of ionic liquids, *Energy Fuels* **2005**, 19, 279-284.

Troter,D. Z.; Todorović, Z. B.; Đokić-Stojanović, D. R.; Stamenković, O. S.; Veljković, V. B. Application of ionic liquids and deep eutectic solvents in biodiesel production: A review, *Renewable and Sustainable Energy Reviews* **2016**, 61, 473–500.

Ueno, K; Tokuda, H; Watanabe, M. Ionicity in ionic liquids: Correlation with ionic structure and physicochemical properties, *Phys. Chem. Chem. Phys.* **2010**, 12(8), 1649-1658.

Urbansky, E. T. Perchlorate chemistry: Implications for analysis and remediation, *Biorem. J.* **1998**, 2, 81–95.

Usuki, A.; Kojima, Y.; Okada, A.; Fukushima, Y.; Kurauchi, T.; Kamigaito, O. Synthesis of nylon 6-clay hybrid, *J. Mater. Res.* **1993**, 8, 1179-1184.

Vaia, R. A.; Teukolsky, R. K.; Giannelis, E. P. Inter layer structure and molecular environment of alkylammonium layered silicates, *Chemistry of Materials* **1994**, 6, 1017-1022.

Vanyúr, R.; Biczók, L.; Miskolczy, Z. Micelle formation of 1-alkyl-3-methylimidazolium bromide ionic liquids in aqueous solution, *Colloids and Surfaces A: Physicochemical and Engineering Aspects* **2007**, 299, 256-261.

Verevkin, S. P.; Emelyanenko, V. N.; Zaitsau, D. H.; Heintz, A.; Muzny, C. D.; Frenkel, M. *Phys. Chem. Chem. Phys*. **2010**, 12, 14994–15000.

Vladimir, N. E.; Sergey, P. V.; Andreas, H. The gaseous enthalpy of formation of the ionic liquid 1-butyl-3-methylimidazolium dicyanamide from combustion calorimetry, vapor pressure measurements, and ab initio calculations, *J. Am. Chem. Soc*. **2007**, 129, 3930-3937.

Vimonses, V.; Lei, S.; Jin, B.; Chow, C. W. K.; Saint, C. Adsorption of congo red by three Australian kaolins, *Appl. Clay Sci*. **2009**, 43, 465–472.

Visser, A. E.; Reichert, W. M.; Swatloski, R. P.; Willauer, H. D.; Huddleston, J. G.; Rogers, R. D. Ionic liquids industrial applications to green chemistry, *ACS Symposium* **2002**, 818, 289–308.

Walden, P. Molecular weights and electrical conductivity of several fused salts, *Bull. Russian Acad. Sci*. **1914**, 8, 405–422.

Wang, F.; Lack, A.; Xie, Z.; Frubing, P.; Taubert, A.; Gerhard, R. Ionic liquid induced ferroelectric polarization in poly(vinylidene fluoride) thin films, *Appl. Phys. Lett*. **2012**, 100, 629031−629034.

Wang, J. W.; Wang, Y.; Wang, F.; Li, S. Q.; Xiao, J.; Shen, Q. D. A large enhancement in dielectric properties of poly(vinylidene fluoride) based all-organic nanocomposite, *Polymer* **2009**, 50, 679–684.

Wang, Y.; Li, J.; Deng, Y. Enhanced ferroelectricity and energy storage in poly(vinylidene fluoride)–clay nanocomposite films via nanofiller surface charge modulation, *RSC Adv*. **2015**, 5, 85884−85888.

Wang, W.; Fan, H.; Ye, Y. Effect of electric field on the structure and piezoelectric properties of poly(vinylidene fluoride) studied by density functional theory, *Polymer* **2010**, 51, 3575-3581.

Wasserscheid, P.; Keim, W. Ionic liquids -New solutions for transition metal catalysis, *Angew. Chem. Int. Ed*. **2000**, 39, 3772-3789.

Wasserscheid, P.; Welton, T. Ionic liquids in synthesis, 2nd edition, *Wiley-VCH*, Weinheim, **2007**.

Weiner, P. K.; Kollman, P. A. AMBER-Assisted Model Building with Energy Refinement. A general program for modeling molecules and their interactions, *J. Comput. Chem.* **1981**, 2, 287-303.

Weingarth, D.; Czekaj, I.; Fei, Z.; Foelske-Schmitz, A.; Dyson, P. J.; Wokaun, A.; Kötz, R. Electrochemical stabilityof imidazolium based ionic liquids containing cyano groups in the anion: A cyclic voltammetry, XPS and DFT Study, *Journal of The Electrochemical Society* **2012**, 159, H611-H615.

Wilkes, J. S.; Levisky, J. A.; Wilson, R. A.; Hussey, C. L. Dialkylimidazolium chloroaluminate melts: a new class of room temperature ionic liquids for electrochemistry, spectroscopy and synthesis, *Inorg. Chem.* **1982**, 21, 1263-1264.

Wilkes, J. S.; Zaworotko, M. J. Air and water stable 1-ethyl-3-methylimidazolium based ionic liquids, *Chem. Commun.* **1992**, 965-967.

Wolff, J. Perchlorate and the thyroid gland, *Pharmacol. Rev.* **1998**, 50, 89–105.

Wu, B. Q.; Reddy, R. G.; Rogers, R. D. Solar energy: The power to choose, *Proceedings of solar forum*, Washington, D.C., **2001**.

Wu, L.; Liao, L.; Lv, G.; Qin, F.; Li, Z. Microstructure and process of intercalation of imidazolium ionic liquids into montmorillonite, *Chemical Engineering Journal* **2014**, 236, 306–313.

Wu, M.; Wang, S.; Gao, N.; Zhu, Y.; Li, L.; Niu, M.; Li, S. Removal of perchlorate from water using a biofilm magnetic ion exchange resin: feasibility and effects of dissolved oxygen, pH and competing ions, *RSC Adv.* **2016**, 6, 73365–73372.

Xie, H.; Li, S.; Zhang, S. Ionic liquids as novel solvents for the dissolution and blending of wool keratin fibers, *Green Chem.* **2005**, 7, 606–608.

Xie, W.; Xie, R.; Pan, W.; Hunter, D.; Koene, B.; Tan, L.; Vaia, R. Thermal stability of quaternary phosphonium modified montmorillonites, *Chemistry of Materials* **2002**, 14, 4837-4845.

Xing, C.; Zhao, M.; Zhao, L.; You, J.; Cao, X.; Li, Y. Ionic liquid modified poly(vinylidene fluoride): crystalline structures, miscibility, and physical properties, *Polym. Chem.* **2013**, 4, 5726–5734.

Xu, X.; Goddard, W. A. Assessment of Handy-Cohen optimized exchange density functional (OPTX), *J. Phys. Chem. A* **2004**, 108, 8495-8504.

Yalcinkaya, E. E.; Pelit, F. O.; Güney, I.; Türkmen, H. Ionic liquid intercalated clay nanofillers for chromatographic applications, *J. Porous Mater.* **2014**, 21, 1151–1158.

Ye, C. F.; Shreeve, J. M. Rapid and accurate estimation of densities of room temperature ionic liquids and salts, *J. Phys. Chem. A* **2007**, 111(8), 1456–1461.

Ye, L.; You, H.; Yao, J.; Su, H. Water treatment technologies for perchlorate: A review, *Desalination* **2012**, 298, 1–12.

Yu, J. I.; Ju, H. Y.; Kim, K. H.; Park, D.W.Cycloadditionof carbon dioxide to butyl glycidylether using imidazolium salt ionic liquid as a catalyst, *Korean Journal of Chemical Engineering* **2010**, 27(2), 446-451.

Yu, Y.; Chen, H.; Liu, Y.; Craig, V. S. J.; Li, L. H.; Chen, Y.; Tricoli, A. Porous carbon nanotube/ polyvinylidene fluoride composite material: Super hydrophobicity/ superoleophilicity and tunability of electrical conductivity, *Polymer* **2014**, 55, 5616–5622.

Zhan, C. G.; Nichols, J. A.; Dixon, D. A. Ionization potential, electron affinity, electronegativity, hardness, and electron excitation energy: Molecular properties from density functional theory orbital energies, *J. Phys. Chem. A* **2003**, 107, 4184–4195.

Zhang, H.; Wang, Z. G.; Zhang, Z. N.; Wu, J.; Zhang, J.; He, H. S. Regenerated cellulose/multiwalled carbon nanotube composite fibers with enhanced mechanical properties prepared with the ionic liquid 1-allyl-3-methyl imidazolium chloride, *Adv. Mater.* **2007**, 19, 698–704.

Zhang, Y.; Gao, H.; Joo, Y. H.; Shreeve, J. M. Ionic liquids as hypergolic fuel, *Angew. Chem. Int. Ed.* **2011**, 50, 9554-9562.

Zhang, Q.; Shreeve, J. M. Ionic liquid propellants: future fuels for space applications, *Chem. Eur. J.* **2013**, 19, 15446-15451.

Zhang, Q.; Shreeve, J. M. Energetic ionic liquids as explosives and propellant fuels: A new journey of ionic liquid chemistry, *Chem. Rev.* **2014**, 114, 10527–10574.

Zhao, D.; Wu, M.; Kou, Y.; Min, E. Ionic liquids: applications in catalysis, *Catalysis Today* **2002**, 74, 157–189.

Zhao, G.; Lu, M. Theoretical studies on the structures and detonation properties of nitramine explosives containing benzene ring, *J. Mol. Model.* **2012**, 18, 2443–2451.

Zhao, H. Innovative applications of ionic liquids as green engineering liquids, *Chem. Eng. Commun.* **2006**, 193, 1660–1677.

Zhao, Y.; Hu, X.; Zhang, Q.; Guan, P. Crystal structure and aggregation behavior in water of ionic liquid 1-hexadecyl-3-methylimidazolium bromide, *Materials Letters* **2010**, 64, 794–797.

Zhao, Y.; Truhlar, D. A new local density functional for main-group thermochemistry, transition metal bonding, thermochemical kinetics, and non-covalent interactions, *J. Chem. Phys.* **2006**, 125, 1-18.

Zhou, Z.; Parr, R. G. Activation hardness: new index for describing the orientation of electrophilic aromatic substitution, *J. Am. Chem. Soc*. **1990**, 112, 5720-5724.

Zhao, Z.; Zheng, W.; Yu, W.; Long, B. Electrical conductivity of poly(vinylidene fluoride)/carbon nanotube composites with a spherical substructure, *Carbon* **2009**, 47, 2112–2142.

Zhu, H.; Mitsuishi, M.; Miyashita, T. Facile preparation of highly oriented poly(vinylidene fluoride) Langmuir–Blodgett nanofilms assisted by amphiphilic polymer nanosheets, *Macromolecules* **2012**, 45, 9076–9084.

Zorn, D. D; Boatz, J.A; Gordon, M. S. Electronic structure studies of tetrazolium based ionic liquids, *J. Phys.Chem. B* **2006**, 110, 11110-11119.

List of Awards

1. "Innovative idea award-2016" from Vikram Sarabhai Space Centre, Thiruvananthapuram for designing "Ionic liquid based green monopropellant for space application".

Mr. Eapen Thomas and Dr. Vijayalakshmi K. P. receiving Innovative Idea Award-2016 from Chairman, ISRO in presence of Director, VSSC.

2. Best paper award, National conference on advanced technologies for material processing and diagnostics, Kochi, September 18-20, 2014,

EAPEN THOMAS
Vikram Sarabhai Space Centre, Indian Space Research Organization

Kappiyil House,
Kanjirappara Post
Kangazha, Kottayam- 686555
Kerala State, India
Email: *eapen85@gmail.com*

EDUCATION

▪	Cochin University of Science and Technology (CUSAT)	*M. Tech. Industrial Catalysis*	7.72 (CGPA)	2013
▪	Mahatma Gandhi University, Kottayam *University topper*	*M.Sc., (Analytical Chemistry)*	81.8%	2008
▪	Mahatma Gandhi University, Kottayam	*B.Sc., (Chemistry)*	85.0%	2006
▪	Navodaya Vidyalaya, Kottayam	*12th*	64.0%	2003
▪	Navodaya Vidyalaya, Kottayam	*10th*	78.7%	2001

RESEARCH TOPIC

Imidazolium based ionic liquids: Computational studies, synthesis and applications

Research highlights

◘ Structural and conformational studies of ionic liquids (ILs) using Gaussian 09 and Materials Studio 4.0 software

◘ Modeled a new ionic liquid as high energetic propellant for future space application- Awarded *"ISRO INNOVATIVE IDEA AWARD -2016"*

◘ Synthesis of novel ILs and extensive characterization using vibrational and NMR spectroscopy and Gas chromatography-mass spectrometry

◘ Explored applications of ILs: (a) IL modified clay for anionic contaminant removal from water, (b) IL modified clay for polymer nanocomposites.

PUBLICATIONS

International Journals: 5

National and International conferences: 8

PROFESSIONAL EXPERIENCES

Vikram Sarabhai Space Centre, Indian Space Research organization   **Feb '13- present**

Research fellow

Synthite Industries Limited, Cochin   **Nov '08- Feb '13**

Junior Scientist

- Analysis of processed, in-process and finalized products by keeping in view the relevant quality standards to be met for food applications

CORE COMPETENCIES

- Computational chemistry
- Chromatography
- Spectroscopy
- Method development and validation

INSTRUMENTS HANDLED

- HPLC
- GC
- FTIR spectrometer
- FTNMR
- UV-Vis-NIR spectrometer
- Pyrolysis GC-MS
- Thermogravimetry
- AAS

PROFESSIONAL AFFILIATIONS

- Life time member of *High Energy Materials Society of India.*

COMPUTER SKILLS

- Software packages :
  Technical: Gaussian 09, Material studio 5.0, NASA chemical equilibrium with applications software, ChemCraft, GaussView, ChemOffice, Origin Pro
- Proficiency in using Windows OS and Microsoft Office Suite

ADDITIONAL SKILLS

- Good at technical writing and documenting
- Strong team building and organizational skills as well as the ability to carry out synthetic research projects independently
- Languages Known: English, Malayalam and Hindi

REFERENCES

1. Dr. Vijayalakshmi K. P.
Scientist/Engineer-SE
Vikram Sarabhai Space Centre, ISRO (Post)
Thiruvananthapuram- 695 022
Email : kp_vijayalakshmi@vssc.gov.in
Phone : 0471-2564478/ +91-9497237242

2. Dr. Benny K. George
Scientist/Engineer-G
Group Director, Analytical, Spectroscopy and Ceramics Group,
Vikram Sarabhai Space Centre, ISRO (Post)
Thiruvananthapuram- 695 022
Email : benny_george@vssc.gov.in
Phone : 0471-2564624/ +91-9447443434

I affirm that the foregoing information in my bio-data is true and correct.

Date: 06-11-2017
Place: Thiruvananthapuram

[Eapen Thomas]